CONTROLLING RESIDUAL METAL IN CARBIDE-DERIVED CARBONS FOR ACID GAS REMOVAL

A Dissertation
Presented to
The Academic Faculty

by

Michael Richard Dutzer

In Partial Fulfillment
of the Requirements for the Degree
Doctor of Philosophy in the
School of Chemical and Biomolecular Engineering

Georgia Institute of Technology
August 2017

CONTROLLING RESIDUAL METAL IN CARBIDE-DERIVED CARBON FOR ACID GAS REMOVAL

Approved by:

Dr. Krista S. Walton, Advisor
School of Chemical and Biomolecular Engineering
Georgia Institute of Technology

Dr. Ryan P. Lively
School of Chemical and Biomolecular Engineering
Georgia Institute of Technology

Dr. Faisal M. Alamgir
School of Materials Science and Engineering
Georgia Institute of Technology

Dr. David S. Sholl
School of Chemical and Biomolecular Engineering
Georgia Institute of Technology

Dr. Pradeep K. Agrawal
School of Chemical and Biomolecular Engineering
Georgia Institute of Technology

Date Approved: July 18, 2017

To my parents, John and Cathy Dutzer

ACKNOWLEDGEMENTS

First, I would like to acknowledge my advisor, Dr. Krista Walton, for her constant guidance, patience, and teachings over the past five years as a part of her research group. She allowed me the necessary space to begin a research project with little more than a title and develop it into a fleshed-out dissertation, to make plenty of mistakes along the way, and to learn from those mistakes to challenge my own preconceived notions and assumptions. Dr. Walton encouraged me to improve upon my weaknesses in writing and public speaking to help me become the person I am today.

I would also like to thank my committee members, Dr. Alamgir, Dr. Agrawal, Dr. Lively, and Dr. Sholl, and my EFRC Thrust Leader, Dr. Jones, for their valuable insight and suggestions to improve this work. Additionally I want to thank the Renewable Bioproducts Institute and the Center for Understanding and Control of Acid Gas-Induced Evolution of Materials for Energy (UNCAGE-ME) Energy Frontier Research Center (EFRC) for sponsoring this work and for the collaborations that they inspired.

Past and present Walton group members (Dr. Bogna Grabicka, Dr. Yang Cai, Dr. Katrina Stults , Dr. Himanshu Jasuja, Dr. Greg Cmarik, Dr. Mike Mangarella, Dr. Chris Murdock, Dr. Cody Morelock, Dr. Ian Walton, Dr. Yi Huang, Dr. Karen Tulig, Dr. Nick Burtch, Dr. Will Mounfield, Dr. Yang Jiao, Ken Onubogu, Erika Garcia-Gutierrez, Lalit Durante, Julian Hungerford, Colton Moran, Jacob Deneff, Jay Joshi, Eli Carter, and Yutao Gong) for their insightful discussions and friendship to make these five years enjoyable and memorable. I’m especially thankful for the advice and mentorship of Dr. Mike Mangarella for introducing me to the world of carbide-derived carbon, the

methodical reasoning and fierceness of Dr. Katrina Stults, and the many enjoyable moments in lab, which taught us that we should never be paired together for actually performing any sort of work, and the constant editing of manuscripts from Dr. Karen Tulig. I also could not have completed my work without Kohl group members for their random assortment of last minute items and characterization equipment and Rod Sefton, the Bunger-Henry building manager, who taught me electrical wiring and helped immensely in the work shop to build necessary items.

Last, but certainly not least, I would like to thank my family and friends for their support, encouragement, and friendship. This work would not have been possible without them.

TABLE OF CONTENTS

LIST OF TABLES

LIST OF FIGURES

LIST OF SYMBOLS AND ABBREVIATIONS

%RH	percent relative humidity
µm	micrometer
Å	ångström
$Al(OH)_3$	aluminum hydroxide
Al_2O_3	aluminum oxide
Al_4C_3	aluminum carbide
$AlCl_3$	aluminum chloride
BET	Brunauer-Emmett-Teller
CDC	carbide-derived carbon
cm	centimeter
CO_2	carbon dioxide
CS_2	carbon disulfide
DI	de-ionized
d_p	particle diameter
EDX	energy-dispersive X-ray spectroscopy
eV	electronvolt
Fe_3C	iron carbide
$FeCl_2$	iron (II) chloride
$FeCl_3$	iron (III) chloride
FTIR	Fourier transform infrared spectroscopy
g	grams or the gravity constant
h	hours

H_2O	water
H_2S	hydrogen sulfide
H_2SO_4	sulfuric acid
HCl	hydrochloric acid
I_D	intensity of the D-band
ID	inner diameter
I_G	intensity of the G-band
in Hg	inches of mercury
IR	infrared
K	Kalvin
KeV	kilo-electronvolt
kV	kilovolts
L	liters
m	meters
m^2/g	meters squared per gram
mg	milligrams
min	minutes
mL	milliliters
mmol	millimole
Mn_2O_3	manganese (III) oxide
Mn_3C	manganese carbide
$MnCl_2$	manganese chloride
Mn_xO_y	manganese oxides
NaOH	sodium hydroxide
NLDFT	non-linear density functional theory

nm	nanometers
NO_x	nitrogen oxides
OD	outer diameter
p/p_0	relative pressure
PFA	perfluoroalkoxy alkane
ppm	parts per million
PSD	pore size distribution
PTFE	polytetrafluoroethylene
PXRD	powder X-ray diffraction
QSDFT	quenched solid state functional theory
s	seconds
S_2Cl_2	disulfur dichloride
SEM	scanning electron microscope
SiCN	silicon carbon nitride
SO_2	sulfur dioxide
SO_3	sulfur trioxide
SS	stainless steel
TGA	thermogravimetric analysis
Ti_3SiC	titanium silicon carbide
TiC	titanium carbide
TiO_2	titanium dioxide
TiS	titanium sulfide
u_{mf}	velocity for minimum fluidization
u_t	terminal velocity
$V_{theoretical}$	theoretical pore volume

wt%	weight percent
XPS	X-ray photoelectron spectroscopy
ε_{mf}	void fraction at minimum fluidization
λ	wavelength
μ	fluid viscosity
ρ_c	density of the solid
ρ_g	density of the fluid
ψ	particles' sphericity

SUMMARY

Activated carbon has been used for millennia. The simple production methods, the capacity to produce them using any organic precursor, and low costs associated with activated carbons contributes to their wide applicability in catalysis and adsorption across numerous industries. Tailoring these carbons for specific interactions by tuning their chemical and physical properties has been a major research focus and allowed the field to expand beyond organic precursors to templated carbons. One such subset of activated carbon is carbide-derived carbon (CDC), where the metal-carbon bonds and crystallinity of the carbide allow for greater control over the physical properties. CDCs are produced through an etching of the metal atoms within a carbide precursor with gaseous chlorine at temperatures exceeding 400°C. The selective reaction between the metal and chlorine produces a metal chloride, which then enters the gas phase for removal. The remaining carbon atoms then rearrange around these metal vacancies to form a porous carbon structure. This work investigates this etching process to create the tools necessary to control metal extraction and examines the resiliency of CDC physical properties against acid gas exposure.

Regulation and public interest has placed emissions from all sources under further scrutiny as they affect human health and the environment. Filters using highly tuned adsorbents are one method to remove harmful emissions before entering the atmosphere, where dilution then produces significant remediation obstacles. Acid gases are a specific type of emission that produces an acid when reacted with water. Sulfur dioxide combines with water to produce sulfuric acid, and the resulting acid rain can corrode buildings and

infrastructure, harm water supplies for drinking and irrigation, and damage agriculture. To remove these acid gases, activated carbons are used; however, a tailored carbon adsorbent such as CDCs could improve their operation and maintenance costs.

Activated carbons typically add specific target interactions through the addition of metal nanoparticles; however, this can block smaller pores necessary for adsorption at low concentrations, and cause non-optimal dispersion of the metal nanoparticles within the carbon structure. This work investigated methods necessary to control the metal extraction process to create partially etched samples with uniform properties. This involved studying reactor design and flow patterns to induce mixing through differences in particle density. Specifically, this work used TiC-CDC and Mn_3C-CDC to examine the relationship between metal chloride properties and metal nanoparticle formation.

This work also probed the effects of SO_2 adsorption and exposure on the physical properties of TiC-CDC. This involved measuring SO_2 adsorption in dry, humid, and aqueous environments. After all exposure conditions, sulfates remained in the porous CDC structure and physical properties suffered accordingly. These properties could be nearly restored through repeated washing steps. However, gas-phase adsorption typically uses a temperature or pressure swing to regenerate the adsorbent, so new regeneration processes would need to be developed to regenerate CDCs.

The overall goal of this Ph.D. research was to uncover the fundamental knowledge that underpinned CDC synthesis techniques and mechanisms to allow for the targeted design of CDCs for adsorptive interactions with acid gases, specifically sulfur dioxide.

CHAPTER 1. INTRODUCTION

1.1 Acid Gases

Since the environmental movement gathered momentum in the 1960s with Rachel Carson's publication of *Silent Spring*, the general public has paid increasing attention to pollution and the environment. The major issue in *Silent Spring* was the spreading of pesticides that ultimately resulted in a drastic decrease in the bird population and a spring without birds chirping. The book inspired people to take action and demand more environmentally friendly pesticides. As time continued, other concerns arose, such as thick smog in cities and acid rain, which led to the US Congress passing the Clean Air Act in 1970 with revisions in 1990.[1]

An acid gas is characterized by its ability to form an acidic solution when mixed with water. These types of gases became an issue when their concentrations in the atmosphere reached high enough levels due to uncontrolled industrialization and growth that they reacted in significant amounts to form acid rain.[2] The contaminated rain etched buildings, caused waterway acidification, and led to human, animal, and environmental health problems. While carbon dioxide is the most common acid gas, sulfur dioxide, nitrogen dioxide, and hydrogen sulfide are more harmful at lower concentrations. Thus removal of these acid gases from industrial emissions is of utmost importance.

There are multiple SO_2 remediation techniques already deployed in the power generation industry due to the Acid Rain SO_2 Reduction Program.[3] These can be divided into once-through or regenerable methods, which can be further classified as wet

or dry methods as seen in Figure 1.1. Methods involving water such as mist eliminators and venturi and packed scrubbers suffer from difficult maintenance due to the corrosive effect of the acidic water created through the contact absorptive removal method and treatment of the purge water or sludge streams.[3, 4] Additionally, using the wet limestone process causes scaling issues where gypsum deposits on the scrubber and related parts. This problem was mitigated with a limestone forced oxidation process, which requires additional compressors and piping for forced air movement within the scrubber.[3] While these limestone oxidation processes work well, they suffer from an inability to regenerate the adsorbent and can use copious amounts of water.

Adsorption allows for the regeneration of the adsorbent bed, instead of a one-way reaction path as seen with various once-through technologies. Here, again, the regenerable processes are divided into two classes: wet and dry. Wet, regenerable processes follow a circular reaction pathway where the sulfur products are either SO_2 or reduced sulfur, depending upon the exact adsorbent used. These processes require a large amount of energy to heat the water and adsorbent mixture to ensure the reaction pathway is followed. For this reason, a dry method is available. By using activated carbon, a gaseous steam can flow through a dry activated carbon bed to remove SO_2. When a temperature swing is induced, a concentrated stream of SO_2 can then be treated more efficiently. However, current activated carbon technology suffers from high operation and maintenance costs, which could be improved through a more tailored activated carbon adsorbent.

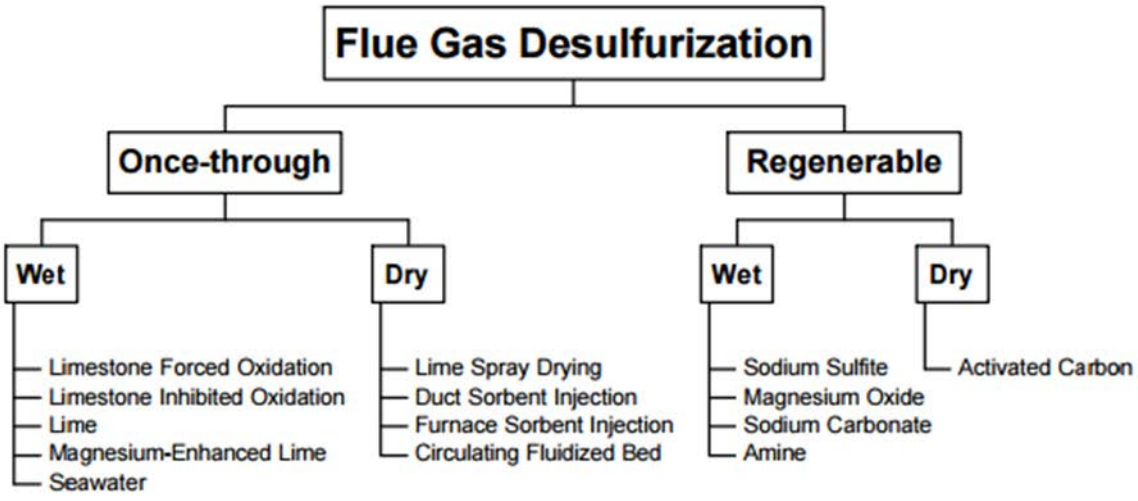

Figure 1.1 – Current technologies for SO_2 capture from flue gases adapted from literature.[3]

1.2 Activated Carbons

Activated carbons have been in use for millennia as ancient Hindus purified drinking water with charcoal as far back as 1500 BC.[5] As the name implies, activated carbons are created from practically any carbon source including lignin,[6, 7] coconut shell,[8-11] and used coffee grounds[9, 11-14] to name a few. These raw materials undergo one of two reactions to create a porous material: physical or chemical activation.[15-17] Physical activation typically occurs in two stages: pyrolysis followed by activation. During a pyrolysis reaction, the carbon precursor is exposed to high temperatures, typically between 600 and 900°C under an inert atmosphere, typically nitrogen or argon, to remove the volatile components. This pyrolyzed char is then activated with steam, carbon dioxide, or air at elevated temperatures to create functional groups and to further the development of pores.[15-17] While physical activation is typically a multi-step synthesis, chemical activation occurs in one step. A carbon source undergoes a chemical treatment, which can consist of either an acidic solution, e.g.

sulfuric acid, phosphoric acid, a basic solution, e.g. potassium hydroxide, sodium hydroxide, or even a metal salt solution, e.g. calcium chloride, zinc chloride, and then is carbonized and activated together in one step generally at lower temperatures around.[18-20] This activation step creates the porous carbon with surface functionality such as acid or base sites.[18, 21-25]

These porous carbons are now considered activated carbons with a wide range of properties. The pore structure is characterized by a wide pore size distribution (PSD) containing micro- (<2 nm in diameter), meso- (between 2 and 50 nm in diameter), and macropores (>50 nm in diameter).[26, 27] Lower pyrolysis and activation temperatures, around 600°C and below, lead to more amorphous carbons, while higher temperatures, around 800°C and above, lead to more graphitic carbons, which tend to have comparably larger pores and lower surface areas.[28, 29] Overall, activated carbons have a wide range of surface areas (500-3000 m^2/g) depending upon the starting material, activated method, and pyrolysis and activation temperatures. Other beneficial properties of activated carbons include low-cost production, chemical and thermal stability, and a limited ability to be tailored through metal impregnation and surface functionality. For these reasons, activated carbons today have wide industrial applications in water filtration,[16, 18, 30, 31] gas separations,[8, 9, 14, 18, 21, 32-35] gas masks to remove chemical agents,[30, 32, 36, 37] and catalyst supports.[18, 38-40]

1.3 Carbide-Derived Carbons

Carbide-derived carbons (CDCs) are a class of activated carbons created through the removal of metal atoms in a carbide. This metal removal typically occurs through a high-temperature etching process, in which chlorine selectively reacts with the metal to

form a metal chloride. With reaction temperatures ranging from 400°C to 1200°C, [41-45] this metal chloride typically readily enters the vapor phase; however, this phenomenon is highly dependent upon the physical properties of the metal chloride. This selective removal of the metal atoms leaves holes in the crystal lattice, and the remaining carbon rearranges itself around these vacancies resulting in a porous carbon. Thus a carbide with minimal surface area transforms into a porous carbon that can achieve surface areas up to 3,200 m^2/g with complete etching of the carbide precursor.[41] As the creation of the pores is due to the removal of the metal atoms, the pores have a similar size resulting in a narrow PSD in contrast to the wide PSD of activated carbons. A high surface area and a narrow, controllable PSD make CDCs ideal for electrochemical applications such as supercapacitors[46-51] and electrodes in lithium-ion batteries,[44, 48, 51-53] in adsorptive applications such as hydrogen or methane storage[54-57] or gas separations,[43, 58, 59] and as catalytic supports.[60-63]

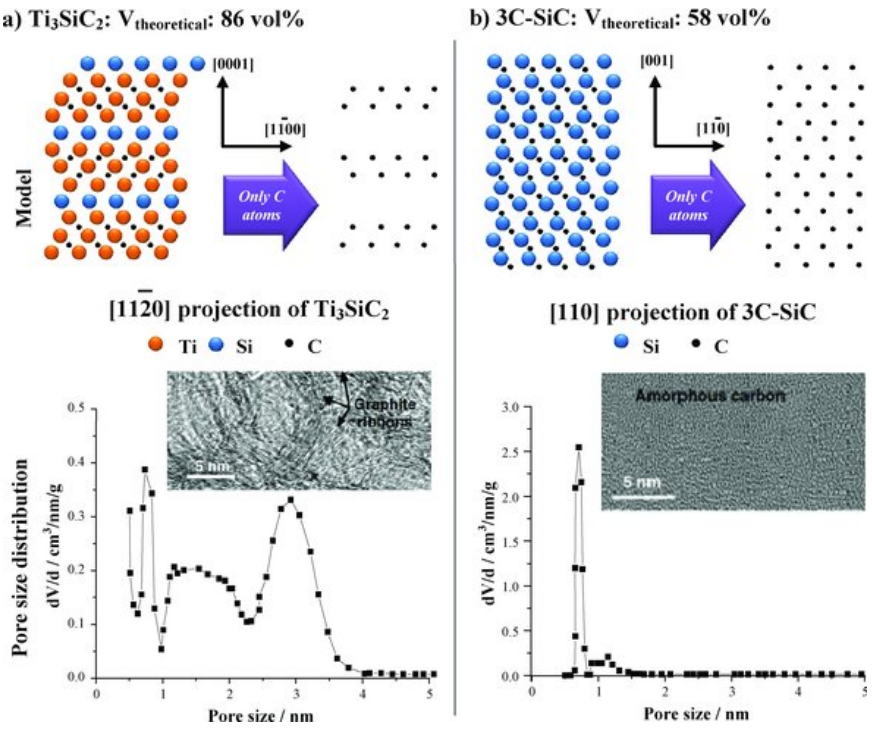

Figure 1.2 – Evolution of the crystal structure to create a porous carbon, where the pores are related to the size and orientation of the metal atoms within the crystal lattice. The figure is adapted from literature.[43]

There are two main factors that allow for ångström-level control over pore size and PSD within the CDC: the size of the metal vacancies and the etching temperature. The arrangement of the metal within the carbide crystal structure vastly affects the resulting PSD as seen in Figure 1.2. This is due to the differing metal atom arrangements and bond lengths found in various crystal structures.[43, 64] Tungsten carbide (WC) with a hexagonal crystal structure[65] or boron carbide with a rhombohedral crystal structure[66] has a broader range of pore sizes than TiC with a cubic structure. Modifying the etching temperature is a straightforward process that affects the carbon reorganization around the metal vacancies. Low to moderate etching temperatures typically results in a microporous CDC, while higher temperatures allow for the formation of mesoporous CDC due to further carbon organization. Thus at lower etching temperatures, the CDC is

typically comprised of disordered amorphous carbon. However, as the etching temperature increases, the carbon is more likely to crystallize into ordered graphite. This ordering affects the porosity of the CDC by creating non-porous graphene sheets, which locally decrease the PSD and globally increase the PSD by creating mesopores.[43, 44, 67] This is seen through a shift in the PSD to larger pores as in Figure 1.3. Other reaction variables will affect the resulting CDC such as the addition of a graphitization catalyst and the etching time.[68, 69] Various other synthesis conditions allow for the formation of other carbon structures such as nanodiamond, graphitic ribbons, and carbon nanotubes among others.[43, 45]

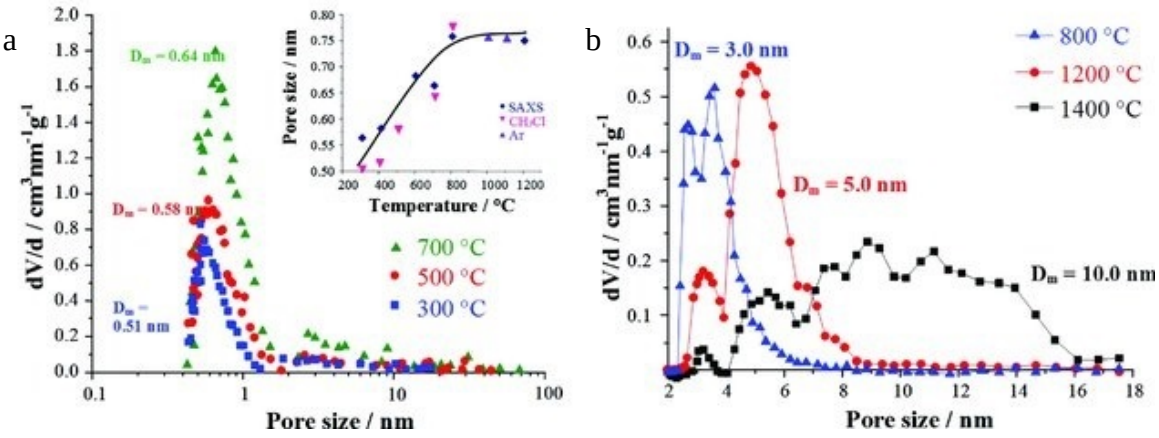

Figure 1.3 – The change in average pore size and in the pore size distribution due to a change in etching temperature for a) Ti_3SiC_2-CDC and b) SiCN-CDC. The figure was adapted from literature.[43]

1.4 Tuning Carbide-Derived Carbons

Activated carbons have proven beneficial not only for their inexpensive cost but for their variety in physical properties that allows them to be highly tailorable for a specific separation process. Like traditional activated carbons, CDCs can be easily tuned for specific applications based upon highly tailorable PSD and high surface areas. These

factors along with high inherent chemical stability make CDCs ideal for gas storage and gas separation applications. However, efforts continue to be made to increase selectivity and capacity for specific adsorbate-adsorbent interactions for catalytic and adsorptive applications. The most common routes are the incorporation of metal nanoparticles or the addition of surface functional groups through the chemical exposure to an acid, base, or other compounds that provide beneficial interaction potentials.

The impregnation of metals in activated carbons is well known to enhance adsorption interactions with target molecules. Activated carbons use metal oxide or metal chloride impregnation to improve adsorption through hydrogen bonding via the oxide or complexation via the chloride metal forms.[11, 22, 70, 71] This method depends on certain features within the carbon structure and for the nanoparticles themselves and typically results in a decrease in surface area and micropores, which innately have strong adsorbate-adsorbent interactions. In gas separation applications, strong, favorable interactions between the adsorbate and the adsorbent's wall are necessary for successful adsorption. These active sites facilitate catalysis, adsorbate selectivity, and stronger adsorbate-adsorbent interactions, especially at low adsorbate concentrations. However, the pores of CDCs are interconnected instead of hierarchical as the pores are created through metal vacancies and carbon reorganization. CDCs thus experience similar issues to activated carbons such as pore blockage and inferior metal integration and dispersion. Yet, the etching reaction to create CDCs allows for the incorporation of metal nanoparticles through other means, namely through metal deposition, nanoparticle addition to the carbide precursor, or an incomplete etching.[60, 61, 72-74]

The surface functionalities of carbon materials can be modified through the addition of functional groups. This is typically done with acid or base treatments to add specific groups to the carbon surface; however, this can also be done through a typical activated carbon physical or chemical activation route. Treatments with potassium hydroxide or CO_2 at temperatures typically above 500°C can further enhance adsorption.[19, 31, 75, 76] Side effects of these post-synthetic modifications include a change in surface area, a decrease in micropore volume, and an increase in mesopore volume.[23, 77] The increased amount of mesopore volume can negate some of the adsorption benefits of having a highly microporous material, but this is hopefully balanced out by an increase in adsorbate-adsorbent interactions.

1.5 Thesis Overview

Due to the combination of high surface areas, control over a narrow PSD, and the ability to innately form metal nanoparticles, CDCs are well suited for tailored interactions with small molecules. However, previous research on the synthesis of CDCs has focused largely on electrochemical applications and target fully etched CDCs. Thus, the methods for creating well-characterized, high surface area CDCs with specific metal sites have not been well developed. Therefore, the overall goal of this Ph.D. research has been to uncover the fundamental knowledge that underpins CDC synthesis techniques and mechanisms to allow for the targeted design of CDCs for adsorptive interactions with a wide range of target molecules. This goal was achieved by completing the following objectives: 1. Develop novel techniques to control residual metal content in CDCs, 2. Control the etching mechanism to form metal nanoparticles from the carbide's residual

metal, and 3. Examine the impact of CDC features on the adsorptive removal of sulfur dioxide.

The first objective is fully covered in CHAPTER 3 of this dissertation; however, a brief summary is included here. Titanium carbide is a well-known CDC precursor that follows the core-shell model of metal extraction. Additionally titanium chloride is highly volatile at low etching temperatures allowing for ideal conditions to study only the control of metal removal from individual particles without graphitization effects from either the chloride or high etching temperatures. Three reactors, with different chlorine flow, were designed and tested: (1) a horizontal flow-over reactor, a vertical flow-through packed-bed reactor, and a vertical fluidized-bed reactor. Only the fluidized-bed reactor controlled the partial etching of titanium carbide-derived carbon (TiC-CDC) with a TiC core and a TiC-CDC shell. Chlorine flow and particle mixing are of particular concern when creating uniform particles with equal residual metal.

Two CDC systems are known to create metal nanoparticles during the etching process: (1) iron carbide-derived carbon and (2) aluminum carbide-derived carbon. Fe_3C-CDC is believed to form iron chloride nanoparticles through a local graphitization reaction.[73] Known graphitization catalysts include iron, cobalt, and nickel, and theoretically, these carbides would form similar metal chloride nanoparticles under similar reaction conditions. Al_4C_3-CDC also forms nanoparticles; however, the mechanism for this metal retention has not been fully investigated.[74] The main theory revolves around the properties of aluminum chloride and aluminum. Aluminum chloride tends to polymerize in the presence of water to form longer chains, exists as both a monomer and dimer, and sublimes from the solid to vapor phase at 180°C.[78-80]

To determine the validity that the metal chloride is polymerizing, a second CDC system was tested for the first time in CHAPTER 5: manganese carbide-derived carbon. Like $AlCl_3$, $MnCl_2$ tends to polymerize in the presence of water and some manganese chloride ions also polymerize.[81, 82] The boiling point temperature of $MnCl_2$ is also higher (1225°C) than typical etching temperatures. This allows for the investigation of CDC formation between the melting and boiling points of the metal chloride for the first time. While metal nanoparticles were not formed during the etching process, metal was partially retained due to the effects of vapor pressure, i.e. the metal fully reacted with the manganese in the carbide, but the chloride could not fully evaporate under the conducted etching conditions.

In CHAPTER 4 TiC-CDC particles were tested to determine their robustness to various environments of sulfur dioxide. TiC-CDC particles with various physical properties were tested in pure, dry SO_2, 85 %RH air with 32±4 ppm SO_2, and a 0.1 M aqueous SO_2 solution. All exposure conditions led to the formation of weakly chemisorbed sulfate groups to the CDC structure with similar sulfur contents regardless of the presence of water or SO_2 concentration. These chemisorbed sulfate species decreased the surface area of the TiC-CDC samples as the exposure time was increased reaching an asymptote around 12 h of exposure. This decrease in surface area is explained by pore blocking as the PSD remained intact despite showing a decrease number of pores. Carbon dioxide was used as a probe molecule to test the adsorption effects of the TiC-CDC samples pre- and post-exposure. CO_2 capacities were decreased due to the decrease in surface area without any benefit from additional interactions between the sulfate groups and CO_2.

CHAPTER 6 reviews the overall conclusions of this work. Specifically discussed are the lessons learned through designing reactors for uniform partial etching, an overview of the theories learned for metal nanoparticle formation in CDCs in a one-pot synthesis, and the effects of SO_2 in various environments on TiC-CDC properties. Recommendations for future work are also included.

Appendix A contains the supplemental information for each chapter.

1.6 References

1. *Air Pollution and the Clean Air Act*. 2014 [cited 2014; Available from: http://www.epa.gov/air/caa/.

2. US, E.P.A. *Acid Rain*. 2015 [cited 2015; Available from: https://www.epa.gov/acidrain.

3. Srivastava, R.K., *Controlling SO_2 Emissions: A Review of Technologies.* National Technical Information Service, 2000(November): p. 113-113.

4. Anderson, W.C., et al., *Innovative site remediation technology : design and application*. 1997: American Academy of Environmental Engineers.

5. Cheremisinoff, P.N. and F. Ellerbusch, *Carbon adsorption handbook.* 1978, Ann Arbor, Michigan: Ann Arbor Science Publishers. 1-54.

6. Rodriguez-Mirasol, J., et al., *Influence of water vapor on the adsorption of VOCs on lignin-based activated carbons.* Separation Science and Technology, 2005. **40**(15): p. 3113-3135.

7. Suhas, P.J. Carrott, and M.M. Ribeiro Carrott, *Lignin--from natural adsorbent to activated carbon: a review.* Bioresour Technol, 2007. **98**(12): p. 2301-12.

8. Bandosz, T.J., *On the adsorption/oxidation of hydrogen sulfide on activated carbons at ambient temperatures.* J Colloid Interface Sci, 2002. **246**(1): p. 1-20.

9. Li, J., et al., *Effect of Relative Humidity on Adsorption of Formaldehyde on Modified Activated Carbons.* Chinese Journal of Chemical Engineering, 2008. **16**(6): p. 871-875.

10. Johns, M.M., W.E. Marshall, and C.A. Toles, *Agricultural by-products as granular activated carbons for adsorbing dissolved metals and organics.* Journal of Chemical Technology and Biotechnology, 1998. **71**(2): p. 131-140.

11. Quiroz Torres, J., et al., *Formaldehyde: catalytic oxidation as a promising soft way of elimination.* ChemSusChem, 2013. **6**(4): p. 578-92.

12. Boonamnuayvitaya, V., S. Sae-ung, and W. Tanthapanichakoon, *Preparation of activated carbons from coffee residue for the adsorption of formaldehyde.* Separation and Purification Technology, 2005. **42**(2): p. 159-168.

13. Carter, E.M., et al., *Gas-phase formaldehyde adsorption isotherm studies on activated carbon: correlations of adsorption capacity to surface functional group density.* Environ Sci Technol, 2011. **45**(15): p. 6498-503.

14. Lu, Y.W., et al., *The effect of activated carbon adsorption on the photocatalytic removal of formaldehyde.* Building and Environment, 2010. **45**(3): p. 615-621.

15. Paraskeva, P., D. Kalderis, and E. Diamadopoulos, *Production of activated carbon from agricultural by products.* Journal of Chemical Technology and Biotechnology, 2008. **83**(5): p. 581-592.

16. Uchimiya, M., et al., *Influence of pyrolysis temperature on biochar property and function as a heavy metal sorbent in soil.* J Agric Food Chem, 2011. **59**(6): p. 2501-10.

17. Evans, R.J. and T.A. Milne, *Molecular Characterization of the Pyrolysis of Biomass .1. Fundamentals.* Energy & Fuels, 1987. **1**(2): p. 123-137.

18. Falcao, E.H.L. and F. Wudl, *Carbon allotropes: beyond graphite and diamond.* Journal of Chemical Technology and Biotechnology, 2007. **82**(6): p. 524-531.

19. Chiang, Y.C. and R.S. Juang, *Surface modifications of carbonaceous materials for carbon dioxide adsorption: A review.* Journal of the Taiwan Institute of Chemical Engineers, 2017. **71**: p. 214-234.

20. Rychlicki, G. and A.P. Terzyk, *The influence of carbon surface oxidation on the adsorption of methanol and ethanol.* Journal of Thermal Analysis and Calorimetry, 1998. **54**(1): p. 343-350.

21. Lisovskii, A., et al., *Adsorption of sulfur dioxide by active carbon treated by nitric acid: II. Effect of preheating on the adsorption properties.* Carbon, 1997. **35**(10-11): p. 1645-1648.

22. Tamon, H. and M. Okazaki, *Influence of acidic surface oxides of activated carbon on gas adsorption characteristics.* Carbon, 1996. **34**(6): p. 741-746.

23. Xing, W., et al., *Oxygen-containing functional group-facilitated CO_2 capture by carbide-derived carbons.* Nanoscale Res Lett, 2014. **9**(1): p. 189.

24. Kuppens, T., et al., *Techno-Economic Assessment of Pyrolysis Char Production and Application - A Review*. Chemical Engineering Transactions, 2014. **37**: p. 67-72.

25. Yin, C.Y., M.K. Aroua, and W.M.A.W. Daud, *Review of modifications of activated carbon for enhancing contaminant uptakes from aqueous solutions.* Separation and Purification Technology, 2007. **52**(3): p. 403-415.

26. Rouquerol, J., et al., *Recommendations for the Characterization of Porous Solids.* Pure and Applied Chemistry, 1994. **66**(8): p. 1739-1758.

27. Jaroniec, M., *Characterization of Nanoporous Materials.* Access in Nanoporous Materials, 2002. **188**: p. 255-272.

28. Rong, H., et al., *Influence of heat treatment of rayon-based activated carbon fibers on the adsorption of formaldehyde.* J Colloid Interface Sci, 2003. **261**(2): p. 207-12.

29. Inagaki, M., *Pores in carbon materials-Importance of their control.* New Carbon Materials, 2009. **24**(3): p. 193-222.

30. Yang, R.T., *Adsorbents: Fundamentals and Applications*. 2003.

31. Otowa, T., Y. Nojima, and T. Miyazaki, *Development of KOH activated high surface area carbon and its application to drinking water purification.* Carbon, 1997. **35**(9): p. 1315-1319.

32. Yoo, J.Y., et al., *Development of an activated carbon filter to remove NO_2 and HONO in indoor air.* J Hazard Mater, 2015. **289**(2): p. 184-9.

33. Baur, G.B., et al., *Activated carbon fibers for efficient VOC removal from diluted streams: the role of surface functionalities.* Adsorption-Journal of the International Adsorption Society, 2015. **21**(4): p. 255-264.

34. Rodriguez-Reinoso, F., et al., *Correlation of methane uptake with microporosity and surface area of chemically activated carbons.* Microporous and Mesoporous Materials, 2008. **115**(3): p. 603-608.

35. Ma, C.J., X.H. Li, and T.L. Zhu, *Removal of low-concentration formaldehyde in air by adsorption on activated carbon modified by hexamethylene diamine.* Carbon, 2011. **49**(8): p. 2873-2875.

36. Jo, W.K. and H.H. Chun, *Application of Fibrous Activated Carbon Filter in Continuous-Flow Unit for Removal of Volatile Organic Compounds under*

Simulated Indoor Conditions. Aerosol and Air Quality Research, 2014. **14**(1): p. 347-354.

37. Moon, H.S., et al., *Adsorption of volatile organic compounds using activated carbon fiber filter in the automobiles.* Carbon Letters, 2014. **15**(3): p. 203-209.

38. Tsoncheva, T., et al., *Activated carbon from waste biomass as catalyst support: formation of active phase in copper and cobalt catalysts for methanol decomposition.* Journal of Porous Materials, 2015. **22**(5): p. 1127-1136.

39. Tsoncheva, T., et al., *Formation of catalytic active sites in iron modified activated carbons from agriculture residues.* Microporous and Mesoporous Materials, 2015. **217**: p. 87-95.

40. Lv, M.M., et al., *Activated-carbon-supported K-Co-Mo catalysts for synthesis of higher alcohols from syngas.* Catalysis Science & Technology, 2015. **5**(5): p. 2925-2934.

41. Borchardt, L., et al., *Preparation and application of cellular and nanoporous carbides.* Chem Soc Rev, 2012. **41**(15): p. 5053-67.

42. Oschatz, M., et al., *Carbide-derived carbon monoliths with hierarchical pore architectures.* Angew Chem Int Ed Engl, 2012. **51**(30): p. 7577-80.

43. Presser, V., M. Heon, and Y. Gogotsi, *Carbide-Derived Carbons - From Porous Networks to Nanotubes and Graphene.* Advanced Functional Materials, 2011. **21**(5): p. 810-833.

44. Gu, W.T. and G. Yushin, *Review of nanostructured carbon materials for electrochemical capacitor applications: advantages and limitations of activated carbon, carbide-derived carbon, zeolite-templated carbon, carbon aerogels, carbon nanotubes, onion-like carbon, and graphene.* Wiley Interdisciplinary Reviews-Energy and Environment, 2014. **3**(5): p. 424-473.

45. Welz, S., M.J. McNallan, and Y. Gogotsi, *Carbon structures in silicon carbide derived carbon.* Journal of Materials Processing Technology, 2006. **179**(1-3): p. 11-22.

46. Zhao, Y.F., et al., *Titanium carbide derived nanoporous carbon for supercapacitor applications.* International Journal of Hydrogen Energy, 2012. **37**(24): p. 19395-19400.

47. Tee, E., et al., *Huge enhancement of energy storage capacity and power density of supercapacitors based on the carbon dioxide activated microporous SiC-CDC.* Electrochimica Acta, 2015. **161**: p. 364-370.

48. Sun, G., et al., *Significantly enhanced rate capability in supercapacitors using carbide-derived carbons electrode with superior microstructure.* Journal of Solid State Electrochemistry, 2011. **16**(3): p. 1263-1270.

49. Tallo, I., et al., *Supercapacitors based on carbide-derived carbons synthesised using HCl and Cl_2 as reactants.* Journal of Solid State Electrochemistry, 2012. **17**(1): p. 19-28.

50. Chmiola, J., et al., *Effect of pore size and surface area of carbide derived carbons on specific capacitance.* Journal of Power Sources, 2006. **158**(1): p. 765-772.

51. Dyatkin, B., et al., *Capacitance, charge dynamics, and electrolyte-surface interactions in functionalized carbide-derived carbon electrodes.* Progress in Natural Science-Materials International, 2015. **25**(6): p. 631-641.

52. Borchardt, L., M. Oschatz, and S. Kaskel, *Tailoring porosity in carbon materials for supercapacitor applications.* Materials Horizons, 2014. **1**(2): p. 157-168.

53. Xu, J., et al., *Mechanism of formation and electrochemical performance of carbide-derived carbons obtained from different carbides.* Carbon, 2013. **64**: p. 444-455.

54. Yeon, S.H., et al., *Enhanced volumetric hydrogen and methane storage capacity of monolithic carbide-derived carbon.* Microporous and Mesoporous Materials, 2010. **131**(1-3): p. 423-428.

55. Seredych, M., et al., *Nitrogen modified carbide-derived carbons as adsorbents of hydrogen sulfide.* J Colloid Interface Sci, 2009. **330**(1): p. 60-6.

56. Jia-lin, J.I., *Hydrogen Chemisorption and Physisorption on the Two-Dimensional TiC Sheet Surface.* Acta Physica Sinica -Chinese Edition, 2014. **30**(10): p. 1821-1826.

57. Yeon, S.H., et al., *Enhanced methane storage of chemically and physically activated carbide-derived carbon.* Journal of Power Sources, 2009. **191**(2): p. 560-567.

58. Lukatskaya, M.R., et al., *Room-temperature carbide-derived carbon synthesis by electrochemical etching of MAX phases.* Angew Chem Int Ed Engl, 2014. **53**(19): p. 4877-80.

59. Sevilla, M. and R. Mokaya, *Activation of carbide-derived carbons: a route to materials with enhanced gas and energy storage properties.* Journal of Materials Chemistry, 2011. **21**(13): p. 4727-4732.

60. Schlange, A., et al., *Titanium carbide-derived carbon as a novel support for platinum catalysts in direct methanol fuel cell application.* Journal of Power Sources, 2012. **199**: p. 22-28.

61. Hasse, B., et al., *Preparation of carbide-derived carbon supported platinum catalysts.* Catalysis Today, 2015. **249**: p. 30-37.

62. Borchardt, L., et al., *Transition metal loaded silicon carbide-derived carbons with enhanced catalytic properties.* Carbon, 2012. **50**(5): p. 1861-1870.

63. Glenk, F., *Synthese von karbidabgeleiteten Kohlenstoffmaterialien im Wirbelschichtreaktor*. 2012, Friedrich-Alexander-Universität Erlangen-Nürnberg.

64. Jeong, M.G., et al., *Effect of lattice structure of silicon carbide on crystal formation of carbide-derived carbon.* Carbon, 2014. **79**: p. 19-27.

65. Tallo, I., et al., *Nanostructured carbide-derived carbon synthesized by chlorination of tungsten carbide.* Carbon, 2011. **49**(13): p. 4427-4433.

66. Dash, R.K., A. Nikitin, and Y. Gogotsi, *Microporous carbon derived from boron carbide.* Microporous and Mesoporous Materials, 2004. **72**(1-3): p. 203-208.

67. Yushin, G., A. Nikitin, and Y. Gogotsi, *Carbide-Derived Carbon*, Y. Gogotsi, Editor. 2006, CRC Press: Boca Raton, FL. p. 237-280.

68. Kaarik, M., et al., *The effect of graphitization catalyst on the structure and porosity of SiC derived carbons.* Carbon, 2008. **46**(12): p. 1579-1587.

69. Maldonado-Hodar, F.J., et al., *Catalytic graphitization of carbon aerogels by transition metals.* Langmuir, 2000. **16**(9): p. 4367-4373.

70. Petit, C. and T.J. Bandosz, *Removal of ammonia from air on molybdenum and tungsten oxide modified activated carbons.* Environ Sci Technol, 2008. **42**(8): p. 3033-9.

71. Wang, Q.S., et al., *Methanol Dehydrogenation to Formaldehyde over Zinc oxide-Modified Sodium Carbonate.* Advanced Engineering Materials Iii, Pts 1-3, 2013. **750-752**: p. 1826-1830.

72. Xu, J., et al., *Effective control of the microstructure of carbide-derived carbon by ball-milling the carbide precursor.* Carbon, 2013. **52**: p. 499-508.

73. Mangarella, M.C. and K.S. Walton, *Tailored Fe_3C-derived carbons with embedded Fe nanoparticles for ammonia adsorption.* Carbon, 2015. **95**: p. 208-219.

74. Moran, C.M., et al., *Synthesis and characterization of aluminum carbide-derived carbon with residual aluminum-based nanoparticles.* Carbon, 2017. **114**: p. 482-495.

75. Portet, C., et al., *Capacitance of KOH activated carbide-derived carbons.* Phys Chem Chem Phys, 2009. **11**(25): p. 4943-5.

76. Oschatz, M., et al., *Carbon dioxide activated carbide-derived carbon monoliths as high performance adsorbents.* Carbon, 2013. **56**: p. 139-145.

77. Wang, H.Y., et al., *Adsorption of acetaldehyde onto carbide-derived carbon modified by oxidation.* Chemical Engineering Journal, 2015. **273**: p. 580-587.

78. Aarset, K., et al., *Molecular structure of the aluminum halides, Al_2Cl_6, $AlCl_3$, Al_2Br_6, $AlBr_3$, and AlI_3, obtained by gas-phase electron-diffraction and ab initio molecular orbital calculations.* Journal of Physical Chemistry A, 1999. **103**(11): p. 1644-1652.

79. Park, K.Y., et al., *Bench-scale decomposition of aluminum chloride hexahydrate to produce poly(aluminum chloride).* Industrial & Engineering Chemistry Research, 2000. **39**(11): p. 4173-4177.

80. Yang, Z.L., et al., *Aluminum fractions in surface water from reservoirs by coagulation treatment with polyaluminum chloride (PAC): Influence of initial pH and OH-/Al_3+ ratio.* Chemical Engineering Journal, 2011. **170**(1): p. 107-113.

81. Lubben, M., A. Meetsma, and B.L. Feringa, *Crystal and Molecular-Structure of Polymeric [$Mncl_2$(Bpy)](N).* Inorganica Chimica Acta, 1995. **230**(1-2): p. 169-172.

82. Morosin, B. and E.J. Graeber, *Crystal Structures of Manganese(II) and Iron(II) Chloride Dihydrate.* The Journal of Chemical Physics, 1965. **42**(3): p. 898-901.

CHAPTER 2. MATERIALS AND METHODS

2.1 Materials

2.1.1 Carbide-Derived Carbon Synthesis

The following CDCs were synthesized using lab-built flow reactors. The specific reactors used are described in detail for each CDC.

2.1.1.1 Titanium Carbide-Derived Carbon

Two titanium carbide (TiC) precursors with different particle sizes are used throughout this work. The horizontal- and packed-bed reactors used the smaller of the particles, which were -325 mesh in size (Sigma-Aldrich, 98 % purity, 307807-100G). These were used as is from the manufacturer without additional sieving. The fluidized-bed reactor operated with the larger particles, which fell between -80 +100 mesh in size (Inframat Advance Materials, 99.7 % purity, 22R-06CG, -60 +100 mesh). These particles were sieved using an 80 mesh sieve (Dual Manufacturing Co., US5-80S) to narrow the particle size distribution, and those particles falling through the sieve were used in the reactor. TiC reacted with a 1:4 mixture of chlorine to argon at 500°C in both reactors to etch selectively the titanium leaving a porous carbon structure.

2.1.1.2 Manganese Carbide-Derived Carbon

The manganese carbide (Mn_3C) precursor was purchased from BOC Sciences (99 % purity) and sieved using a 325 mesh sieve (Dual Manufacturing Co., US5-325S); those

particles larger than 325 mesh were used in the horizontal bed reactor. Mn_3C was etched with a chlorine-to-argon ratio of 1:5 at 500, 700, and 900°C and at various etching times.

2.2 Experimental Methods

2.2.1 Experimental Setup for Carbide-Derived Carbon Synthesis

Three lab-built reactors were used for CDC synthesis: a horizontal-bed reactor, a packed-bed reactor, and a fluidized-bed reactor. The horizontal-bed reactor was designed similarly to those conventionally found in literature, while the packed- and fluidized-bed reactors were based upon a vertical version of the horizontal-bed reactor. When working with chlorine gas, safety is of upmost importance. For this reason, the chlorine lecture bottle, regulator, safety valves, and mass flow meter were housed inside a fume hood along with the reactor and sodium hydroxide scrubber. The switch for a chlorine safety valve was located outside the fume hood for a quick and safe method to stop chlorine flow in case of a leak. Chlorine concentration was also diluted with argon, which acted as a carrier gas for the chlorine, metal chlorides, and other chloride species created during the reaction process and allowed for lower chlorine concentration levels in the reactor.

The pieces in the system are connected via ¼” OD perfluoroalkoxy alkane (PFA) tubing and 316 stainless steel (SS) fittings. PFA has an excellent rating against chlorine (dry and wet) and hydrochloric acid, while 316 SS has an excellent rating against dry chlorine, a fair rating for wet chlorine, and a severe effects rating for hydrochloric acid. As the system is purged with argon before and after every etching reaction, problems arising from the conversion of chlorine to hydrochloric acid in the presence of humidity are largely mitigated. However, issues can be easily seen through the translucent PFA

when the yellow color of HCl appears. No leaks were found through either the PFA or the Swagelok fittings. To monitor for leaks, Cl_2 sensors (Honeywell GAXT-C-DL-Yellow) are deployed inside and outside the fume hood.

2.2.1.1 Horizontal-Bed Reactor

Based upon conventional design from literature,[1-6] the horizontal-bed reactor consisted of a quartz boat (18 mm OD, 16 mm ID, 4" long) placed into a quartz tube (25 mm OD, 19 mm ID, 20" long), which was then placed into a horizontal tube furnace (Thermo Scientific Lindberg® Blue M® Mini-Mite™) for chlorine etching at temperatures between 500 and 900°C. A lecture bottle supplied chlorine gas (Airgas, 99.5 %), which was connected and sealed via a polytetrafluoroethylene (PTFE) O-ring to a chlorine gas regulator with an attached cross purge (Nexair PRS40223731-180D). With the safety of the user in mind, an actuator ball valve (Swagelok SS-43GS4-42AC) was attached downstream. This ball valve was controlled with a switch located outside the fume hood so that the sash could be in the closed position for chlorine flow; this switch also acted as an emergency shut off valve in case of an accidental leak elsewhere in the system. To regulate the flow of chlorine, a mass flow controller (Aalborg**,** GFC17S-VAL6-A0, SKUW-508105 with appropriate power supply PS-GFC-110NA-2) was placed downstream of the ball valve. This chlorine line was combined with a line containing argon (Airgas, Ultra High Purity), and the argon flow rate was set by a mass flow meter. The argon line was also split into two with one line connecting to the chlorine line and the other connecting to the cross purge and chlorine regulator. From here, the chlorine and argon line was expanded from ¼" to 1" via a reducer union (Swagelok, SS-400-R-16). Ultra-Torr Vacuum fittings with Viton O-rings (SS-16-UT-6) connected the reducing

union to the quartz tube. The downstream side of the quartz tube connected to a reducing union with Ultra-Torr Vacuum fittings. This was connected to a sodium hydroxide scrubber in a Büchner flask that is sealed at the top with a rubber stopper, while tubing connected to the hose barb carried the neutralized effluent removal to the top of the fume hood.

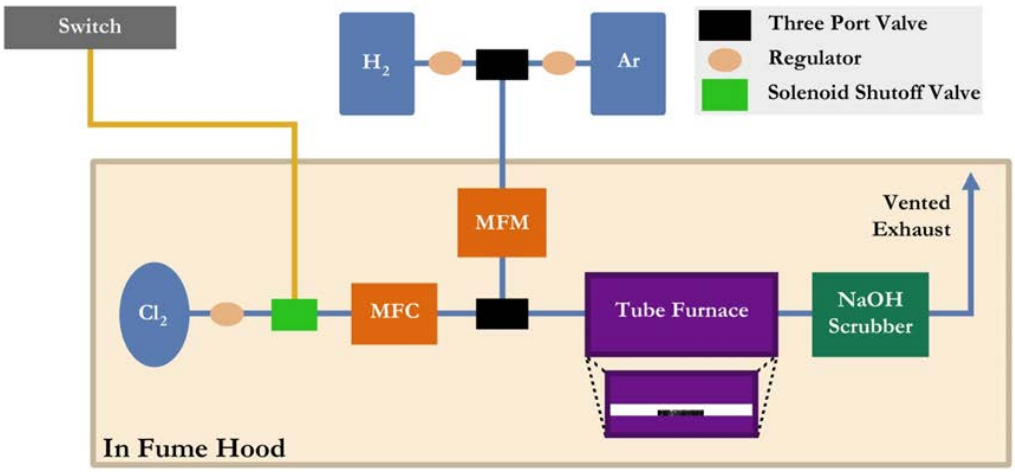

Figure 2.1 – Schematic of the horizontal flow-over reactor design that is typical for CDC synthesis.

2.2.1.2 Packed- and Fluidized-Bed Reactors

The packed- and fluidized-bed reactors utilized the same setup with important usage differences: 1) the particle size of the carbide[7] and 2) the flow rate of the chlorine and argon mixture. The design was modelled off of the horizontal-bed reactor with a vertically mounted furnace instead of a horizontal one. The quartz tubing (19 mm OD, 16 mm ID, 27” tall contained a quartz frit (Technical Glass, porosity 1, 15 mm diameter) 10” from one end of the tube. The other end had the male portion of a vacuum joint (Technical Glass, JTS19-38M) attached. A second piece of quartz tubing contained the

female portion of the vacuum joint (Technical Glass, JTS19-38F) and extended for 5” total until it reached a 90° elbow; the arm of the elbow measured 10”. This elbow portion was necessary to ensure the heat from the reactor did not melt the Viton O-rings in the vacuum fittings that connected the quartz reaction tube to the rest of the system. The vertical tube furnace (Thermo Scientific, 30764-015) and temperature controller (Thermo Scientific, 30783-107) were wired appropriately together. The furnace itself was mounted on a home-built scaffold to support its weight in the opened and closed position with approximately 6” between the lab bench and the bottom of the furnace. As with the horizontal-bed reactor, the chlorine lecture bottle is attached to a regulator with a cross purge which continues to the actuator ball valve and chlorine mass flow controller (Aalborg, GFC17S-VAL6-A0, GFCS-013189 with appropriate power supply PS-GFC-110NA-2). The argon line was again split with one line connecting to the cross purge and the second merging with the chlorine line. Argon flow was controlled by a mass flow meter (Aalborg, P11S1-VF0, 112-02-CA-VA, SKUW-196241). The combined chlorine and argon line was expanded to 19 mm OD via a reducing union (Swagelok, SS-400-R-12). This union and the reactor tube were connected via Ultra-Torr Vacuum fittings with Viton O-rings (Swagelok, SS-12-UT-6). The elbow connected to the reaction tube via the quartz vacuum fittings. The arm of the elbow connected to a reducing union (Swagelok, SS-400-R-6) with the same Ultra-Torr Vacuum fittings. A hose connected the reducing union to a 1 L Büchner flask going through a rubber stopper. The neutralized effluent continued through the hose barb and additional tubing to the top of the fume hood.

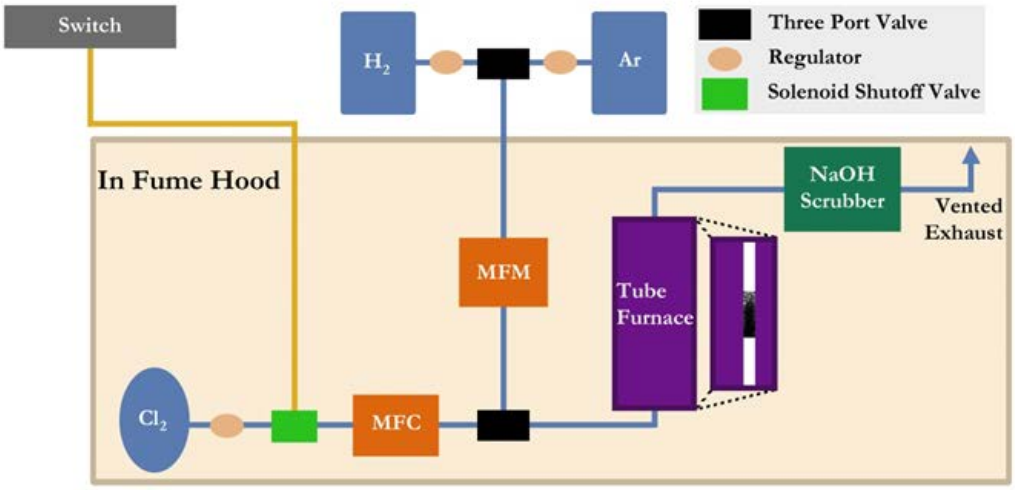

Figure 2.2 - Schematic of the packed- and fluidized-bed reactors.

A fluidized-bed reactor suspends particles by flowing a gas vertically through the bed with sufficient force to oppose the force of gravity on the carbide particles. The flow rate of the gas controls the amount of upward force the bed experiences. By applying too much force, the particles will escape the reactor, while too little force will result in bubbling and unequal mixing of the particles. This force balance allows lighter particles to rise or float to the top of the bed, while the denser particles sink to the bottom. For partial carbide etching, this movement within the bed is favorable. There will always be a chlorine gradient as the reaction consumes the chlorine gas; therefore, mixing the sample while it reacts will negate the chlorine concentration gradient effects found in the horizontal flow-through reactor. As the metal in a particle is removed, the density decreases while the particle shape remains the same, and the upward flow pushes these less dense particles to the top of the bed where the chlorine concentration is lower. Particles that have not been etched to the same extent will move to the bottom of the bed where the chlorine concentration is higher due to their greater density from the embedded

metal atoms. This ensures that each particle will be etched more uniformly than the horizontal reactors currently in widespread use.

Fogler and Brown have presented a set of design equations for fluidized-bed reactors[8] The two most important equations estimate the minimum velocity for fluidization (u_{mf}) and terminal velocity (u_t), beyond which point the particles exit the reactor. The optimal fluid velocity would be between the two extremes. By knowing the bed diameter, the volumetric flow rates can be calculated. The estimation for u_{mf} is below in Equation 2.1:

$$u_{mf} = \frac{\left(\psi d_p\right)^2}{150\mu}\left[g\left(\rho_c - \rho_g\right)\right]\frac{\varepsilon_{mf}^3}{1-\varepsilon_{mf}} \tag{2.1}$$

where ψ represents the particles' sphericity or an evaluation of a particle's nonideality in shape, d_p the particle diameter, μ the fluid viscosity, g the gravity constant, ρ_c the density of the solid, ρ_g the density of the fluid, and ε_{mf} the void fraction at minimum fluidization. ψ ranges in values from 0.5 to 1, where 0.6 is a standard value for typical particles.[8] As the etching process continues and the density of the particles decreases, the velocity needed to fluidize the bed will also decrease. The terminal velocity, u_t, is calculated according to Equation 2.2:

$$u_t = \frac{g\left(\rho_c - \rho_g\right)d_p^2}{18\mu} \tag{2.2}$$

These equations overestimated the flow rates and were reduced by trial and error until suitable flow rates were found for the whole reaction duration; however, they did provide a good estimate of necessary flowrates for particle fluidization.

2.2.2 Material Characterization

2.2.2.1 Powder X-ray Diffraction

Powder X-ray diffraction (PXRD) was performed to determine the crystallinity of the CDC samples. This non-destructive technique uses X-rays focused on a sample at various angles to measure the constructive interference given by parallel planes of crystals. This is due to the X-ray diffracting at the same angle at which it contacts a plane of molecules. By measuring the constructive interference peaks, a diffraction pattern can be created. This technique only works well for crystalline materials such as titanium carbide, but not for amorphous materials such as fully etched titanium carbide-derived carbon as there are no crystals for the X-ray to diffract. The lattice geometry of the crystals can then be gleaned from the diffraction patterns through Bragg's Equation.[9] PXRD patterns were gathered on a PANalytical X'Pert Pro (Cu Kα) for angles between 5-90°.

2.2.2.2 Adsorption Isotherms

Nitrogen physisorption at 77 K was performed not only to determine the amount of nitrogen adsorbed over a specific pressure range but to use this data to calculate the surface area and pore size distribution of the materials. Prior to measurement on a Quantachrome Quadrasorb EVO, samples were activated in a Quantachrome FloVac

Degasser at 150°C under dynamic vacuum for 16 h. The tubes were back filled with nitrogen after degassing and weighed to calculate an activated sample mass. The isotherms were gathered for relative pressures ranging from 3 x 10^{-5} to 0.99; the surface area calculations were performed by applying the Brunauer, Emmett, and Teller model,[10] which assumes a monolayer coverage of nitrogen on the substrate, using a relative pressure range of 0.05 to 0.3. The pore size distribution was calculated using Quenched Solid Density Functional Theory (QSDFT). This is a modified DFT model that calculates pore size distribution for disordered carbons. The model assumes that a slit-shaped pore is present between graphene sheets, while taking into account the heterogeneity of the rough, disordered carbon surface.[11]

Carbon dioxide isotherms were collected at 273 K over a relative pressure range of 4 x 10^{-6} to 0.032 on a Micromeritics 3Flex. Non-Linear Density Functional Theory assuming slit-shaped pores was used to calculate a pore size distribution. Prior to measurement samples were degassed at 150°C for 12 h under dynamic pressure using a Micromeritics Smart VacPrep System.

Sulfur dioxide (SO_2) isotherms at 298 K and pressures up to 3 bar were measured on a lab-built volumetric system. This is a classic pressure decay system equipped with two sample cells so two samples could be measured at the same time. The difference in pressure readings were converted to moles of gas through the use of the Peng-Robinson equation of state with appropriate constants and normalized on a per mass basis.[12] Prior to measurement samples were measured in situ at 150°C under dynamic vacuum.

2.2.2.3 Thermogravimetric Analysis

Thermogravimetric analysis (TGA) was performed to determine the amount of residual metal in the CDCs. This was done by heating the samples under an air flow at 40 mL min^{-1} on a TA Instruments TGA Q50. The sample was allowed to equilibrate at 25°C before ramping to 1000°C at a rate of 5°C min^{-1}; at 1000°C the temperature was maintained for 4 h to ensure all organic matter was combusted. Residual metal calculations were performed assuming all residual material was TiO_2.

2.2.2.4 X-ray Photoelectron Spectroscopy

X-ray photoelectron spectroscopy (XPS) was conducted to determine which elements were present on the surface of the CDCs and how they were bonded. This technique involves exposing the samples to an Al Kα X-ray causing the emission of photoelectrons, which can then be measured for their energy and number. From this binding energy, the element and its bonding nature can be determined.[13] All XPS spectra were gathered on a Thermo K-Alpha XPS, and the samples were degassed for 16 h in a 100°C dynamic vacuum oven.

2.2.2.5 Electron Microscopy

Scanning electron microscopy (SEM) and energy-dispersive X-ray spectroscopy (EDX) were used to determine residual metal location within the samples. This technique uses electrons to interact with the atoms within the samples to give information that can then be pieced together to create an image. Samples were collected one two SEMs: LEO 1530 Thermally-Assisted Field Emission Scanning Electron Microscope (TFE-SEM)

using an accelerating voltage of 10 KeV with an Oxford-7426 EDX detector and a Hitachi SU8030 FE-SEM with an accelerating voltage of 15 KeV with a Thermo NORAN System 7 X-ray microanalysis system for EDX.

For accurate determination of the residual metal location for the large particle sizes, a cross-section of the particles was obtained. To achieve the cross-section of the fluidized-bed samples for SEM/EDX analysis, the following procedure was followed. Each sample was first mounted in a rectangular microtomy mold using EpoxiCure resin and hardener. This initial mounting step was necessary to maintain the area concentration of particles at an appropriate level. The samples were placed under vacuum at -25 in hg while they cured. Upon curing, the samples were then mounted in a 1.25" round mold for polishing. The cured round mounts were then ground to a base finish with 600 grit paper. The polishing steps included 6 µm diamond paste, 1 µm diamond paste, and 0.3 µm alumina. After polishing, the samples were carbon coated with a Quorum Q-150T coater for conductivity.

2.2.2.6 Raman Spectroscopy

Raman spectra are gathered by pointing a laser (λ = 514 nm) at a sample to interact with the vibrations within the molecule. This causes the energy of the laser's photons to shift, which gives rise to Raman spectra. This information can then be used identify the types of bonds within the sample. For CDC samples, the ratio between the I_D (1350 cm^{-1}) and I_G (1580 cm^{-1}) which corresponds to the a_{1g} stretching found in aromatic rings and e_{2g} stretching found in all sp^2 hybridized carbon.[14] This ratio is indicative of the degree of carbon ordering.

2.3 References

1. Dash, R., et al., *Titanium carbide derived nanoporous carbon for energy-related applications.* Carbon, 2006. **44**(12): p. 2489-2497.

2. Perez, C.R., et al., *Structure and Electrochemical Performance of Carbide-Derived Carbon Nanopowders.* Advanced Functional Materials, 2013. **23**(8): p. 1081-1089.

3. Hoffman, E.N., et al., *Synthesis of carbide-derived carbon by chlorination of Ti_2AlC.* Chemistry of Materials, 2005. **17**(9): p. 2317-2322.

4. Chmiola, J., et al., *Effect of pore size and surface area of carbide derived carbons on specific capacitance.* Journal of Power Sources, 2006. **158**(1): p. 765-772.

5. Portet, C., et al., *Capacitance of KOH activated carbide-derived carbons.* Phys Chem Chem Phys, 2009. **11**(25): p. 4943-5.

6. Gogotsi, Y., et al., *Nanoporous carbide-derived carbon with tunable pore size.* Nat Mater, 2003. **2**(9): p. 591-4.

7. Glenk, F., *Synthese von karbidabgeleiteten Kohlenstoffmaterialien im Wirbelschichtreaktor*. 2012, Friedrich-Alexander-Universität Erlangen-Nürnberg.

8. Fogler, H.S. and L.F. Brown, *Predictions of Fluidized Bed Operation Under Two Limiting Conditions: Reaction Control and Transport Control.* Chemical Reactors, 1981: p. 31-54.

9. Bragg, W.L., *The structure of some crystals as indicated by their diffraction of x-rays.* Proceedings of the Royal Society of London Series a-Containing Papers of a Mathematical and Physical Character, 1913. **89**(610): p. 248-277.

10. Brunauer, S., P.H. Emmett, and E. Teller, *Adsorption of gases in multimolecular layers.* Journal of the American Chemical Society, 1938. **60**(1): p. 309-319.

11. Gor, G.Y., et al., *Quenched solid density functional theory method for characterization of mesoporous carbons by nitrogen adsorption.* Carbon, 2012. **50**(4): p. 1583-1590.

12. Smith, J.M., H.C. Van Ness, and M.M. Abbott, *Introduction To Chemical Engineering Thermodynamics*. 7th Ed. ed. 2005: McGraw-Hill.

13. Turner, N.H., *Surface analysis: X-ray photoelectron spectroscopy and Auger electron spectroscopy.* Anal Chem, 1988. **60**(12): p. 377R-387R.

14. Ferrari, A.C. and J. Robertson, *Interpretation of Raman spectra of disordered and amorphous carbon.* Physical Review B, 2000. **61**(20): p. 14095-14107.

CHAPTER 3. THE EFFECTS OF REACTOR DESIGN ON THE SYNTHESIS OF TITANIUM CARBIDE-DERIVED CARBON

3.1 Introduction

Activated carbons are among the oldest and most widely used adsorbents in water purification,[1] gas purification,[2] metal extraction,[3] and multiple other applications[4]. Typical synthesis methods include pyrolysis of precursors including wood, fruit pits, and shells to create a hierarchal pore structure. The resulting carbon structures can be chemically tuned through the addition of functional groups or by inserting metal nanoparticles to target specific compounds in post-carbonization treatment processes.[5, 6] While these methods are beneficial for adsorption, newer carbon sources have been evaluated to target a narrow pore size distribution in the final porous carbon. A uniform pore size distribution enables more effective molecular sieving, which allows for selective adsorption based upon adsorbate size while other aspects of the carbon material introduce selective adsorption based upon chemical properties.

Carbide-derived carbons are a class of amorphous carbon materials defined by their narrow pore size distribution, which is created through the selective removal of the metal heteroatom from a crystalline carbide structure. This removal or etching process is typically done with chlorine gas at temperatures at or exceeding 400°C; the chlorine reacts with the metal to form a metal chloride, which immediately enters the gas phase and is removed from the system. The remaining carbon then rearranges around these metal vacancies to form tunable pore sizes based upon the metal atom size, metal

configuration within the carbide, and etching temperature.[7] In addition to a narrow pore size distribution, CDCs offer physical and chemical properties that make CDCs ideal for use in electronic,[8, 9] adsorption,[10] and reactive applications.[11] For adsorption applications, the addition of metal nanoparticles is beneficial, as seen with other activated carbons, [12, 13] to introduce active sorption sites for the selective adsorption of target molecules. These nanoparticles can be created in a CDC through a partial etching of the carbide precursor,[14] rather than a post-synthesis impregnation necessary for activated carbons. To control the residual metal loading, composition, and location, and in-depth understanding of the reaction mechanism is of utmost importance.

The reactor design can significantly impact how the metal is removed from the bulk carbide sample by affecting the flow of Cl_2 gas at high etching temperatures. Conventionally, CDCs are created in a horizontal flow-over tube reactor.[15] In this reactor design, chlorine must diffuse through the sample bed to react with the metal. If the reaction kinetics are faster than chlorine diffusion through the bed, layers form.[14] A packed-bed reactor allows chlorine to flow through the sample, which should reduce the effects of chlorine diffusion through the bed. However, uneven etching could still occur through the bed, especially if channels form. A fluidized-bed reactor allows for mixing within the bed based upon differences in density and has not been studied widely in CDC literature.[16] The mixing of CDC particles during etching should negate any chlorine diffusion limitations through the bed and create uniformly etched CDC samples.

Titanium carbide is a well-studied CDC that is known to follow a core-shell model of Ti extraction, where Ti is removed first from the surface of the particle according to reaction described in Equation 3.1 and then deeper to the particle's core[17]

$$TiC_{(s)} + 2Cl_{2(g)} \rightarrow TiCl_{4(g)} + C_{(s)}. \quad (3.1)$$

Depending upon the exact reaction conditions, including temperature and chlorine concentration, various products are formed. At higher Cl_2 concentrations (greater than 5:1 Cl_2:TiC), the products are dependent upon reaction temperature. Specifically, at temperatures below 400°C, $TiCl_4$ and CCl_4 are equally thermodynamically favored, while at temperatures exceeding 600°C, only $TiCl_4$ is thermodynamically preferred. However, these thermodynamic calculations were performed in a closed system, while the reactors tested herein are open systems. This allows for the preferential formation of $TiCl_4$ at lower temperatures.[7, 18] In addition, titanium metal[19] and titanium dioxide[20] have shown promise for selectively adsorbing chemicals and is a widely used catalyst. Titanium chloride has not been shown to form metal nanoparticles in literature or act as a graphitization catalyst, which would affect the resulting carbon structure.[21, 22] For these reasons, TiC is a good candidate to understand fundamentally how metal removal on a bulk scale affects individual particle properties. By testing three reactor designs, insight can be gained into controlling the amount and location of residual metal.

3.2 Materials and Methods

3.2.1 Materials

Titanium carbide-derived carbon (TiC-CDC) was synthesized using three different reactors depicted in Figure A.1: (1) a horizontal-bed reactor; (2) a packed-bed reactor; and (3) a fluidized-bed reactor. The samples were prepared under similar conditions for all reactors. The reactors were purged with Ar while being heated to 500°C at a 5°C min^{-1} ramp rate. The samples were etched at 500°C with a mixture of 1:4 Cl_2:Ar

(Airgas, 99.5% purity; Airgas, Ultra High Purity, respectively) ratio, and the reaction time was varied. The horizontal- and packed-bed reactor samples had etching times ranging from 0.50 – 2.00 h in 0.50 h increments with an additional sample etched at 3.00 h, while the fluidized-bed reactor samples had chlorination times ranging from 0.25-1.50 h in 0.25 h increments. After the reaction, the reactors were cooled under a pure Ar purge. A NaOH scrubber is placed at the outlet of each reactor to neutralize the acidic metal chlorides and unreacted Cl_2.

For samples prepared in the horizontal-bed reactor, 2 g of TiC (Sigma-Aldrich, 98% purity, -325 mesh) were placed into a quartz boat and inserted into a quartz tube (OD 1”, 20” long) in a horizontal tube furnace. The previously described etching reaction was performed at a total flow rate of 200 mL min^{-1} and an Ar purge flow rate of 160 mL min^{-1}. For reaction times less than 3.00 h, two horizontal layers were formed in the sample: a black top layer and a silvery gray bottom layer. These layers were mixed for bulk sample analysis for each reaction time. For layer characterization, an additional sample was chlorinated for 1.50 h, and the layers were manually separated. Samples are identified through their chlorination time, e.g. 1.50 h.

For the packed-bed reactor, TiC-CDC samples were created in a vertical tube furnace. 2 g of -325 mesh TiC were funneled into a quartz tube (OD 0.75”, 28” long) containing a quartz frit (Technical Glass, porosity 1). The samples were prepared using the same reaction parameters as the horizontal-bed reactor. Due to the absence of any noticeable layering and system setup limitations, only bulk sample characterization was performed.

The fluidized-bed reactor is similar to the packed-bed reactor; however, Ar and Cl_2 flow rates and TiC particle size were increased to ensure bed fluidization. TiC (Inframat Advanced Materials, 99.7% purity, +100 -60 mesh) was sieved to have a narrower particle size distribution of +100 -80 mesh. The same quartz tube used in the packed-bed reactor was filled with two grams of TiC and then tube placed in the vertical tube furnace. The etching reactions were then performed at a total flow rate of 400 mL min^{-1}. The Ar purge was set to 400 mL min^{-1} while the reactor heated and to 320 mL min^{-1} as the reactor cooled.

3.2.2 Methods

3.2.2.1 Powder X-ray Diffraction (PXRD)

PXRD was used to analyze the crystal structure of the resulting TiC-CDC samples. A PANalytical X-ray diffractometer with a Cu Kα X-ray source (λ = 1.54 Å) was used to obtain PXRD patterns. The samples were evaluated from 15-90° with a step size of 0.02°. All samples were run at room temperature without activation.

3.2.2.2 Nitrogen Adsorption at 77 K

Nitrogen (Airgas, Ultra High Purity) adsorption experiments were performed at 77 K on a Quantachrome Quadrasorb EVO to determine the surface areas and pore size distributions. The surface areas and pore size distributions were calculated using the Brunauer, Emmett, and Teller (BET) theory using $0.005 < p/p_0 < 0.03$ and Quenched Solid Density Functional Theory (QSDFT) assuming slit-shaped pores are present between graphene sheets, respectively.[23, 24] QSDFT is a modified DFT model that

calculates pore size distribution for disordered carbons and takes into account the heterogeneity of the rough, disordered carbon surface.[25] Prior to N_2 adsorption, approximately 25 mg of sample were outgassed under dynamic vacuum on a Quantachrome FloVac Degasser at 150°C for approximately 16 h.

3.2.2.3 Carbon Dioxide Adsorption at 273 K

Carbon dioxide (Airgas, Bone Dry) adsorption isotherms for the fluidized-bed reactor samples were performed at 273 K on a Micromeritics 3Flex. Non-Linear Density Functional Theory (NLDFT) using $4 \times 10^{-6} < p/p_0 < 0.032$ and assuming slit-shaped pores calculated a pore size distribution. NLDFT is another modified DFT model that calculates pore size distribution based upon partial CO_2 adsorption isotherms. Prior to measurement, approximately 30 mg of sample were outgassed at 150°C for 12 h under dynamic vacuum using Micromeritics Smart VacPrep System.

3.2.2.4 Thermogravimetric Analysis (TGA)

Residual metal loading was calculated using thermogravimetric analysis (TGA) data, gathered on a TA Instruments TGA Q50. Approximately 30 mg of sample were placed in a platinum sample pan and allowed to equilibrate at 25°C. Then the sample was heated at 5°C min^{-1} under air flow (Airgas, Ultra Zero Grade) at 20 mL min^{-1} to a final temperature of 900°C, which was maintained for 2 h for the samples created with the horizontal- and packed-bed reactors and for 4 h for the samples synthesized with the fluidized-bed reactor to ensure the carbon was completely combusted due to the larger particle size. Residual metal calculations were performed assuming that all residual material is TiO_2.

3.2.2.5 Raman Spectroscopy

Raman spectra were obtained on a Renishaw system with microscope. Three accumulations, each collected for 40 s, over the spectrum range 100-3200 cm^{-1} were gathered for each sample using a 514 nm laser wavelength and 50x objective lens.

3.2.2.6 Scanning Electron Microscopy (SEM) and Energy-Dispersive X-ray Spectroscopy (EDX)

SEM images of TiC-CDC samples created in the horizontal- and packed-bed reactors were taken on a LEO 1530 Thermally-Assisted Field Emission Scanning Electron Microscope (TFE-SEM). All samples were prepared by suspending the sample in methanol and drop-casting onto aluminum foil. Images were obtained using an accelerating voltage of 10 keV. EDX spectra were obtained using an Oxford-7426 EDX detector attached to the LEO 1530 TFE-SEM. Spectra were gathered using an area scan for the horizontal-bed reactor samples and a point scan for the packed-bed reactor samples.

For samples prepared using the fluidized-bed reactor, a cross-section of the sample was prepared and then imaged via SEM. To achieve the cross-section of the fluidized-bed samples for SEM/EDX analysis, the following procedure was followed. Each sample was first mounted in a rectangular microtomy mold using EpoxiCure resin and hardener. This initial mounting step was necessary to maintain the area concentration of particles at an appropriate level. The samples were placed under vacuum at 0.167 bar (-25 in hg) while they cured. Upon curing, the samples were then mounted in a 3.175 cm (1.25”) round mold for polishing. The cured round mounts were then ground to a base

finish with 600 grit paper. The polishing steps included 6 µm diamond paste, 1 µm diamond paste, and 0.3 µm alumina. After polishing, the samples were carbon coated with a Quorum Q-150T coater for conductivity.

Each sample was examined by SEM using a Hitachi SU8030 FE-SEM. Images were captured of the polished particle cross-sections at various magnifications with a voltage of 15 kV. Elemental assays by EDX of the particle cores, outer shells, and other features of interest were performed with a Thermo NORAN System 7 X-ray microanalysis system integrated with the Hitachi SU8030. This includes point EDX, area EDX, and line scans.

3.2.2.7 X-ray Photoelectron Spectroscopy (XPS)

XPS spectra were acquired for the samples created with the fluidized-bed reactor on a Thermo K-Alpha XPS, monochromated Al Kα source with a double-focusing hemispherical analyzer. High resolution spectra were taken of C1s, N1s, O1s, and Cl2p with 25 total scans at 0.1 eV step size, 50 ms dwell time, 50 eV pass energy, and 400 µm spot size.

3.3 Results and Discussion

3.3.1 Horizontal-and Packed-Bed Reactors

3.3.1.1 Physical Properties

Figure 3.1 illustrates the structural evolution of crystalline TiC to amorphous TiC-CDC as a function of reaction time. For both the horizontal- and packed-bed reactors, the

carbide peaks appear in all samples until 3.00 h of etching, when only a broad peak, which is indicative of amorphous carbon, is seen. As the reaction time increases, the intensity of the TiC peaks decreases. This observation combined with an absence of peaks corresponding to TiO_2 suggests that the residual metal remains in the TiC form and $TiCl_4$ is effectively removed from the samples. In addition, the lack of sharp graphitic peaks suggests that Ti does not act as a graphitization catalyst as other metals such as Fe, Co, and Ni[21] and that the remaining carbon structure only rearranges to form a narrow pore size distribution as a function of temperature.

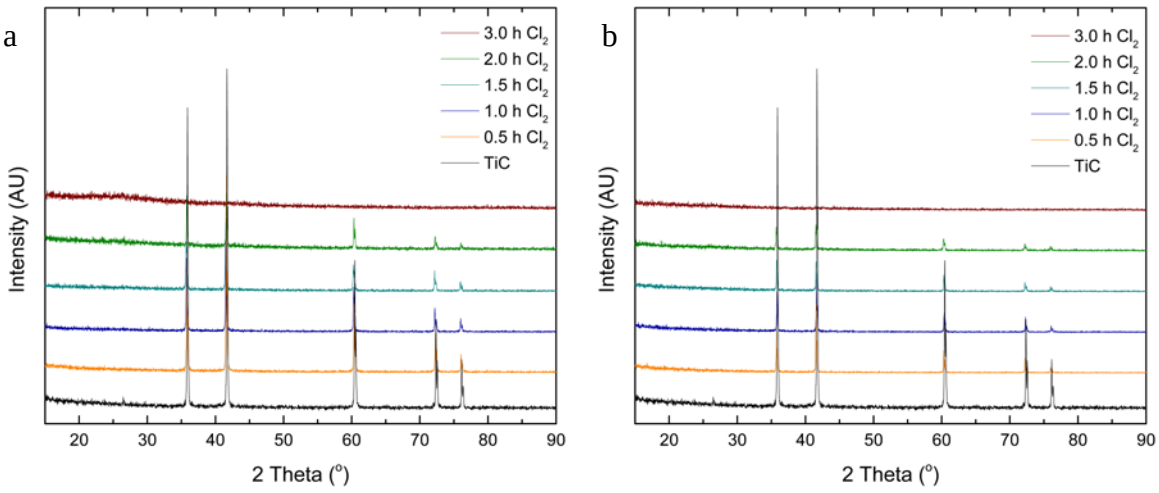

Figure 3.1 – PXRD patterns for (a) horizontal-bed reactor and (b) the packed-bed reactor showing the degradation of the TiC structure to the amorphous carbon of the TiC-CDC.

To calculate residual metal loadings, TGA was performed in air to combust the carbon and convert the residual Ti to TiO_2. This resulting TiO_2 can be used to calculate the residual Ti in the sample after chlorination. As etching reaction time increases, less residual metal remains in the TiC-CDC structure as shown in Figure 3.2; however, the two reactors remove Ti at different rates throughout the etching process. The horizontal-bed reactor removes metal more slowly for chlorination times less than 1.00 h compared

to the packed-bed reactor. At etching times greater than 1.00 h, the reaction in the horizontal-bed reactor removes more metal than the comparable reaction in the packed-bed reactor until 3.00 h of chlorination. At this time, the samples contain minimal residual Ti (~5 wt%). While the chlorination reaction in the horizontal-bed reactor removes Ti in a sigmoidal fashion, the reaction in the packed-bed reactor removes the metal in a more linear fashion. This could suggest that there are more diffusion limitations in the flow-over horizontal-bed reactor than in the flow-through packed-bed reactor.

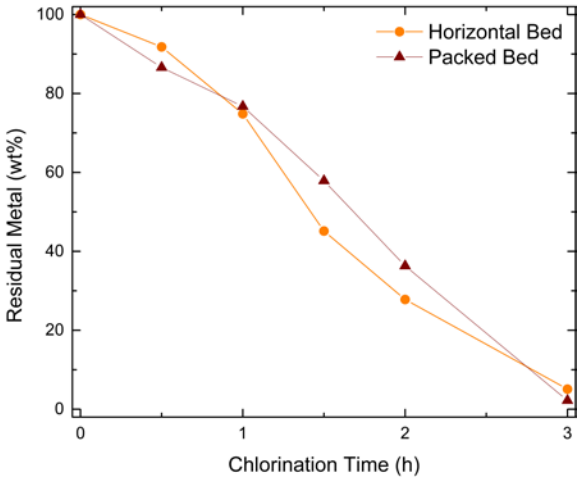

Figure 3.2 – Residual metal loading as a function of chlorination time for both horizontal- and packed-bed reactors.

From N_2 adsorption measurements at 77 K, the BET surface areas were calculated and plotted as a function of residual metal as seen in Figure 3.3. For both the horizontal- and packed-bed systems, the surface areas increase as residual metal loading decreases. While the two systems create TiC-CDC samples with similar surface areas for residual metal loadings greater than 75 wt %, which corresponds to etching times less than 1.00 h,

the packed-bed reactor consistently produces samples with higher BET surface areas at residual metal loadings less than 75 wt %.

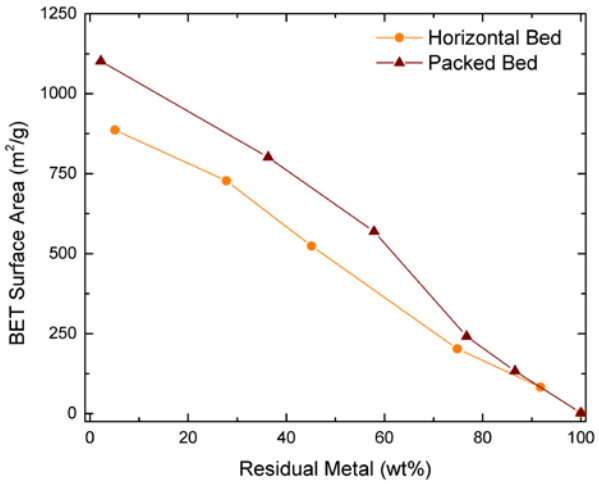

Figure 3.3 – Comparison of BET surface areas as a function of residual metal for TiC-CDC samples created with the horizontal- and packed-bed reactor systems.

The BET surface area is typically a function of the amount of metal removed and the degree of carbon graphitization. For a specific residual metal loading and carbon arrangement, the BET surface areas should be comparable; therefore, Raman spectra were gathered for select samples to determine the effect that reaction time has on the carbon structure. To determine the carbon structure, two bands are notable: the D-band at ~1350 cm^{-1} and the G-band at ~1580 cm^{-1}. The D-band corresponds to a_{1g} stretching that can only be found in aromatic rings, while the G-band corresponds to e_{2g} stretching, which is found in all sp^2 hybridized carbon.[26] The ratio of these intensities (I_D/I_G) is indicative of the degree of carbon ordering. As the I_D/I_G ratio does not appreciably change as seen in Table 3.1, we can deduce that the carbon ordering is similar for all TiC-CDC etching times. This implies that the differences seen in BET surface area are not due to differences in carbon ordering but are due to differences in etching mechanics, which

are caused by differences in the Cl_2 flow patterns and concentration gradients through the bed caused by the various reactor designs.

Table 3.1 – I_D/I_G ratios for select samples for the horizontal- and packed-bed reactors.

Reactor	Sample	I_D/I_G Ratio
Horizontal-Bed Reactor	0.50 h Cl_2	0.88±0.02
	1.50 h Cl_2	0.89±0.03
	3.00 h Cl_2	0.89±0.00
Packed-Bed Reactor	0.50 h Cl_2	0.89±0.02
	1.50 h Cl_2	0.89±0.00
	3.00 h Cl_2	0.89±0.01

3.3.1.2 Residual Metal Location

The above results probe the porosity, carbon structure, and residual metal content of TiC-CDC prepared at various etching times. However, it does not give insight into where the residual metal remains and in which form. For the horizontal-bed reactor, two distinct layers formed for all etching times shorter than 3.00 h: (1) a black top layer and (2) a silver, gray bottom layer. These layers initially appeared to correspond to a TiC-CDC top layer and an unreacted TiC bottom layer as their depth would change depending upon chlorination time. To investigate these layers, an additional sample was chlorinated for 1.50 h, and the layers were hand separated and analyzed through PXRD, TGA, N_2 adsorption isotherms at 77 K, and SEM/EDX. This is an imperfect separation method, but it produces reasonable data to determine how the etching reaction progresses through the bed. The packed-bed reactor produced samples that appear uniform in color with no obvious layering. As these samples could only be analyzed in bulk, SEM and EDX were utilized to determine residual metal location.

PXRD patterns in Figure 3.4 indicate that the top layer, closest to the Ar/Cl_2 flow in the horizontal-bed reactor, is primarily amorphous carbon with low intensity TiC peaks. The PXRD pattern for the bottom layer does not have this broad graphite peak and only contains sharp peaks with high intensities corresponding to TiC. BET surface areas and residual metal loadings point to a similar conclusion. The top layer is highly porous as shown by the high surface area, which is comparable to a fully etched sample. The residual metal loading for the top layer is higher than the fully etched sample; however, this is most likely due to the non-ideal manual separation of the layers. The bottom layer contains almost no porosity and nearly 100 wt% of residual metal. This indicates that the Ti atoms in the bottom layer did not interact with Cl_2. The PXRD patterns along with residual metal loadings and BET surface areas in Table 3.2 suggest that the initial hypothesis was correct: the horizontal-bed reactor produces samples with a fully etched top layer and an unreacted TiC bottom layer, which suggests that the reactor has severe Cl_2 diffusion limitations.

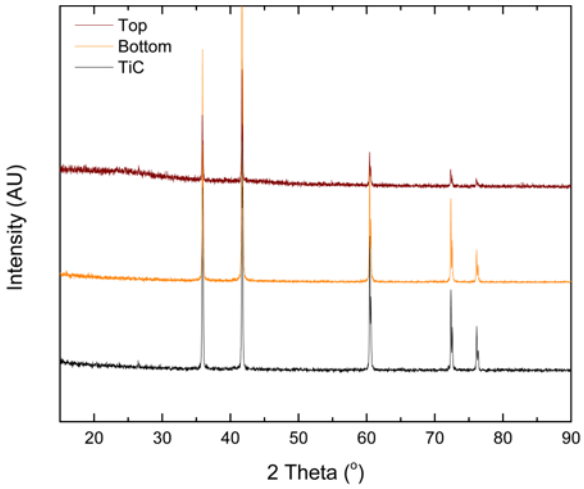

Figure 3.4 – PXRD patterns for the top and bottom layers created in the horizontal-bed reactor at 500°C and etched for 1.50 h.

Table 3.2 – Physical properties of manually separated layers for a TiC-CDC sample etched for 1.50 h along with a fully etched sample using the horizontal-bed reactor.

Sample	BET Surface Area (m^2/g)	Residual Metal (wt%)
Top	882	18.7
Bottom	41	98.3
500°C, etched 3.00 h	867	4.1

In contrast to the horizontal-bed reactor, the packed-bed reactor produces TiC-CDC samples uniform in color. This initially appeared to indicate that a more uniform etching process was occurring and that perhaps the core-shell model of Ti extraction was observed. SEM and EDX were used to verify this hypothesis. From the SEM images alone, depicted in Figure 3.5, there is a difference in contrast between the particles. By performing multiple spot scans for EDX, shown in Figure A.11, we can conclude that some particles contain residual Ti contents similar to unreacted TiC particles as in Figure 3.5a, while others are metal-free as in Figure 3.5b. This indicates that the packed-bed reactor also has Cl_2 diffusion limitations that could be the result of channeling.

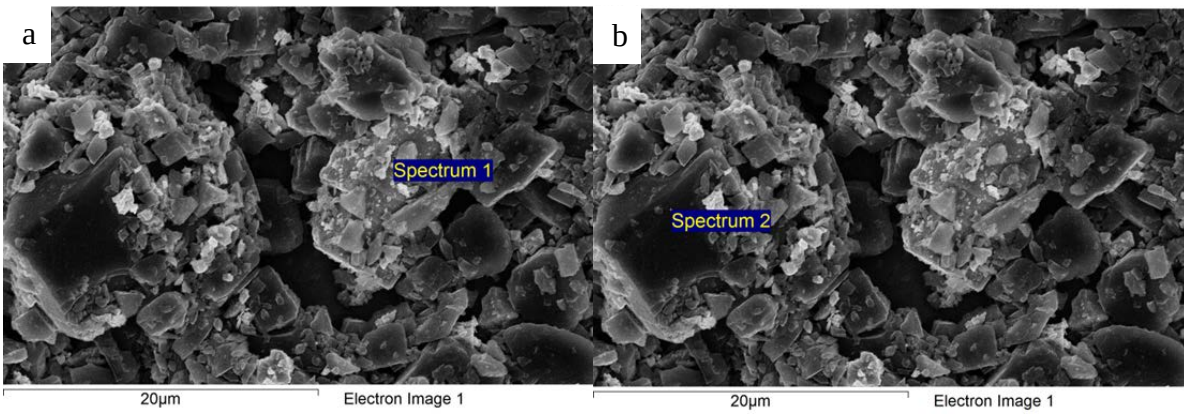

Figure 3.5 – SEM images of a packed-bed reactor sample, where spectrum 1 shows residual Ti and spectrum 2 shows no residual Ti.

The above results signify that reactor design influences the etching process through the TiC reactor bed. The horizontal-bed reactor, by design, is meant to flow the Cl_2 gas over the sample. For the Cl_2 to react with particles at the bottom of the bed, it must diffuse through the bed. However, previous experiments have shown that the reaction between Ti atoms in TiC and Cl_2 occurs quickly. If the reaction kinetics occurs more quickly than Cl_2 diffusion through the bed, layering will occur. Indeed, this result occurs for all etching times that result in significant loadings of residual metal. At the shortest chlorination time (0.25 h), there was a large bottom layer corresponding to unreacted TiC. As the etching time increased, this bottom layer shrank in size until fully disappearing at 3.00 h.

The packed-bed reactor theoretically should minimize the effects from Cl_2 diffusion as the Cl_2 flows through the bed rather than over it. However, the reactor produces no distinct layers due to Cl_2 diffusion limitations nor results in control of the core-shell model. The former would produce top and bottom layers that can be observed by the naked eye in a fully optimized packed-bed reactor. As the Cl_2 flowed from the

bottom to the top of the reactor, the fully etched region would be the bottom layer, and the unreacted region would be the top layer. As this did not occur, Cl_2 diffusion limitations along the bed length were not present here. The latter case also did not occur as shown by the non-uniform etching from particle to particle. The results we found can be explained by channel formation. When TiC particles are less than 150 μm in diameter, the particles often aggregate and form channels where Cl_2 flows preferentially. Instead of layers forming in the direction of Cl_2 flow, unevenness in etching now preferentially occurs radially from these channels. This results in fully etched particles near and partially or unreacted particles farther away from the channels and the bottom of the bed. This result indicates that the packed-bed reactor is also diffusionally limited. The particles in the transition region, those that are potentially partially etched, most likely explains the difference in BET surface areas and the location of the residual metal in the samples between the horizontal- and packed-bed reactors.

3.3.2 Fluidized-Bed Reactor

Both the horizontal-bed and packed-bed reactors are limited by Cl_2 diffusion through the bed, which inhibits control of the etching reaction. In order to mitigate the Cl_2 diffusion limitations, a fluidized-bed reactor was utilized to agitate the particles during the reaction. In a fluidized-bed reactor, the flow rate of the gas through the sample must be high enough to provide enough force to overcome the force of gravity while remaining below the terminal velocity of the particles. The sample is mixed based on the density of the individual particles. Therefore, as the TiC particles are etched, they will become less dense and move away from the Cl_2 source allowing for uniform etching throughout the particles. In order to overcome particle aggregation for proper

fluidization, +100 -80 mesh-sized TiC particles were used with higher Ar and Cl_2 flowrates compared to the previous reactor designs.

3.3.2.1 Physical Properties

PXRD patterns in Figure 3.6 show that the TiC structure quickly changes from the crystalline carbide to amorphous carbon. This degradation occurs more rapidly in the fluidized-bed reactor than for the previous reactors, indicating that metal removal occurs at a higher rate despite a 15x increase in particle diameter. This higher etching rate could indicate that diffusion limitations seen in the previous reactors are now mitigated as the reaction kinetics and subsequent residual metal loadings should be the same among the three reactors. Similar to the PXRD patterns for previous reactor samples, PXRD patterns for the fluidized-bed reactor samples do not have peaks corresponding to TiO_2. As there are no PXRD peaks corresponding to TiC for all etching times, except 0.25 h, we cannot yet conclude the form of residual metal. In contrast to previous PXRD patterns, there is a slight graphite peak at 26° for samples created with the fluidized-bed reactor.

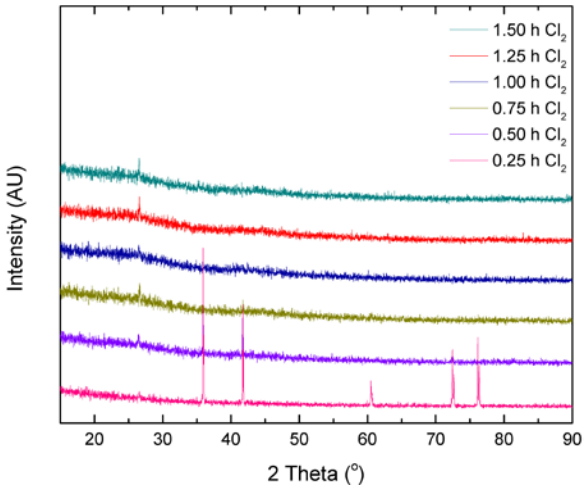

Figure 3.6 – PXRD patterns showing the degradation of TiC into the amorphous TiC-CDC with a slight peak at 26° corresponding to graphite.

By plotting the residual metal content as a function of etching time, Figure 3.7 also shows that Ti atoms are removed at a faster rate in the fluidized-bed reactor compared to the previous reactors (Figure 3.2). The shape of the various curves in these figures indicates that metal removal rate is a function of the flow patterns. Unlike the previous reactors, where the rate of metal removal was linear, the fluidized-bed reactor quickly removes Ti until 0.75 h of etching, when the removal rate drops significantly. As these particles are 15x larger in diameter than those used in the previous reactors, this observation can be attributed to internal particle diffusion limitations rather than interparticle diffusion limitations[17]; however, this does not appear to occur until there is ~5 wt % residual Ti.

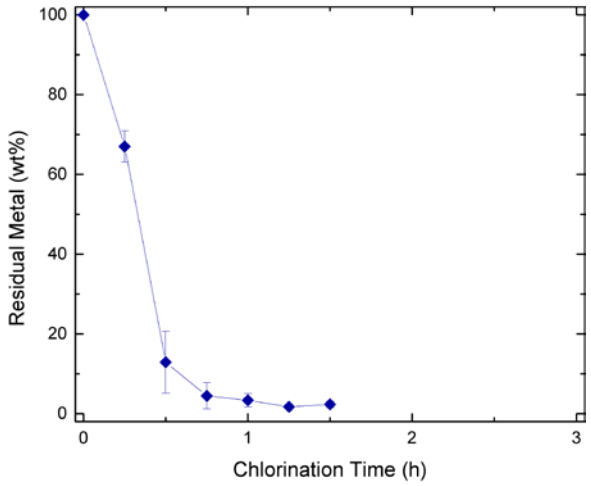

Figure 3.7 – Residual Metal loading (wt%) as a function of etching time (h) for the fluidized-bed reactor.

The porosity of the larger TiC-CDC particles was determined through N_2 adsorption at 77 K. The BET surface areas (Figure 3.8a) have a linear relationship with respect to decreasing residual metal loading. The maximum BET surface area for samples created with the fluidized-bed reactor correspond well with the maximum surface area for samples synthesized in the packed-bed reactor. The linear relationship between residual metal loading and surface area indicates that etching proceeds without significant intraparticle diffusional limitations and that there are minimal diffusion limitations through the particles or the fluidized bed. This suggests that the core-shell model of metal extraction occurs for these samples.

To determine a pore size distribution (PSD), QSDFT calculations were applied to the N_2 adsorption isotherms. For etching times 1.00 h and less, there is a unimodal distribution, as seen in Figure 3.8b. However, for etching times greater than 1.00 h, there is a bimodal distribution with each mode centered on ~3 and ~5 Å in pore radius. To gain a better understanding of this phenomenon, three additional samples were etched for

0.25, 0.50 and 0.75 h and then maintained at 500°C under pure Ar flow for a total duration of 1.50 h. For these additional samples, the bimodal PSD appears which indicates the PSD is also a function of time and not just temperature. This additional time at high temperatures appears to allow the development of structural changes in the carbon that are unrelated to removing Ti atoms from the structure. Figure 3.8d shows PSDs that were also calculated using CO_2 adsorption at 273 K to gain further insight in the micropore region. While QSDFT calculations with N_2 adsorption isotherms are limited to pore sizes ~3 Å in radius, NLDFT calculations with CO_2 adsorption isotherms shows additional pores 1.79 Å in radius. Both models indicate that the PSD is narrow and all pores are microporous as is typical for TiC-CDCs etched at 500°C.

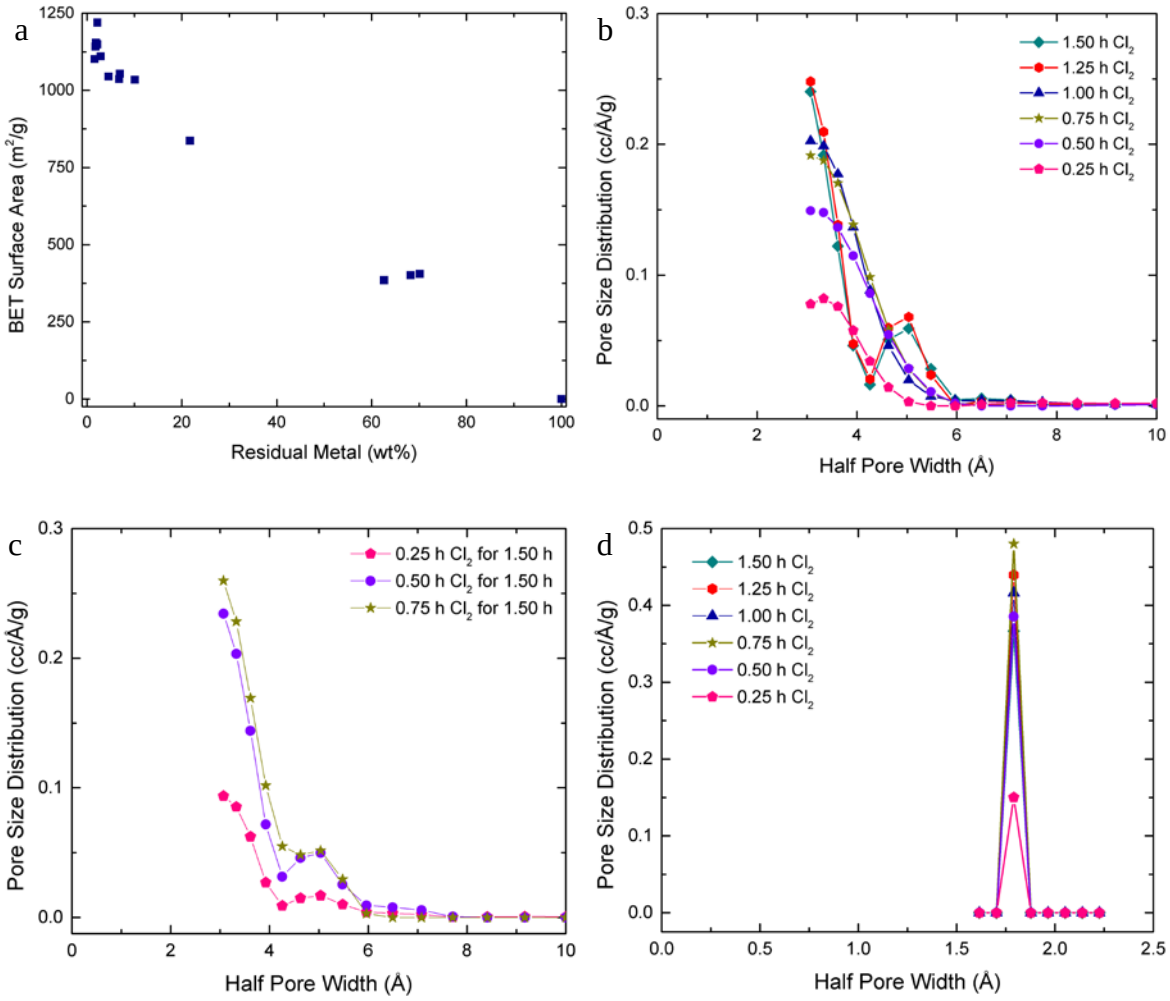

Figure 3.8 – Characterization of fluidized-bed reactor samples including (a) BET surface area for 150-180 µm TiC-CDC particles as a function of residual Ti loading, (b) pore size distributions for various chlorination times calculated with QSDFT using N_2 adsorption isotherms at 77 K, (c) pore size distributions for samples etched for less than 1.00 h and held at 500°C for a total time at 1.50 h, and (d) pore size distributions for various chlorination times calculated with NLDFT using CO_2 adsorption isotherms at 298 K.

Table 3.3 – I_D/I_G ratios for select samples created with the fluidized-bed reactor.

Sample	I_D/I_G Ratio
0.25 h Cl_2	0.64±0.28
0.75 h Cl_2	0.78±0.24
1.50 h Cl_2	0.85±0.09
0.25-1.50 h Cl_2	0.90±0.00
0.75-1.50 h Cl_2	0.82±0.18

Table 3.4 – Composition of elements and types of bonds (atomic %), acquired by processing XPS spectra, within TiC-CDC etched for various times in the fluidized-bed reactor.

	TiC	0.25 h	0.50 h	0.75 h	1.00 h	1.25 h	1.50 h
Element Bond	Atomic %						
C	39.8	83.4	78.3	80.6	78.4	81.7	79.9
C=C	-	60.8	58.6	64.6	54.1	42.5	56.9
C-C	-	0	17.1	0	20.5	24.4	19.4
C-N	-	17.8	12.5	16.9	8.9	13.6	5.3
C-O	-	8.1	6.9	6.4	5.4	4.3	3.6
C=N, C=O	-	5.6	4.7	4.5	4.2	4.8	3.7
C-Cl	-	4.8	4.0	4.7	4.1	7.3	8.7
$C-Cl_2$	-	3.1	2.7	3.0	2.9	3.0	2.4
Cl	-	5.8	7.7	6.9	8.4	8.5	7.8
O	35.7	5.4	4.8	5.9	6.0	3.9	5.4
N	4.1	5.4	9.0	6.6	7.2	5.9	6.9
Ti	20.4	-	-	-	-	-	-

Further insight into the structure including terminal groups on the carbon was gained through Raman spectroscopy and XPS. The I_D/I_G ratio gives an indication to the degree of carbon ordering. In Table 3.3 there is wide variation in the I_D/I_G ratios, where, as time increases, the degree of graphitization decreases. The wide variation within a sample is indicative that this graphitization does not occur evenly throughout the sample possibly due to the large particle sizes and short reaction times. Indeed as the etching time increases, the additional time allows the carbon to reorganize completely throughout a particle, which results in a lower error. When etching a sample for a short period and then holding the sample at 500°C for a total time of 1.50 h, the carbon also has the ability to reorganize fully as evident in the higher I_D/I_G ratio and lower error. This additional organization fully explains the differences seen in the PSD in Figure 3.8b. The XPS spectra show that 40-60 atomic % of the surface is sp^2 hybridized carbon with additional bonds to chlorine (6-10 atomic %), oxygen (7-13 atomic %), and nitrogen (8-20 atomic

%). Carbon-chlorine bonds are due to the reaction itself. While the Ti and Cl_2 reaction is favored at the high reaction temperature, a small amount of Cl^- ions reacts with unpaired carbon electrons while carbon is reorganizing itself around the Ti vacancy. Oxygen bonds most likely occur due to a passive layer of oxygen on the carbide surface before etching occurs. Most likely these C-O bonds are located only on the surface as this is where the carbide passivation occurs. Nitrogen bonds are most likely due to exposure to air after the etching reaction occurs.

3.3.2.2 Residual Metal Location

SEM images were taken of the cross-sections of select samples synthesized with the fluidized-bed reactor, and EDX spectra were gathered to determine the elemental identity of the layers formed within TiC-CDC particles. Figure 3.9 shows that the fluidized-bed reactor controls the core-shell model of Ti extraction. The TiC precursor is cleaved in half and generally shows no cracking from the grinding process due to the physical properties of TiC. In Figure 3.9a and b, the core appears to shrink as the reaction time increases. The shape of the TiC core further supports the layer-by-layer titanium extraction method as the core follows the contour of the particle and the TiC-CDC shell has a uniform thickness. Figure 3.9d shows that etching for 1.50 h completely removes the TiC core. Here the particle contains cracks due to the grinding process used to create these cross-sections. As TiC-CDC is a porous material, air pockets appear between the particle and the resin during the preparation steps.

EDX spectra in Figure A.20-Figure A.23 determine that the core of the particles is TiC, while the shell is comprised of primarily C with Cl, O, and N species. XPS spectra

(Figure A.13-Figure A.19) previously determined the bonds between these four elements. The TiC core in Figure 3.9c appears to be off center; however, this is due to particle shape and the grinding method. Based upon EDX results we can conclude that the core extends to the left underneath the TiC-CDC layer in an iceberg-like formation. We cannot conclude how far this core extends as EDX only penetrates 1-3 μm in depth. Similarly, there is no conclusive evidence of a transition region between the TiC core and TiC-CDC shell.

TGA data combined with the SEM preparation method used to create the cross-sections of the TiC-CDC particles highly suggest that as the etching time increases the TiC core decreases in size. We cannot definitively conclude that the TiC-CDC particles are uniformly etched within a sample based purely upon the limitations of this SEM preparation method. As not all particles are of equal size, the amount of grinding to create this cross-section is not equal for all particles. For this reason, depending on where the cross-section is taken, similar results for different samples are a possibility. However, an understanding of the flow patterns within the fluidized-bed reactor suggests that these samples are more uniformly etched than samples prepared with the horizontal- and packed-bed reactors.

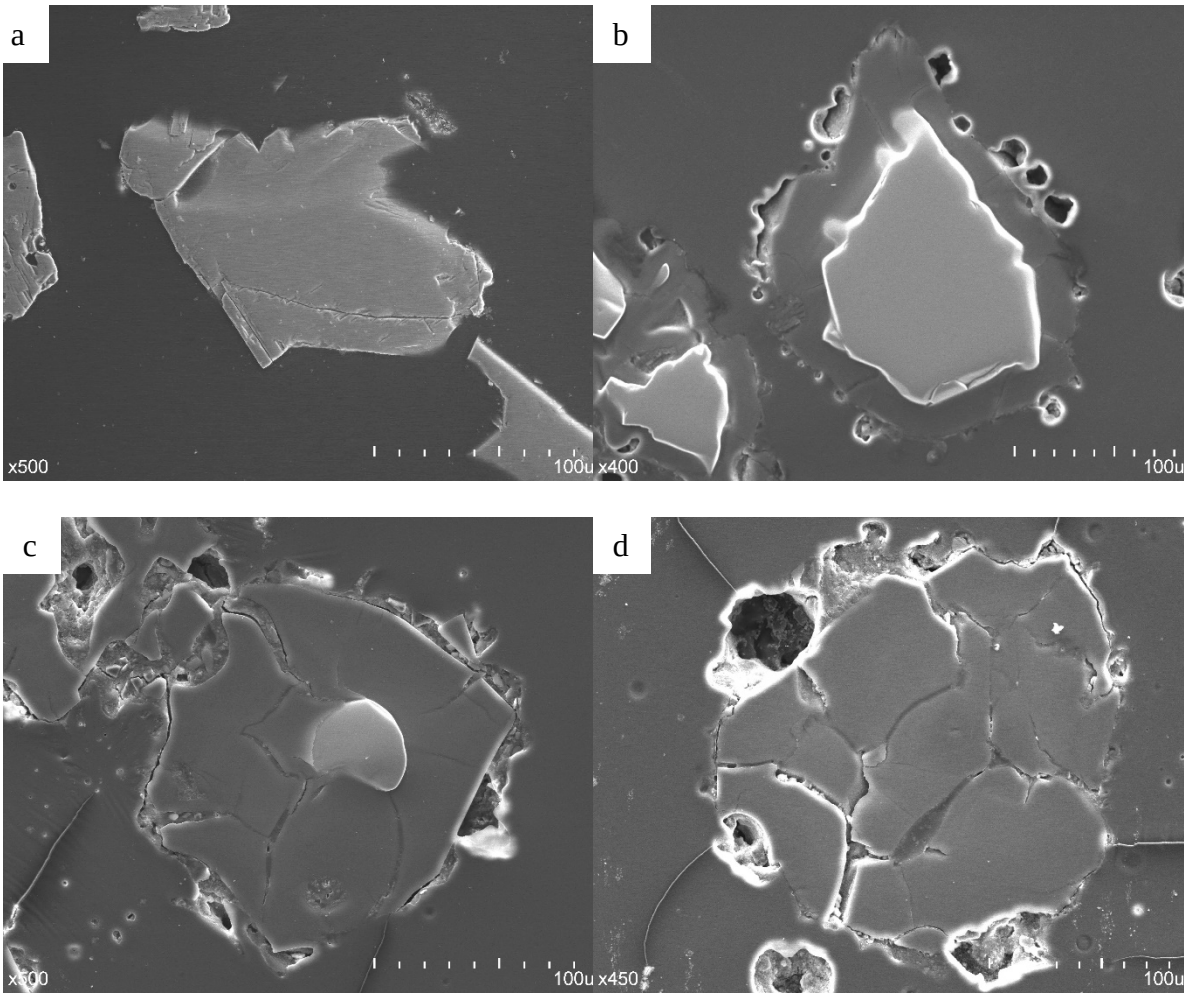

Figure 3.9 – SEM images of a) TiC, b) TiC-CDC etched for 0.25 h, c) TiC-CDC etched for 0.75 h, and d) TiC-CDC etched for 1.50 h showing that the TiC core shrinks as reaction time increases. Pockets between the TiC-CDC shell and the resin are air pockets due to the porous nature of TiC-CDC.

The physical properties and residual metal location are directly related to the gas flow within the fluidized-bed reactor. The reaction between Cl_2 and Ti naturally creates a Cl_2 concentration gradient along the bed length. The highest concentration of Cl_2 is at the bottom, while the lowest concentration is at the top of the bed. The flow within the fluidized-bed reactor separates particles based upon density: denser particles sink to the bottom of the reactor bed as the force from the fluid is not enough to counteract gravity, while less dense particles rise to the top of the bed. TiC-CDC particles change density as

metal is removed; therefore, particles that contain less Ti rise to the top of the bed, while particles with more residual Ti sink to the bottom. Since dense particles with more residual Ti are located where the Cl_2 concentration is highest, these particles will undergo etching at a greater rate than the less dense particles located where the Cl_2 concentration is lowest. Once enough metal is etched, the density decreases and these now lighter particles rise to the top of the bed. This mixing appears sufficient to uniformly etch the particles within the bed and reduce any effects caused by the Cl_2 concentration gradient.

3.4 Conclusions

Three reactor designs and their capacity to partially etch TiC-CDC were investigated. While each reactor produced partially etched samples, their effectiveness was not uniform. The horizontal-bed reactor produced samples consisting of two layers: (1) a fully-etched top layer consisting of pure TiC-CDC and (2) an unreacted bottom layer of TiC. This layering occurs due to diffusional limitations through the bed in the flow-over design. The packed-bed reactor produced samples consistent in color; however, further inspection revealed that the particles were not uniformly etched. Channeling in the reactor bed created particles with a gradient of residual metal; as the distance from the channels increased, the more residual metal remained. Even if channels had not formed within the packed bed, it is unlikely that the resulting samples would have been uniformly etched as there was no mixing of particles to alleviate effects from the Cl_2 concentration gradient. Both the horizontal- and packed-bed reactors are significantly diffusion limited. Alternatively, the fluidized-bed reactor etched TiC following a core-shell mechanism of Ti removal to leave a TiC core with a fully etched TiC-CDC shell. The Cl_2 concentration gradient proved beneficial for the density-based separation and

mixing that occurred within the fluidized bed as the reaction proceeded. Samples synthesized with the fluidized-bed reactor had high surface areas, uniform pore size distributions, and surface groups due to a passive oxide layer on the TiC precursor and Cl^- ions reacting with unpaired C electrons. To control the core-shell mechanism of Ti extraction and leave behind residual Ti, the fluidized-bed reactor was the most successful in creating uniform properties throughout the bed.

3.5 References

1. Otowa, T., Y. Nojima, and T. Miyazaki, *Development of KOH activated high surface area carbon and its application to drinking water purification.* Carbon, 1997. **35**(9): p. 1315-1319.

2. Carter, E.M., et al., *Gas-phase formaldehyde adsorption isotherm studies on activated carbon: correlations of adsorption capacity to surface functional group density.* Environ Sci Technol, 2011. **45**(15): p. 6498-503.

3. Johns, M.M., W.E. Marshall, and C.A. Toles, *Agricultural by-products as granular activated carbons for adsorbing dissolved metals and organics.* Journal of Chemical Technology and Biotechnology, 1998. **71**(2): p. 131-140.

4. Matisova, E. and S. Skrabakova, *Carbon Sorbents and Their Utilization for the Preconcentration of Organic Pollutants in Environmental-Samples.* Journal of Chromatography A, 1995. **707**(2): p. 145-179.

5. Bandosz, T.J., et al., *Effect of surface chemistry on sorption of water and methanol on activated carbons.* Langmuir, 1996. **12**(26): p. 6480-6486.

6. Rychlicki, G. and A.P. Terzyk, *The influence of carbon surface oxidation on the adsorption of methanol and ethanol.* Journal of Thermal Analysis and Calorimetry, 1998. **54**(1): p. 343-350.

7. Presser, V., M. Heon, and Y. Gogotsi, *Carbide-Derived Carbons - From Porous Networks to Nanotubes and Graphene.* Advanced Functional Materials, 2011. **21**(5): p. 810-833.

8. Chmiola, J., et al., *Anomalous increase in carbon capacitance at pore sizes less than 1 nanometer.* Science, 2006. **313**(5794): p. 1760-3.

9. Portet, C., et al., *Capacitance of KOH activated carbide-derived carbons.* Phys Chem Chem Phys, 2009. **11**(25): p. 4943-5.

10. Presser, V., et al., *Effect of pore size on carbon dioxide sorption by carbide derived carbon.* Energy & Environmental Science, 2011. **4**(8): p. 3059-3066.

11. Borchardt, L., et al., *Transition metal loaded silicon carbide-derived carbons with enhanced catalytic properties.* Carbon, 2012. **50**(5): p. 1861-1870.

12. Rezaee, A., et al., *High photocatalytic decomposition of the air pollutant formaldehyde using nano-ZnO on bone char.* Environmental Chemistry Letters, 2014. **12**(2): p. 353-357.

13. Tsoncheva, T., et al., *Cobalt and iron modified activated carbon from coal tar pitch: preparation and application as catalysts for methanol decomposition.* Journal of Porous Materials, 2014. **21**(5): p. 503-512.

14. Mangarella, M.C., et al., *Synthesis of embedded iron nanoparticles in Fe_3C-derived carbons.* Carbon, 2014. **79**: p. 74-84.

15. Gogotsi, Y., et al., *Nanoporous carbide-derived carbon with tunable pore size.* Nat Mater, 2003. **2**(9): p. 591-4.

16. Glenk, F., *Synthese von karbidabgeleiteten Kohlenstoffmaterialien im Wirbelschichtreaktor*. 2012, Friedrich-Alexander-Universität Erlangen-Nürnberg.

17. Becker, P., et al., *Chlorination of titanium carbide for the processing of nanoporous carbon: A kinetic study.* Chemical Engineering Journal, 2010. **159**(1-3): p. 236-241.

18. Yushin, G., A. Nikitin, and Y. Gogotsi, *Carbide-Derived Carbon*, Y. Gogotsi, Editor. 2006, CRC Press: Boca Raton, FL. p. 237-280.

19. Hanson, D.M., R. Stockbauer, and T.E. Madey, *The Interaction of Methanol with a Titanium(001) Surface Investigated Using Photon Stimulated Desorption and Uv Photoemission Spectroscopy.* Journal of Chemical Physics, 1982. **77**(3): p. 1569-1575.

20. Liu, H., et al., *Kinetic analysis of photocatalytic oxidation of gas-phase formaldehyde over titanium dioxide.* Chemosphere, 2005. **60**(5): p. 630-5.

21. Leis, J., et al., *Catalytic effects of metals of the iron subgroup on the chlorination of titanium carbide to form nanostructural carbon.* Carbon, 2002. **40**(9): p. 1559-1564.

22. Xu, J., et al., *Effect of iron catalyst on the microstructure and electrochemical properties of vanadium carbide-derived carbons.* Materials Chemistry and Physics, 2013. **141**(1): p. 540-548.

23. Kleitz, F., et al., *Probing Adsorption, Pore Condensation, and Hysteresis Behavior of Pure Fluids in Three-Dimensional Cubic Mesoporous KIT-6 Silica.* Journal of Physical Chemistry C, 2010. **114**(20): p. 9344-9355.

24. Neimark, A.V., et al., *Quenched solid density functional theory and pore size analysis of micro-mesoporous carbons.* Carbon, 2009. **47**(7): p. 1617-1628.

25. Gor, G.Y., et al., *Quenched solid density functional theory method for characterization of mesoporous carbons by nitrogen adsorption.* Carbon, 2012. **50**(4): p. 1583-1590.

26. Ferrari, A.C. and J. Robertson, *Interpretation of Raman spectra of disordered and amorphous carbon.* Physical Review B, 2000. **61**(20): p. 14095-14107.

CHAPTER 4. THE EFFECTS OF VARIOUS SO_2 ENVIRONMENTS ON TITANIUM CARBIDE-DERIVED CARBON WITH VARIOUS RESIDUAL METAL LOADINGS

4.1 Introduction

Acid gases are ubiquitous in industrial emissions and other industrial applications and cause corrosion issues in the presence of water. Mitigating these effects is of great interest for the safety and protection of humans, the environment, and infrastructure. Therefore, removing these acid gases is of utmost importance. Activated carbons have been studied extensively for their applicability in SO_2 oxidation at room temperature for SO_2 conversion to SO_3 and subsequent formation of H_2SO_4 upon reaction with water.[1-5] Previous studies have shown a correlation between SO_2 adsorption and the oxygen content of the carbon adsorbent. Oxygen-containing functional groups typically are added to the carbon matrix through a nitric acid treatment. These studies have also shown acid-base interactions between SO_2 and the amount of basic sites incorporated into the activated carbon.[1, 5, 6] However, when comparing these two methods (an increase in oxygen content or an increase in basic sites) for dry SO_2 scrubbing applications, the higher oxygen content exhibits higher SO_2 adsorption loadings than acid-base interactions. This behavior is due to the acid bonding more strongly to the oxygen functional groups on the carbon than an acid-base reaction. This stronger bonding, however, makes it more difficult to regenerate the adsorbent.[1]

While much research has focused on the removal of SO_2 and determining factors necessary to increase their adsorption loadings,[7-10] there is a dearth of knowledge focusing on how the carbon's physical properties evolve in various acidic environments. Herein, titanium carbide-derived carbon with various metal loadings was exposed to dry, humid, and aqueous SO_2. A pure, dry SO_2 environment allowed for the measurement of SO_2 adsorption; however, as many real-world applications generally occur in the presence of humidity, we have also investigated adsorption properties at low concentrations of SO_2 with a high relatively humidity. This humid environment ensures the oxidation of SO_2. Two reactions, seen in Equation 4.1 and 4.2, can occur to form both sulfuric and sulfurous acids through a reaction with water vapor and adsorbed oxygen or a sulfur trioxide can form with adsorbed oxygen on the carbon surface as seen in Equation 4.3. The sulfur trioxide then reacts with water vapor to form sulfuric acid. An aqueous SO_2 environment follows a similar reaction scheme to oxidize the SO_2, but the starting acid is diluted sulfurous acid.

$$SO_2 + 1/2\ O_2 + H_2O + C \rightarrow C–H_2SO_4 \quad (4.1)$$

$$SO_2 + H_2O + C \rightarrow C–H_2SO_3 \quad (4.2)$$

$$SO_2 + C–O \rightarrow C–SO_3 \quad (4.3)$$

Traditional activated carbons are typically made from any number of organic sources including wood, fruit pits, and coconut shells; however, a subset of porous carbons has been created from metal carbide precursors. These carbide-derived carbons (CDCs) are a class of porous carbon materials defined by their narrow pore size distribution, high surface areas, and high pore volumes, which are all created through the

use of a high temperature, halogen reaction. Chlorine gas selectively reacts with the metal in metal carbides at temperatures ranging from 400-1200°C to form a metal chloride, which is then vaporized at the reaction temperature and removed from the carbon structure. The remaining carbon atoms then rearrange around these metal vacancies to form the porous carbon structure. A key advantage of CDCs over traditional activated carbon is that this narrow pore size distribution is more easily tunable depending upon the starting carbide precursor and etching temperature.

4.2 Experimental Materials and Methods

4.2.1 Materials

A fluidized-bed reactor was used to create titanium carbide-derived carbon (TiC-CDC) samples with various amounts of residual metal. The reactor was purged with Ar while being heated to 500°C at a 5°C min^{-1} ramp rate. The samples were etched at 500°C with a mixture of 1:4 Cl_2:Ar (Airgas, 99.5% purity; Airgas, Ultra High Purity, respectively) ratio, and the reaction time was varied. TiC (Inframat Advanced Materials, 99.7% purity, +100 -60 mesh) was sieved to have a narrower particle size distribution of +100 -80 mesh, 150 to 180 μm in diameter. The quartz tube was filled with two grams of TiC, and the tube was placed in the vertical tube furnace. The etching reactions were then performed at a total flow rate of 400 mL min^{-1}. Samples were etched for 0.25 h and 1.50 h, while an additional sample was etched for 0.25 h and held under heat for an additional 1.25 h for a total time at 500°C of 1.50 h. The Ar flow rate varied depending upon the specific stage in the reaction sequence. During the heating period, the Ar flow rate was maintained at 400 mL min^{-1}; however, once at the etching temperature and during cooling

after etching with Cl_2, the flow rate was maintained at 320 mL min^{-1}. The reasons for this decrease in Ar flow rate were twofold: (1) the TiC particles were denser than etched TiC-CDC particles, therefore, requiring a lower flow rate to maintain fluidization and (2) the combined flow rate for Ar and Cl_2 could not exceed 400 mL min^{-1} to remain below the terminal velocity of the particles. A NaOH scrubber was placed at the outlet to neutralize the acidic metal chlorides and unreacted Cl_2.

4.2.2 Acid Exposure

Dry sulfur dioxide (SO_2) (Airgas, Anhydrous, 99.98% Purity) isotherms at 25°C were measured using a lab-built volumetric system. The samples were activated by heating the material at 150°C for 16 h under dynamic vacuum yielding approximately 30 mg of activated sample for SO_2 exposure at pressuring ranging from 0 to approximately 2.5 bar. This exposure took place over approximately 3.5 h. After the adsorption measurement, the samples were held under vacuum for 24 h to remove the SO_2 from the system and samples. The Peng-Robinson equation of state was used to convert SO_2 pressure readings to moles. The difference between the beginning and final amount of moles was normalized by sample mass to determine the adsorption loadings.

Activated samples were exposed to 32±4 ppm of SO_2 in air with relative humidity of 85% for 72 h at room temperature (25°C). The acid gas mixture was prepared per previous literature and was described in our previous work.[11-13] Briefly, the SO_2 gas was generated from a 400 mL aqueous solution of 0.5 mg mL^{-1} $NaHSO_3$ at a pH of 3.7 at 45°C. Air was bubbled through the solution at 60 mL min^{-1} and carried humid SO_2 gas stream to the exposure unit (Secador mini-desiccator). Gas concentration inside the

transparent exposure unit was continuously monitored with the portable PAC 7000 SO_2 detector purchased from Dräger. The relative humidity was continuously monitored by a commercially available humidity sensor (Ambient Weather). The $NaHSO_3$ solution was refilled every two days to maintain SO_2 levels. The water bath, acid gas generator unit, and exposure unit were all placed inside a fume hood with high exhaust rates and handled with caution at all times. Samples were fully characterized with no post-exposure washing. Additional XPS and N_2 sorption at 77 K tests were performed twice after each post-exposure washing sequence: (1) after decanting with DI water three times and rinsing with methanol, and (2) after sonicating in DI water for 0.25 h and rinsing in methanol. Samples were dried under dynamic vacuum at 60°C prior to testing to remove all methanol.

TiC and TiC-CDCs were also exposed to aqueous solutions of SO_2 at 0.1 M (~82000 ppm), which were prepared by diluting a stock solution of SO_2 (6.2 wt%, Sigma Aldrich) with deionized water that had been degassed with N_2. The solution was introduced into a 20 mL glass vial with PTFE-lined silicone septum in the cap with approximately 50 mg of TiC or TiC-CDC, and the vial sealed. The head space of the vial was purged with Ar through the septum to eliminate CO_2. The solutions were briefly sonicated to ensure good dispersion. The vials were then stored at room temperature or in an oven set to 75°C. After the desired length of exposure time, particles were filtered then washed copiously with deionized water and methanol and finally dried under dynamic vacuum at 60°C.

4.2.3 Methods

4.2.3.1 Thermogravimetric Analysis (TGA)

To determine the amount of residual metal in the TiC-CDC samples, the organic species were combusted and the residual titanium was converted to an oxide. A platinum sample pan with approximately 30 mg of TiC-CDC sample was placed in a TA Instruments TGA Q50 and equilibrated to 25°C. After the temperature equilibration, the instrument increased the temperature to 900°C at a rate of 5°C min^{-1} under air flow (Airgas, Ultra Zero Grade) at 40 mL min^{-1}. The temperature of the instrument was maintained at 900°C for 4 h to insure oxidization of all species. Residual metal calculations were conducted assuming that only TiO_2 remained.

4.2.3.2 Nitrogen Adsorption at 77 K

Nitrogen (Airgas, Ultra High Purity) adsorption experiments were performed at 77 K on a Quantachrome Quadrasorb EVO to determine the surface areas and pore size distributions. The Brunauer, Emmett, and Teller (BET) theory using $0.005 < p/p_0 < 0.03$ was used to calculate the surface area, while Quenched Solid Density Functional Theory (QSDFT) assuming slit-shaped pores was used to calculate the pore size distribution for samples pre- and post-acid gas exposure.[14, 15] By taking into account the heterogeneity of the rough, disordered carbon surface, QSDFT gives a more accurate accounting of the pore size distribution over the standard DFT model.[16] A Quantachrome FloVac Degasser activation yielded approximately 25 mg of sample at 150°C for approximately 16 h prior to N_2 adsorption.

4.2.3.3 Carbon Dioxide Adsorption at 273 K

CO_2 adsorption isotherms at 273 K were collected using a Micromeritics 3Flex. N_2 physisorption at 77 K combined with QSDFT calculations probed the micropore region of pores as small as to 6.14 Å in diameter, while CO_2 physisorption at 273 K with NLDFT calculations probed pores as small as 3.23 Å in diameter. Using data from both CO_2 and N_2 isotherms allowed for a more complete understanding of the micropore region. The sorption region followed a geometric distribution of relative pressures in the range $4 \times 10^{-6} < p/p_0 < 0.032$. A pore size distribution was calculated using Non-Linear Density Functional Theory (NLDFT) assuming slit-shaped pores. Approximately 30 mg of sample was activated at 150°C for 12 h under dynamic vacuum using a Micromeritics Smart VacPrep System.

4.2.3.4 X-ray Photoelectron Spectroscopy (XPS)

Chemical bonds were probed using a Thermo K-Alpha XPS with a monochromated Al Kα source with a double-focusing hemispherical analyzer. The elements for high resolution spectra included C1s, O1s, Cl2p, and S2p with 25 total scans at 0.1 eV step size, 50 ms dwell time, 50 eV pass energy, and 400 μm spot size.

4.3 Results and Discussion

TiC-CDC samples were prepared in a fluidized-bed reactor by flowing a mixture of Cl_2 and Ar at 500°C. The etch time was varied for two samples, 0.25 h and 1.50 h, in order to vary the residual metal content. Additionally, a third sample was prepared by etching TiC with the same Cl_2 and Ar mixture for 0.25 h, then held at the etching

temperature under a pure Ar flow. Previous research has shown that additional time at the etching temperature without Cl_2 flow ensured that the pores had ample time to reach a stable configuration for large TiC-CDC particles.[17] These samples were then tested for their residual metal contents and BET surface areas. As seen in Table 4.1, the samples etched for 0.25 h contained roughly 63 wt% of residual Ti, while the samples etched for 1.50 h contained 3 wt% Ti. Due to the method to determine residual metal content, these represent a maximum value as there was the potential that the remaining residue contains ash and was not completely TiO_2. The surface areas for completely etched materials compares favorably to known literature[18-20] at 1216 m^2 g^{-1}, while samples etched for 0.25 h had BET surface areas around 465 m^2 g^{-1}. Holding the samples at 500°C for an additional 1.25 h did not significantly alter the surface area. However, this additional time at temperature modified the pore size distribution (PSD) as seen in Figure 4.4 and was consistent with previous work.[17] These samples were then exposed to SO_2 in dry, humid, and aqueous environments to determine how various acidic situations affected the physical properties of these carbon materials.

Table 4.1 – BET surface area and residual metal content for TiC-CDC samples created at 500°C.

Sample	Surface Area (m^2 g^{-1})	Residual Metal (wt%)
0.25 h	478±89.9	61.7±11.9
0.25 - 1.50 h	451±65.1	64.9±3.9
1.50 h	1216±57.4	2.91±2.5

TiC-CDC samples were exposed to dry SO_2 in a volumetric system to measure adsorption equilibrium at pressures up to 2.5 bar. The resulting Type I isotherm, shown in

Figure A.26, suggests that the SO_2 interacts favorably with the carbon walls. This behavior was generally unexpected for carbon materials due to the non-polarity of the carbon and the polarity of the SO_2;[6] however, favorable interactions between the carbon walls and SO_2 can be introduced with oxygen containing moieties.[5] XPS data show that there was oxygen present in the starting CDC matrix most likely due to the CDC reacting with ambient air and humidity after the etching reaction.[21] While the adsorption loading of SO_2 onto TiC-CDC samples varies depending upon the surface area of the material – higher surface area materials displayed higher SO_2 adsorption – all isotherms reach saturation at 0.5 bar.

Fresh TiC-CDC samples were exposed separately to 32±4 ppm of SO_2 in 85% RH at 25°C for 72 h and to a solution of SO_2 in deionized water at a concentration of 0.1 M at 25 and 75°C for 6, 24, and 72 h. Due to the exposure methods for humid and aqueous SO_2 exposure, SO_2 adsorption loadings could not be determined. The humid samples were characterized three times: (1) as exposed without washing, (2) washed with DI water and rinsed with methanol, and (3) sonicated in DI water and rinsed with methanol. The aqueous samples were washed with deionized water and rinsed with methanol after removal from the acidic solution.

Activated carbons are structurally stable in the presence of acids. However, their physical properties can be modified by chemisorbed species. For TiC-CDC samples exposed to SO_2, XPS spectra were first gathered to determine any changes to the surface chemistry from the exposure methods mentioned above. Indeed, these spectra displayed changes that suggested sulfur functional groups were being added to the carbon structure.

XPS results in Figure 4.1 show that samples exposed to dry SO_2 contain about 1 atomic percent of sulfur remaining on the surface. This compares favorably to both the humid samples washed once and aqueous exposed samples at 25°C. Humid samples without washing contain higher amounts of residual sulfur species compared to the aqueous-exposed samples at 75°C. This is likely due to their post-exposure treatments, as the humid samples were initially not washed post-exposure. The subsequent reduction in sulfur content upon the initial and secondary washes indicate that these sulfur species are weakly chemisorbed to the surface as they were removed through contact with water but not through the temperature or pressure swing that samples underwent prior to XPS measurement. For aqueous SO_2 exposure, residual sulfur content is dependent upon temperature. At higher temperatures, the amount of residual sulfur roughly doubled for partially etched samples and quadrupled for fully etched samples exposed to aqueous SO_2 at 75°C compared to exposure at 25°C. The higher temperature likely allows for a higher rate of reaction between the aqueous SO_2 and the oxygen in CDC matrix or the water to form sulfate groups, which then bind to the carbon surface. The XPS data indicate that most of the sulfur was added in significant amounts until 6 h of exposure. After this period, the sulfur content remains mostly constant. These three exposure environments indicate that at 25°C, the amount of added sulfur species was not dependent upon the exposure method or the concentration of the SO_2. Indeed, as all samples have similar levels of sulfur, this likely represents the maximum amount of chemisorbed SO_2.

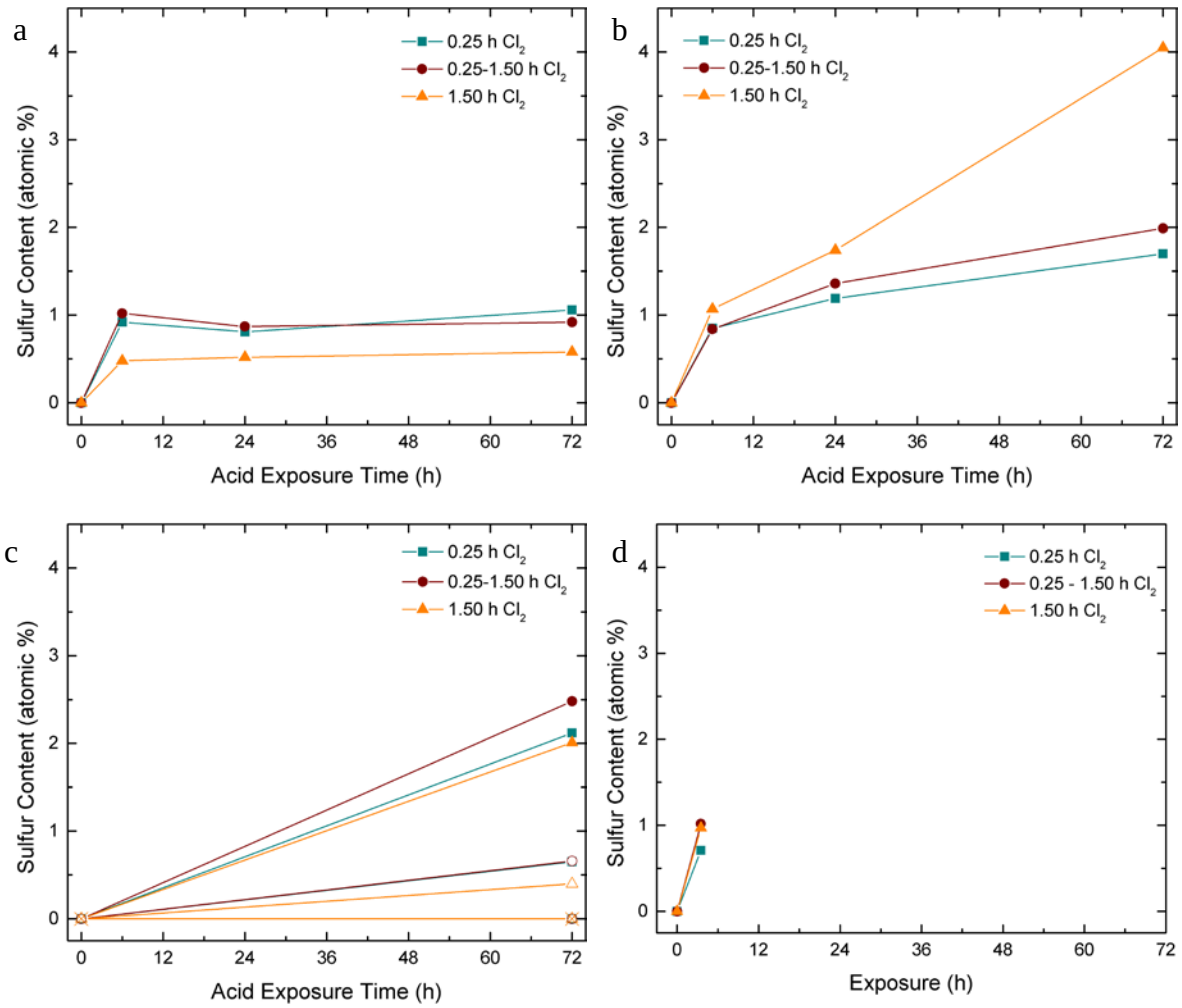

Figure 4.1 – Sulfur content for TiC-CDC samples exposed to a) aqueous SO_2 at 25°C, b) aqueous SO_2 at 75°C, c) humid SO_2 at 25°C, where the open symbols represent samples after the first washing procedure and close symbols the as-exposed samples, and d) dry SO_2 at 25°C. The lines are not data points but meant to guide the eye.

Activated carbons have been shown to act as a support to oxidize chemisorbed SO_2 to form sulfate species in the presence of adsorbed oxygen or water. When the XPS spectra were further analyzed for the specific sulfur species, sulfate species were found on all samples at a binding energy of 168 eV. As dry exposed samples were exposed to ambient air and humidity after exposure, the chemisorbed SO_2 likely reacted to form sulfate groups in a similar manner as samples exposed to humid and aqueous SO_2. However, this cannot be confirmed as the TiC-CDC also contained oxygen moieties, which could

facilitate this oxidation reaction. While both the dry- and humid-exposed samples only showed sulfate groups retained on the surface of the TiC-CDCs, aqueous-exposed samples showed sulfate groups and another group at a binding energy of 164 eV. Initially, this sulfur group was thought to be a thiol group; however, reducing SO_2 to S requires energy,[22, 23] which the CDC system and testing environment likely did not provide, and subsequent FTIR data in the supplemental information did not contain a peak for S-H stretching. There are multiple other sulfur functional groups in this area including CS_2,[24] TiS,[25] S_2Cl_2,[24] and SO/sulfonyl[24] groups. As the first three of these require the sulfur to be reduced from its oxide form, the most likely functional group is the sulfonyl group addition to the carbon structure. This functional group is more abundant at short exposure times and higher temperatures, and the amount decreased as exposure time increased as seen in Figure 4.2.

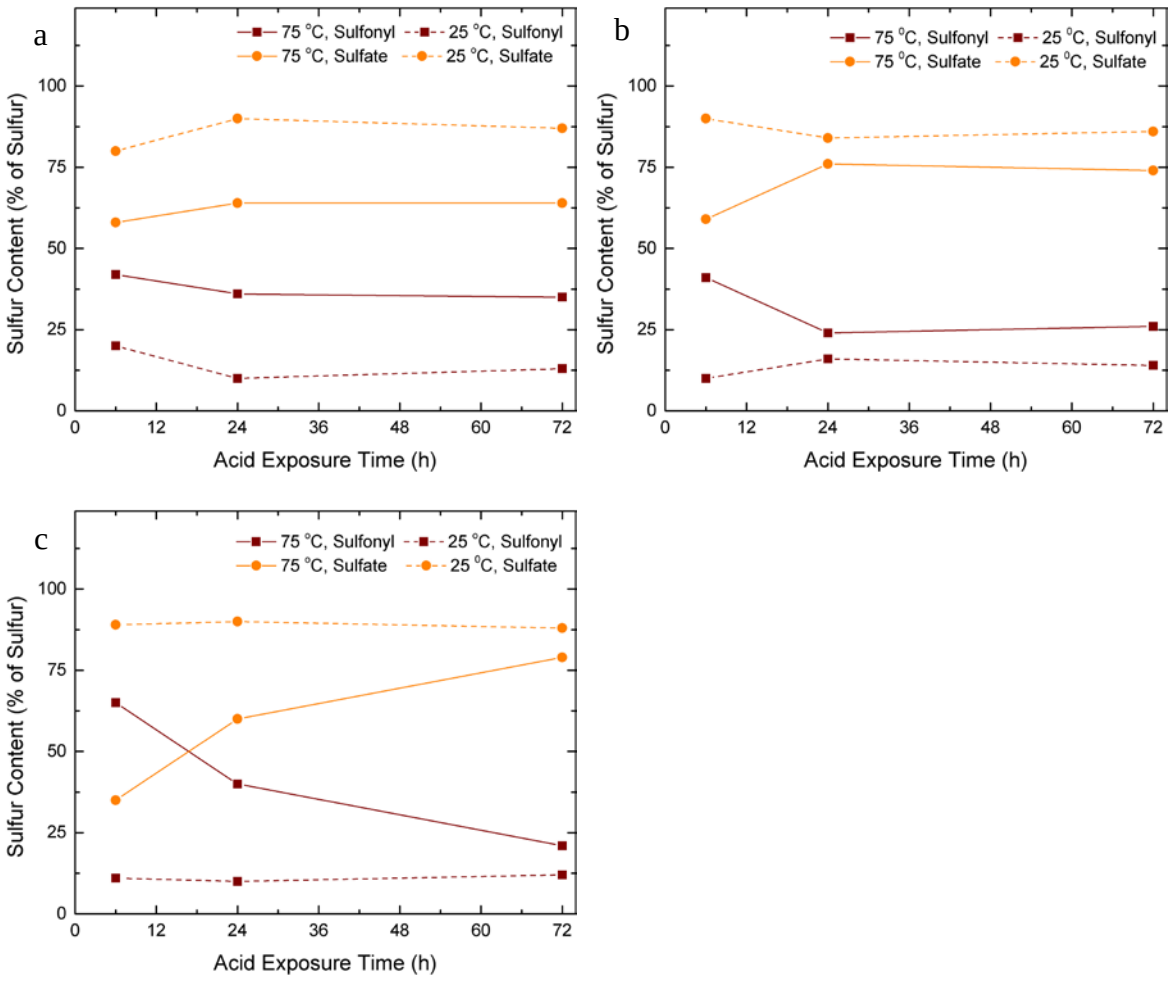

Figure 4.2 – Evolution of the sulfur species in TiC-CDC samples etched for a) 0.25 h, b) 0.25 h and held at temperature for an additional 1.25 h, and c) 1.50 h and exposed to aqueous SO_2 at 25 and 75°C. The lines are not data points but meant to guide the eye.

To determine the degree of degradation due to the sulfur functional groups, N_2 sorption at 77 K was performed for BET surface area and PSD calculations seen in Figure 4.3 and Figure 4.4, respectively. For all samples, the accessible surface area decreased due to the sulfate and sulfonyl functional groups. Samples exposed to dry SO_2 experienced a reduction in BET surface area of 8 and 25% for fully and partially etched samples, respectively. The humid- and aqueous-exposed samples display a more significant decrease in BET surface area comparatively, which suggests that the kinetics

of incorporating sulfate species into the TiC-CDC matrix is slow. Indeed these samples were exposed to the highest concentration of SO_2 but experienced the shortest exposure time. Even though the samples were allowed to reach equilibrium with the SO_2 gas for each point in the isotherm, the kinetics of adding sulfate functional groups was not quick enough to compensate for the vast increase in concentration. Additionally, as the samples underwent a temperature and pressure swing prior to measurement, these residual sulfate groups remained chemisorbed to the carbon structure.

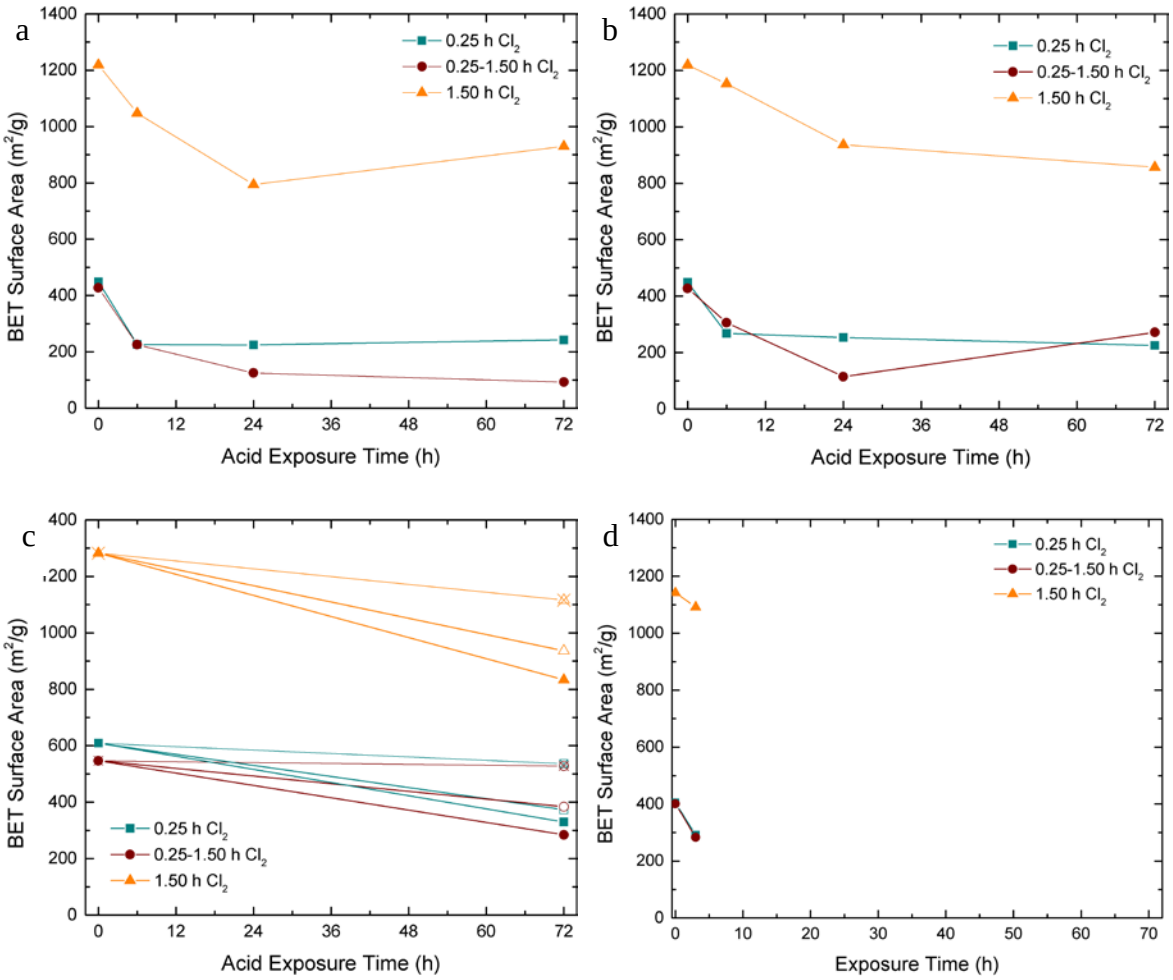

Figure 4.3 – BET surface areas (m^2 g^{-1}) for TiC-CDC samples exposed to (a) aqueous SO_2 at 25°C, (b) aqueous SO_2 at 75°C, (c) humid SO_2 at 25°C and 85% RH, where closed symbols represent as exposed samples, open samples washed once, and open with crosses washed twice, and (d) dry SO_2 at 25°C as a function of their exposure time (h). The lines are not data points but meant to guide the eye.

Humid SO_2 exposed samples were exposed to a lower concentration of 32±4 ppm of SO_2 for 72 h. Without any post-exposure treatment, the samples exhibit a decrease in BET surface area of ~33-50%, which was greater than that experienced under dry conditions. After the first washing sequence, where the samples were washed three times with DI water and rinsed in methanol, the BET surface areas increased relative to the non-washed samples, but the surface areas were still below that of the pre-exposed TiC-

CDC samples. After the second washing sequence, where the samples were sonicated with DI water and rinsed with methanol, the BET surface area increased to within 10% of the original unexposed samples. This continued increase in surface area after washing indicates that the initially high sulfur content was weakly chemisorbed to the carbon surface as they remained after a temperature and pressure swing induced before N_2 sorption measurements.[26, 27] As the washing techniques became more vigorous, more sulfate species were removed until only trace amounts remained.

For aqueous SO_2 exposed samples, as seen in Figure 4.3a and b, all samples display similar behavior regardless of exposure temperature. After 6 h, the surface area of completely etched samples decreases 5-10%, while at 24 h, the decrease is 25-33% from the original. After this time, the decrease in surface area is negligible. Partially etched samples exhibit a 50% reduction in surface area after 6 h, after which time the rate of decrease in surface area slows and reaches a steady state. This BET surface area analysis provides additional information compared to the XPS data analysis alone. As XPS data showed there was no increase in surface sulfate groups after 6 h, the BET surface area analysis suggests that the carbon matrix continued to add sulfate groups due to sufficient time for the diffusion of sulfate species into the particle. The difference in the percent reduction of surface area between partially and fully etched samples could lead credence that SO_2 must diffuse through the carbon pores. As the porous shell of the CDC was necessarily smaller in thickness than a fully etched particle, the porous shell likely experienced a higher number of interactions with sulfate groups, which could lead to the addition of more functional groups in a given area compared to a fully etched sample. These additional functional groups per a given area would lead to a further reduction in

BET surface area. The effect of exposure temperature on BET surface area showed a minimal impact, which was in contrast to the XPS data that showed higher sulfur content at the higher exposure temperature. The contradiction was likely due to the small changes in the reported sulfur contents, 1 vs 2 atomic percent.

The sulfate groups play a significant role in decreasing the accessible BET surface area; however, they do not appear to influence the size of the pores as seen in Figure 4.4. Instead, the quantity of pores seems to change. Likely, the functional groups completely block access to some number of pores, which would reduce the amount available for N_2 adsorption and would also decrease the calculated BET surface area. After acid exposure, the materials maintain their microporosity, one of the hallmarks of CDCs. Furthermore samples were tested for their micropore stability. Samples initially etched for 0.25 h and cooled immediately showed only pores 3 Å in radius, while samples etched for the same time but then maintained at the etching temperature for additional time showed micropores 3 and 5 Å in radius.[17] Notably, the samples originally displaying only the 3 Å pore radius relaxed the carbon structure to form both 3 and 5 Å radius pores. This relaxation showed the samples continued to evolve even at room temperature. Previous research showed that the PSD changes due to the length of time the samples remain at the etching temperature.[17] Samples etched at shorter time scales could have the same PSD as those etched at longer time scales by keeping the samples at temperature for longer periods of times. This likely means that the PSD of the samples etched for longer times represents the stable, amorphous carbon configuration. The data shown in Figure 4.4 indicates that this stable carbon configuration can be induced either through a high

temperature heat treatment for short periods of time or at room temperature over a period of months.

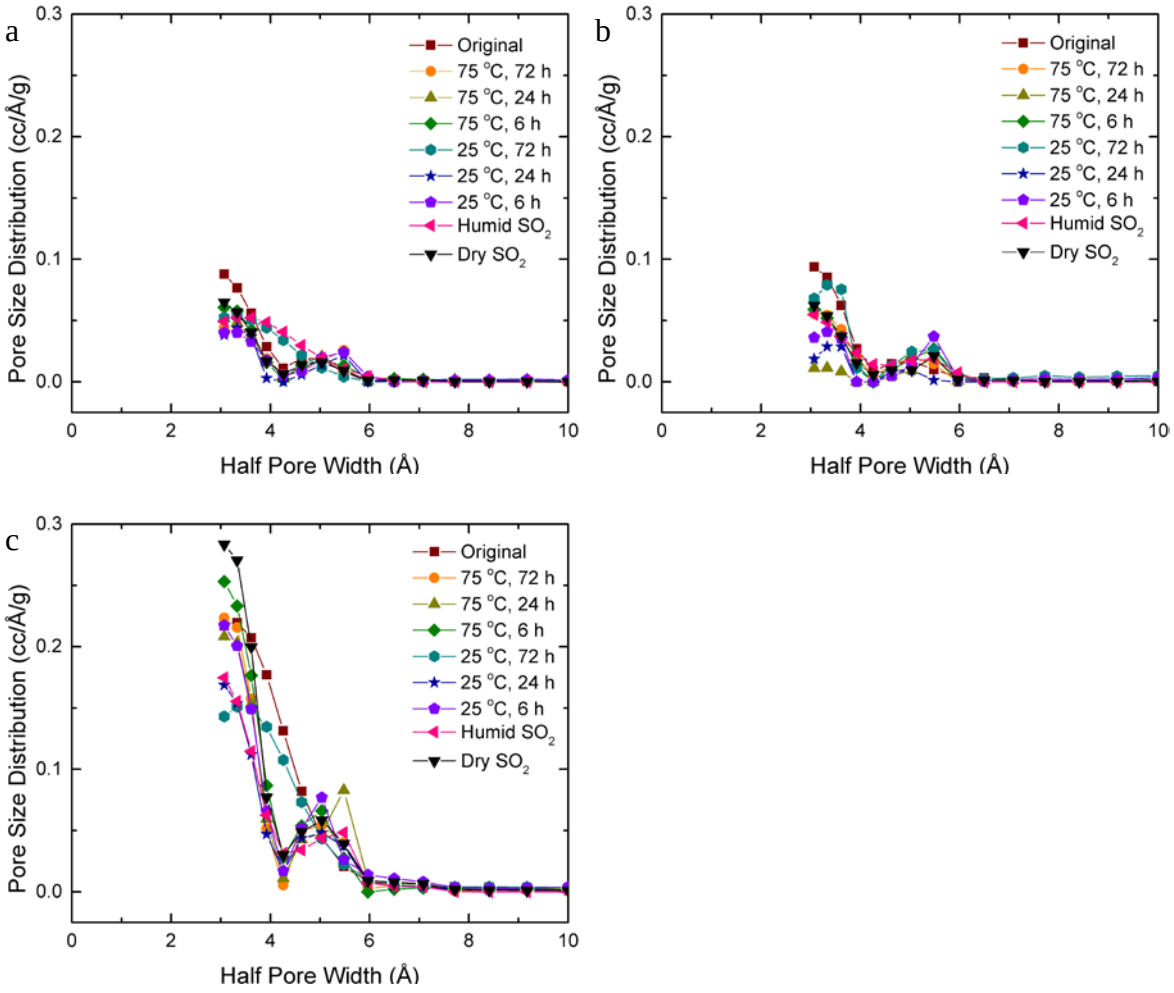

Figure 4.4 – Pore size distributions (PSD) for TiC-CDC samples using QSDFT calculations from N_2 sorption isotherms at 77 K. The aqueous SO_2 samples were labelled according to exposure temperature (°C) and time (h). Figures correspond to the etching time: (a) 0.25 h, (b) 0.25 h and held at temperature for a total of 1.50 h, and (c) 1.50 h. The lines are not data points but meant to guide the eye.

The micropore structure was also studied, as seen in Figure A.27, using CO_2 adsorption at 273 K as CO_2 adsorption data is widespread for TiC-CDC materials and is fully reversible.[20, 28-31] For all samples tested, hysteresis was not seen, which indicated TiC-CDC remained a strictly microporous material. Indeed, NLDFT

calculations show that the pore size was not modified by the various acid exposure environments and remained at 3.58 Å in diameter. The only modification was a decrease in the number of pores. This corroborated the PSD data given by N_2 sorption at 77 K. Also since all pore sizes are reduced in number, the sulfate groups affected all pores equally by completely blocking them rather than causing a shift toward smaller pores.

CO_2 isotherms gathered at 25°C, shown in Figure 4.5, provide additional data for determining interactions between CO_2 and the sulfate groups. A comparison between the pre-SO_2 exposed samples suggested that CO_2 adsorption appears to be a function of BET surface area rather than strong interactions between residual TiC, the porous carbon, and CO_2. While a clear trend was difficult to discern within the SO_2 exposure conditions, CO_2 adsorption capacity decreased for every exposure condition and the amount adsorbed decreased in all regions of the adsorption curve. At lower pressures, the adsorption of CO_2 was compromised due to the acidic sulfate groups. These functional groups most likely hinder CO_2 adsorption due to electrostatic repulsion and a lower number of open pores available for adsorption due to pore blockage. These sulfate groups also completely blocked pores, which results in the decrease in surface area as discussed earlier. This manifests itself at the higher CO_2 pressure region, where surface area and pore volume are the dominate features in determining adsorption capacity, and lower CO_2 capacities.

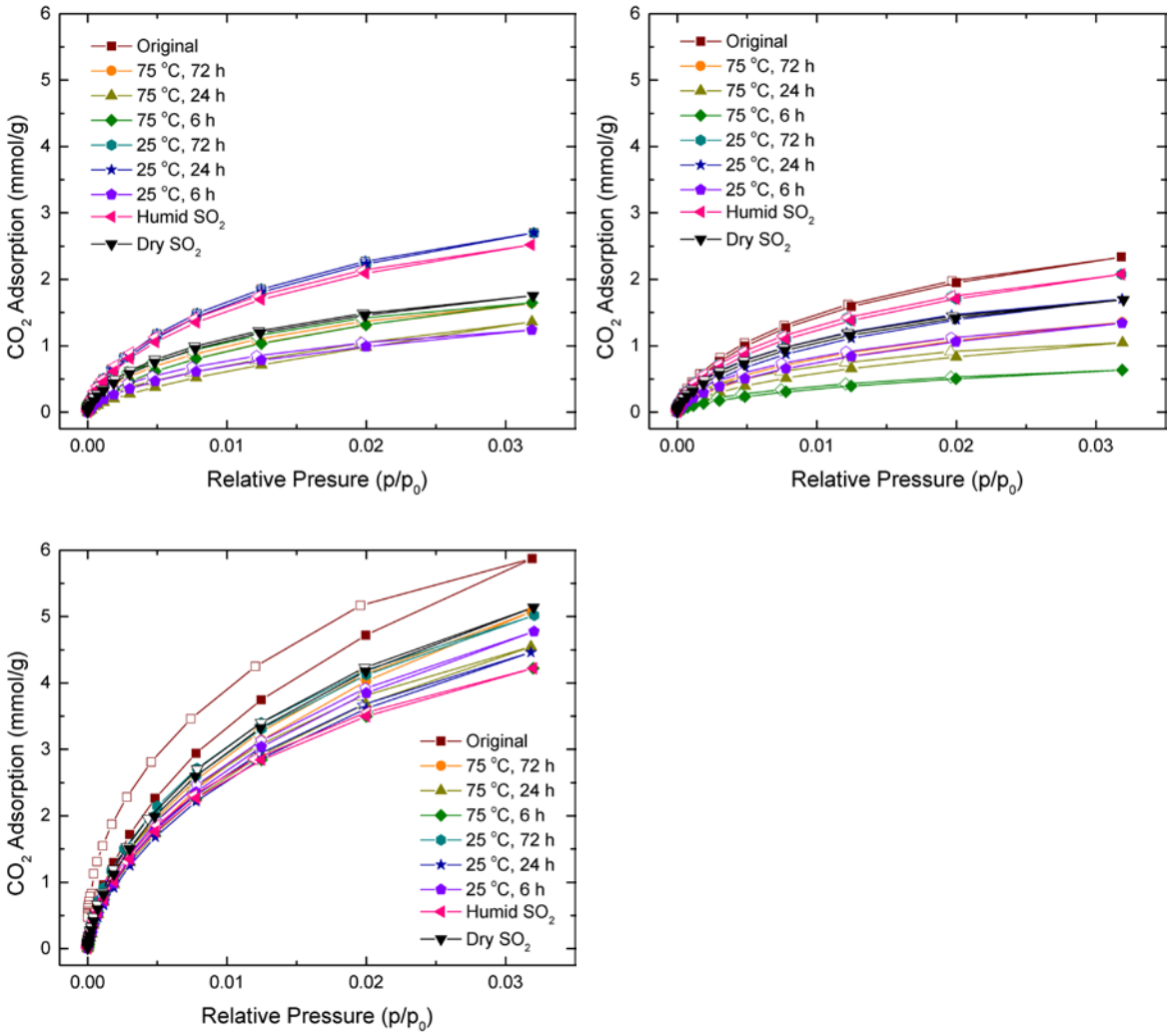

Figure 4.5 – CO_2 sorption curves measured at 0°C for TiC-CDC samples etched for a) 0.25 h, b) 0.25 h and held at temperature for an additional 1.25 h, and c) 1.50 h. The temperature (°C), time (h) designate aqueous SO_2 exposure conditions. The lines are not data points but meant to guide the eye.

4.4 Conclusions

Herein, we tested TiC-CDC samples to determine the effects that various environments of SO_2 have on the physical and adsorptive properties. SO_2 adsorption was not completely reversible under the conditions tested due to chemisorbed sulfate groups, which increased in number as exposure time increased, bound to the carbon surface. These functional groups manifested themselves through a decrease in the BET surface

area and through a reduction in the number of pore available for adsorption due to pore blockage. The degree of degradation in physical properties was roughly the same regardless of the SO_2 concentration and environment. The weakly chemisorbed sulfate groups cannot be removed through the induction of a temperature or pressure swing typically seen in gas-phase desorption techniques but can be removed through vigorous washing with DI water. These data show that titanium carbide-derived carbon is a good candidate for SO_2 removal for its structural stability and regeneration potential. However, standard regeneration methods used in gas-phase adsorption will lead to degradation in adsorption properties. This paper shows that better regeneration methods, such as washing vigorously with water, are necessary to fully retain the adsorption properties for cyclic processes.

4.5 References

1. Lisovskii, A., et al., *Adsorption of sulfur dioxide by active carbon treated by nitric acid: II. Effect of preheating on the adsorption properties.* Carbon, 1997. **35**(10-11): p. 1645-1648.

2. Mangun, C.L., J.A. DeBarr, and J. Economy, *Adsorption of sulfur dioxide on ammonia-treated activated carbon fibers.* Carbon, 2001. **39**(11): p. 1689-1696.

3. Guo, J. and A.C. Lua, *Microporous activated carbons prepared from palm shell by thermal activation and their application to sulfur dioxide adsorption.* J Colloid Interface Sci, 2002. **251**(2): p. 242-7.

4. Brodzinsky, R., et al., *Kinetics and Mechanism for the Catalytic-Oxidation of Sulfur-Dioxide on Carbon in Aqueous Suspensions.* Journal of Physical Chemistry, 1980. **84**(25): p. 3354-3358.

5. Komiyama, H. and J.M. Smith, *Sulfur dioxide oxidation in slurries of activated carbon. Part I. Kinetics.* AIChE Journal, 1975. **21**(4): p. 664-670.

6. Rodriguez-Reinoso, F., M. Molina-Sabio, and M.A. Munecas, *Effect of microporosity and oxygen surface groups of activated carbon in the adsorption of*

molecules of different polarity. The Journal of Physical Chemistry, 1992. **96**(6): p. 2707-2713.

7. Tanada, S., et al., *Removal of Formaldehyde by Activated Carbons Containing Amino Groups.* J Colloid Interface Sci, 1999. **214**(1): p. 106-108.

8. Foo, G.S. and C. Sievers, *Synergistic effect between defect sites and functional groups on the hydrolysis of cellulose over activated carbon.* ChemSusChem, 2015. **8**(3): p. 534-43.

9. Inagaki, M., *Pores in carbon materials-Importance of their control.* New Carbon Materials, 2009. **24**(3): p. 193-222.

10. Yin, C.Y., M.K. Aroua, and W.M.A.W. Daud, *Review of modifications of activated carbon for enhancing contaminant uptakes from aqueous solutions.* Separation and Purification Technology, 2007. **52**(3): p. 403-415.

11. Hashimoto, Y. and S. Tanaka, *A new method of generation of gases at parts per million levels for preparation of standard gases.* Environ Sci Technol, 1980. **14**(4): p. 413-6.

12. Bhattacharyya, S., et al., *Interactions of SO_2-Containing Acid Gases with ZIF-8: Structural Changes and Mechanistic Investigations.* Journal of Physical Chemistry C, 2016. **120**(48): p. 27221-27229.

13. Mounfield, W.P., et al., *Synergistic Effects of Water and SO_2 on Degradation of MIL-125 in the Presence of Acid Gases.* Journal of Physical Chemistry C, 2016. **120**(48): p. 27230-27240.

14. Kleitz, F., et al., *Probing Adsorption, Pore Condensation, and Hysteresis Behavior of Pure Fluids in Three-Dimensional Cubic Mesoporous KIT-6 Silica.* Journal of Physical Chemistry C, 2010. **114**(20): p. 9344-9355.

15. Neimark, A.V., et al., *Quenched solid density functional theory and pore size analysis of micro-mesoporous carbons.* Carbon, 2009. **47**(7): p. 1617-1628.

16. Gor, G.Y., et al., *Quenched solid density functional theory method for characterization of mesoporous carbons by nitrogen adsorption.* Carbon, 2012. **50**(4): p. 1583-1590.

17. Dutzer, M.R., et al., *The effects of reactor design on the synthesis of titanium carbide-derived carbon.* Chemical Engineering Science, 2017. **160**(August 2016): p. 191-199.

18. Zhao, Y.F., et al., *Titanium carbide derived nanoporous carbon for supercapacitor applications.* International Journal of Hydrogen Energy, 2012. **37**(24): p. 19395-19400.

19. Dash, R., et al., *Titanium carbide derived nanoporous carbon for energy-related applications.* Carbon, 2006. **44**(12): p. 2489-2497.

20. Zhang, L., et al., *A new route for preparation of titanium carbide derived carbon and its performance for supercapacitors.* Materials Letters, 2014. **122**: p. 78-81.

21. Portet, C., et al., *Impact of synthesis conditions on surface chemistry and structure of carbide-derived carbons.* Thermochimica Acta, 2010. **497**(1-2): p. 137-142.

22. Frivik, S.K. and S.E. Ebeler, *Influence of sulfur dioxide on the formation of aldehydes in white wine.* American Journal of Enology and Viticulture, 2003. **54**(1): p. 31-38.

23. Soni, S.K., *Microbes : a source of energy for 21st century*. 2007: New India Pub. Agency. 574-574.

24. Gelius, U., et al., *Molecular Spectroscopy by Means of ESCA III.Carbon compounds.* Physica Scripta, 1970. **2**(1-2): p. 70-80.

25. Franzen, H.F., et al., *Xps Spectra of Some Transition-Metal and Alkaline-Earth Monochalcogenides.* Journal of Solid State Chemistry, 1976. **18**(4): p. 363-368.

26. Lizzio, A.a. and J.a. Debarr, *Mechanism of SO_2 Removal by Carbon §*. Energy, 1997. **0624**(22): p. 284-291.

27. Mochida, I., et al., *Removal of SO_x and NO_x over activated carbon fibers.* Carbon, 2000. **38**(2): p. 227-239.

28. Schlange, A., et al., *Titanium carbide-derived carbon as a novel support for platinum catalysts in direct methanol fuel cell application.* Journal of Power Sources, 2012. **199**: p. 22-28.

29. Chmiola, J., et al., *Effect of pore size and surface area of carbide derived carbons on specific capacitance.* Journal of Power Sources, 2006. **158**(1): p. 765-772.

30. Silvestre-Albero, A., et al., *High selectivity of TiC-CDC for CO_2/N_2 separation.* Carbon, 2013. **59**: p. 221-228.

31. Presser, V., et al., *Effect of pore size on carbon dioxide sorption by carbide derived carbon.* Energy & Environmental Science, 2011. **4**(8): p. 3059-3066.

CHAPTER 5. SYNTHESIZING PARTIALLY ETCHED MANGANESE CARBIDE-DERIVED CARBON

5.1 Introduction

Porous carbon adsorbents are an ancient technology for use in liquid- and gas-phase separation applications, with perhaps the most notable being water purification.[1-4] Activated carbons specifically are known for their cheap and easy production from any number of carbon sources including wood and fruit pits and shells. By themselves, activated carbons are a great adsorbent for a number of contaminants due to their hierarchal pore structure, where micro- and mesopores exist alongside macropores, and high surface areas for physically adsorbing these contaminants. However, researchers have strived to improve adsorption capabilities for activated carbons by controlling the pore size distribution, typically by controlling the pyrolysis temperature and precursor material, and by adding metal nanoparticles for specific adsorbate-adsorbent interactions and chemisorption.[5-7] The natural disorder in most carbon precursors does not easily allow for a narrow pore size distribution. Due to the hierarchal pore structure, the addition of metal nanoparticles also has the ability to block micropores, which are a key attribute for adsorption especially at low concentrations of the adsorbate, where interactions between the adsorbate and the carbon walls is of utmost importance. For these reasons, researchers have focused on templated carbons to achieve their adsorption goals.[8, 9]

There is a subset of activated carbon called carbide-derived carbon, where metal carbides are employed as the carbon source. Similar to a templated carbon synthesis, the carbide is typically a crystalline structure composed of metal and carbon atoms in a repeating unit. To create a porous carbon, the metal atoms are removed through a high-temperature etching process, typically using chlorine, to selectively react with the metal atoms. The metal chloride is then removed through the vapor phase due to the high temperature used during the etching reaction. The remaining carbon then rearranges around these vacancies to create pores. The size of these micropores is dependent upon the specific metal carbide, the metal spacing in the crystal lattice, and the etching temperature.[10] Carbides with larger metal atoms will form larger micropores than those with smaller metal atoms, while the spacing of the metal and carbon atoms within the crystal structure will also determine how the carbon can rearrange itself around the metal vacancies. The etching temperature influences how much energy is in the system with higher energies forcing the carbon to become ordered and graphitic rather than disordered and amorphous; the amount of disorder directly impacts the resulting surface area.

Research on carbide-derived carbons has historically focused on electromechanical applications, where full metal removal is necessary.[11-14] However, partial etching allows for the retention of metal atoms, which are beneficial in adsorptive applications. Partially etching CDCs has been a narrow focus in the wider CDC literature, and the intermediate steps in the etching process are not well understood.[15, 16] Indeed, most articles that report on partially etched samples were concerned with partial etching as a tool for determining the reaction and metal chloride extraction rates for fully etched samples. Recently, work has been done to purposely create partially etched samples with

the goal of creating usable residual metal sites for adsorption. This has been documented with both iron carbide (Fe_3C)[17] and aluminum carbide (Al_4C_3)[16]. While the basics of metal removal are known, the opposing metal retention mechanism found in these two CDC systems is not well understood.

Carbide-derived carbon research has focused on creating porous carbon structures from readily available, and structurally stable carbides including boron,[18, 19] silicon,1[20-22] titanium,[23-25] vanadium,[12, 26, 27] zirconium,[28] chromium,[29, 30] molybdenum,[31-33] niobium,[34, 35] and tungsten[36, 37] carbides among others. To the best of the authors' knowledge, none of the resulting CDCs have been reported to produce residual metal nanoparticles. A common property for all CDCs is that the metal chloride byproduct has a high vapor pressure. This volatility allows for the metal chloride to easily be removed from the remaining porous carbon through the vapor phase. Indeed for partially etched SiC- and TiC-CDCs, the center of the particle remains in the carbide form and is covered in a carbon shell with no residual metal.[10, 16, 17, 22, 25]

More recent studies have focused on thermodynamically unstable carbides and their resulting CDCs. When Fe_3C was subjected to a long etching procedure, which is known to remove all metal in the carbon from metal carbides that produce volatile metal chlorides, iron chloride nanoparticles remained despite the low boiling point of $FeCl_3$ (306°C).[17] Earlier studies have shown that by adding small amounts of iron the resulting CDC structure included nanodiamond and barrel like carbon nanoparticles.[27, 38, 39] When looking at the chlorination of ferrocene, another carbon and iron system, $FeCl_3$ and $FeCl_2$ remain in the carbon structure.[40, 41] Together these earlier studies and the known ability of iron to graphitize carbon, it was proposed that the iron chloride

locally graphitizes carbon, which then creates pores too small for $FeCl_3$ to escape. This allowed $FeCl_3$ to accumulate locally and, as the reactor cooled, to form solid metal nanoparticles. Similarly, Al_4C_3 also formed aluminum nanoparticles upon partial etching.[16] The reaction process here is less understood, but thought to occur through one of three means: (1) the ability for $AlCl_3$ to exist as a monomer and a dimer, which affects diffusion through the porous carbon, (2) polymerization of $AlCl_3$ in the presence of water, affecting its vaporization rate, and/or (3) the reaction of $AlCl_3$ with O_2 using a Cl_2 catalyst to form Al_2O_3. Further inspection of these metal nanoparticles indicated that they were a combination of Al_2O_3, $AlCl_3$, and $Al(OH)_3$.[42-45] The common theme among all CDC systems is that the properties of the metal chloride dictate how these systems behave during an etching reaction.

To expand upon the very limited number of partially etched CDCs with residual metal nanoparticles, we looked at all single metal carbides and the properties of their corresponding metal chlorides. Graphitization catalysts include Fe, Co, and Ni;[46] metal chlorides with polymerization potential include Al,[42] Mn,[47-49] Zr,[50] and Hf[98] chlorides; and metal chlorides with high boiling points include Sc, Cr, Mn, Rb, Sr, Yc, and Ce chlorides. Based upon this limited list, the focus for this study stemmed from those properties potentially similar to Al_4C_3 and $AlCl_3$. For this reason Mn_3C was chosen for its innovative potential, the ability for manganese chloride ion species to polymerize, and the high boiling point of $MnCl_2$. Those properties allow partial etching at high temperatures, which induces graphitization and was deemed important for $FeCl_3$ retention, and also allows for the ability to etch between the melting and boiling points of $MnCl_2$.

5.2 Materials and Methods

5.2.1 Materials

Manganese carbide-derived carbon (Mn_3C-CDC) samples were produced using a standard horizontal, flow-over reactor at various temperatures and time scales to determine the reaction conditions necessary to create a CDC from manganese carbide. One gram of Mn_3C (BOC Sciences, 99% purity) was laid and levelled into a quartz boat, which was then inserted into a quartz tube (0.025 m OD, 0.5 m in length) in a horizontal tube furnace. The system was purged under Ar (Airgas, Ultra High Purity) at a flow rate of 125 mL min^{-1} as the furnace heated to 500, 700, or 900°C at a ramp rate of 5°C min^{-1}. Cl_2 gas (Airgas, 99.5%) at a flow rate of 25 mL min^{-1} was introduced at the specified temperature. At 500 and 700°C, the etching time was 1.0 h, while at 900°C, the etching reaction occurred for 0.25, 0.5, 1.0 and 2.0 h. After the specified time had elapsed, the Cl_2 flow was halted and the furnace cooled to 25°C at a ramp rate of 5°C min^{-1}. A NaOH scrubber neutralized the acidic effluent before purging into the fume hood.

5.2.2 Methods

5.2.2.1 Thermogravimetric Analysis (TGA)

Residual metal in any form (carbide, chloride, oxide) was determined through thermogravimetric analysis under air flow (40 mL min^{-1}, Airgas, Ultra Zero Grade) to combust the organic material and convert the metal to Mn_2O_3. Using a platinum sample pan, approximately 30 mg of material was placed into TA Instruments TGA Q50 and equilibrated to 25°C. After reaching equilibrium, the instrument increased the

temperature at a rate of 5°C min^{-1} until 600°C, where the temperature remained for 5 h. Residual metal calculations assumed that only Mn_2O_3 remained.

5.2.2.2 Powder X-ray Diffraction (PXRD)

Diffraction patterns were collected on a PANalytical X'Pert PRO Alpha-1. Approximately 5 mg of sample were placed on a zero background holder and scanned from 5-70° using a step-size of 0.016 and exposure time of 30 s while spinning the sample.

5.2.2.3 Raman Spectroscopy

Raman spectra were obtained using a Bruker Senterra Raman Microscope. This system is equipped with a 532 nm laser and a dispersive spectrometer. Measurements spanning three diffraction gratings with a combined spectral range from 55 to 3700 cm^{-1} were integrated for 5 s each at 10 mW laser power.

5.2.2.4 Nitrogen Sorption at 77 K

A Quantachrome Quadrasorb EVO performed nitrogen sorption experiments at 77 K to determine the surface areas and pore size distributions of the resulting Mn_3C-CDC samples. Quenched Solid Density Functional Theory (QSDFT) calculations were used to determine the pore size distributions assuming slit- and cylindrical-shaped pores. Prior to N_2 sorption characterization, a Quantachrome FloVac Degasser outgassed approximately 50 mg of sample under dynamic vacuum at 150°C for approximately 16 h.

5.2.2.5 X-ray Photoelectron Spectroscopy (XPS)

XPS spectra were collected on a Thermo K-Alpha XPS using a monochromated Al Kα X-ray source with a double-focusing hemispherical analyzer. Specific elements probed for high resolution spectra included C1s, O1s, Cl2p, and Mn2p with 25 total scans at 0.1 eV step size, 50 ms dwell time, 50 eV pass energy, and 400 μm spot size.

5.3 Results and Discussion

TGA analysis shows that high amounts of residual metal are retained in the resulting Mn_3C-CDC. For the purposes of this report, residual Mn is classified as any Mn species, Mn_3C, $MnCl_2$, or Mn_xO_y, which remain in the CDC. As the etching time increases, the residual metal content decreases as expected as seen in Figure 5.1. Based upon the results, residual metal content remains steady between 0.25 h and 1.0 h of etching. This likely is not true, based upon BET surface areas in Figure 5.2, due to the assumptions in the residual metal calculations that assumed only carbon and manganese were in the precursor material. Supporting data suggest this residual metal is $MnCl_2$, which would convolute the calculations as the quantities and ratios of $MnCl_2$ and Mn_3C are unknown. That assumption also likely explains the data points for samples soaked in water for samples etched less than 1.0 h. Once the samples have been etched for at least 1.0 h and exposed to heat for a further 1.0 h, the residual metal content stabilizes. This suggests that $MnCl_2$ is indeed removed at these longer exposure times and explains the stability of their residual metal contents between no post-synthetic treatment and post-synthetic treatment.

The TGA curves in Figure A.62 show two reductions in mass that can be attributed to dehydration of the $MnCl_2 \cdot 4H_2O$. The first reduction occurs below 100°C, while the second occurs at 135°C. These two regions correspond to where water, adsorbed from ambient humidity, in the pores is evaporated along with the dehydration of $MnCl_2 \cdot 4H_2O$ at 58°C and 135°C. The increase in mass is due to oxidization of Mn_3C and $MnCl_2$ to Mn_2O_3, while the largest reduction is oxidization and removal of carbon.

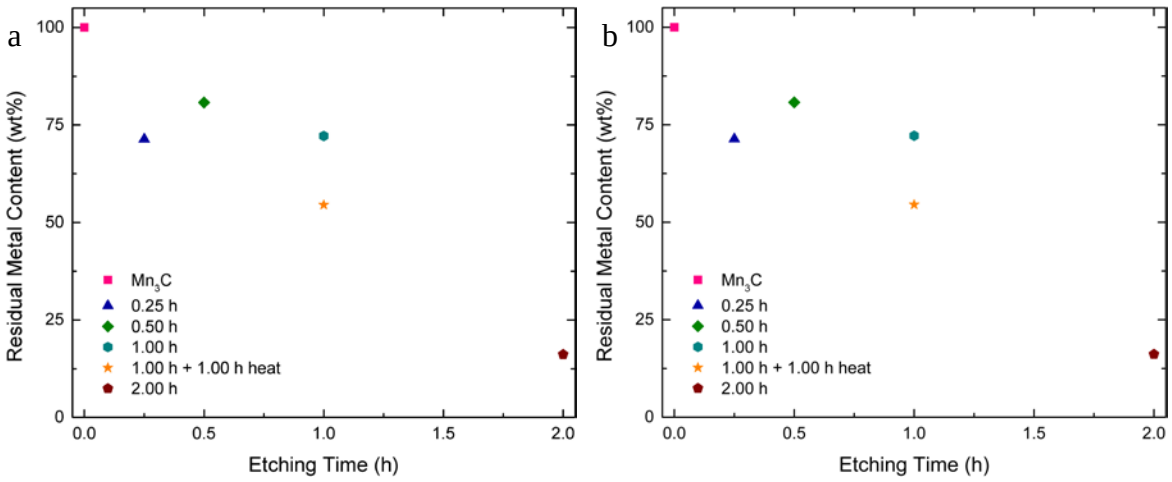

Figure 5.1 – Residual metal content based upon TGA data assuming residual material was Mn_2O_3 for (a) samples created at 900°C and (b) samples in (a) soaked in water to dissolve $MnCl_2$.

The high level of residual manganese content displays itself in the relatively low BET surface areas seen in Figure 5.2. While fresh and heated samples, with no exposure to Cl_2, remained non-porous with negligible surface areas and pore volumes, those samples etched at 900°C exhibit an increase in surface area with an increase in etching time. Therefore, heating the sample likely does not degrade Mn_3C, and etching below the melting point of $MnCl_2$ (654°C) results in small gains in porosity. This conforms well to TGA results that show a decrease in the amount of residual metal occurs at temperatures above the melting point of $MnCl_2$.

Additional Mn_3C samples were etched at 900°C, which is between the melting and boiling point of $MnCl_2$. Here the BET surface area increases with an increase in etching time as would be expected. However, the data also support the theory that the metal removal depends not only upon the etching time but also upon the vapor pressure of $MnCl_2$. This was confirmed by etching a sample for 1 h at 500°C, for 1 h at 700°C, and for 1 h at 900°C while allowing the sample to stay at 900°C for an additional hour without Cl_2 flow. When the reaction takes place below the melting point of $MnCl_2$ (654°C), there is still large amount of nonporous material as shown by the low BET surface area in Figure A.65 and pore volume in Figure A.66. For a sample etched at 1 h and allowed to remain at 900°C for an additional hour without Cl_2 flow, the surface area and pore volume approaches that of a sample etched for 2 h. This confirms that vapor pressure is a factor in $MnCl_2$ removal when the etching temperature is below the boiling point of the metal chloride.

The side product of the etching reaction, $MnCl_2$, not only has a high boiling point but is also water soluble. Partially etched Mn_3C-CDC samples and Mn_3C were soaked in excess DI water for 24 h to determine changes in porosity. Mn_3C became a porous material, which is most likely a manganese oxide due to no other elemental species being present, according to XPS spectra in Figure A.76, with little residual carbon. This is in agreement with previous studies which showed that manganese carbide degrades in the presence of water to form manganese oxides and methane with other very short chain, gaseous hydrocarbons.[51, 52] Partially etched samples remained porous with BET surface area and pore volume increasing for all samples except for the sample etched for 1 h and allowed to remain at temperature for an additional hour without Cl_2 flow. This

increase in surface area is most likely due to the removal of water soluble $MnCl_2$; however, the increase in the surface area for Mn_3C convolutes this interpretation.

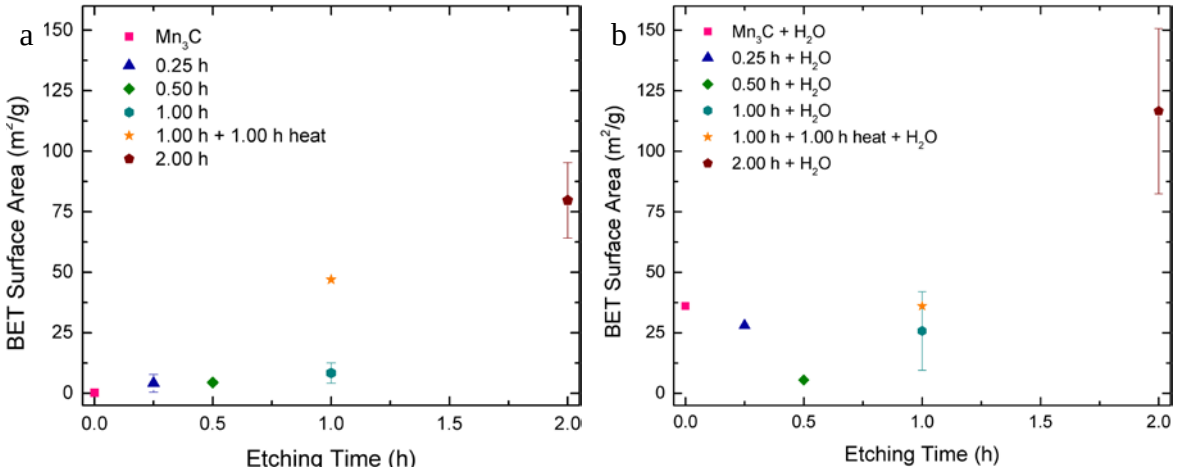

Figure 5.2 – BET surface areas for samples etched at 900°C (a) without soaking in water and (b) soaking in water.

In addition to the BET surface area and pore volume, the pore size distribution (PSD) was also investigated and shown in Figure 5.3. A key characteristic of CDCs is their very narrow PSD primarily based upon the metal orientation within the carbide crystal structure and the etching temperature. Mn_3C-CDC shows a very wide PSD that is more characteristic of activated carbons. Samples etched for less than an hour largely show non-porosity and, therefore, have few pores. Samples etched for longer times show little evidence of micropores, those with half pore widths smaller than 10 Å, and instead form only mesopores. This could suggest that as the Mn_3C precursor was not crystalline, the CDC formation here behaved similarly to an organic carbon source used to create traditional activated carbons. Samples etched with sufficient time to remove $MnCl_3$ contain mesopores with a range of half pore widths between 25 and 175 Å. However, after these same samples were soaked in DI water for 24 h to dissolve the $MnCl_3$, smaller

pores with half pore widths ranging from 10 to 50 Å appeared. The carbide exposed to DI water does show an increase in porosity, but it is unlikely that this results in the increase in mesoporosity for pore radii smaller than 25 Å as the PSDs are not consistent across samples that should have residual Mn_3C. That is samples etched for shorter times are expected to have higher amounts of residual Mn_3C, and these water-exposed samples should experience PSD more similar to water-exposed Mn_3C. Overall, the PSDs suggest that the carbon does rearrange to form these smaller pores but the $MnCl_2$ blocks access to them.

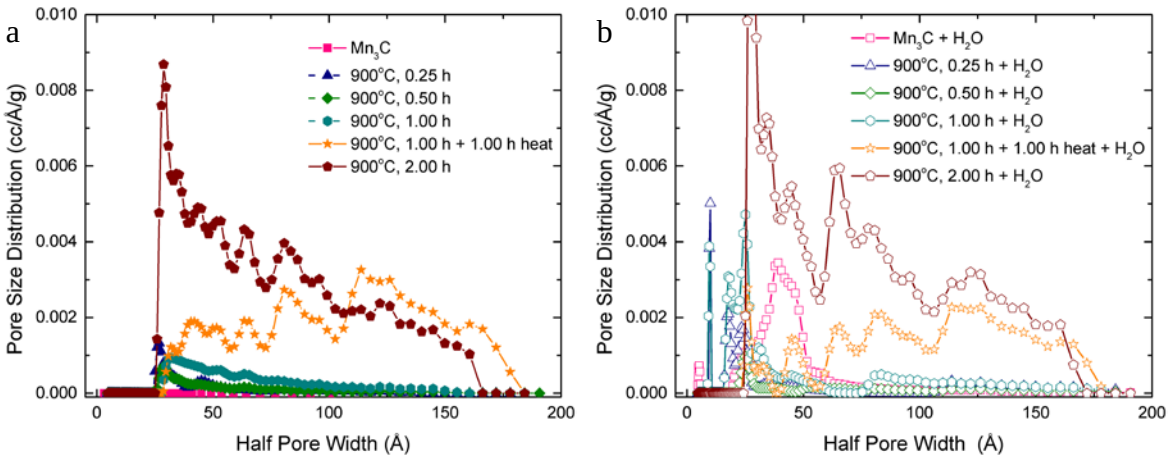

Figure 5.3 – The PSD for samples etched at 900°C (a) without soaking in water and (b) with soaking in water to dissolve $MnCl_2$.

To investigate the structural properties of Mn_3C-CDC powder X-ray diffraction in Figure 5.4 and Raman spectroscopy in Figure 5.5 were used to determine information about the crystal structure and carbon structure, respectively. The PXRD pattern of the carbide is relatively amorphous with a prominent peak at 46° compared to previous studies.[53-55] The relative lack of crystallinity of Mn_3C compared to other carbides is likely due to the short range order of any Mn_3C crystals. Peaks corresponding to

manganese oxides and graphitic carbon are missing, which indicates that these species are likely not present in the precursor. As the etching time increased in sample production, peaks corresponding to $MnCl_2$ begin to appear in the PXRD patterns. This indicates that the $MnCl_2$ remains in the pores of the remaining carbon atoms undergoing a rearrangement. As the etching time is further increased, the peak height of the $MnCl_2$ begins to decrease and a peak, corresponding to the (002) peak for graphite, appears at 26°. This graphitic peak is expected for the high etching temperature used to create these Mn_3C-CDC samples.

The PXRD patterns further suggest that $MnCl_2$ removal is vapor pressure dependent. At 1 h of etching, there are high-intensity peaks corresponding to $MnCl_2$ and no graphite peak. However, a sample etched for 1 h and allowed to remain at temperature for an additional hour without Cl_2 flow has a PXRD pattern that suggests the $MnCl_2$ is removed from the system. This additional chloride removal time combined with more degrees of freedom for carbon rearrangement allowed the carbon to fully reorganize into graphitic carbon. A sample etched for 2 h further confirms this theory as the $MnCl_2$ peaks are reduced even further and the graphite peak is more intense.

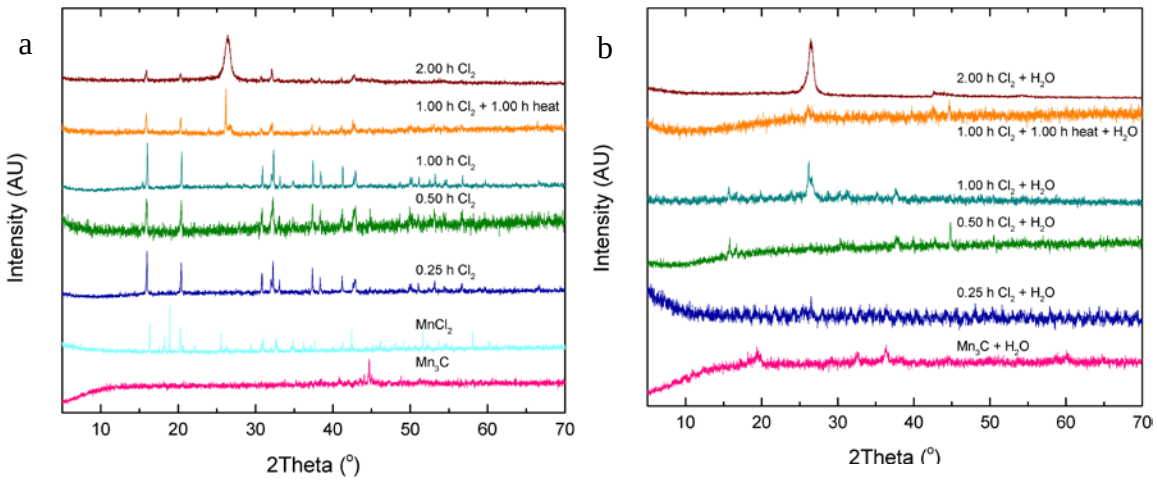

Figure 5.4 – PXRD patterns of Mn_3C-CDC samples created at 900°C (a) without soaking in water and (b) with soaking with water to dissolve $MnCl_2$

The degree of carbon ordering found in PXRD was confirmed with Raman spectra. There are two significant peaks corresponding to the D-band at ~1350 cm^{-1} for stretching found in aromatic rings and the G-band at ~1580 cm^{-1} for stretching found in all sp^2 hybridized carbon.[56-58] The ratio of the I_D/I_G bands provides information about the quality of the carbon ordering and the number of defects in carbon-carbon bonds. When the samples have only been etched for a short amount of time, the intensities of the D- and G-bands are quite low. This is indicative of low carbon ordering. As the etching time increases, peak intensities at low wavenumbers decrease, likely signifying the degradation of the carbide, and the D- and G-band peak intensities increase. I_D/I_G ratios in Figure A.69 in the supplemental show a decrease as the etching time increases. This further supports the view that the manganese converts from the carbide form to a chloride and that this chloride must be removed before carbon organization can take place. Indeed, the G-band peak increases in intensity as etching time increases allowing for this further carbon ordering and fewer defects in the carbon structure.

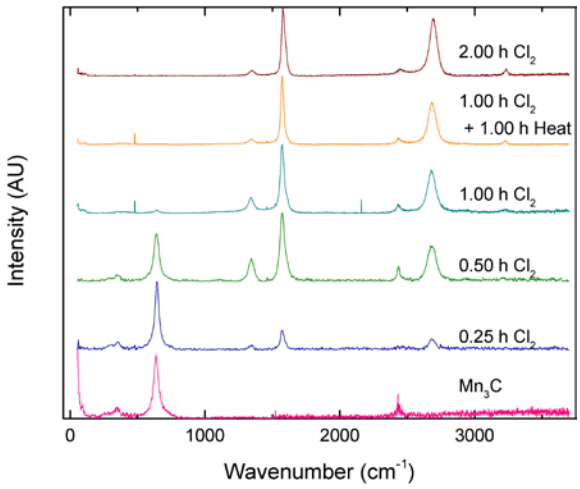

Figure 5.5 – Raman spectra of Mn_3C-CDC samples created at 900°C show the evolution of the carbon structure from a carbide to an ordered structure without defects.

Together the PXRD patterns and Raman spectra correlate well with the results of the BET surface area analysis. The residual metal oxides likely add density without an increase in surface area resulting in a lower overall BET surface area. Additionally, CDC literature showed that BET surface area increases in CDCs with an increase in etching temperature until around 900°C.[9, 10] This is due to the carbon reorganization around the metal vacancies. At lower etching temperatures the carbon remains amorphous, while at higher temperatures, the carbon begins to become graphitic. This additional ordering of the carbon to graphitic structures lowers the surface area. The high etching temperature used to create these Mn_3C-CDC samples and the amorphous nature of the precursor, due to additional carbon ordering than is necessary to form a CDC from a precursor with a crystalline structure, likely contribute to the relatively low surface area.

Thus far, interpreted data indicate that $MnCl_2$ remains in the pore structure of the resulting Mn_3C-CDC. This viewpoint was further investigated with X-ray photoelectron spectroscopy to determine Mn, O, and Cl bonds on the surface of the partially etched

samples. The spectra in Figure A.71-Figure A.75 show a $MnCl_2 \cdot 4H_2O$ complex. Normally $MnCl_2$ has a peak position of about 642.0 eV;[59, 60] however, the hydrated form would introduce further shielding due to the additional oxygen bonds to shift the required energy to induce the photoelectron effect to a higher energy state.[61] This shielding effect also appears to be occurring in XPS spectra for oxygen and chlorine. There do not appear to be any Mn peaks at low enough energy levels where one would find manganese oxides; therefore, the assignment at 643.5 eV was assigned to the hydrated $MnCl_2$.

5.4 Conclusions

For the first time to the authors' knowledge, a manganese carbide-derived carbon was created through a high-temperature etching process. The resulting manganese chloride has a low vapor pressure and its slow removal from the remaining CDC is due to this physical property. $MnCl_2$ can be removed either through longer exposure to the high etching temperature or through a soak in water to dissolve the chloride. The data for this new Mn_3C-CDC gave further insight into metal removal processes for CDCs. Metal removal for Mn_3C was dependent upon the vapor pressure of $MnCl_2$. It seemed unlikely that other Mn_xCl_y species were formed during the etching process, residual Mn was due to a polymerization reaction, which would increase the difficulty of metal chloride vaporization. Overall, CDC formation seems to purely be a function of the physical properties of the most stable metal chloride, which is formed during the etching process.

5.5 References

1. Otowa, T., Y. Nojima, and T. Miyazaki, *Development of KOH activated high surface area carbon and its application to drinking water purification.* Carbon, 1997. **35**(9): p. 1315-1319.

2. Paraskeva, P., D. Kalderis, and E. Diamadopoulos, *Production of activated carbon from agricultural by products.* Journal of Chemical Technology and Biotechnology, 2008. **83**(5): p. 581-592.

3. Parmentier, J., et al., *Structural/textural properties and water reactivity of fluorinated activated carbons.* Carbon, 2012. **50**(14): p. 5135-5147.

4. Suhas, P.J. Carrott, and M.M. Ribeiro Carrott, *Lignin--from natural adsorbent to activated carbon: a review.* Bioresour Technol, 2007. **98**(12): p. 2301-12.

5. Rong, H., et al., *Influence of heat treatment of rayon-based activated carbon fibers on the adsorption of formaldehyde.* J Colloid Interface Sci, 2003. **261**(2): p. 207-12.

6. Baur, G.B., et al., *Activated carbon fibers for efficient VOC removal from diluted streams: the role of surface functionalities.* Adsorption-Journal of the International Adsorption Society, 2015. **21**(4): p. 255-264.

7. Yin, C.Y., M.K. Aroua, and W.M.A.W. Daud, *Review of modifications of activated carbon for enhancing contaminant uptakes from aqueous solutions.* Separation and Purification Technology, 2007. **52**(3): p. 403-415.

8. Sakintuna, B. and Y. Yurum, *Templated porous carbons: A review article.* Industrial & Engineering Chemistry Research, 2005. **44**(9): p. 2893-2902.

9. Yushin, G., A. Nikitin, and Y. Gogotsi, *Carbide-Derived Carbon,* Y. Gogotsi, Editor. 2006, CRC Press: Boca Raton, FL. p. 237-280.

10. Presser, V., M. Heon, and Y. Gogotsi, *Carbide-Derived Carbons - From Porous Networks to Nanotubes and Graphene.* Advanced Functional Materials, 2011. **21**(5): p. 810-833.

11. Portet, C., et al., *Capacitance of KOH activated carbide-derived carbons.* Phys Chem Chem Phys, 2009. **11**(25): p. 4943-5.

12. Thomberg, T., A. Janes, and E. Lust, *Energy and power performance of vanadium carbide derived carbon electrode materials for supercapacitors.* Journal of Electroanalytical Chemistry, 2009. **630**(1-2): p. 55-62.

13. Chmiola, J., et al., *Effect of pore size and surface area of carbide derived carbons on specific capacitance.* Journal of Power Sources, 2006. **158**(1): p. 765-772.

14. Chmiola, J., et al., *Anomalous increase in carbon capacitance at pore sizes less than 1 nanometer.* Science, 2006. **313**(5794): p. 1760-3.

15. Mangarella, M.C. and K.S. Walton, *Tailored Fe_3C-derived carbons with embedded Fe nanoparticles for ammonia adsorption.* Carbon, 2015. **95**: p. 208-219.

16. Moran, C.M., et al., *Synthesis and characterization of aluminum carbide-derived carbon with residual aluminum-based nanoparticles.* Carbon, 2017. **114**: p. 482-495.

17. Mangarella, M.C., et al., *Synthesis of embedded iron nanoparticles in Fe_3C-derived carbons.* Carbon, 2014. **79**: p. 74-84.

18. Borchardt, L., et al., *Preparation and application of cellular and nanoporous carbides.* Chem Soc Rev, 2012. **41**(15): p. 5053-67.

19. Dash, R.K., A. Nikitin, and Y. Gogotsi, *Microporous carbon derived from boron carbide.* Microporous and Mesoporous Materials, 2004. **72**(1-3): p. 203-208.

20. Jeong, M.G., et al., *Effect of lattice structure of silicon carbide on crystal formation of carbide-derived carbon.* Carbon, 2014. **79**: p. 19-27.

21. Welz, S., M.J. McNallan, and Y. Gogotsi, *Carbon structures in silicon carbide derived carbon.* Journal of Materials Processing Technology, 2006. **179**(1-3): p. 11-22.

22. Lee, A., R. Zhu, and M. McNallan, *Kinetics of conversion of silicon carbide to carbide derived carbon.* J Phys Condens Matter, 2006. **18**(32): p. S1763-70.

23. Portet, C., et al., *Impact of synthesis conditions on surface chemistry and structure of carbide-derived carbons.* Thermochimica Acta, 2010. **497**(1-2): p. 137-142.

24. Dash, R., et al., *Titanium carbide derived nanoporous carbon for energy-related applications.* Carbon, 2006. **44**(12): p. 2489-2497.

25. Dutzer, M.R., et al., *The effects of reactor design on the synthesis of titanium carbide-derived carbon.* Chemical Engineering Science, 2017. **160**(August 2016): p. 191-199.

26. Janes, A., T. Thomberg, and E. Lust, *Synthesis and characterisation of nanoporous carbide-derived carbon by chlorination of vanadium carbide.* Carbon, 2007. **45**(14): p. 2717-2722.

27. Xu, J., et al., *Effect of iron catalyst on the microstructure and electrochemical properties of vanadium carbide-derived carbons.* Materials Chemistry and Physics, 2013. **141**(1): p. 540-548.

28. Dash, R.K., G. Yushin, and Y. Gogotsi, *Synthesis, structure and porosity analysis of microporous mesoporous carbon derived from zirconium carbide.* Microporous and Mesoporous Materials, 2005. **86**(1-3): p. 50-57.

29. Gonzalez-Garcia, P., et al., *Nanostructure, porosity and electrochemical performance of chromium carbide derived carbons.* Carbon, 2015. **85**: p. 38-49.

30. Zhao, Q.L., et al., *Surface Modification and Performance Enhancement of Carbon Derived from Chromium Carbide for Supercapacitor Applications.* Journal of the Electrochemical Society, 2015. **162**(6): p. A845-A851.

31. Thomberg, T., A. Janes, and E. Lust, *Energy and power performance of electrochemical double-layer capacitors based on molybdenum carbide derived carbon.* Electrochimica Acta, 2010. **55**(9): p. 3138-3143.

32. Janes, A., et al., *Nanoscale fine-tuning of porosity of carbide-derived carbon prepared from molybdenum carbide.* Carbon, 2009. **47**(1): p. 23-29.

33. Kim, H.S., et al., *Molybdenum carbide-derived carbon for hydrogen storage.* Microporous and Mesoporous Materials, 2009. **120**(3): p. 267-271.

34. Tolosa, A., et al., *Niobium carbide nanofibers as a versatile precursor for high power supercapacitor and high energy battery electrodes.* Journal of Materials Chemistry A, 2016. **4**(41): p. 16003-16016.

35. Yuan, X.L., et al., *Unique graphitized mesophase carbon microbead@niobium carbide-derived carbon composites as high performance anode materials of lithium-ion battery.* Electrochimica Acta, 2017. **238**: p. 112-119.

36. Sepp, S., et al., *Impact of the Pt catalyst on the oxygen electroreduction reaction kinetics on various carbon supports.* Journal of Solid State Electrochemistry, 2014. **18**(5): p. 1223-1229.

37. Tallo, I., et al., *Nanostructured carbide-derived carbon synthesized by chlorination of tungsten carbide.* Carbon, 2011. **49**(13): p. 4427-4433.

38. Leis, J., et al., *Catalytic effects of metals of the iron subgroup on the chlorination of titanium carbide to form nanostructural carbon.* Carbon, 2002. **40**(9): p. 1559-1564.

39. Tsoncheva, T., et al., *Formation of catalytic active sites in iron modified activated carbons from agriculture residues.* Microporous and Mesoporous Materials, 2015. **217**: p. 87-95.

40. Katcho, N.A., et al., *Carbon hollow nanospheres from chlorination of ferrocene.* Chemistry of Materials, 2007. **19**(9): p. 2304-2309.

41. Urones-Garrote, E., et al., *Amorphous carbon nanostructures from chlorination of ferrocene.* Carbon, 2005. **43**(5): p. 978-985.

42. Aarset, K., et al., *Molecular structure of the aluminum halides, Al_2Cl_6, $AlCl_3$, Al_2Br_6, $AlBr_3$, and AlI_3, obtained by gas-phase electron-diffraction and ab initio molecular orbital calculations.* Journal of Physical Chemistry A, 1999. **103**(11): p. 1644-1652.

43. Hartman, M., O. Trnka, and O. Solcova, *Thermal decomposition of aluminum chloride hexahydrate.* Industrial & Engineering Chemistry Research, 2005. **44**(17): p. 6591-6598.

44. Yang, Z.L., et al., *Aluminum fractions in surface water from reservoirs by coagulation treatment with polyaluminum chloride (PAC): Influence of initial pH and OH-/Al_3+ ratio.* Chemical Engineering Journal, 2011. **170**(1): p. 107-113.

45. Park, H.K., K.Y. Park, and H.J. Kim, *Kinetics of Gas-Phase Hydrolysis of Aluminum Chloride for Alumina Particles.* Industrial & Engineering Chemistry Research, 2014. **53**(39): p. 14956-14962.

46. Maldonado-Hodar, F.J., et al., *Catalytic graphitization of carbon aerogels by transition metals.* Langmuir, 2000. **16**(9): p. 4367-4373.

47. Lubben, M., A. Meetsma, and B.L. Feringa, *Crystal and Molecular-Structure of Polymeric [Mncl$_2$(Bpy)](N).* Inorganica Chimica Acta, 1995. **230**(1-2): p. 169-172.

48. Morosin, B. and E.J. Graeber, *Crystal Structures of Manganese(II) and Iron(II) Chloride Dihydrate.* The Journal of Chemical Physics, 1965. **42**(3): p. 898-901.

49. Zalkin, A., J.D. Forrester, and D.H. Templeton, *The Crystal Structure of Manganese Dichloride Tetrahydrate.* Inorganic Chemistry, 1964. **3**(4): p. 529-533.

50. Hummers, W.S., et al., *Zirconium and Hafnium Tetrachlorides*. John Wiley & Sons, Inc. p. 121-126.

51. Myers, W.R. and W.P. Fishel, *The Preparation and Hydrolysis of Manganese Carbide (Mn_3c).* Journal of the American Chemical Society, 1945. **67**(11): p. 1962-1964.

52. Putnam, G.L. and K.A. Kobe, *Hydrocarbons from carbides.* Chemical Reviews, 1937. **20**(1): p. 131-143.

53. Dierkes, H. and R. Dronskowski, *High-Resolution Powder Neutron Diffraction on Mn_3C.* Zeitschrift Fur Anorganische Und Allgemeine Chemie, 2014. **640**(15): p. 3148-3152.

54. Picon, M. and J. Flahaut, *Manganese Carbides.* Comptes Rendus de l'Académie des Sciences, Série B, 1957. **275**: p. 62-64.

55. Bouchaud, J.P., *Structural Study of Manganese Carbides.* Annales de Chimie, 1967. **14**(6): p. 353-366.

56. Barros, E.B., et al., *D band Raman intensity calculation in armchair edged graphene nanoribbons.* Physical Review B, 2011. **83**(24): p. 245435-245435.

57. Ferrari, A.C. and J. Robertson, *Interpretation of Raman spectra of disordered and amorphous carbon.* Physical Review B, 2000. **61**(20): p. 14095-14107.

58. Urbonaite, S., L. Halldahl, and G. Svensson, *Raman spectroscopy studies of carbide derived carbons.* Carbon, 2008. **46**(14): p. 1942-1947.

59. Aoki, A., *X-Ray Photoelectron Spectroscopic Studies on ZnS-MnF_2 Phosphors.* Japanese Journal of Applied Physics, 1976. **15**(2): p. 305-311.

60. Carver, J.C., G.K. Schweitzer, and T.A. Carlson, *Use of X-Ray Photoelectron Spectroscopy to Study Bonding in Cr, Mn, Fe, and Co Compounds.* The Journal of Chemical Physics, 1972. **57**(2): p. 973-982.

61. Turner, N.H., *Surface analysis: X-ray photoelectron spectroscopy and Auger electron spectroscopy.* Anal Chem, 1988. **60**(12): p. 377R-387R.

CHAPTER 6. CONCLUSIONS AND RECOMMENDATIONS

6.1 Overview

Metal nanoparticles have the potential to increase performance for gas adsorption and catalysis through stronger chemisorption as opposed to weakly adsorbed physisorption, such as the insertion of platinum nanoparticles in templated carbon,[1] photo-oxidation of volatile organic compounds with gold nanoparticles,[2] or the addition of zinc oxide nanoparticles inserted into graphene oxide for enhanced carbon dioxide adsorption.[3] This positive feature is consistently observed in activated carbon literature and their related applications. As the CDC precursor already contains metal atoms, a controlled extraction of the metal atoms has the potential to create a porous carbon with residual metal nanoparticles. The overall goal of this research has been to provide the knowledge to design carbide-derived carbides (CDCs) for use in adsorptive gas applications. The broad goal of this Ph.D. was divided into three objectives to uncover the techniques and mechanisms necessary to successfully control the residual metal in CDCs. The first objective resulted in the development of successful synthesis techniques to control the shrinking core model of metal extraction from titanium carbide (TiC). Next, the mechanism and chemical properties necessary to form metal nanoparticles was investigated by synthesizing a new CDC, manganese carbide-derived carbide. Lastly, the interactions between sulfur dioxide in dry, humid, and aqueous environments and TiC-CDC were explored with the determination that residual sulfate species remain to completely block pores.

6.2 Control of the Core-Shell Model of Metal Extraction from Titanium Carbide

CHAPTER 3 focused on creating a uniform sample throughout the reaction bed. Previous literature focused on fully etched carbides without residual metal for electrochemical applications such as supercapacitors. While early research into CDCs primarily focused on these fully etched CDCs, a few researchers concentrated on the rate of metal extraction during various stages of the etching process. While this metal removal rate is noteworthy, investigators have only recently directed their efforts explicitly to create partially etched CDCs for adsorptive applications. These most recent studies synthesizing partially etched CDCs have found that shorter etching using the standard flow-over, horizontal-bed reactor results in the formation of layers with various properties in each layer. To overcome this, the first objective investigated reactor design and the impact of flow patterns within the reaction tube on titanium carbide derived carbon (TiC-CDC) properties. TiC was specifically chosen as the metal chloride did not form metal nanoparticles at the etching temperature due to its volatility. This study found optimal conditions to create partially etched TiC-CDC samples with uniform properties. The synthesis conditions necessary to control the shrinking core model of titanium extraction could be extended to other CDC systems, such as iron carbide-derived carbon, that do form metal nanoparticles.

Three reactors were designed and implemented to assess the role of flow patterns and agitation within the reactor bed for the purpose of partially etching TiC. The first design is a conventional fabrication seen repeatedly in CDC literature: a flow-over, horizontal tube reactor. The second and third designs included a vertical packed-bed reactor and a fluidized-bed reactor, respectively. The horizontal-bed reactor was

diffusionally limited as completely etched and completely non-etched layers were formed. This result indicated that Cl_2 must progress slowly through the sample bed due to the slow diffusion of Cl_2 to the bottom of the reactor bed and the fast reaction kinetics creating $TiCl_4$, which is then easily removed due to its volatility. The Cl_2/Ar stream flowed through the bed of the packed-bed reactor; however, this design suffered from channeling effects due to the natural aggregation of the carbide and carbon particles, which resulted in non-uniform properties within the sample. As flowing Cl_2 through the sample bed did not achieve the stated goal of this objective, agitation was introduced through a fluidized-bed reactor. This reactor allowed for a density-based separation of the particles, the density of which was directly related to the amount of etching that had occurred within a particle. The separation of particles by density and exploitation of the naturally ensuing Cl_2 concentration gradient produced by the reaction, particles with uniform properties could then be synthesized.[4, 5]

Future research should focus on optimizing reactor design for a wider range of particle sizes and to limit excess Cl_2. The essential conditions to establish particle fluidization can be difficult to control as flow rate, particle size and density, and fluid viscosity and density must be within a narrow window of operating conditions. For example, carbide particles smaller than 150 μm in diameter cannot be fluidized due to aggregation; however, large particles can suffer from internal diffusional limitations potentially hampering their ability for certain applications. Any particle size could be synthesized by investigating, for example, rotating horizontal tube reactors with a cross flow of carbide particles and Cl_2 with a carrier gas or by investigating other sources of Cl_2 for use in vacuum batch or similar reactors.

6.3 Investigation in to Possible Metal Nanoparticle Formation

Previous research indicated that the physical properties of the metal chloride created through the etching reaction had the greatest effect on in-situ metal nanoparticle formation. For Fe_3C-CDC, $FeCl_2$ and $FeCl_3$ were theorized to locally graphitize the reorganized carbon, which then enabled the vaporized iron chlorides to condense and become trapped within these carbon structures. Co and Ni are two other metals that can form carbides and act as a graphitization catalyst; thus, they are expected to behave similarly. Al_4C_3-CDC also created metal nanoparticles; however, this mechanism is not yet well understood. $AlCl_3$ sublimes at 180°C, exists as either a monomer or dimer, and polymerizes in the presence of water. CHAPTER 5 examined manganese carbide, which had not been previously used as a CDC precursor. Mn_3C was chosen because certain manganese chloride ions have the ability to polymerize and the metal removal was dependent upon the vapor pressure as the etching reaction was performed between the melting and boiling point of $MnCl_2$. Ultimately there was no evidence of nanoparticle formation; however, metal removal was indeed dependent upon the etching temperature and length of etching time. At temperatures below the melting point of $MnCl_2$, there was minimal metal removal. At longer etching times, more $MnCl_2$ was allowed to enter the vapor phase for removal.

While studying the Mn_3C-CDC system did not provide the solution to the puzzle of how metal nanoparticles are formed in-situ during the etching process, this study did provide further knowledge of relevant conditions. Specifically with manganese carbide, higher etching temperatures could be used to ensure that the reaction takes place at temperatures above the boiling point of $MnCl_2$ (1225°C). Instead of using Mn_3C, other

manganese carbide precursors, such as Mn_7C_3, Mn_5C_2 and $Mn_{23}C_6$, which are more thermodynamically stable than Mn_3C,[6] could be used, and the effects of various crystal packings on CDC properties could be further investigated. Additionally the bond nature between the metal and chlorine atoms should be noted. Bonds found within $MnCl_2$ are more ionic in nature than covalent, which leads to higher etching temperatures necessary for efficient metal removal. This more ionic bonding nature also allows for the residual metal salt to be easily dissolvable in water for post-etching treatment. Ultimately, further research is needed to investigate other carbide systems that could provide similar reaction pathways to Fe_3C and Al_4C_3 to create in-situ metal nanoparticles in CDCs. These studies should explore other unique properties of the metal chloride, such as ability to sublimate and to exist in multiple forms at similar conditions. Constraints include the ability of the metal to form a stable carbide in most conditions and the ability of the metal chloride to vaporize at the specific etching temperature.

6.4 Stability of TiC-CDC in Acidic Environments

TiC-CDC samples with various amounts of residual metal were examined for their performance stability in dry, humid, and aqueous SO_2 environments. For all exposure conditions regardless of the presence of H_2O and the concentration of SO_2, the samples gained similar levels of weakly chemisorbed sulfate groups, which completely blocked pores. These functional groups could not be removed through a pressure or temperature swing, and subsequently, the physical properties of TiC-CDC were degraded. Specifically, the surface area was decreased, but the pore size distribution remained the same. In order to restore the original CDC properties, vigorous water washing involving sonication was needed to remove the sulfate groups from the pores.

Activated carbons are renowned for their chemical stability; however, their physical properties can change due to the addition of functional groups, which are typically added through acid and base treatments. While the pore structure of activated carbons is hierarchical, the pores of CDCs are uniform in size due to the crystalline nature of the carbide precursor. Further investigation should involve other acids commonly found in separation applications such as NO_x and H_2S. These gases have the potential to add permanent functional groups that cannot be removed through vigorous washing cycles. Understanding how the adsorption properties of CDCs are modified through their potential application is of upmost importance for determining CDC lifetime and cyclability.

This work has led to increased understanding of the mechanism and methods used to control the metal etching process in the formation of CDCs. Particle agitation during etching is necessary for the creation of uniform properties in partially etched samples, while the properties of the metal chloride are of utmost importance in predicting whether the carbide will form metal nanoparticles in-situ. However, further research should focus on reactor designs with a wide range of potential operating conditions for a variety of particle sizes and on expanding the theorized criteria necessary for accessible residual metal for adsorption and catalysis to increase CDC systems capable of in-situ metal nanoparticle formation.

6.5 References

1. Joo, S.H., et al., *Ordered nanoporous arrays of carbon supporting high dispersions of platinum nanoparticles.* Nature, 2001. **412**(6843): p. 169-172.

2. Tangale, N.P., et al., *Enhanced Mineralization of Gaseous Organic Pollutant by Photo-Oxidation Using Au-Doped TiO_2/MCM-41*. Water Air and Soil Pollution, 2014. **225**(2): p. 1847-1847.

3. Chiang, Y.C. and R.S. Juang, *Surface modifications of carbonaceous materials for carbon dioxide adsorption: A review*. Journal of the Taiwan Institute of Chemical Engineers, 2017. **71**: p. 214-234.

4. Ariyanto, T., et al., *Synthesis of carbon core-shell pore structures and their performance as supercapacitors*. Microporous and Mesoporous Materials, 2015. **218**: p. 130-136.

5. Ariyanto, T., et al., *Controlled synthesis of core-shell carbide-derived carbons through in situ generated chlorine*. Carbon, 2017. **115**: p. 422-429.

6. Moattar, F. and J.S. Anderson, *Thermodynamics of the manganese carbides Mn_7C_3, Mn_5C_2 and $Mn_{23}C_6$*. Transactions of the Faraday Society, 1971. **67**: p. 2303.

APPENDIX A. SUPPLEMENTAL INFORMATION

A.1 Chapter 3: The Effects of Reactor Design on the Synthesis of Titanium Carbide-Derived Carbon

Reproduced (adapted) from Dutzer, M.R., et al., *The effects of reactor design on the synthesis of titanium carbide-derived carbon.* Chemical Engineering Science, 2017. **160**(August 2016): p. 191-199.

A.1.1 Supplemental and Raw Data for Chapter 3

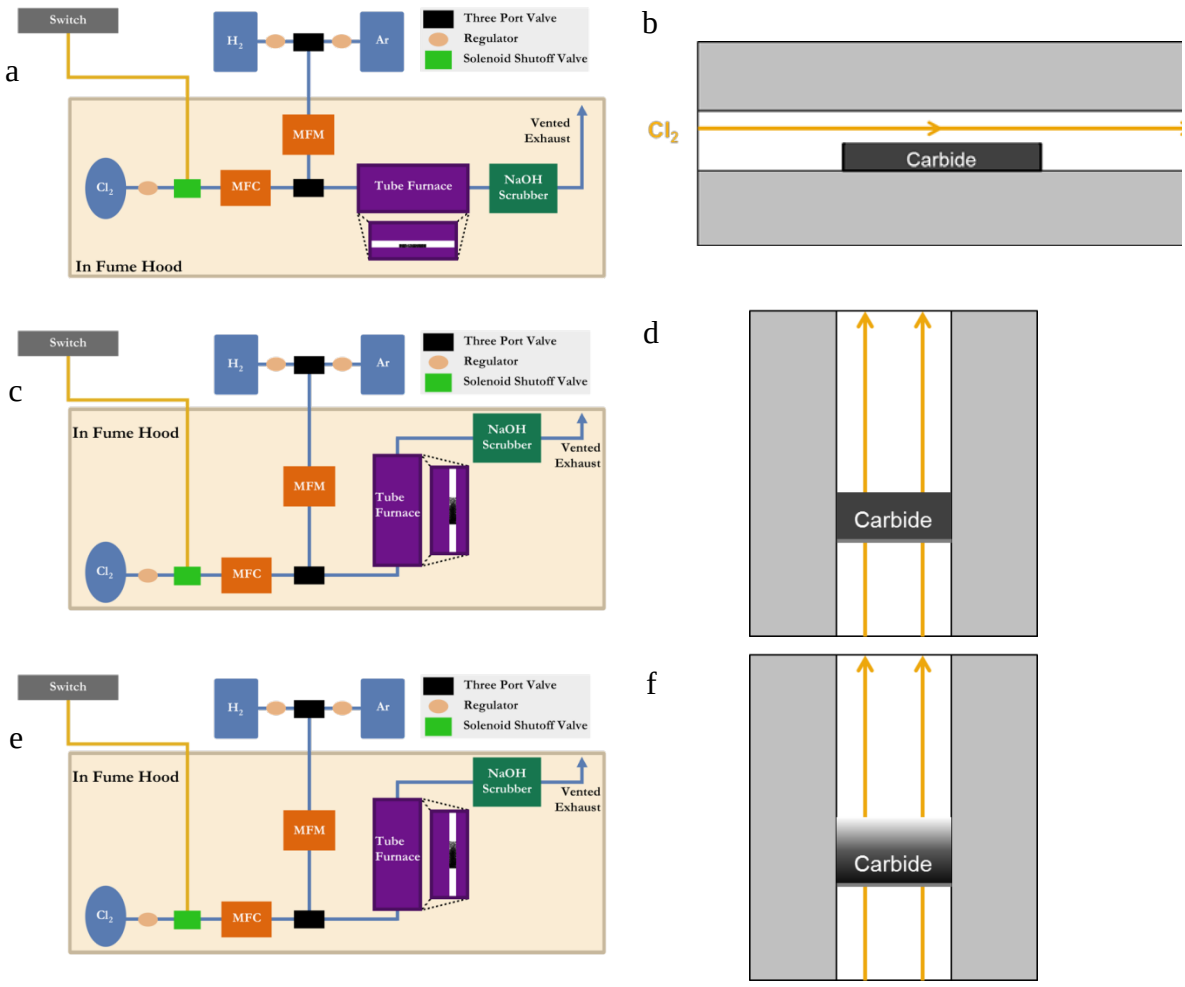

Figure A.1 – Reactor diagrams and Cl_2 flow patterns through the reaction tube for (a,b) the horizontal-bed reactor, (c,d) the packed-bed reactor, and (e,f) the fluidized-bed reactor.

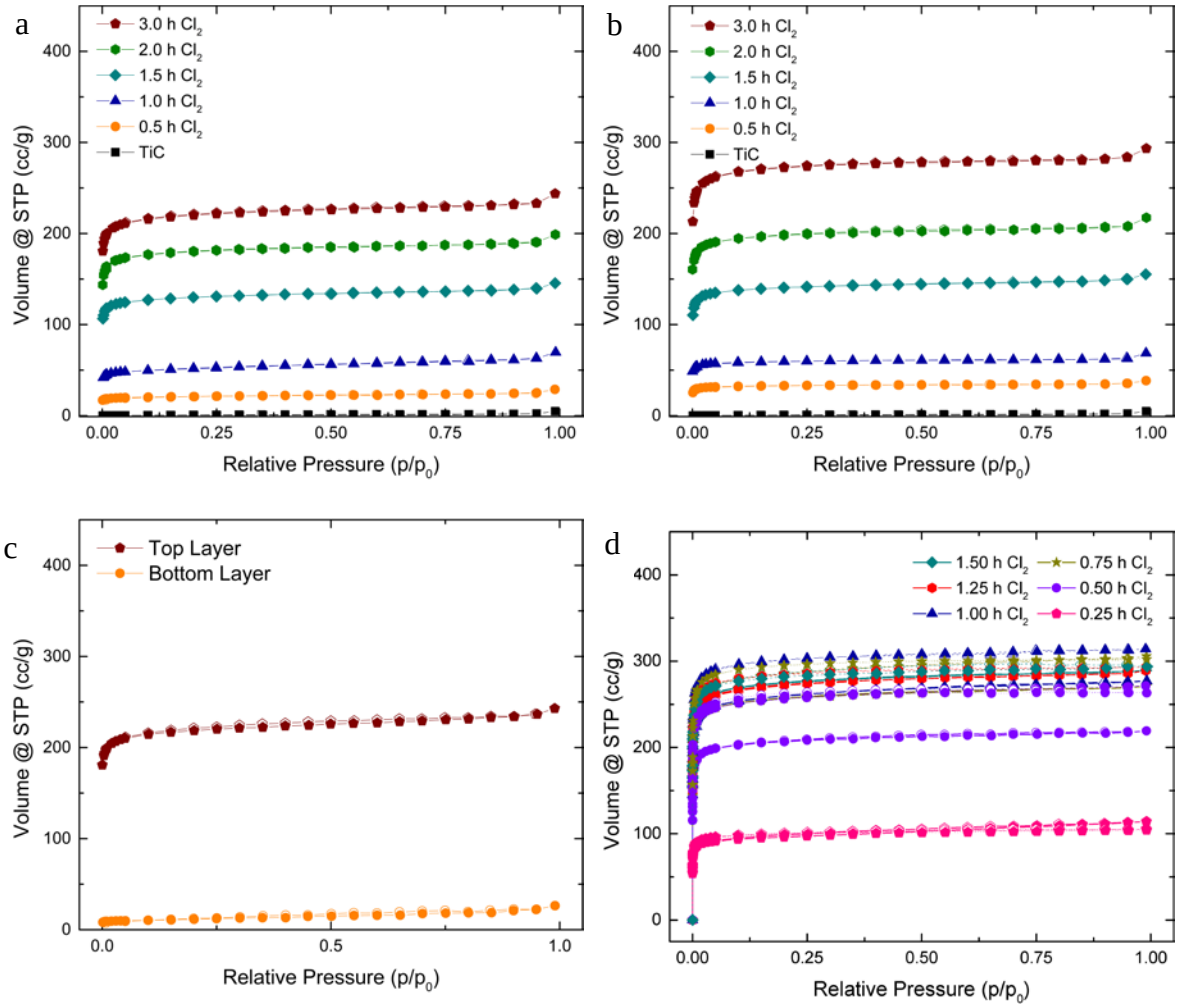

Figure A.2 – N_2 sorption at 77 K isotherms for (a) horizontal-bed reactor samples, (b) packed-bed reactor samples, (c) the horizontal layers from a horizontal-bed reactor sample, and (d) fluidized-bed reactor samples.

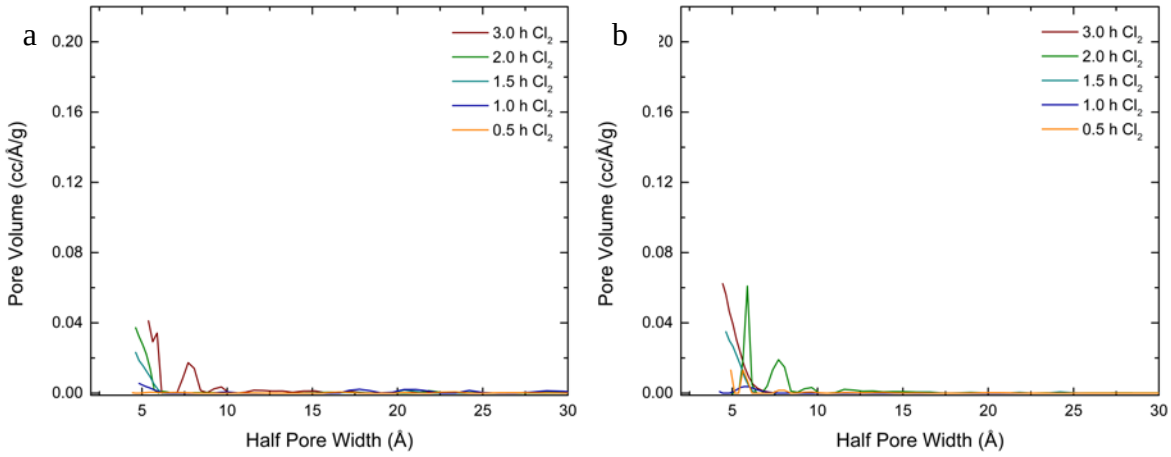

Figure A.3 – Pore size distributions for the (a) horizontal-bed reactor samples and (b) packed-bed reactor samples.

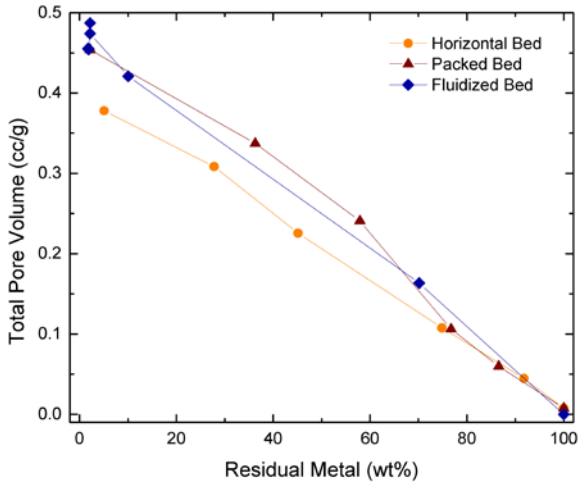

Figure A.4 – Total pore volume as a function of residual metal measured at $p/p_0 = 0.99$.

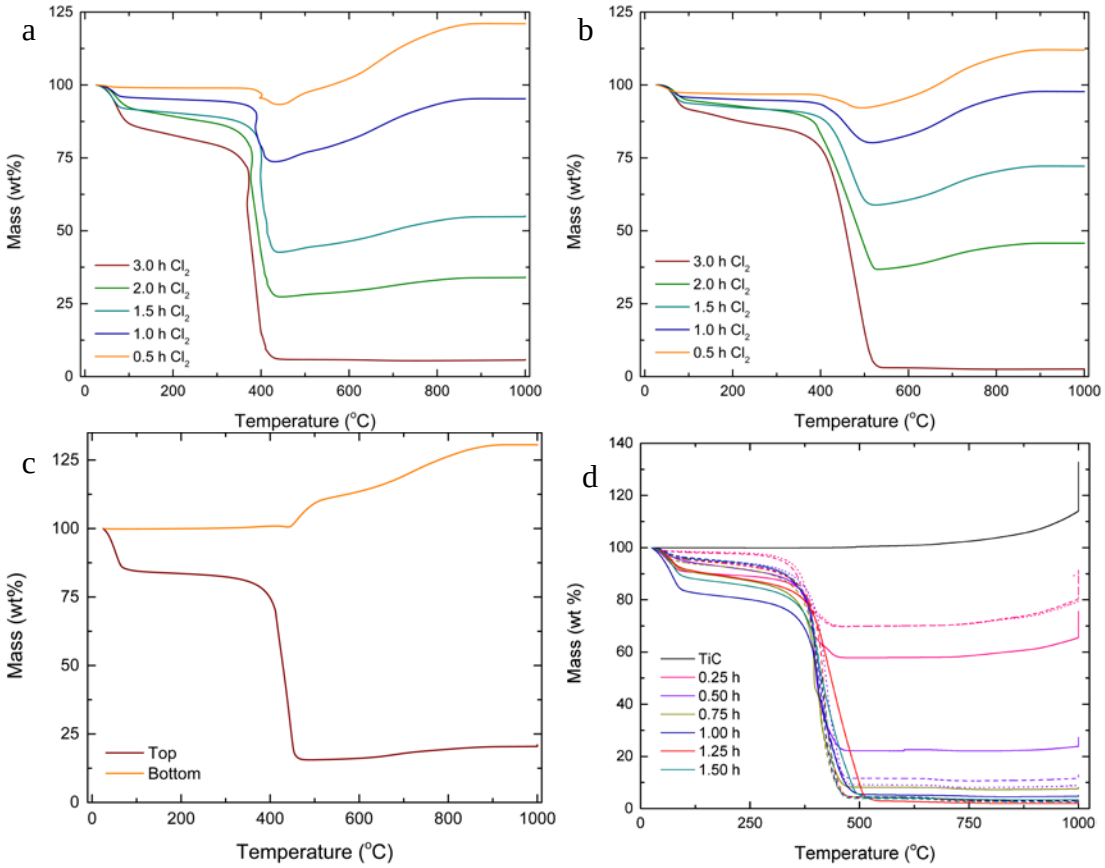

Figure A.5 – TGA curves for (a) horizontal-bed reactor samples, (b) packed-bed reactor samples, (c) horizontal layers, and (d) fluidized-bed reactor samples, where the dashed lines refer to a second set of fluidized-bed reactor samples and the dotted lines to samples held 1.50 h.

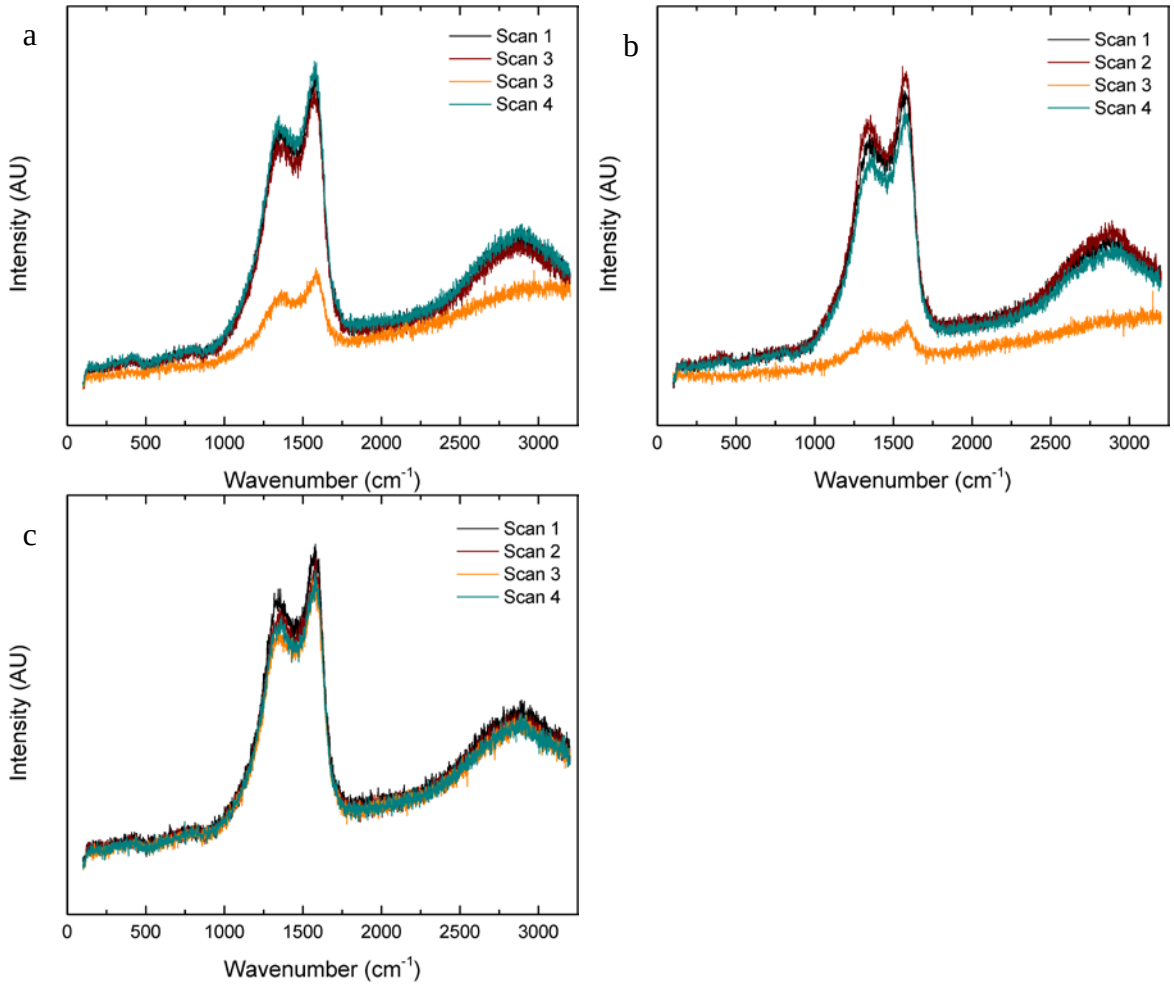

Figure A.6 – Raman spectra for samples chlorinated for (a) 0.5 h, (b) 1.5 h, and (c) 3.0 h performed on the horizontal-bed reactor.

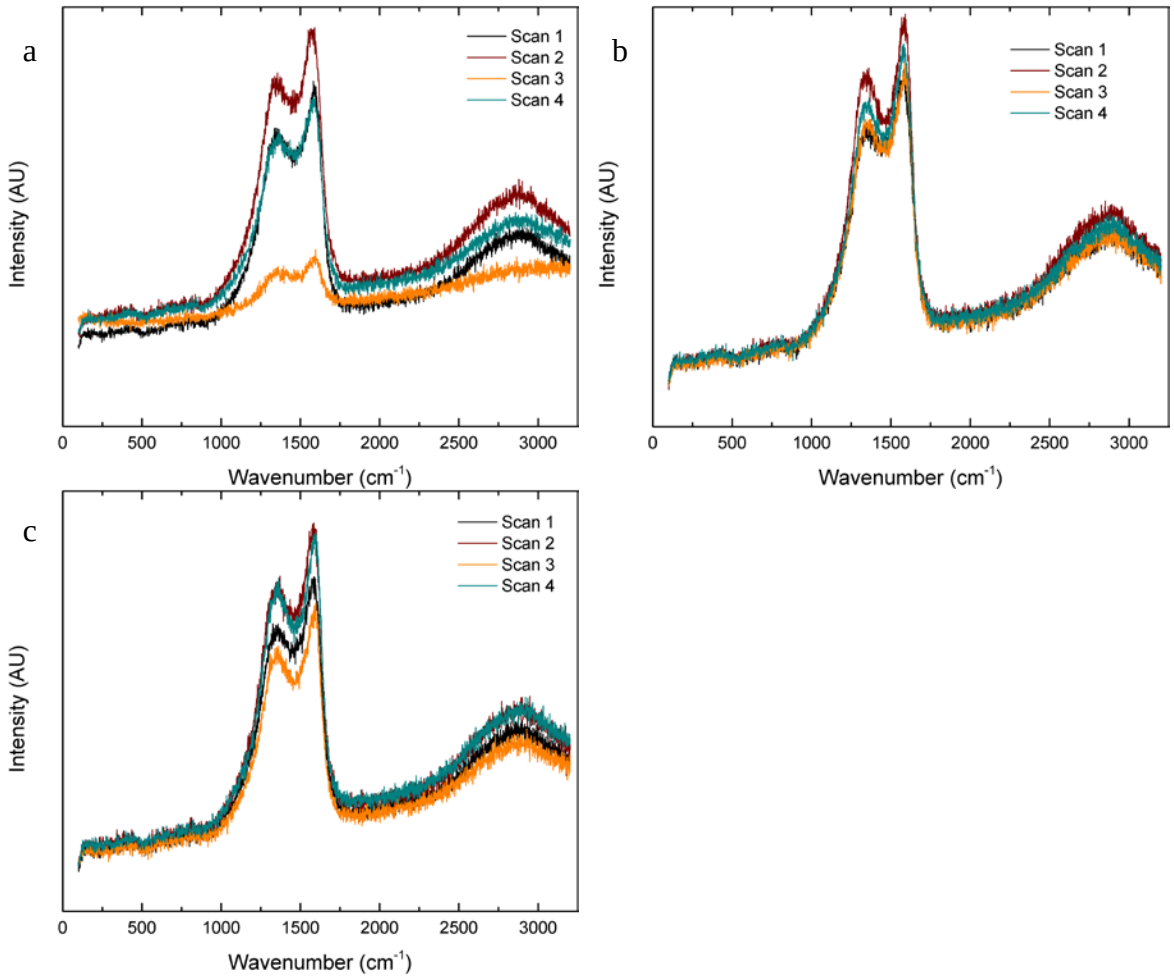

Figure A.7 – Raman spectra for samples chlorinated for (a) 0.50 h, (b) 1.50 h, and (c) 3.00 h performed on the packed-bed reactor.

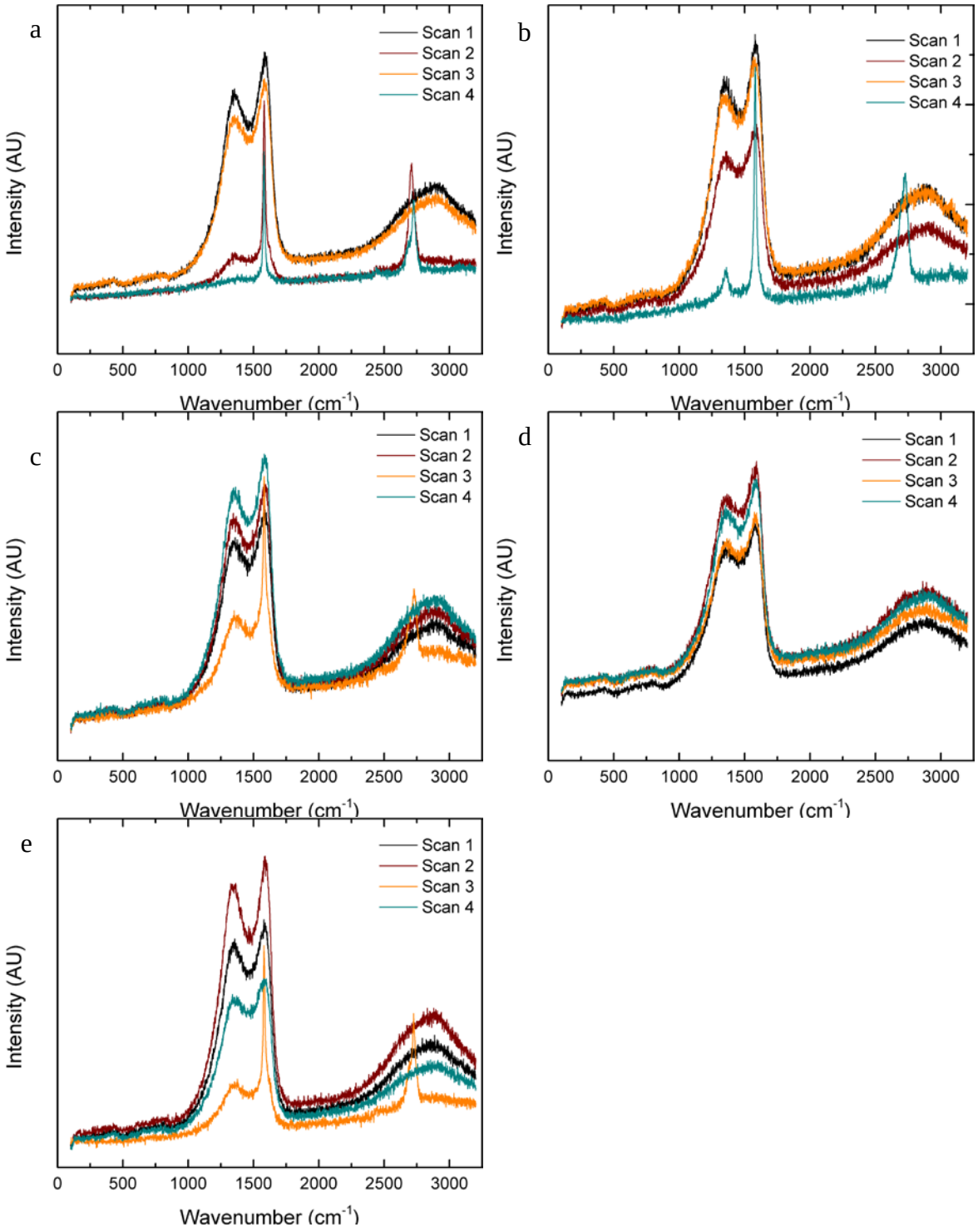

Figure A.8 – Raman spectra for sample chlorinated for (a) 0.25 h, (b) 0.75 h, and (c) 1.50 h, (d) 0.25 h Cl_2 sample held at 500°C for 1.50 h in total from the fluidized-bed reactor, and (e) 0.75 h Cl_2 sample held at 500°C for 1.50 h in total performed on the fluidized-bed reactor.

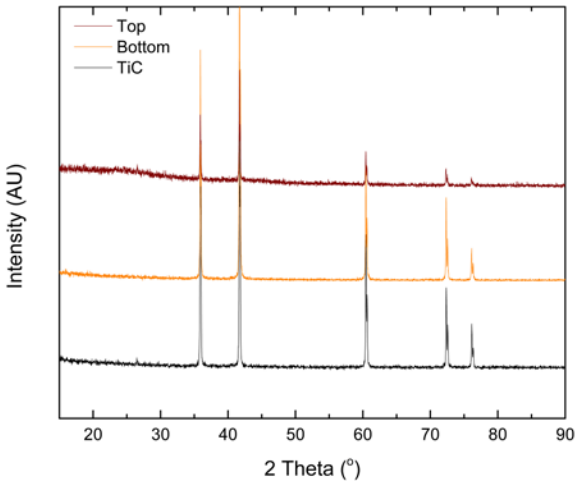

Figure A.9 – PXRD patterns for the top and bottom layers of a hand-separated 0.50 h Cl_2 TiC-CDC sample etched on the horizontal-bed reactor.

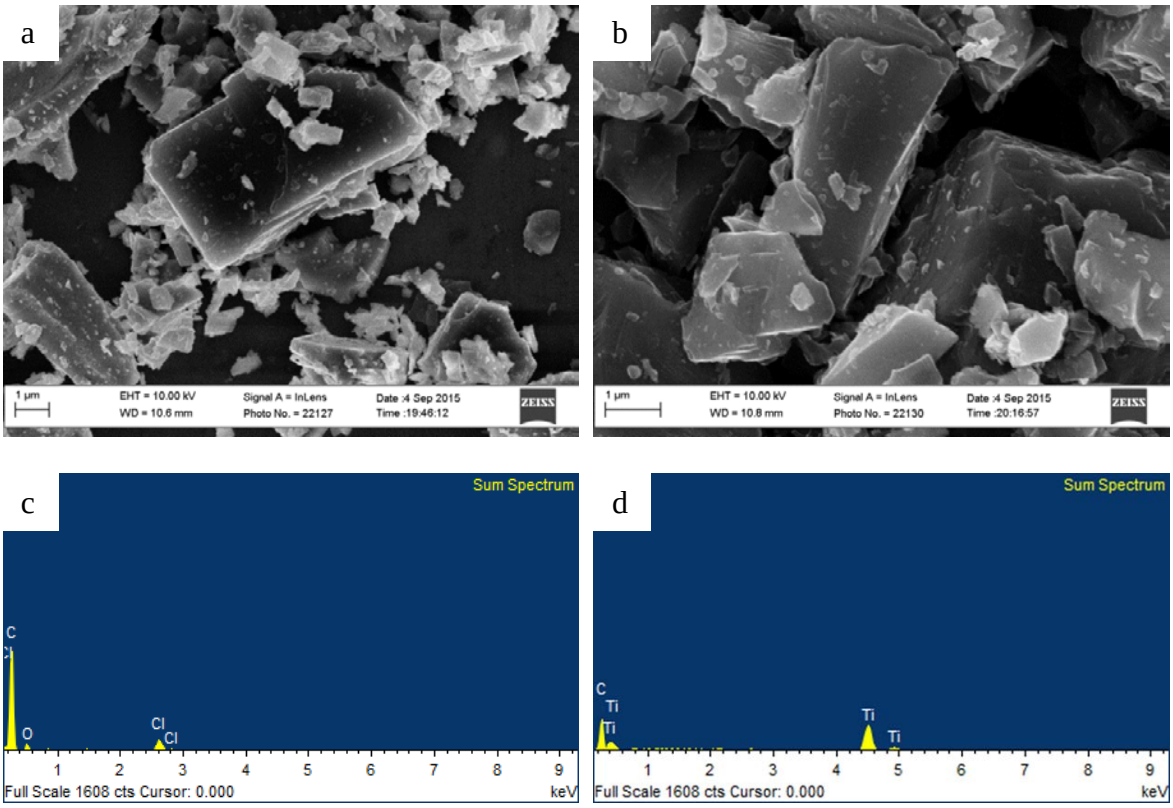

Figure A.10 – SEM images and EDX data of the (a, c) bottom and (b, d) top layers of the horizontal-bed reactor.

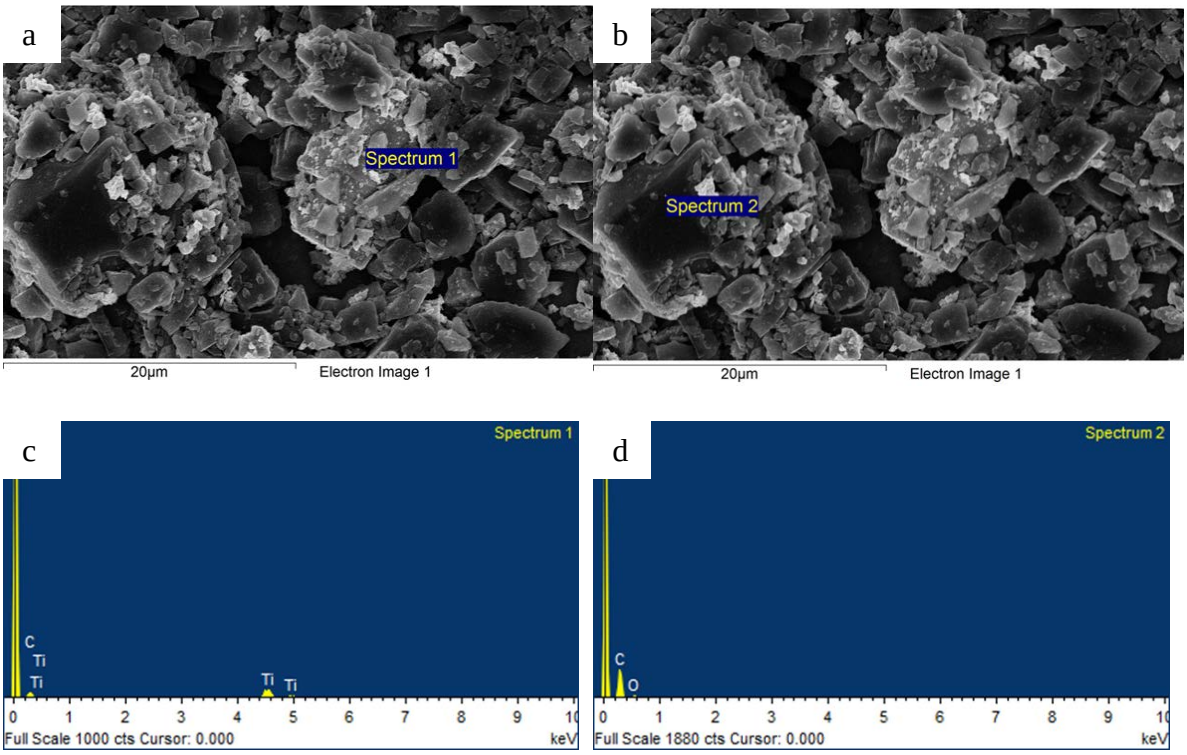

Figure A.11 – SEM images (a, b) of and EDX data (c, d) for a packed-bed reactor sample.

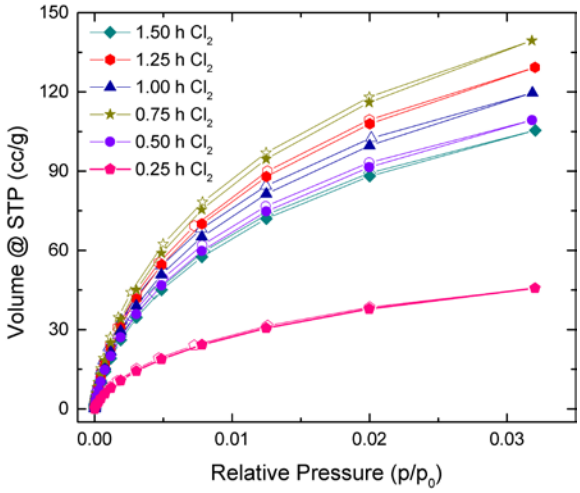

Figure A.12 – CO_2 isotherms measured at 298 K for fluidized-bed reactor samples etched for various times.

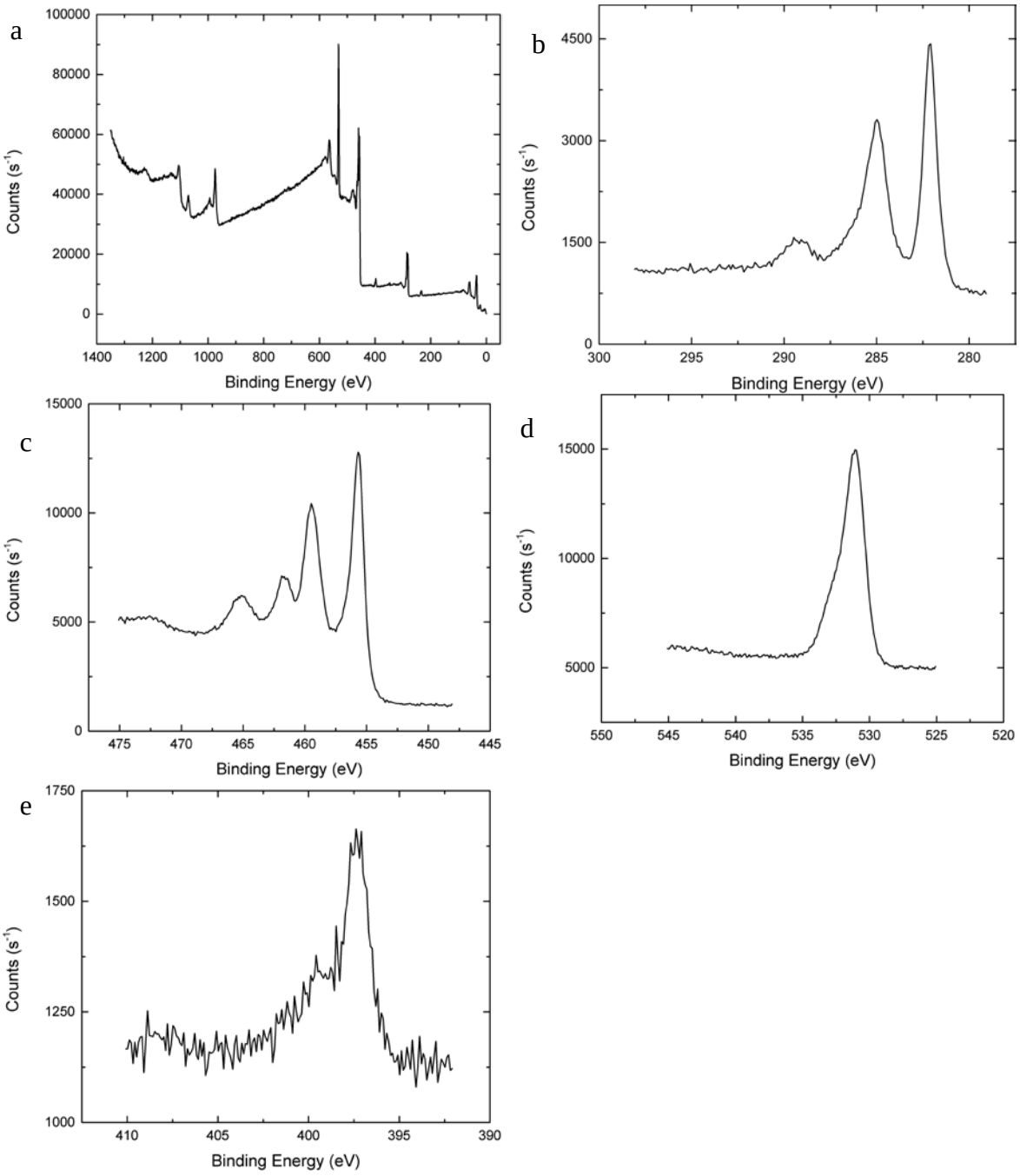

Figure A.13 – XPS scans for TiC (a) overall, (b) carbon, (c) titanium, (d) oxygen, and (e) nitrogen.

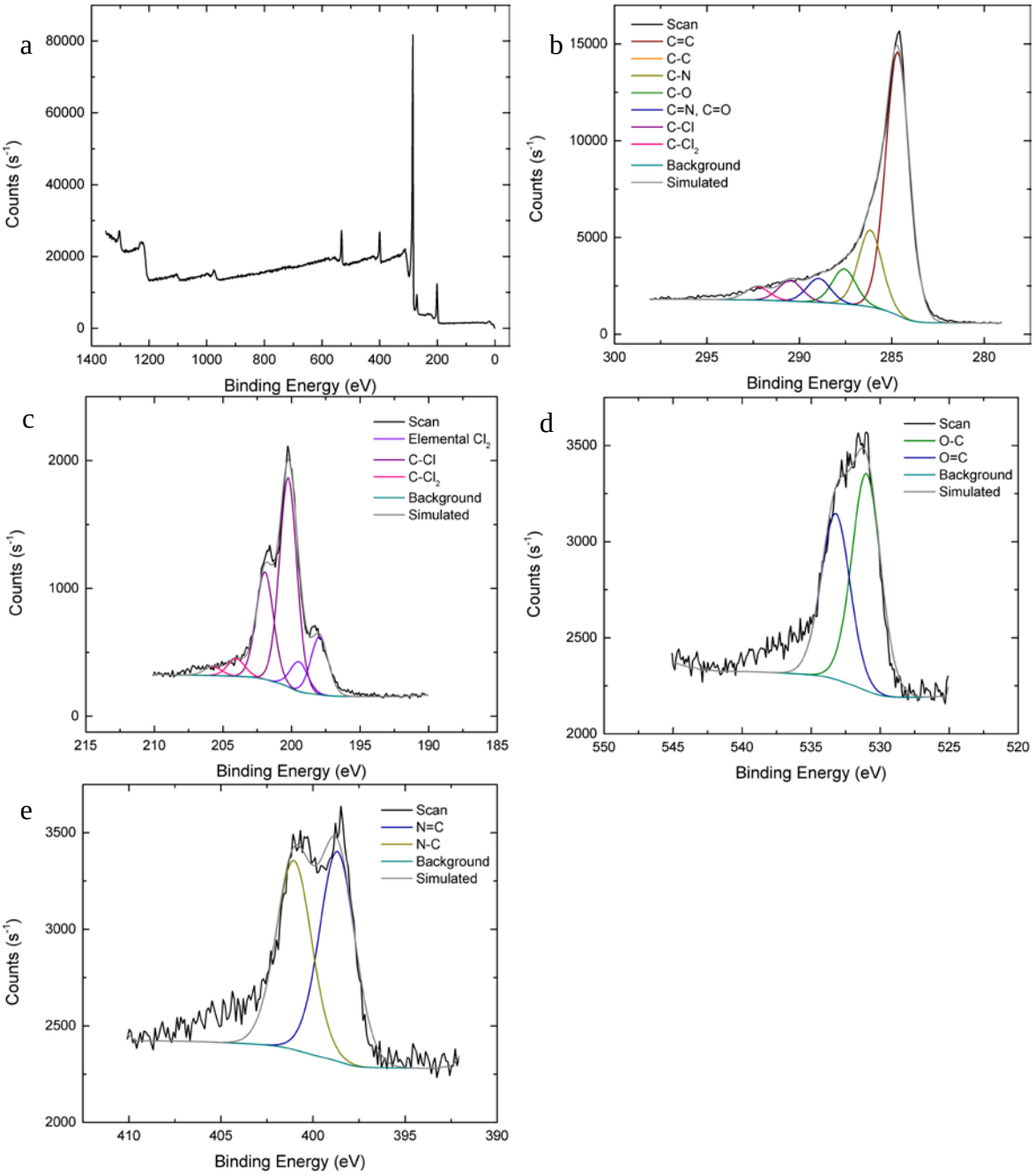

Figure A.14 – XPS scans for a sample etched for 0.25 h in a fluidized-bed reactor for (a) overall, (b) carbon, (c) chlorine, (d) oxygen, and (e) nitrogen.

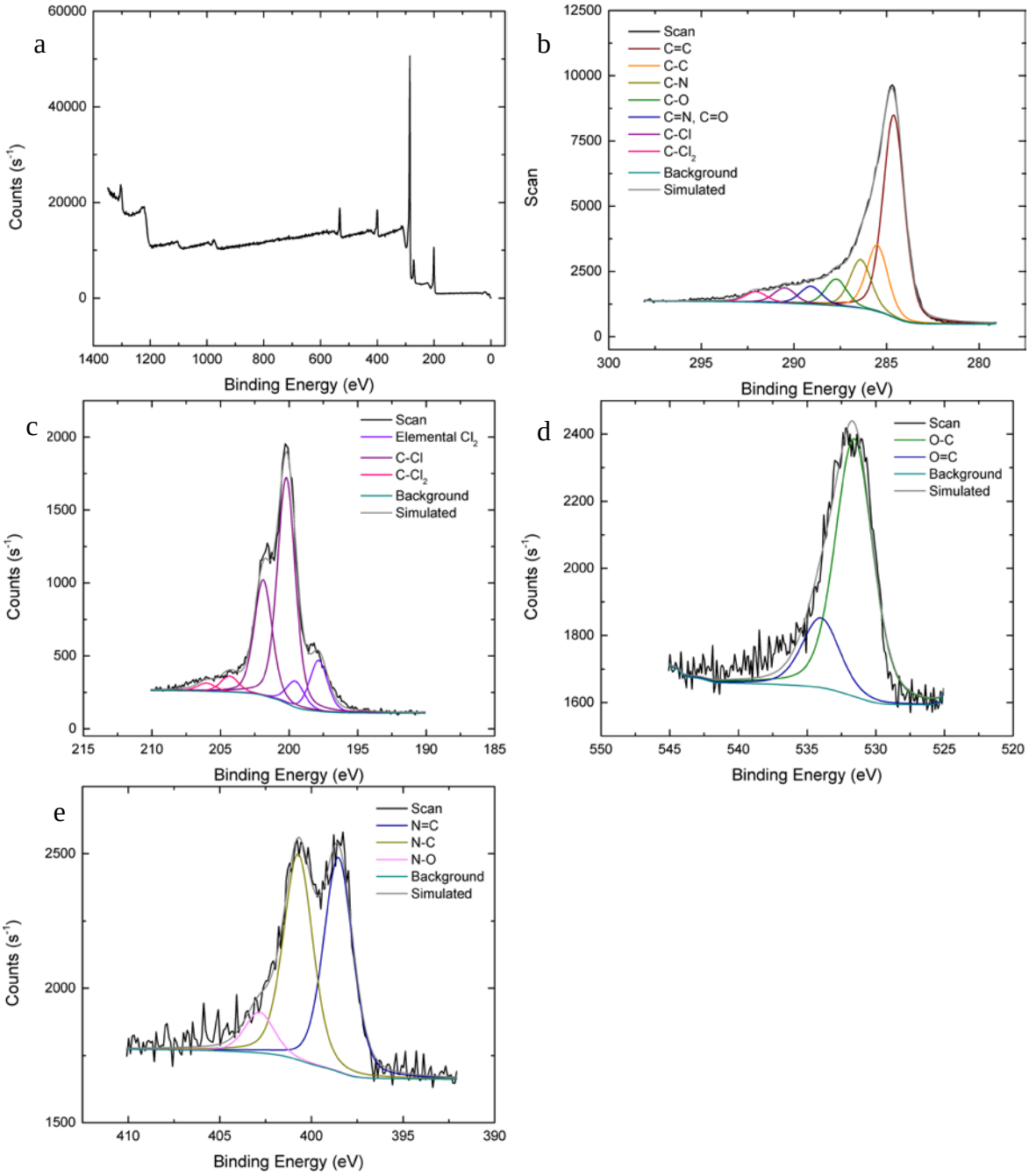

Figure A.15 – XPS scans for a sample etched for 0.50 h in a fluidized-bed reactor for (a) overall, (b) carbon, (c) chlorine, (d) oxygen, and (e) nitrogen.

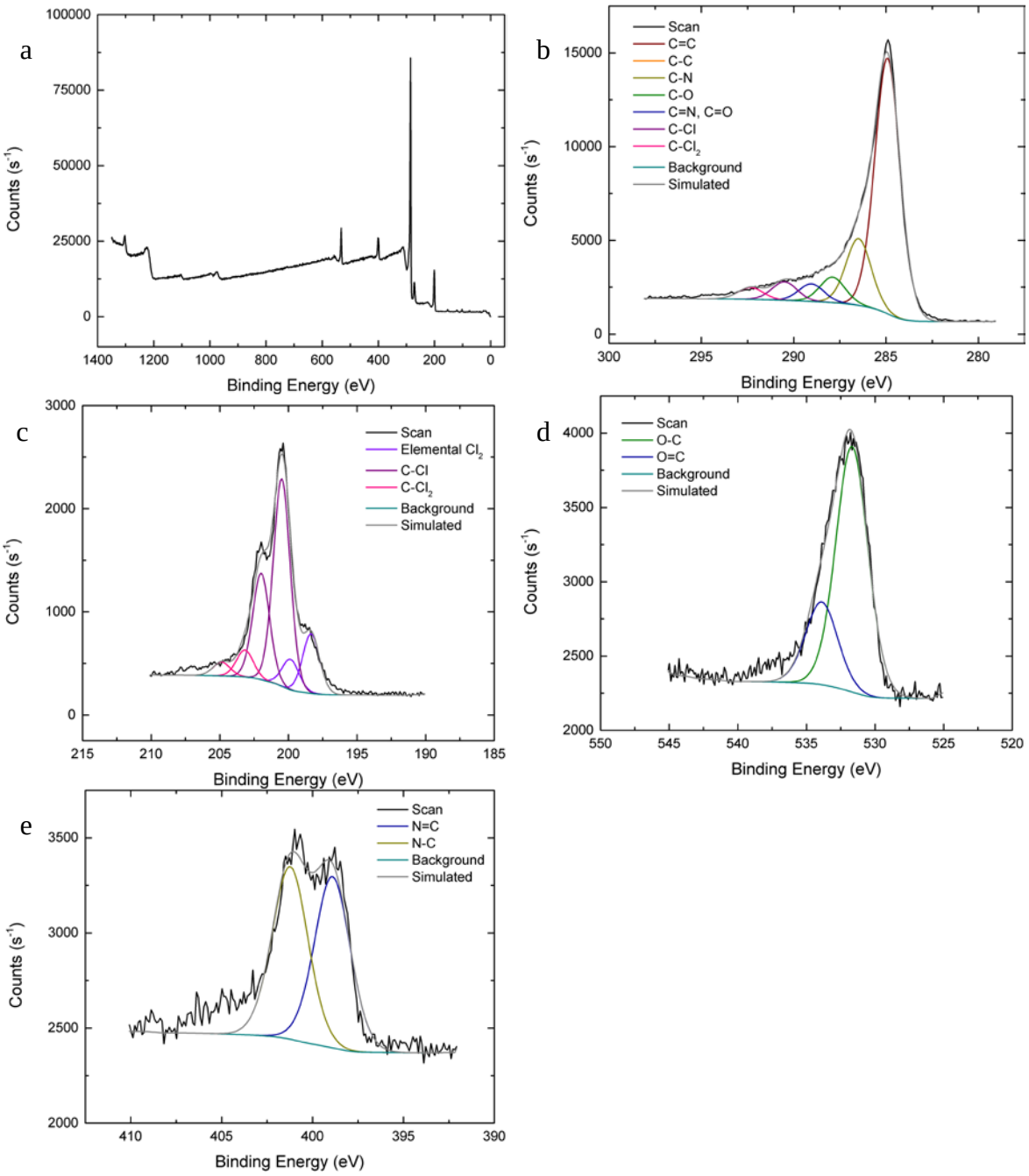

Figure A.16 – XPS scans for a sample etched for 0.75 h in a fluidized-bed reactor for (a) overall, (b) carbon, (c) chlorine, (d) oxygen, and (e) nitrogen.

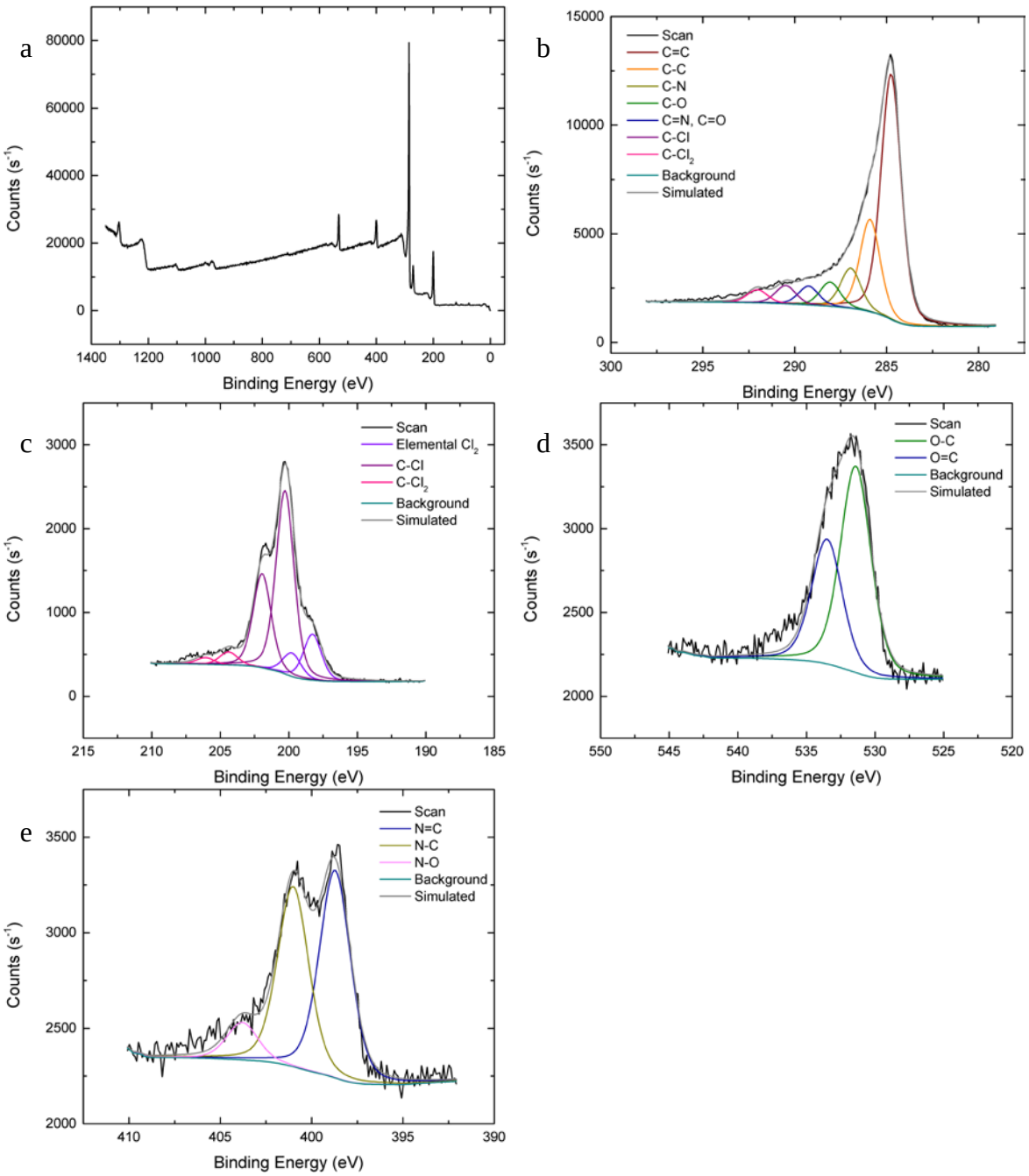

Figure A.17 – XPS scans for a sample etched for 1.00 h in a fluidized-bed reactor for (a) overall, (b) carbon, (c) chlorine, (d) oxygen, and (e) nitrogen.

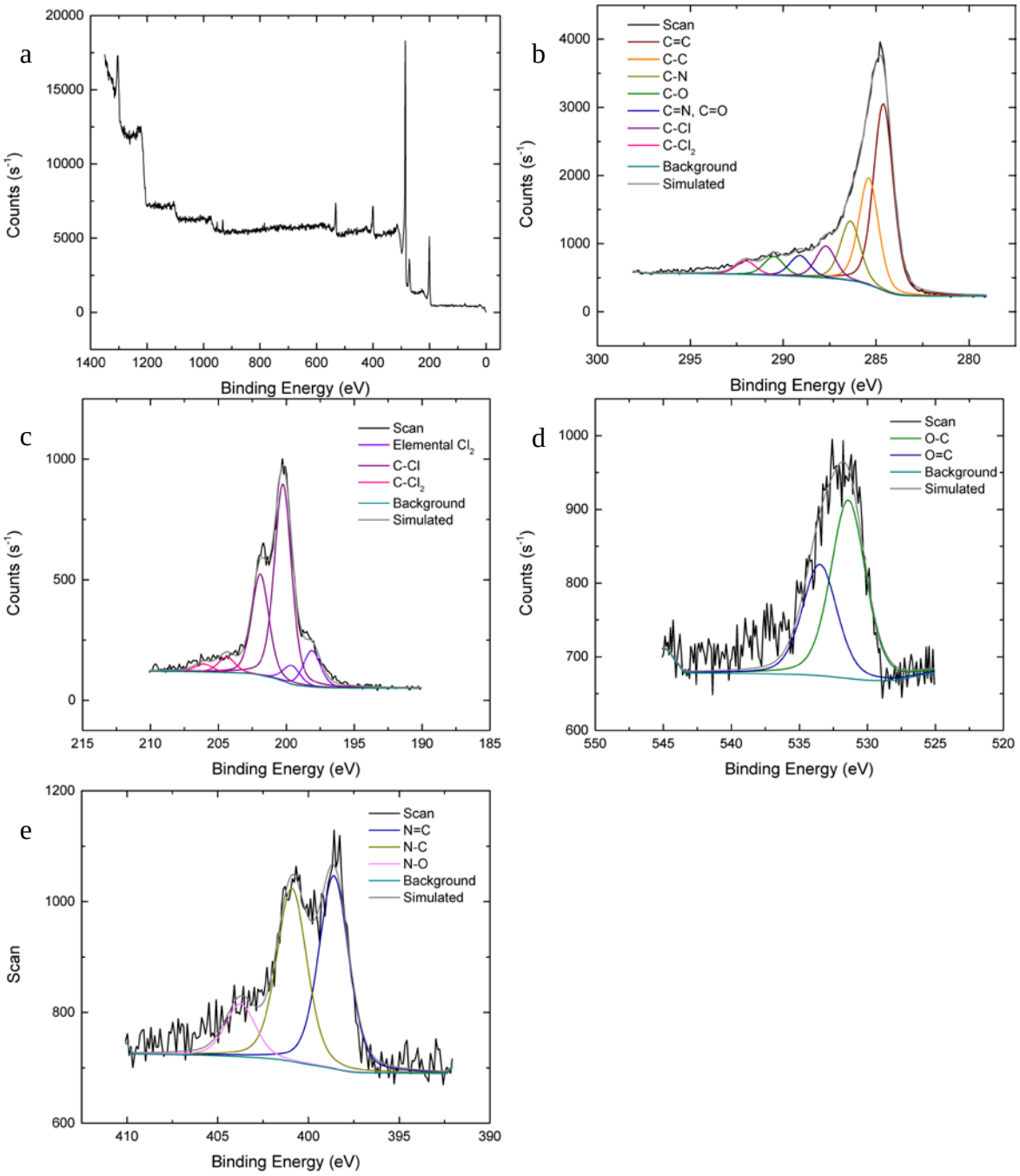

Figure A.18 – XPS scans for a sample etched for 1.25 h in a fluidized-bed reactor for (a) overall, (b) carbon, (c) chlorine, (d) oxygen, and (e) nitrogen.

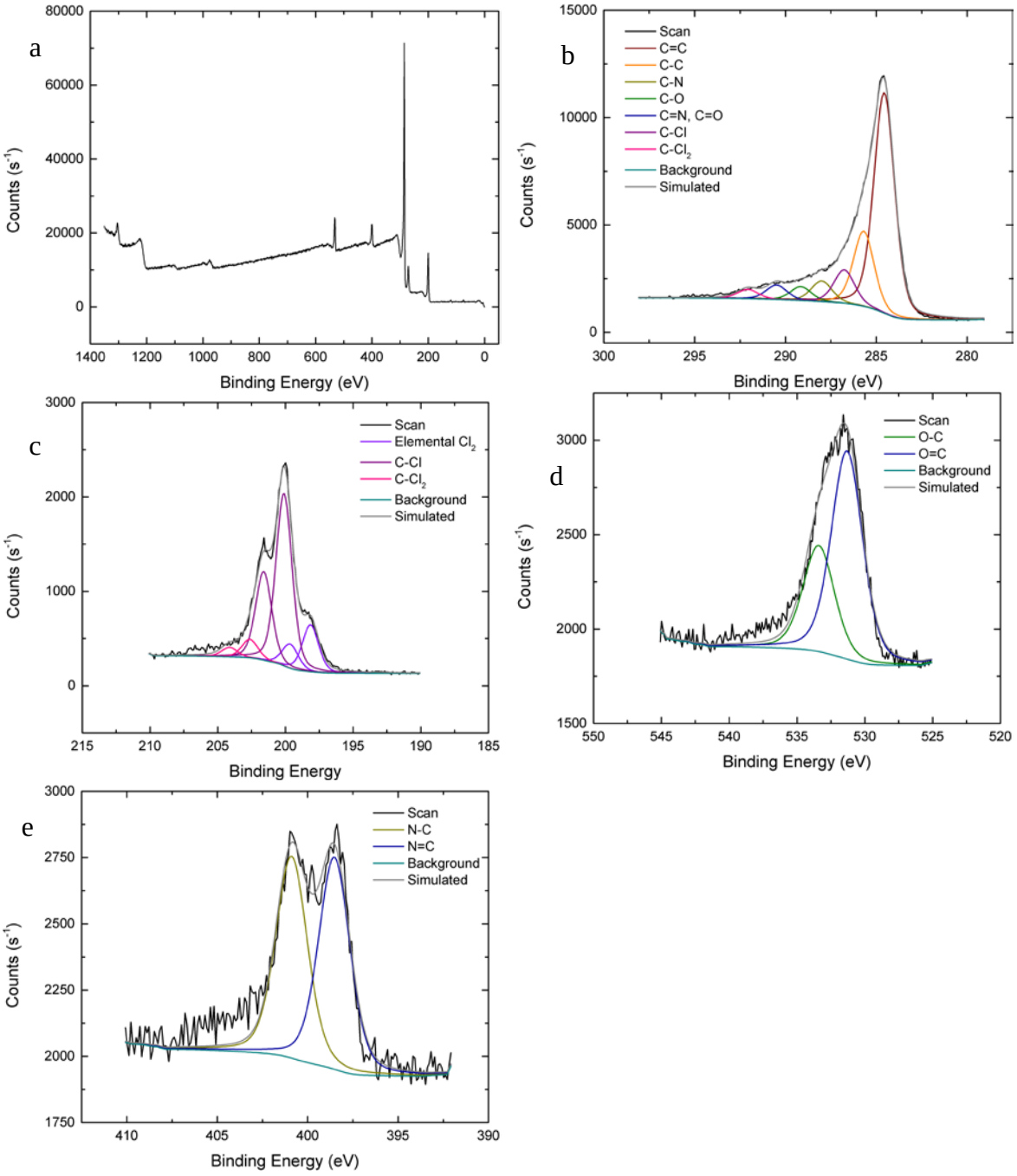

Figure A.19 – XPS scans for a sample etched for 1.50 h in a fluidized-bed reactor for (a) overall, (b) carbon, (c) chlorine, (d) oxygen, and (e) nitrogen.

a

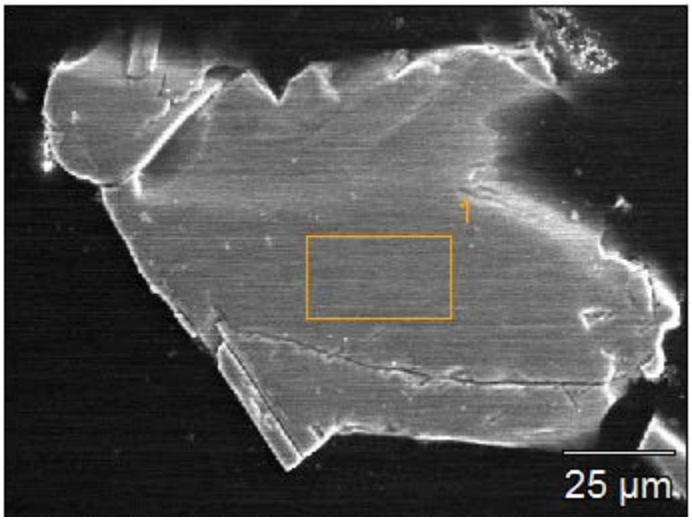

b

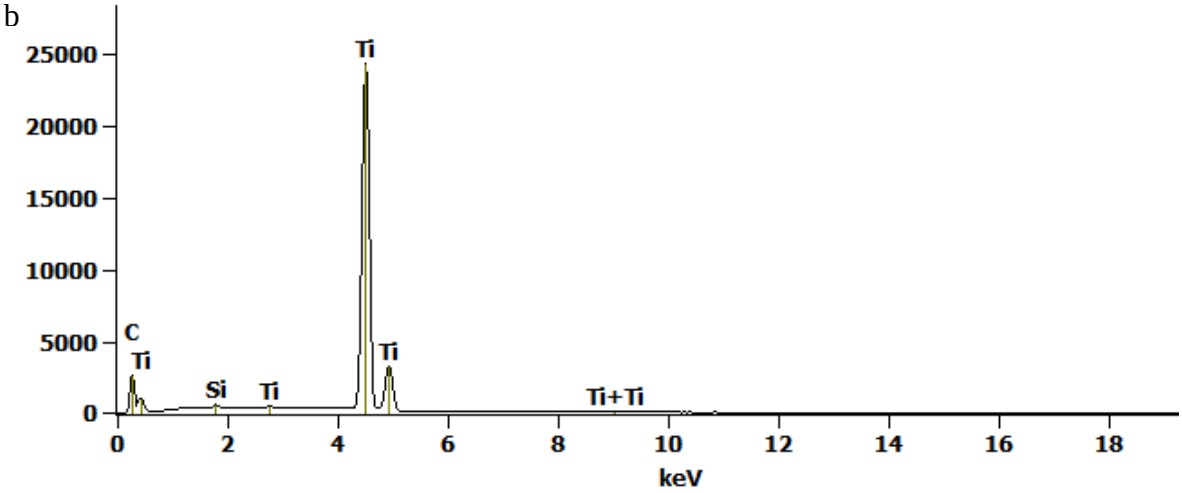

Figure A.20 – SEM image (a) and EDX data (b) for TiC.

a

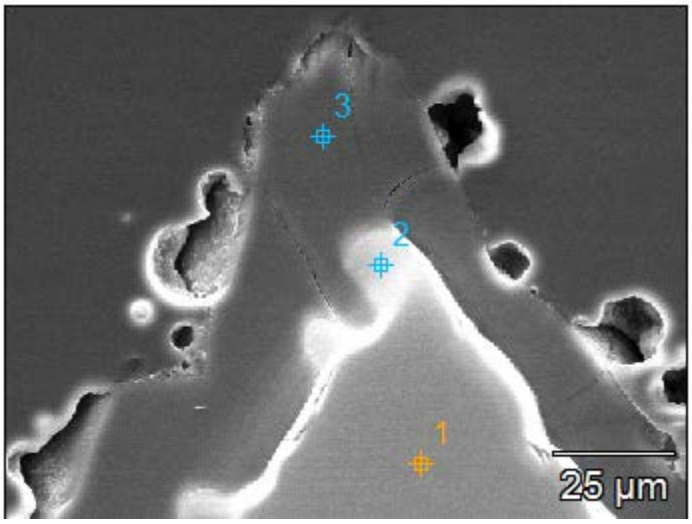
3
2
1
25 µm

b

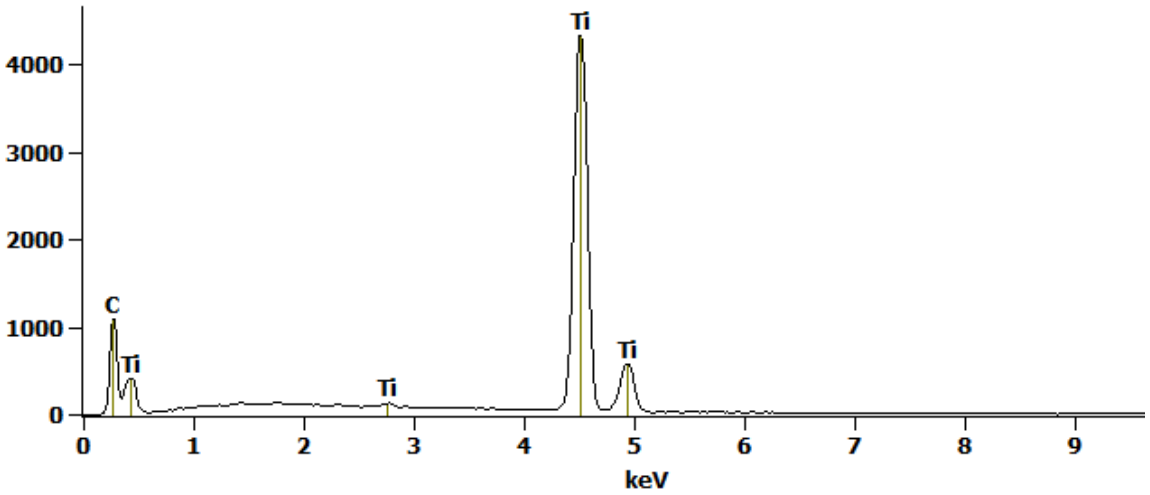
Ti
C
Ti
Ti
Ti
4000
3000
2000
1000
0
0 1 2 3 4 5 6 7 8 9
keV

c

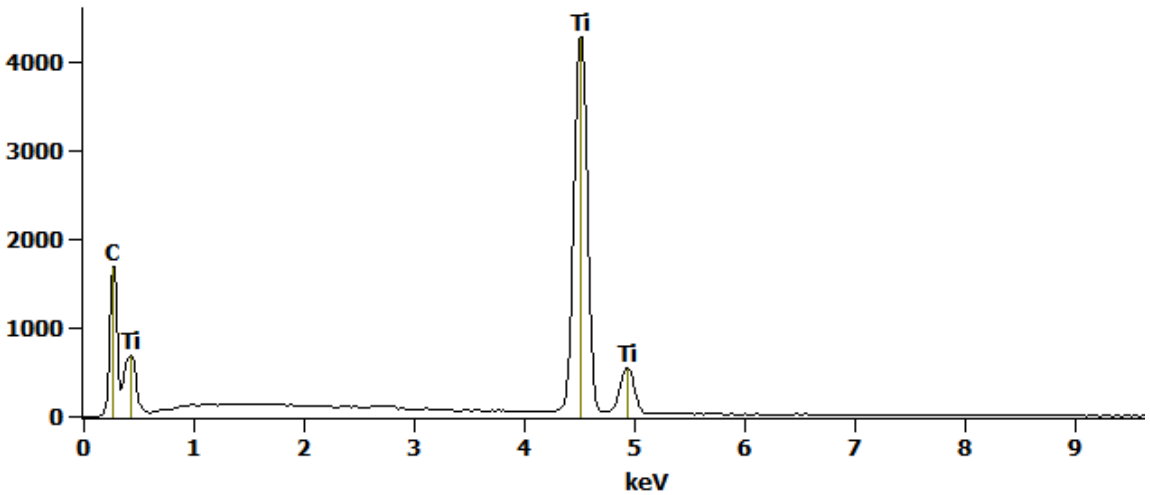
Ti
C
Ti
Ti
4000
3000
2000
1000
0
0 1 2 3 4 5 6 7 8 9
keV

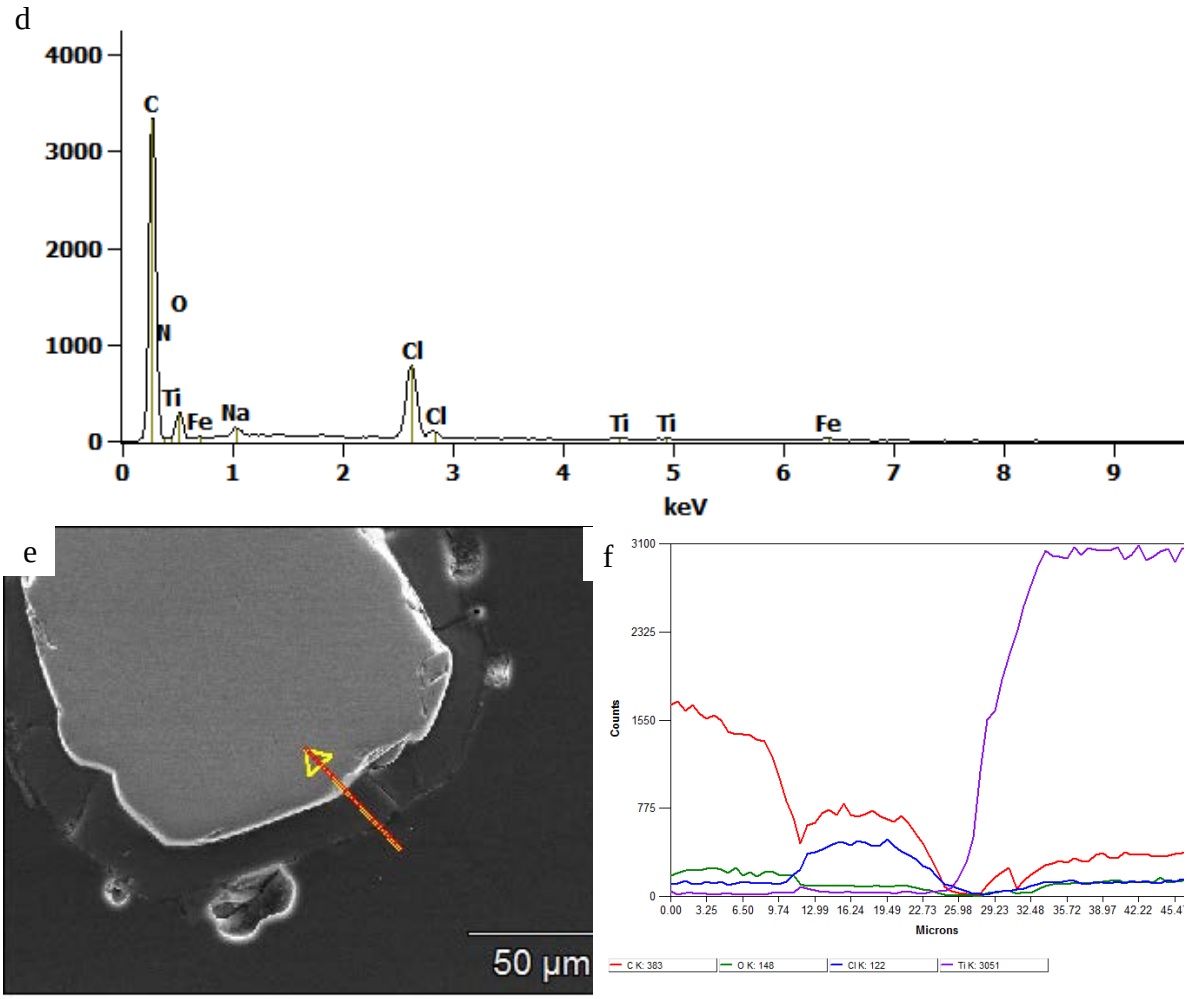

Figure A.21 – SEM images (a, e) and EDX (b, c, d) for a particle etched for 0.25 h in the fluidized-bed reactor, where (b, c, d) refer to points 1, 2, and 3, respectively. EDX line scan is shown in (f) for the particle in (e).

a

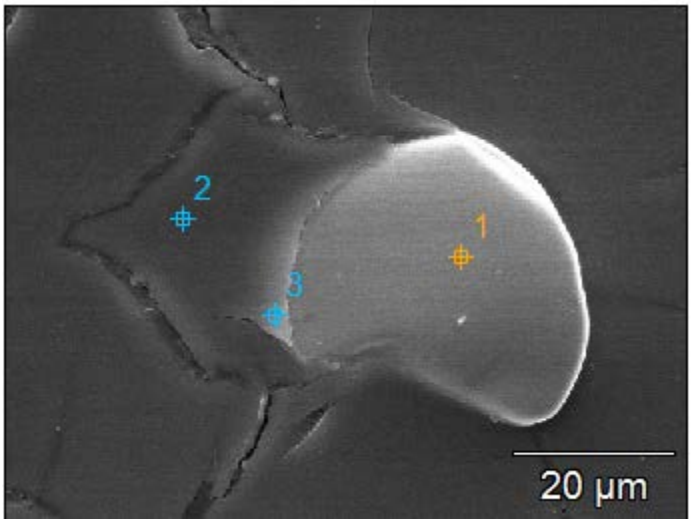
2
1
3
20 µm

b

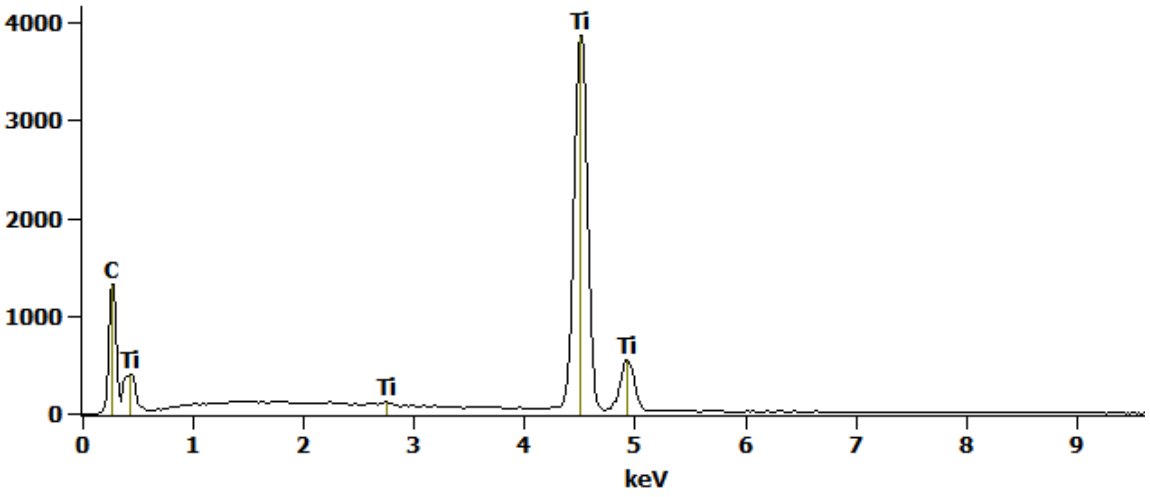
4000
3000
2000
1000
0
C
Ti
Ti
Ti
Ti
0 1 2 3 4 5 6 7 8 9
keV

c

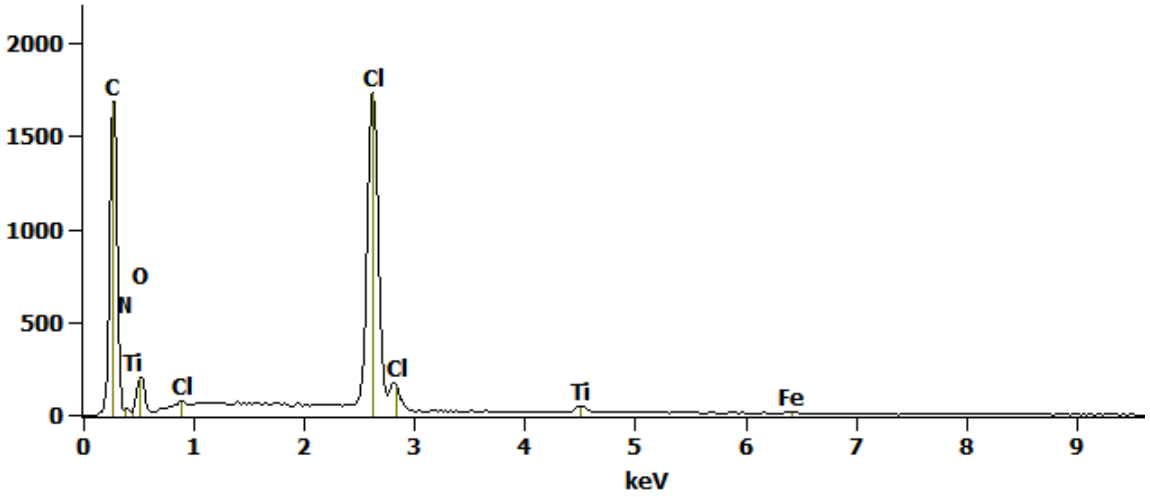
2000
1500
1000
500
0
C
O
N
Ti
Cl
Cl
Cl
Ti
Fe
0 1 2 3 4 5 6 7 8 9
keV

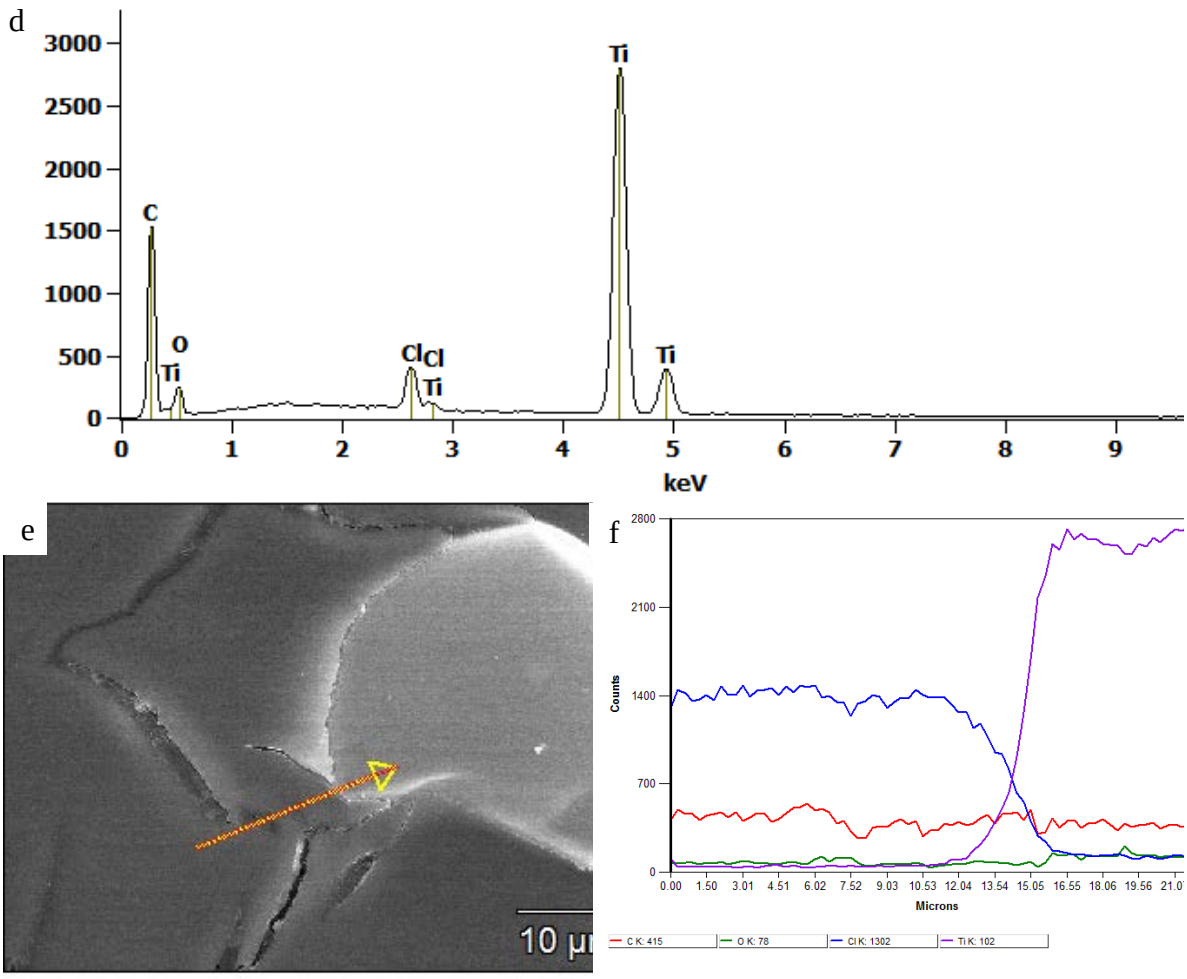

Figure A.22 – SEM images (a, e) and EDX (b, c, d) for a particle etched for 0.75 h in the fluidized-bed reactor, where (b, c, d) refer to points 1, 2, and 3, respectively. EDX line scan is shown in (f) for the particle in (e).

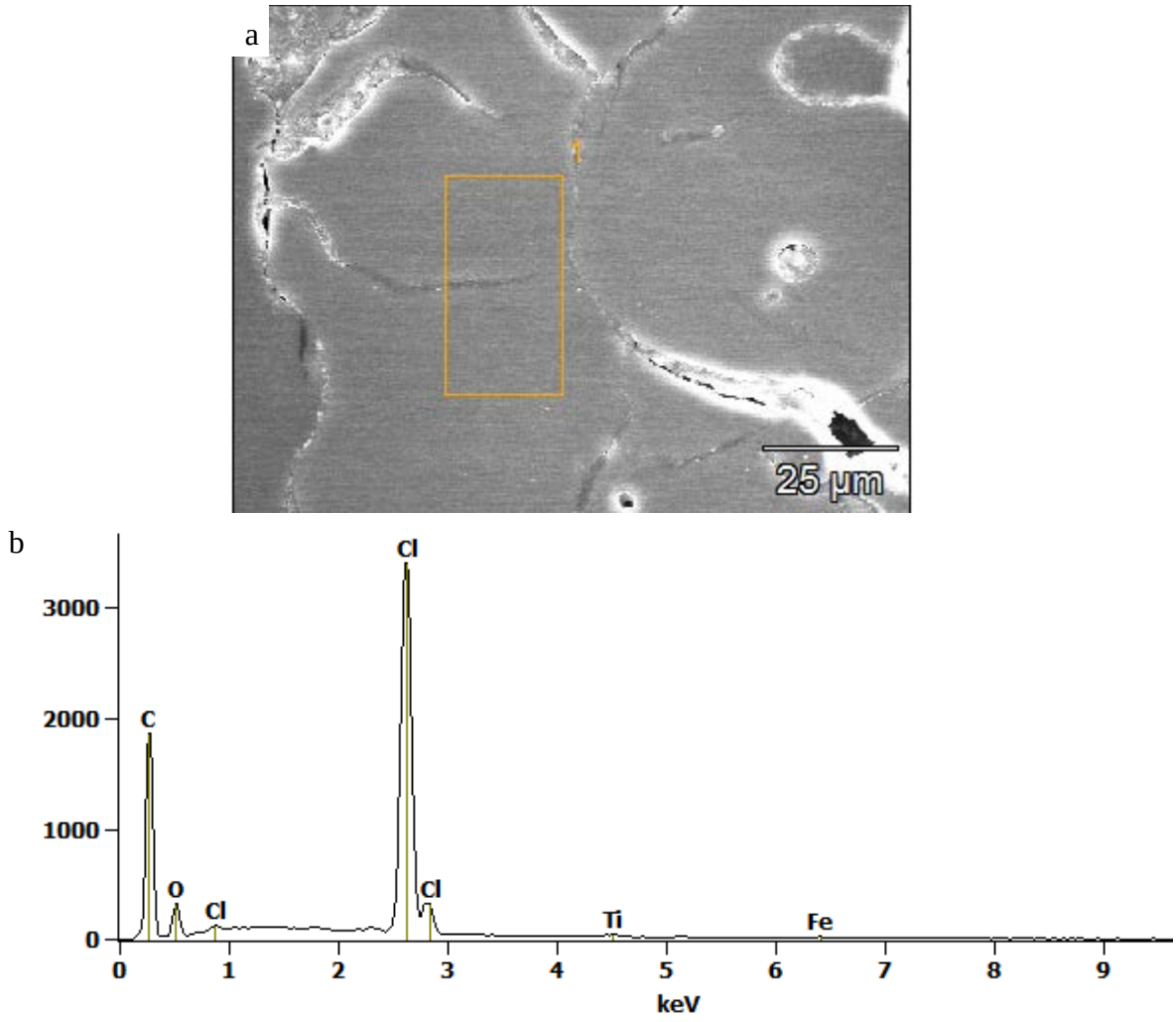

Figure A.23 – SEM image (a) and EDX (b) data for a particle etched 1.50 h in the fluidized-bed reactor.

A.2 Chapter 4: The Effects of Various SO_2 Environments on Titanium Carbide-Derived Carbon with Various Residual Metal Loadings

A.2.1 Supplemental and Raw Data for Chapter 4

Table A.1 – Reaction conditions for creating TiC-CDC for acid exposure in the fluidized-bed reactor.

Reaction Temperature (°C)	Reaction Time (h)	Additional Time (h) at Reaction Temperature
500	0.25	0
500	0.25	1.25
500	1.50	0

Table A.2 – Argon flow rates during the temperature cycle for the fluidized-bed reactor.

Temperature (°C)	Sequence	Ar Flow Rate (mL min^{-1})
25-500	Heating	400
500	Holding	320
500-25	Cooling	320

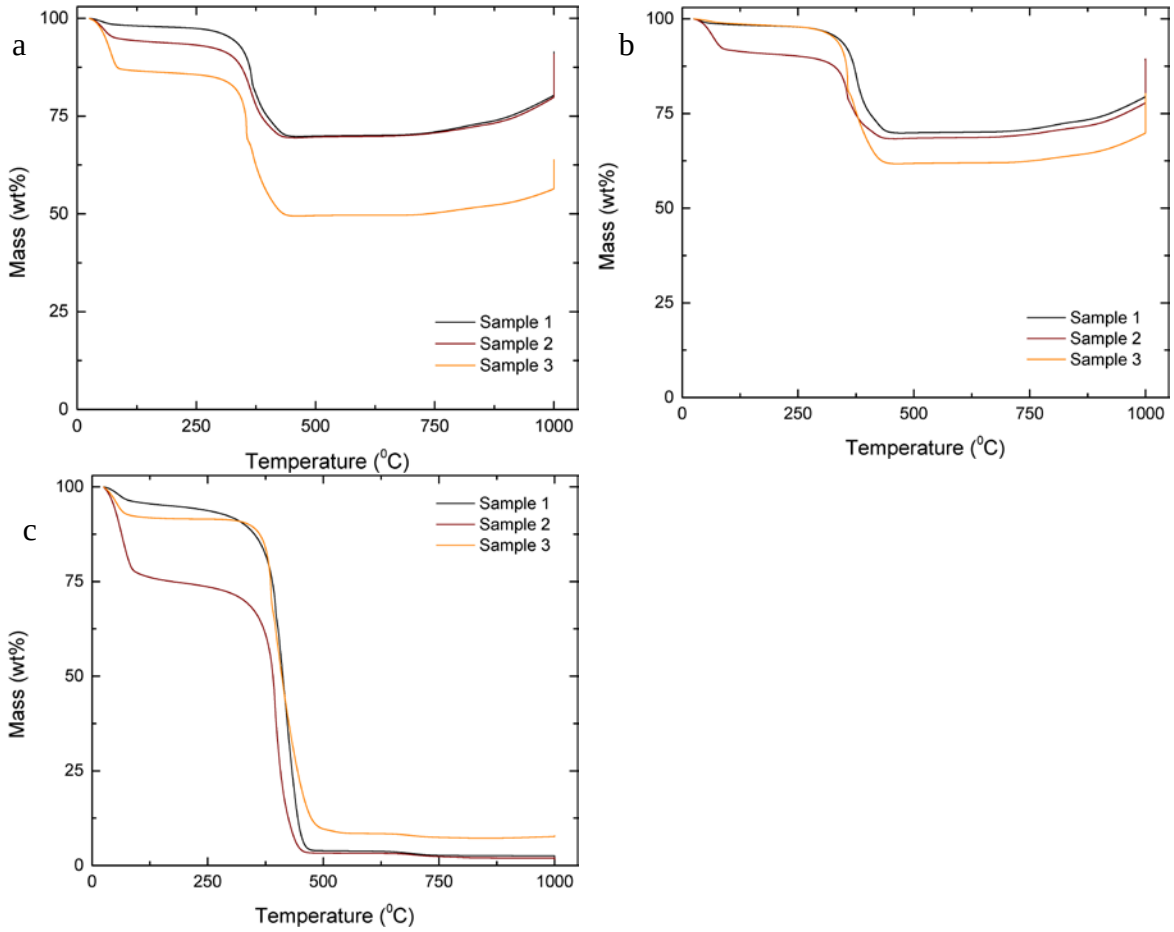

Figure A.24 – Thermogravimetric analysis curves for TiC-CDC etched for a) 0.25 h, b) etched for 0.25 h and held at temperature for an additional 1.25 h, and c) etched for 1.50 h.

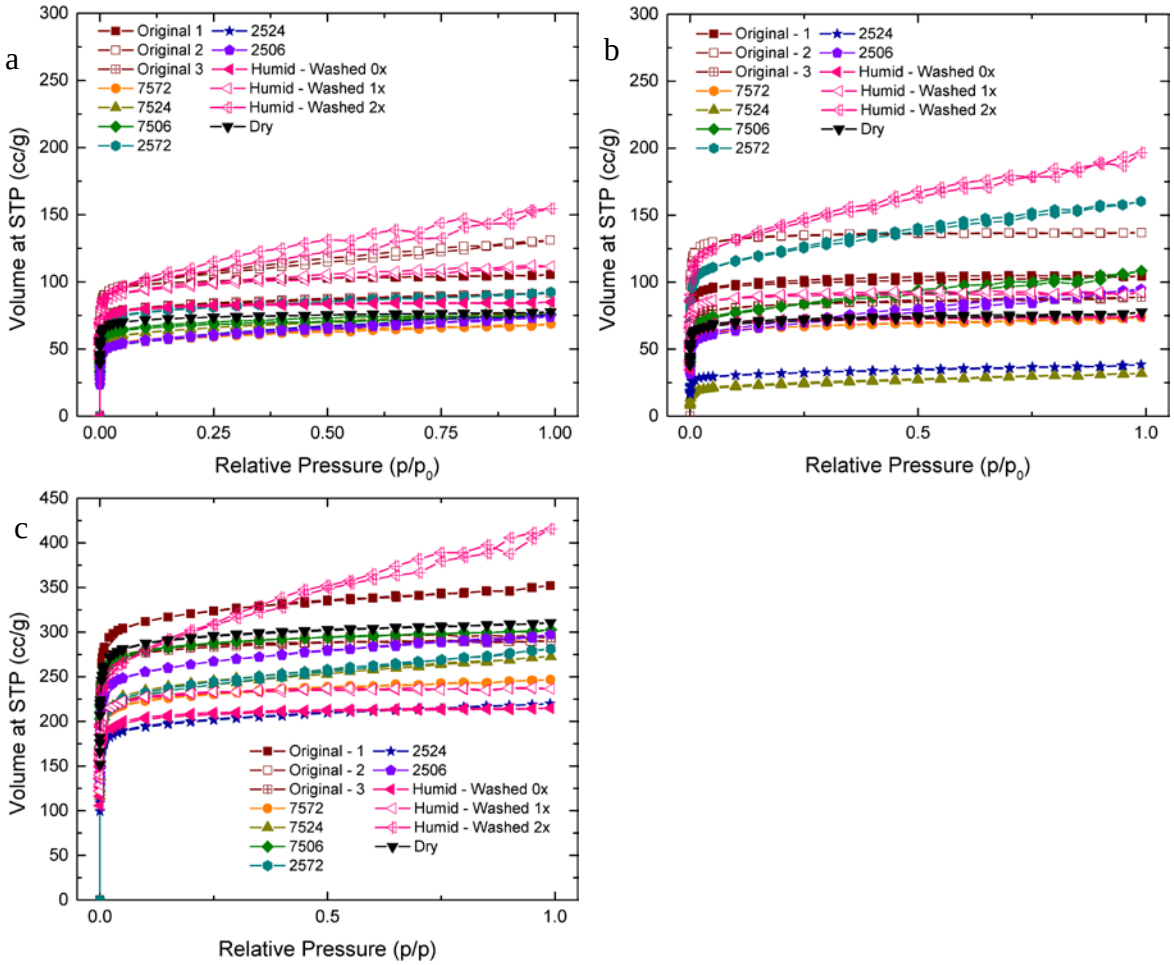

Figure A.25 – Nitrogen sorption curves for TiC-CDC etched for a) 0.25 h, b) etched for 0.25 h and held at temperature for an additional 1.25 h, and c) etched for 1.50 h. The lines are not data and are meant to guide the eye.

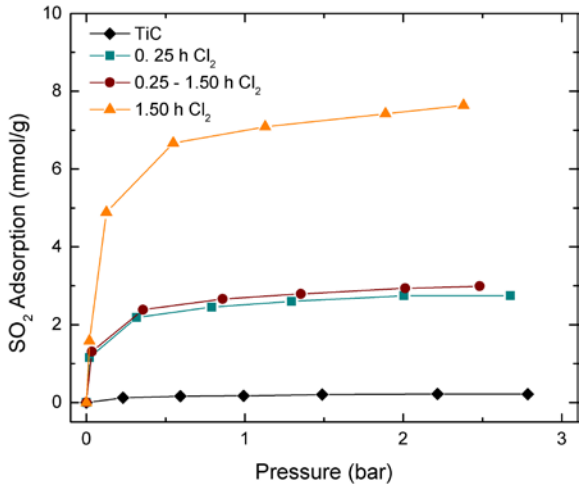

Figure A.26 – SO_2 isotherms collected at 25°C. The lines are not data and meant to guide the eye.

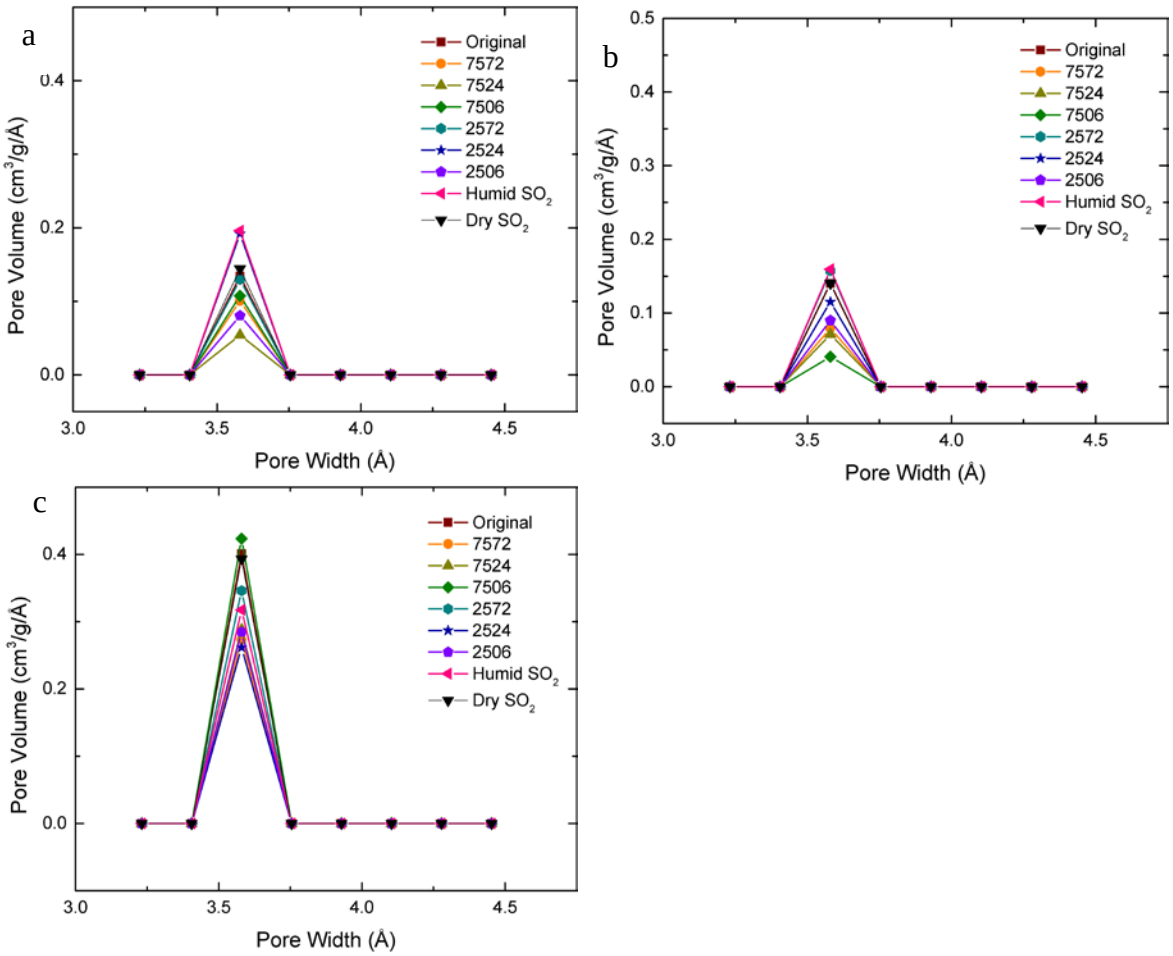

Figure A.27 – Pore size distributions from CO_2 sorption at 273 K for TiC-CDC etched for a) 0.25 h, b) etched for 0.25 h and held at temperature for an additional 1.25 h, and c) etched for 1.50 h. The lines are not data and meant to guide the eye.

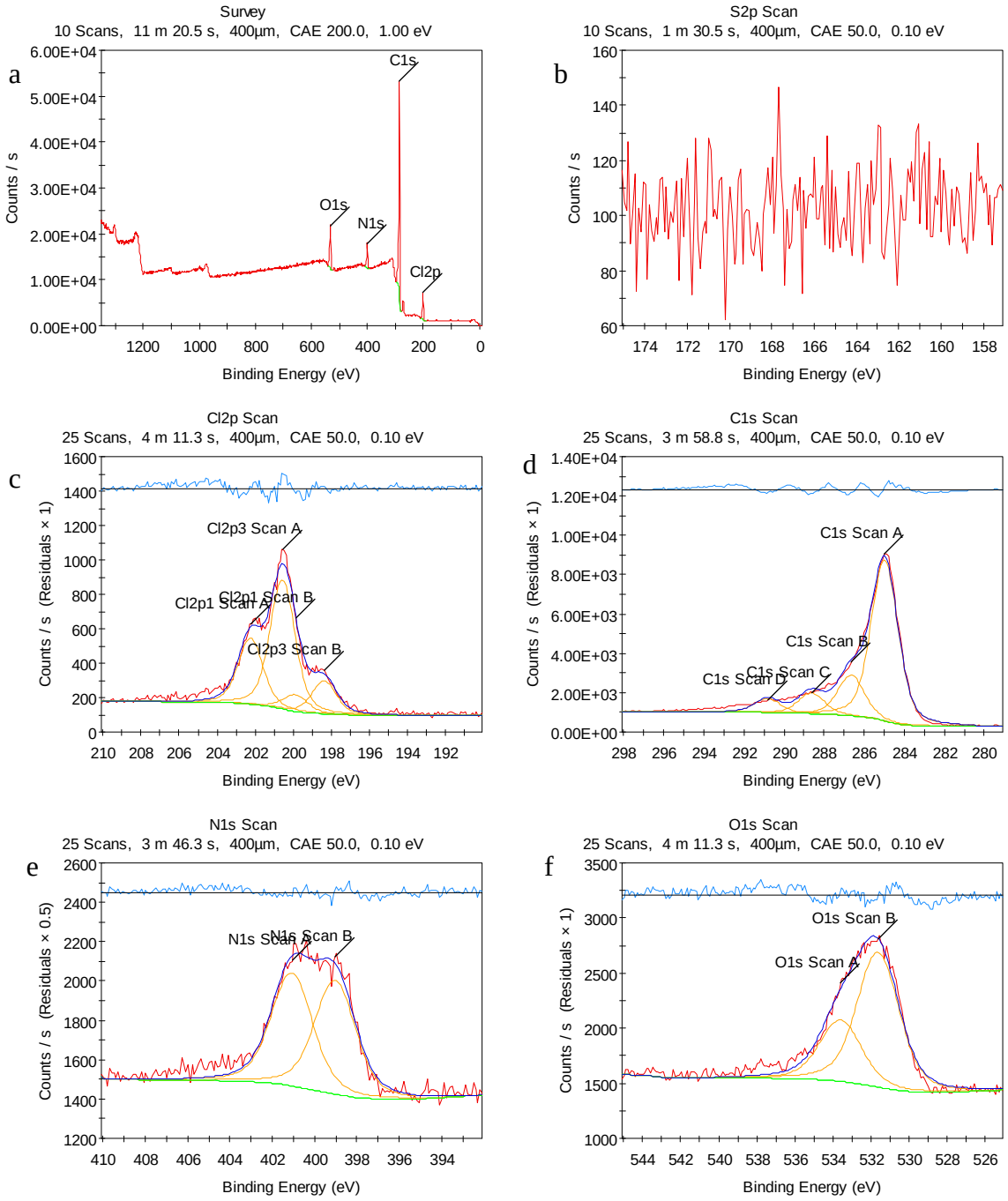

Figure A.28 – X-ray photoelectron spectra for a TiC-CDC sample etched for 0.25 h. Included spectra are for the a) survey scan, b) S2p scan showing no sulfur species, c) Cl2p scan showing elemental Cl_2 and C-Cl bonds, d) C1s scan showing C-C, C-N/C-O, C=N, C=O, and C-Cl bonds, e) N1s scan showing N-C and N=C bonds, and f) O1s scan showing O-C and O=C bonds.

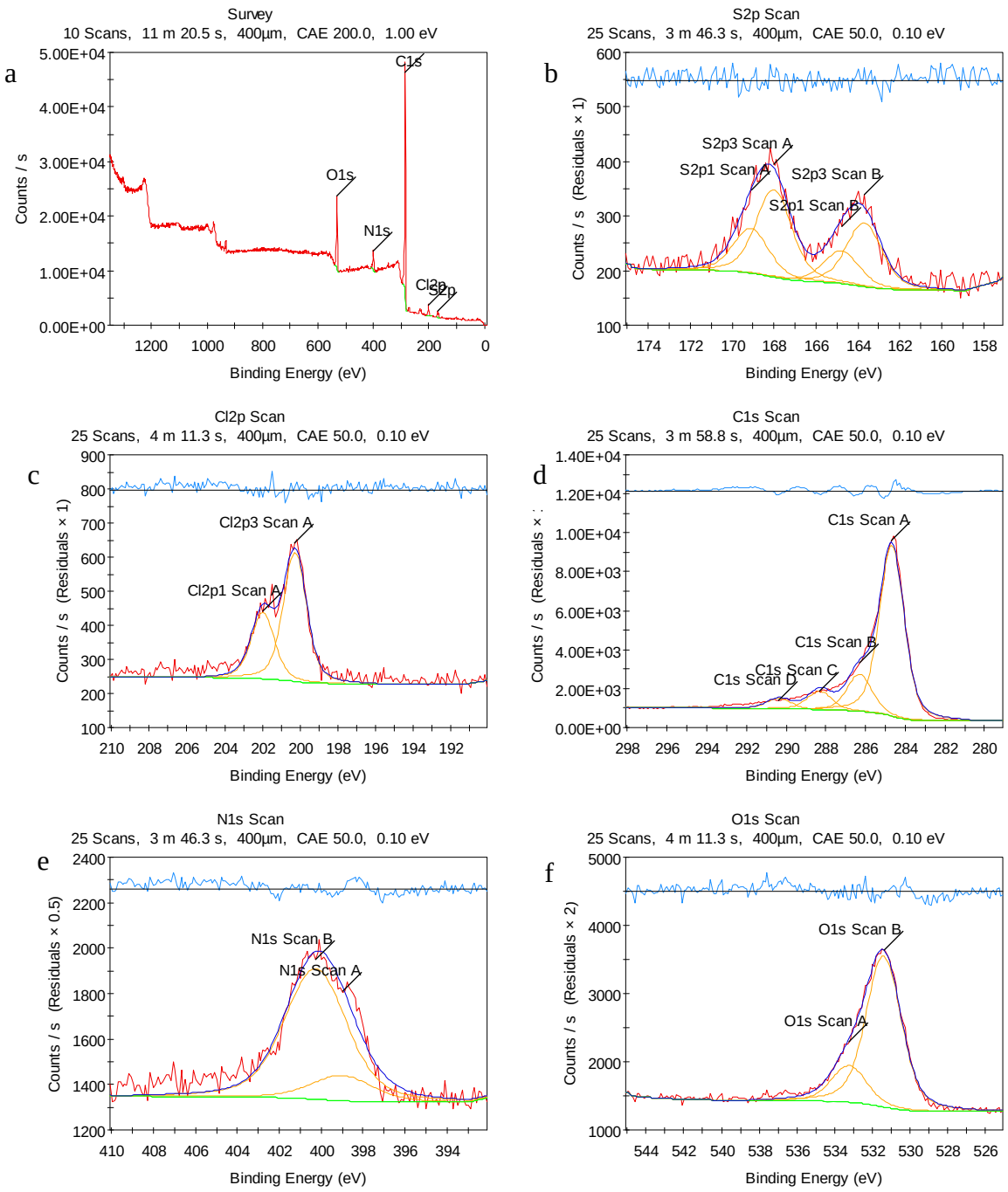

Figure A.29 – X-ray photoelectron spectra for a TiC-CDC sample etched for 0.25 h and exposed to aqueous SO_2 at 75°C for 72 h. Included spectra are for the a) survey scan, b) S2p scan showing sulfate and a possible sulfonyl groups, c) Cl2p scan showing C-Cl bonds, d) C1s scan showing C-C, C-N/C-O, C=N, C=O, and C-Cl bonds, e) N1s scan showing N-C and N=C bonds, and f) O1s scan showing O-C and O=C bonds.

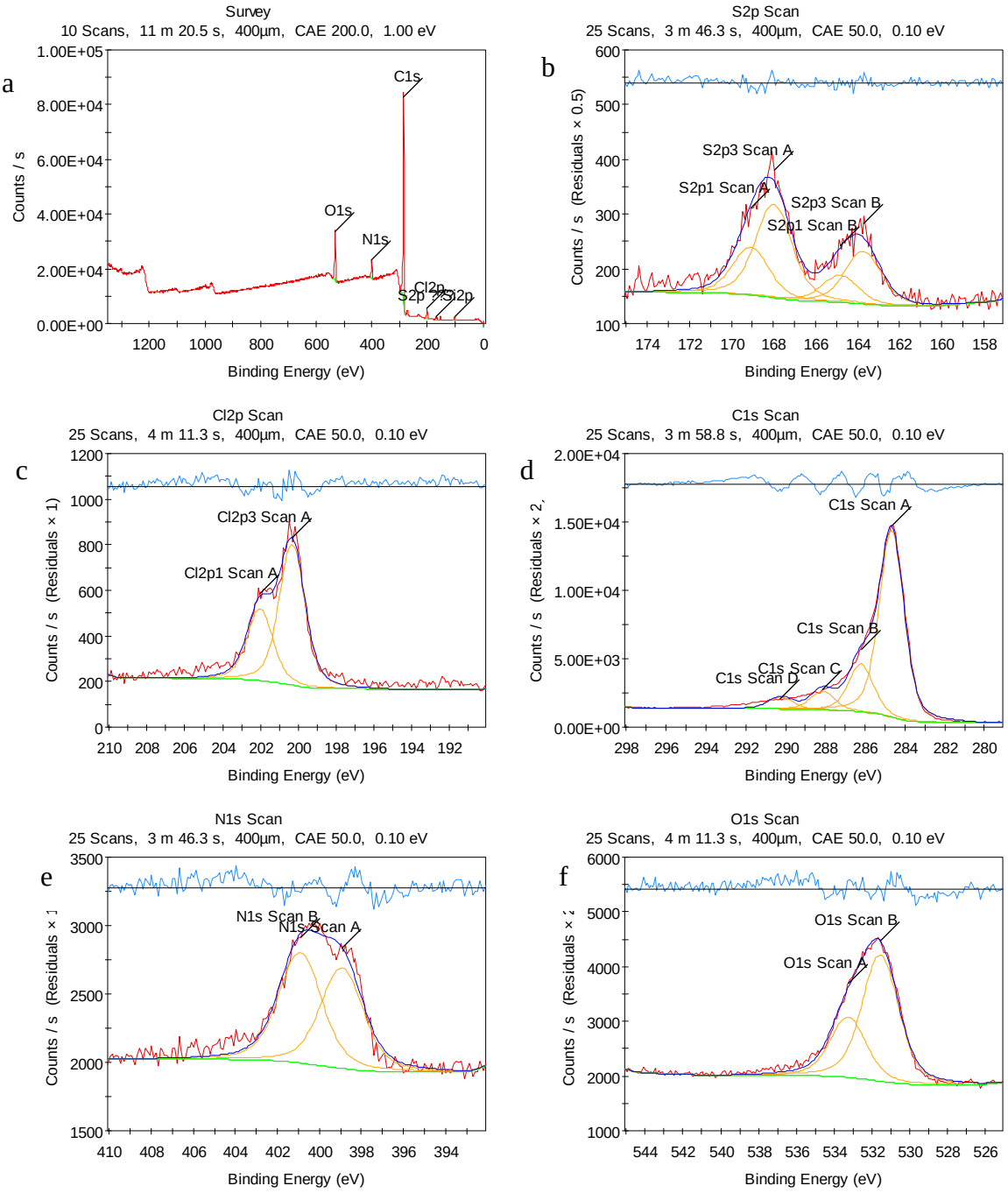

Figure A.30 – X-ray photoelectron spectra for a TiC-CDC sample etched for 0.25 h and exposed to aqueous SO_2 at 75°C for 24 h. Included spectra are for the a) survey scan, b) S2p scan showing sulfate and a possible sulfonyl groups, c) Cl2p scan showing C-Cl bonds, d) C1s scan showing C-C, C-N/C-O, C=N, C=O, and C-Cl bonds, e) N1s scan showing N-C and N=C bonds, and f) O1s scan showing O-C and O=C bonds.

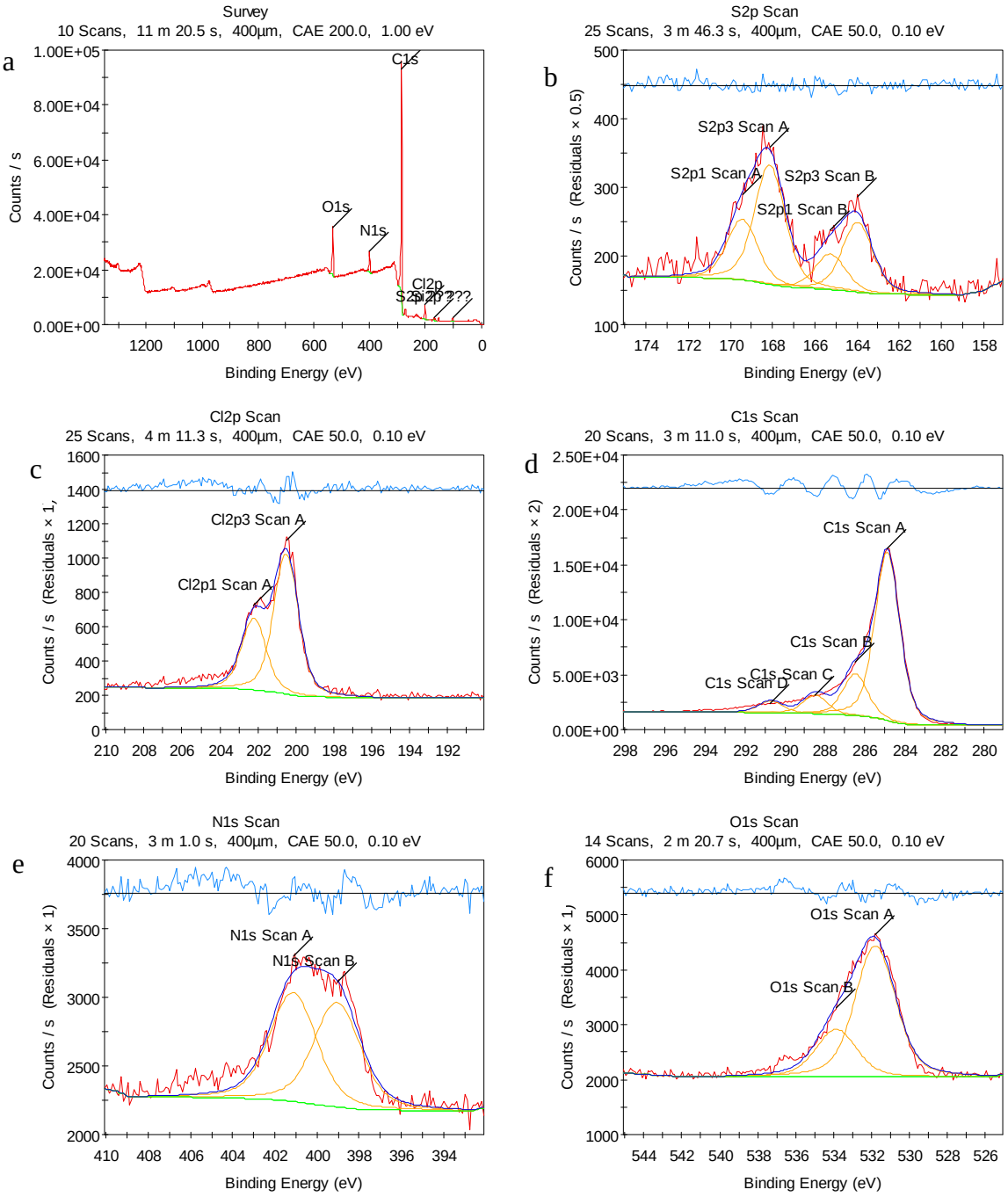

Figure A.31 – X-ray photoelectron spectra for a TiC-CDC sample etched for 0.25 h and exposed to aqueous SO_2 at 75°C for 6 h. Included spectra are for the a) survey scan, b) S2p scan showing sulfate and a possible sulfonyl groups, c) Cl2p scan showing C-Cl bonds, d) C1s scan showing C-C, C-N/C-O, C=N, C=O, and C-Cl bonds, e) N1s scan showing N-C and N=C bonds, and f) O1s scan showing O-C and O=C bonds.

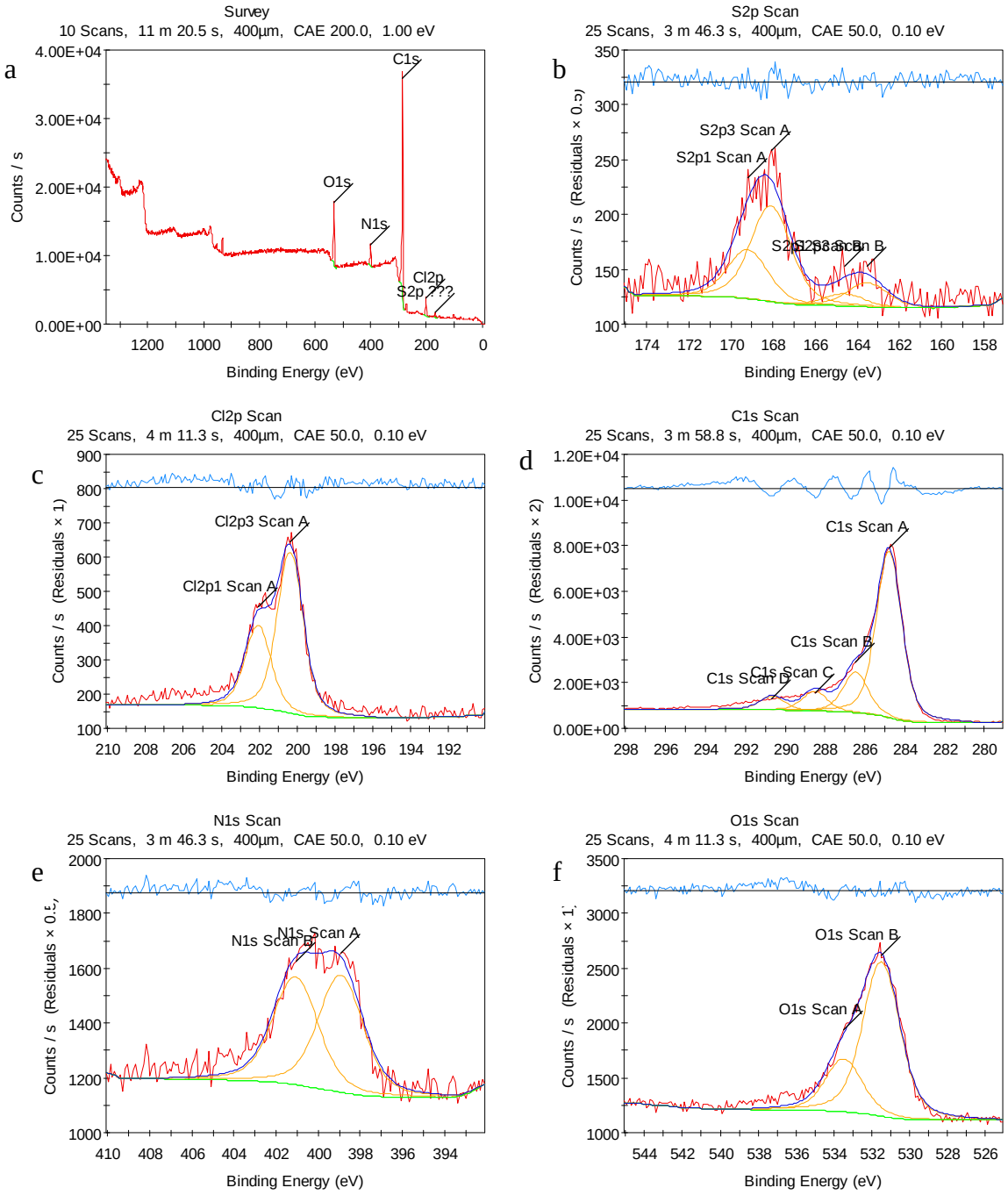

Figure A.32 – X-ray photoelectron spectra for a TiC-CDC sample etched for 0.25 h and exposed to aqueous SO_2 at 25°C for 72 h. Included spectra are for the a) survey scan, b) S2p scan showing sulfate and a possible sulfonyl groups, c) Cl2p scan showing C-Cl bonds, d) C1s scan showing C-C, C-N/C-O, C=N, C=O, and C-Cl bonds, e) N1s scan showing N-C and N=C bonds, and f) O1s scan showing O-C and O=C bonds.

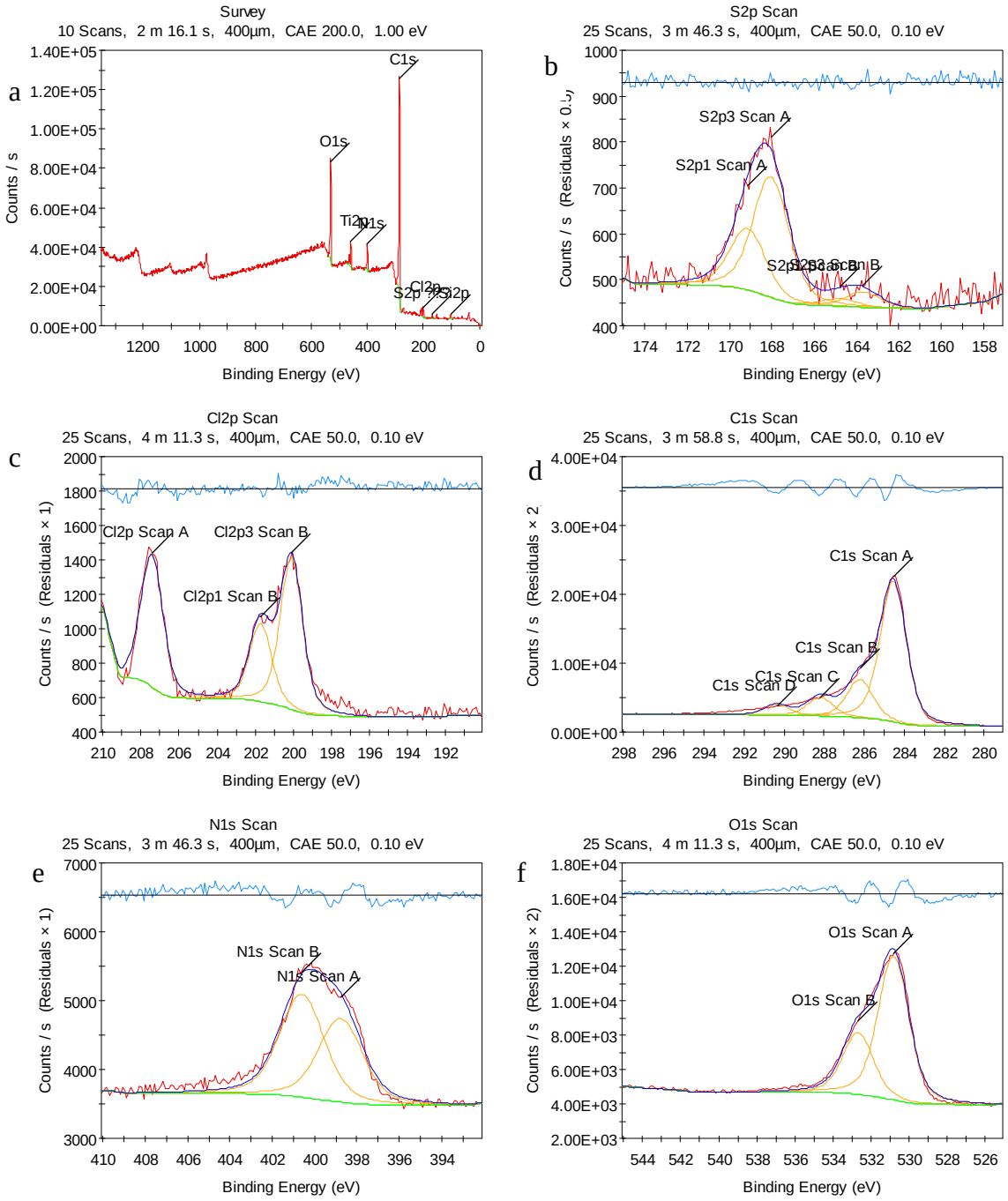

Figure A.33 – X-ray photoelectron spectra for a TiC-CDC sample etched for 0.25 h and exposed to aqueous SO_2 at 25°C for 24 h. Included spectra are for the a) survey scan, b) S2p scan showing sulfate and a possible sulfonyl groups, c) Cl2p scan showing C-Cl and Cl-O bonds, d) C1s scan showing C-C, C-N/C-O, C=N, C=O, and C-Cl bonds, e) N1s scan showing N-C and N=C bonds, and f) O1s scan showing O-C and O=C bonds.

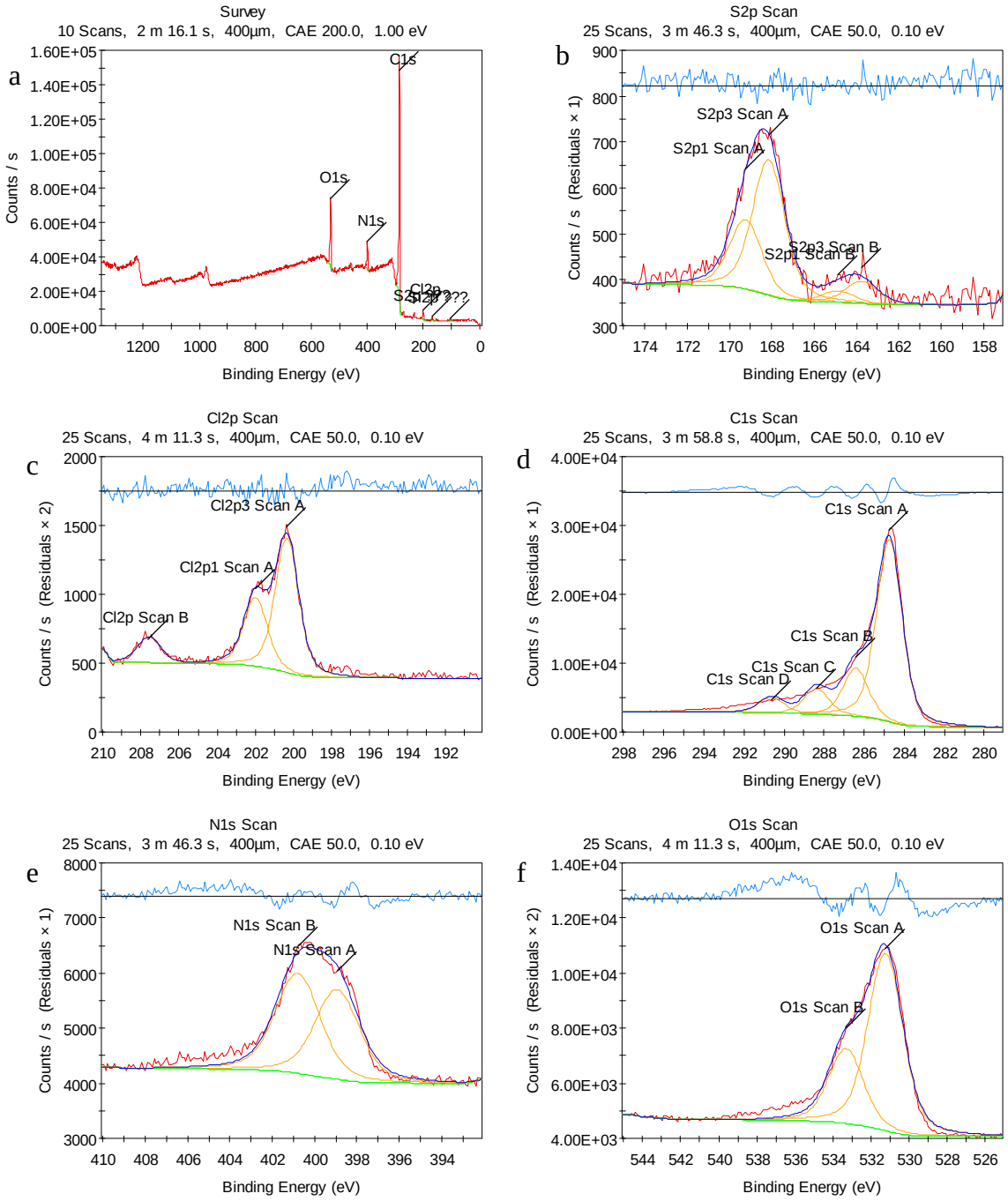

Figure A.34 – X-ray photoelectron spectra for a TiC-CDC sample etched for 0.25 h and exposed to aqueous SO_2 at 25°C for 6 h. Included spectra are for the a) survey scan, b) S2p scan showing sulfate and a possible sulfonyl groups, c) Cl2p scan showing C-Cl and Cl-O bonds, d) C1s scan showing C-C, C-N/C-O, C=N, C=O, and C-Cl bonds, e) N1s scan showing N-C and N=C bonds, and f) O1s scan showing O-C and O=C bonds.

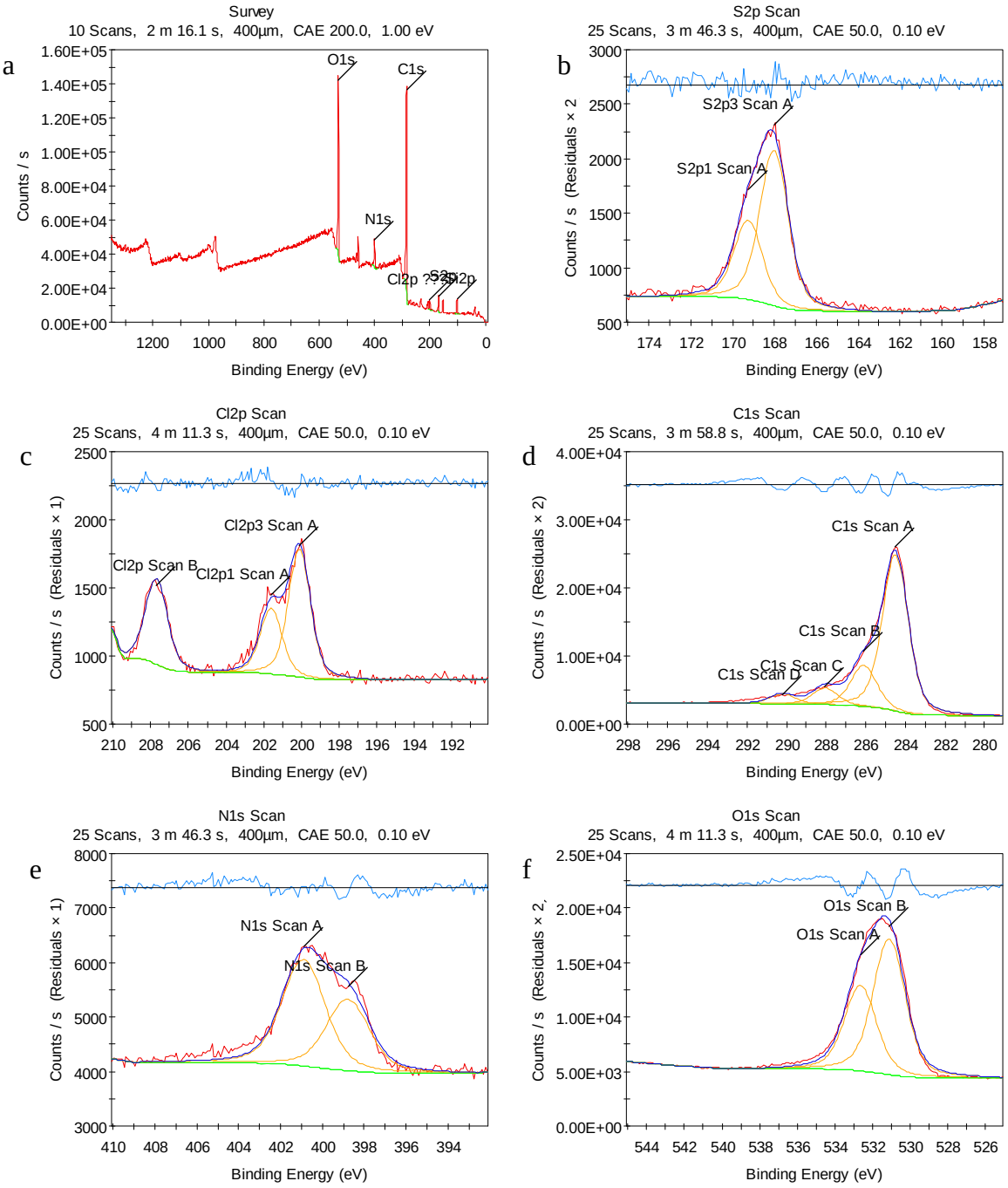

Figure A.35 – X-ray photoelectron spectra for a TiC-CDC sample etched for 0.25 h and exposed to humid SO_2 at 25°C for 72 h. Included spectra are for the a) survey scan, b) S2p scan showing sulfate groups, c) Cl2p scan showing C-Cl and Cl-O bonds, d) C1s scan showing C-C, C-N/C-O, C=N, C=O, and C-Cl bonds, e) N1s scan showing N-C and N=C bonds, and f) O1s scan showing O-C and O=C bonds.

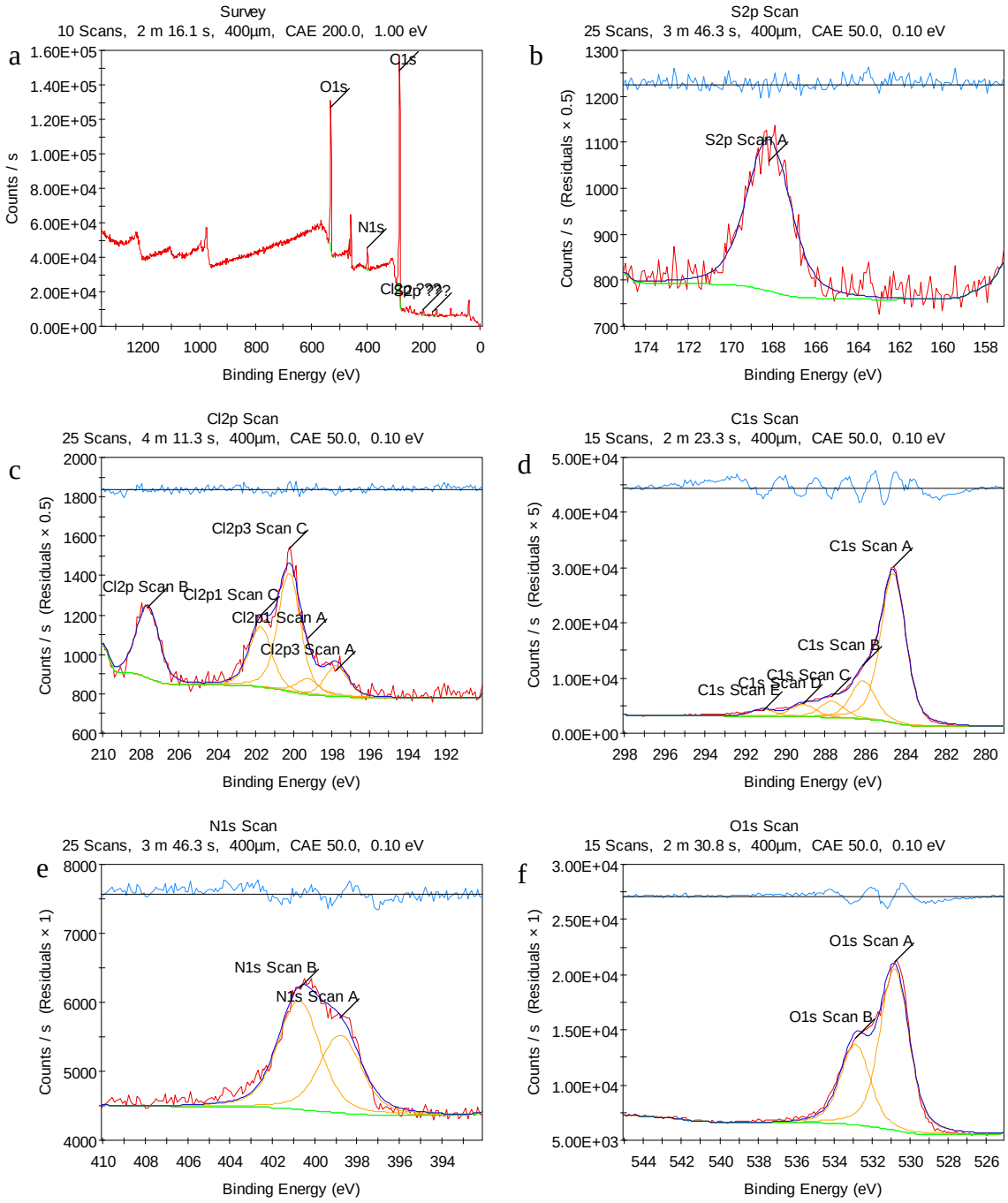

Figure A.36 – X-ray photoelectron spectra for a TiC-CDC sample etched for 0.25 h and exposed to humid SO_2 at 25°C for 72 h and decanted with water. Included spectra are for the a) survey scan, b) S2p scan showing sulfate groups, c) Cl2p scan showing elemental Cl_2, C-Cl, and Cl-O bonds, d) C1s scan showing C-C, C-N/C-O, C=N, C=O, C-Cl/Cl_2 bonds, e) N1s scan showing N-C and N=C bonds, and f) O1s scan showing O-C and O=C bonds.

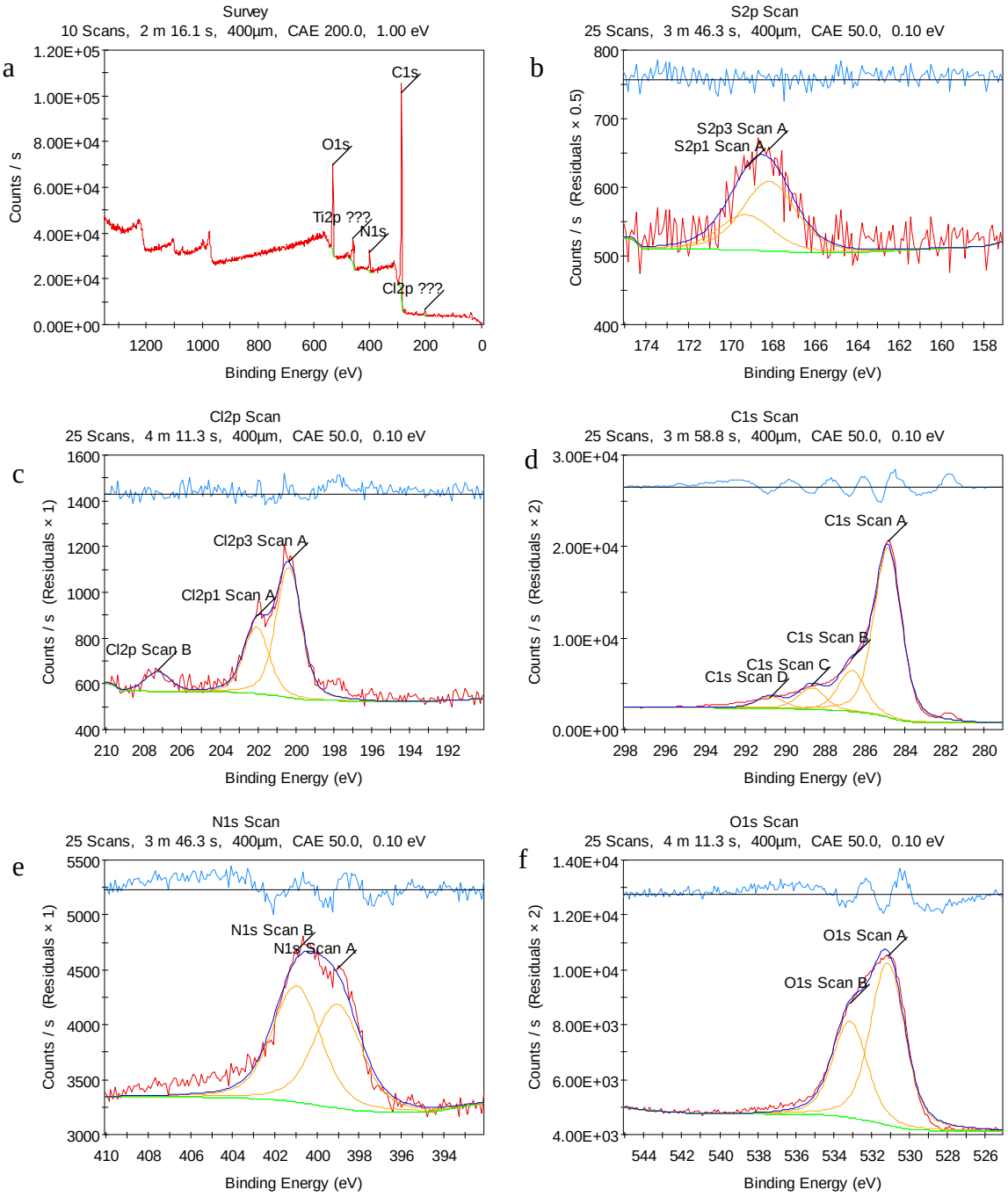

Figure A.37 – X-ray photoelectron spectra for a TiC-CDC sample etched for 0.25 h and exposed to humid SO_2 at 25°C for 72 h and sonicated with water. Included spectra are for the a) survey scan, b) S2p scan showing sulfate groups, c) Cl2p scan showing elemental Cl_2, C-Cl, and Cl-O bonds, d) C1s scan showing C-C, C-N/C-O, C=N, C=O, C-Cl bonds, e) N1s scan showing N-C and N=C bonds, and f) O1s scan showing O-C and O=C bonds.

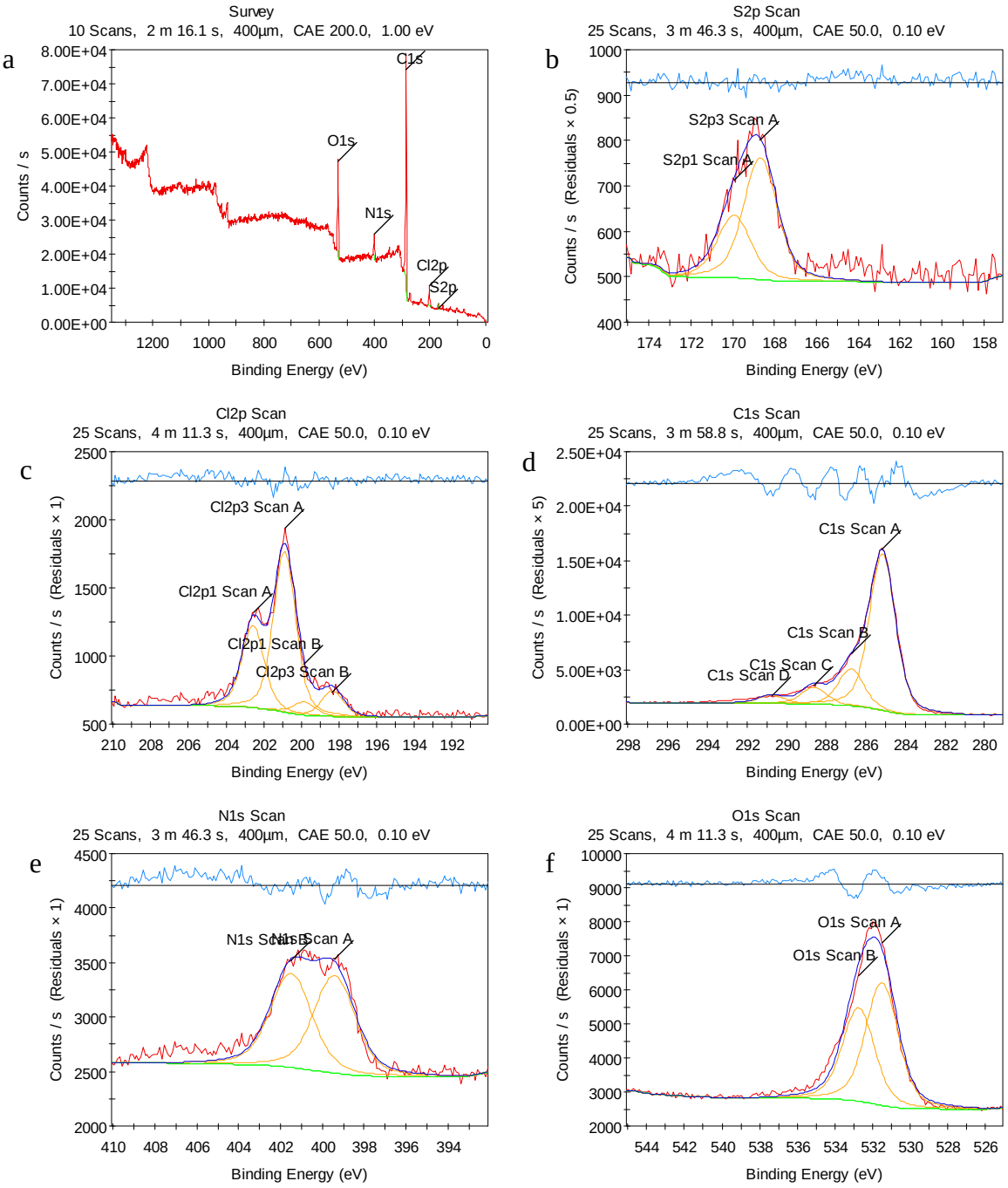

Figure A.38 – X-ray photoelectron spectra for a TiC-CDC sample etched for 0.25 h and exposed dry SO_2 at 25°C for approximately 3 h. Included spectra are for the a) survey scan, b) S2p scan showing sulfate groups, c) Cl2p scan showing elemental Cl_2 and C-Cl bonds, d) C1s scan showing C-C, C-N/C-O, C=N, C=O, C-Cl bonds, e) N1s scan showing N-C and N=C bonds, and f) O1s scan showing O-C and O=C bonds.

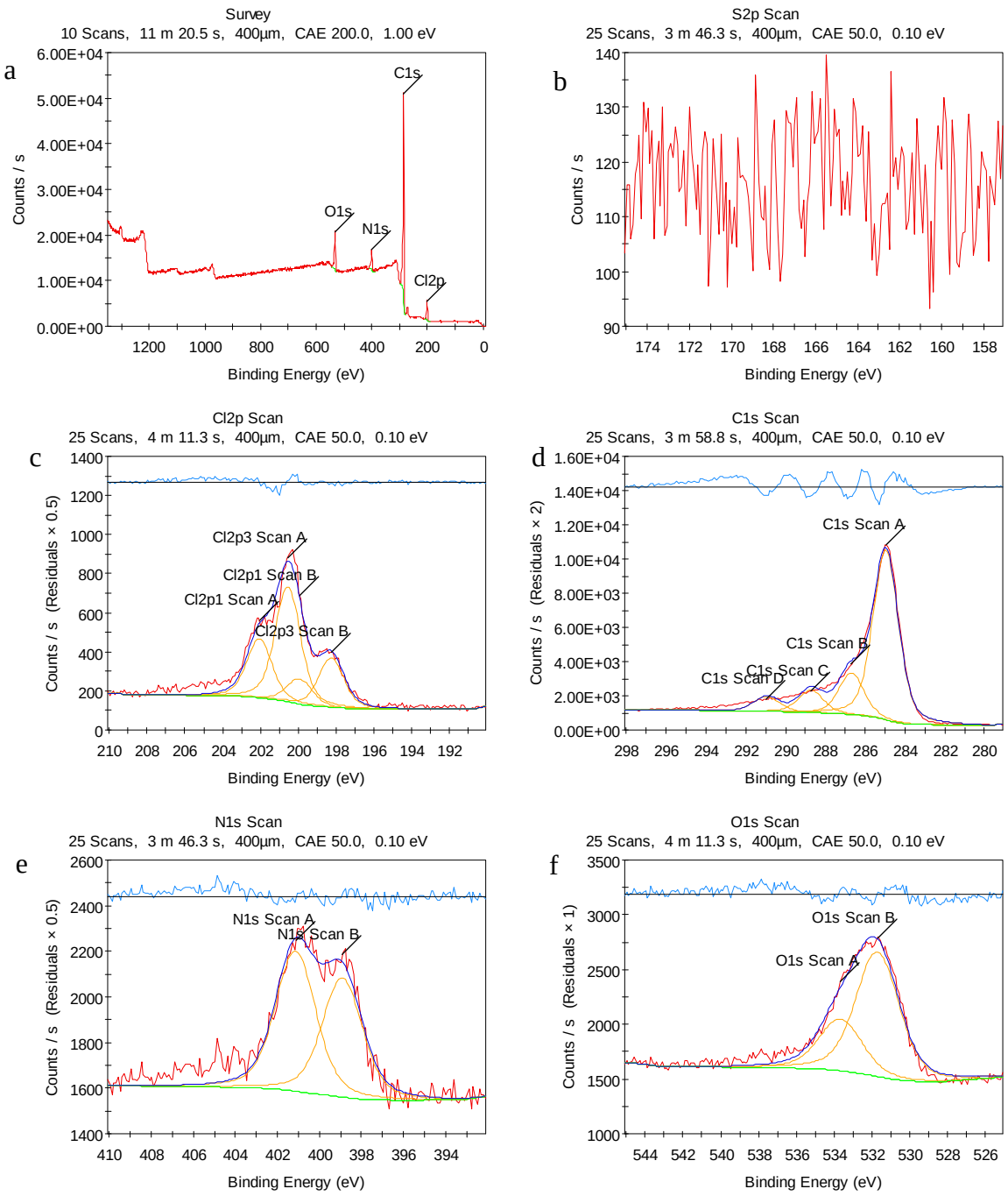

Figure A.39 – X-ray photoelectron spectra for a TiC-CDC sample etched for 0.25 h and held at temperature for an additional 1.25 h. Included spectra are for the a) survey scan, b) S2p scan showing no sulfur species, c) Cl2p scan showing elemental Cl_2 and C-Cl bonds, d) C1s scan showing C-C, C-N/C-O, C=N, C=O, C-Cl bonds, e) N1s scan showing N-C and N=C bonds, and f) O1s scan showing O-C and O=C bonds.

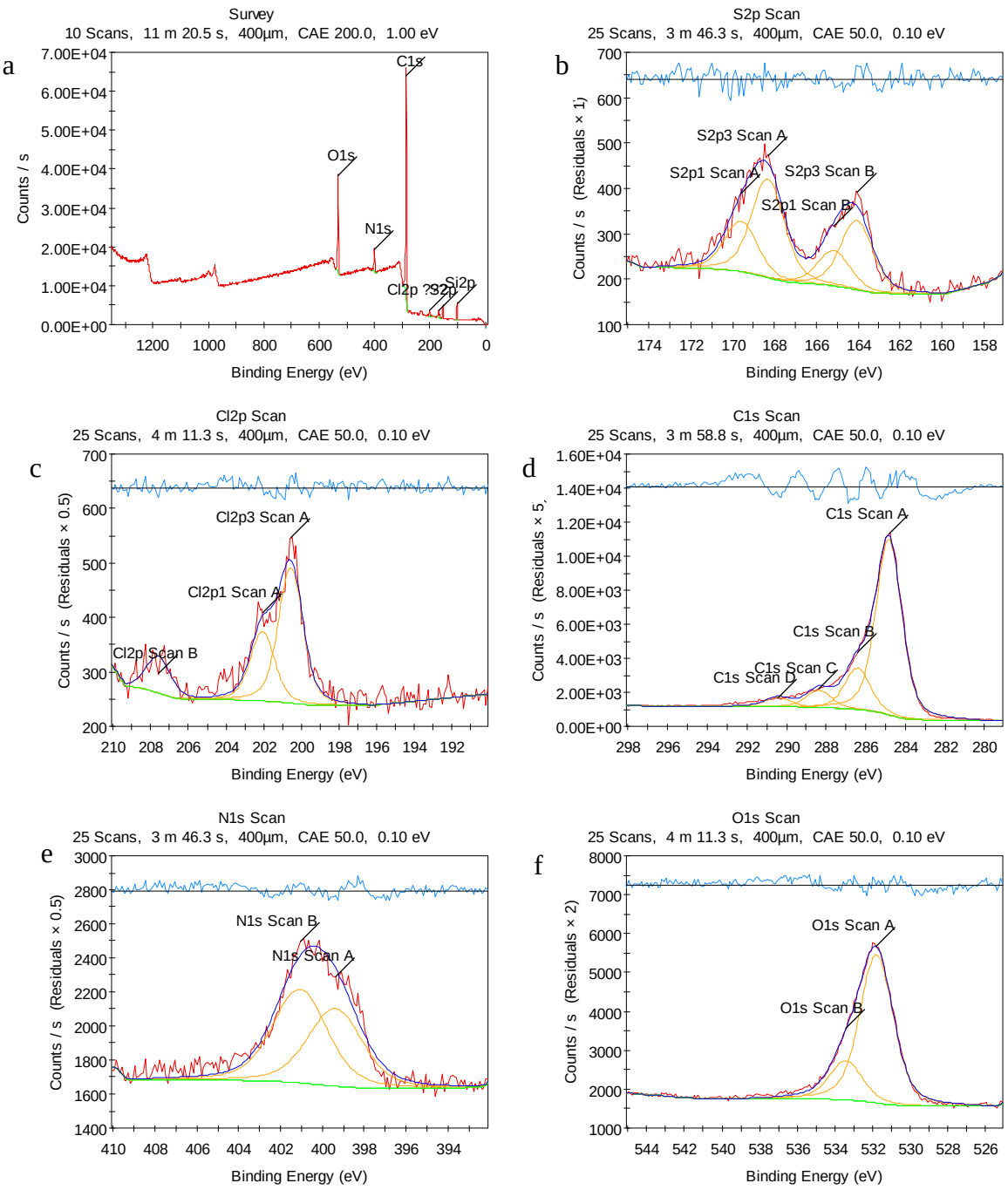

Figure A.40 – X-ray photoelectron spectra for a TiC-CDC sample etched for 0.25 h, held at temperature for an additional 1.25 h, and exposed to aqueous SO_2 at 75°C for 72 h. Included spectra are for the a) survey scan, b) S2p scan showing no sulfur species, c) Cl2p scan showing C-Cl and Cl-O bonds, d) C1s scan showing C-C, C-N/C-O, C=N, C=O, C-Cl bonds, e) N1s scan showing N-C and N=C bonds, and f) O1s scan showing O-C and O=C bonds.

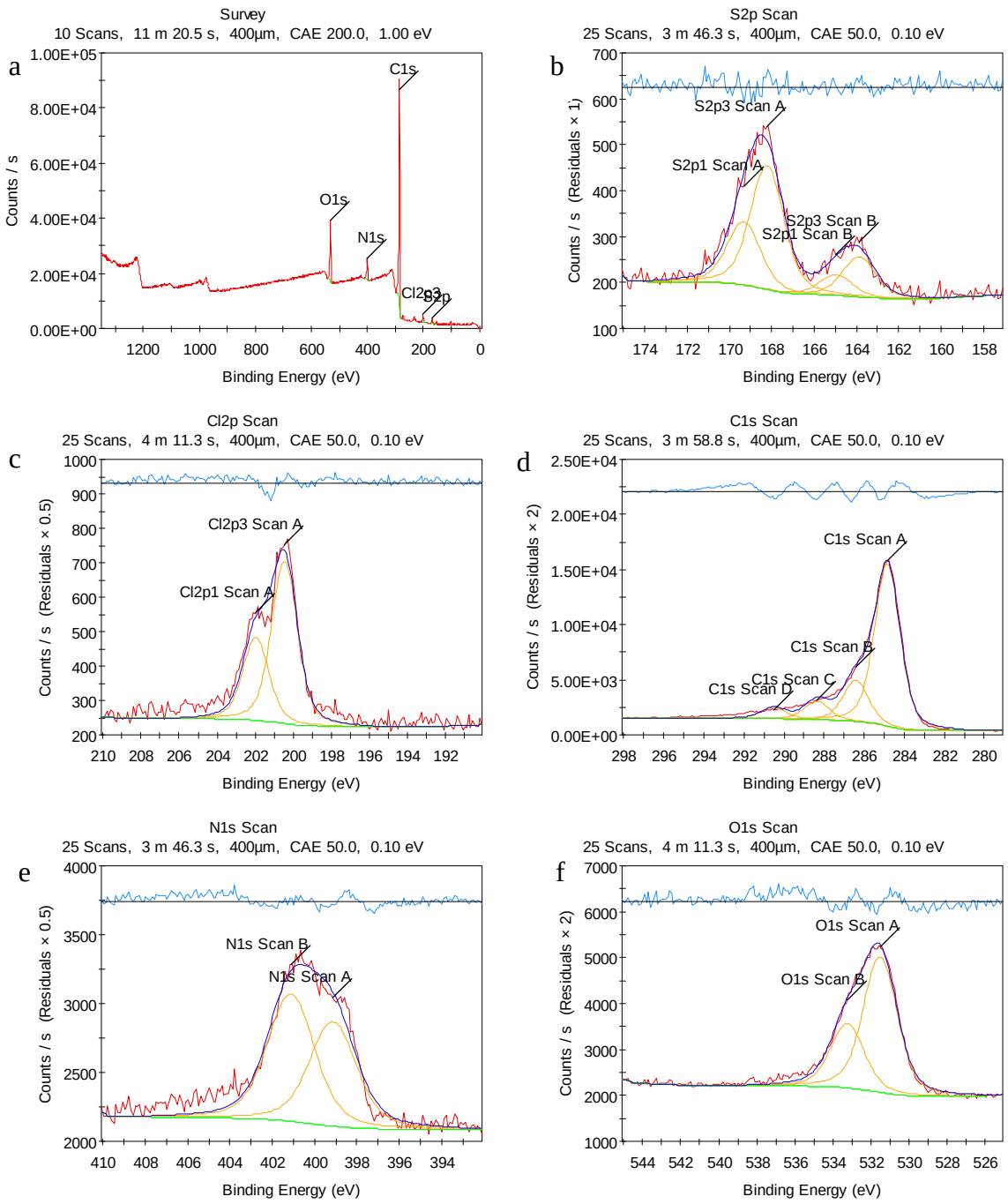

Figure A.41 – X-ray photoelectron spectra for a TiC-CDC sample etched for 0.25 h, held at temperature for an additional 1.25 h, and exposed to aqueous SO_2 at 75°C for 24 h. Included spectra are for the a) survey scan, b) S2p scan showing no sulfur species, c) Cl2p scan showing C-Cl bonds, d) C1s scan showing C-C, C-N/C-O, C=N, C=O, C-Cl bonds, e) N1s scan showing N-C and N=C bonds, and f) O1s scan showing O-C and O=C bonds.

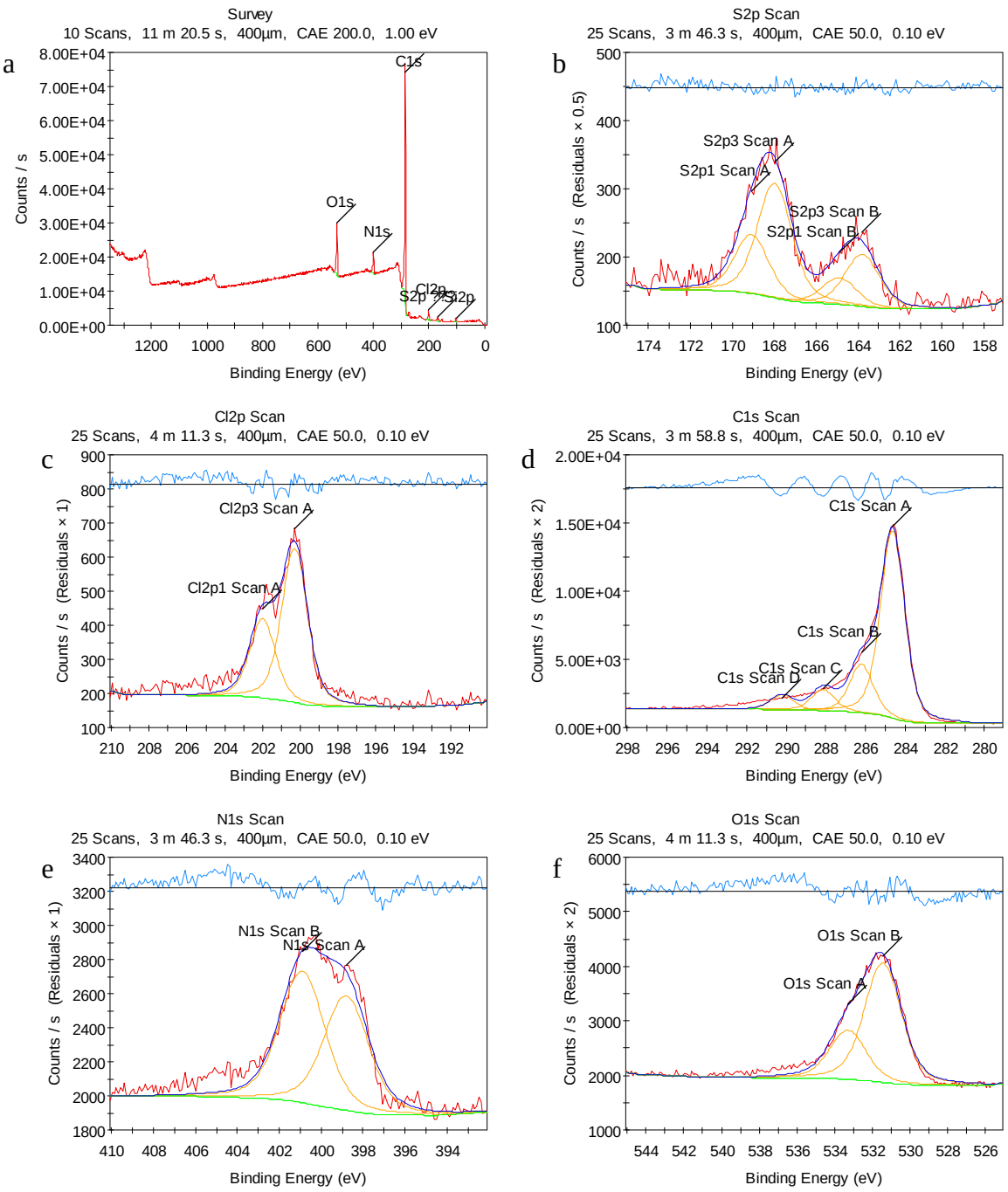

Figure A.42 – X-ray photoelectron spectra for a TiC-CDC sample etched for 0.25 h, held at temperature for an additional 1.25 h, and exposed to aqueous SO_2 at 75°C for 6 h. Included spectra are for the a) survey scan, b) S2p scan showing sulfate and a possible sulfonyl groups, c) Cl2p scan showing C-Cl bonds, d) C1s scan showing C-C, C-N/C-O, C=N, C=O, C-Cl bonds, e) N1s scan showing N-C and N=C bonds, and f) O1s scan showing O-C and O=C bonds.

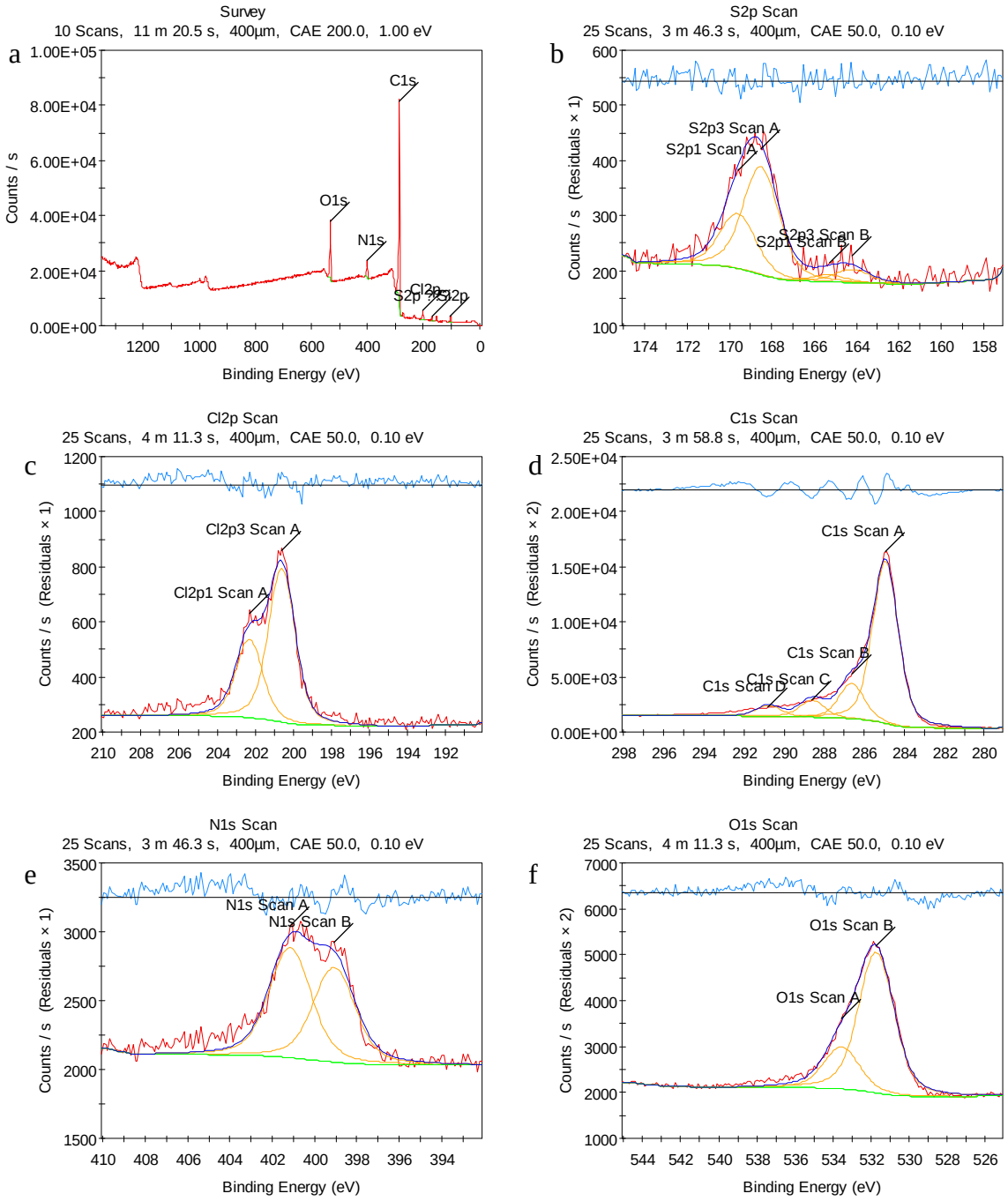

Figure A.43 – X-ray photoelectron spectra for a TiC-CDC sample etched for 0.25 h, held at temperature for an additional 1.25 h, and exposed to aqueous SO_2 at 25°C for 72 h. Included spectra are for the a) survey scan, b) S2p scan showing sulfate and a possible sulfonyl groups, c) Cl2p scan showing C-Cl bonds, d) C1s scan showing C-C, C-N/C-O, C=N, C=O, C-Cl bonds, e) N1s scan showing N-C and N=C bonds, and f) O1s scan showing O-C and O=C bonds.

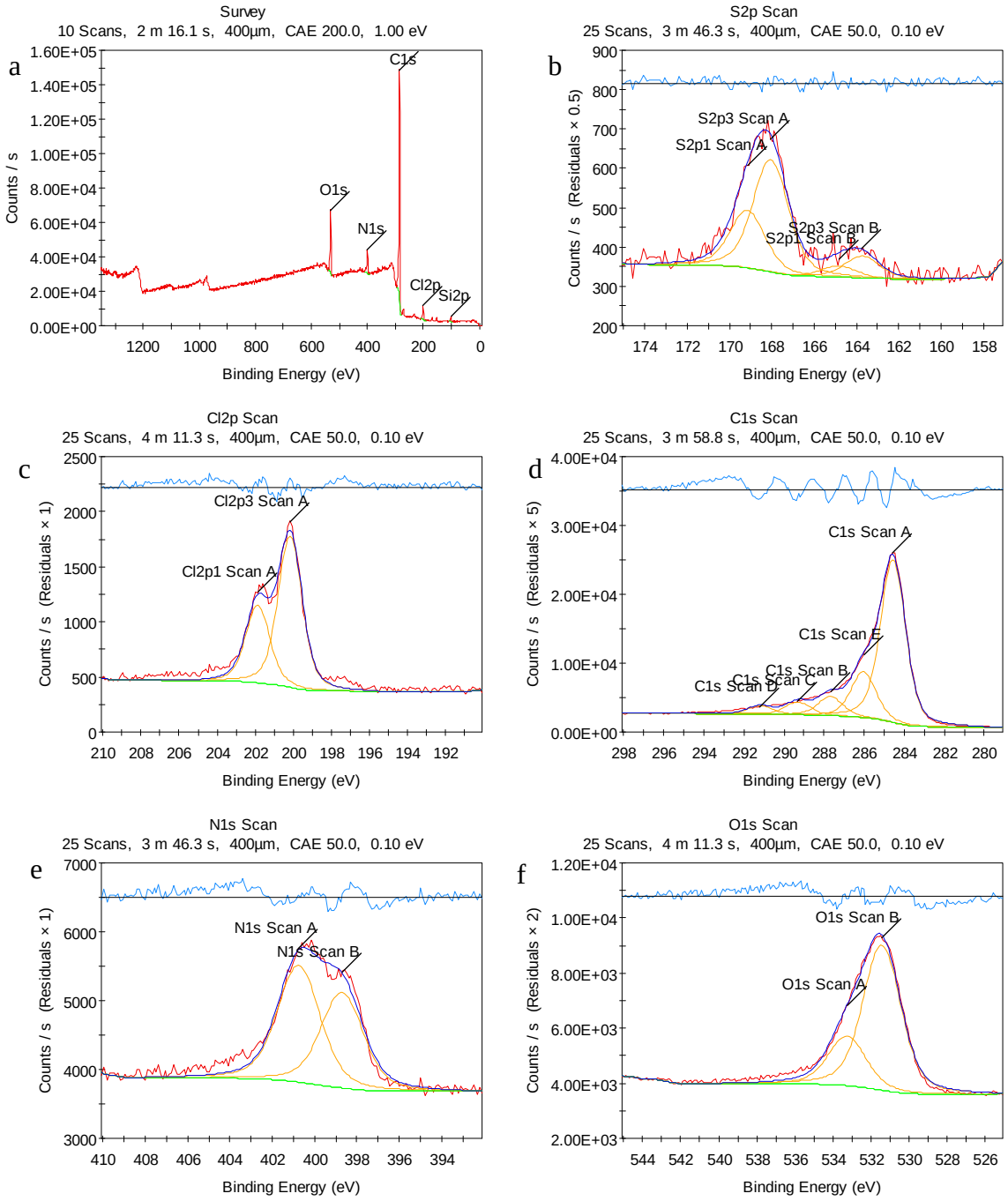

Figure A.44 – X-ray photoelectron spectra for a TiC-CDC sample etched for 0.25 h, held at temperature for an additional 1.25 h, and exposed to aqueous SO_2 at 25°C for 24 h. Included spectra are for the a) survey scan, b) S2p scan showing sulfate and a possible sulfonyl groups, c) Cl2p scan showing C-Cl bonds, d) C1s scan showing C-C, C-N/C-O, C=N, C=O, C-Cl/Cl_2 bonds, e) N1s scan showing N-C and N=C bonds, and f) O1s scan showing O-C and O=C bonds.

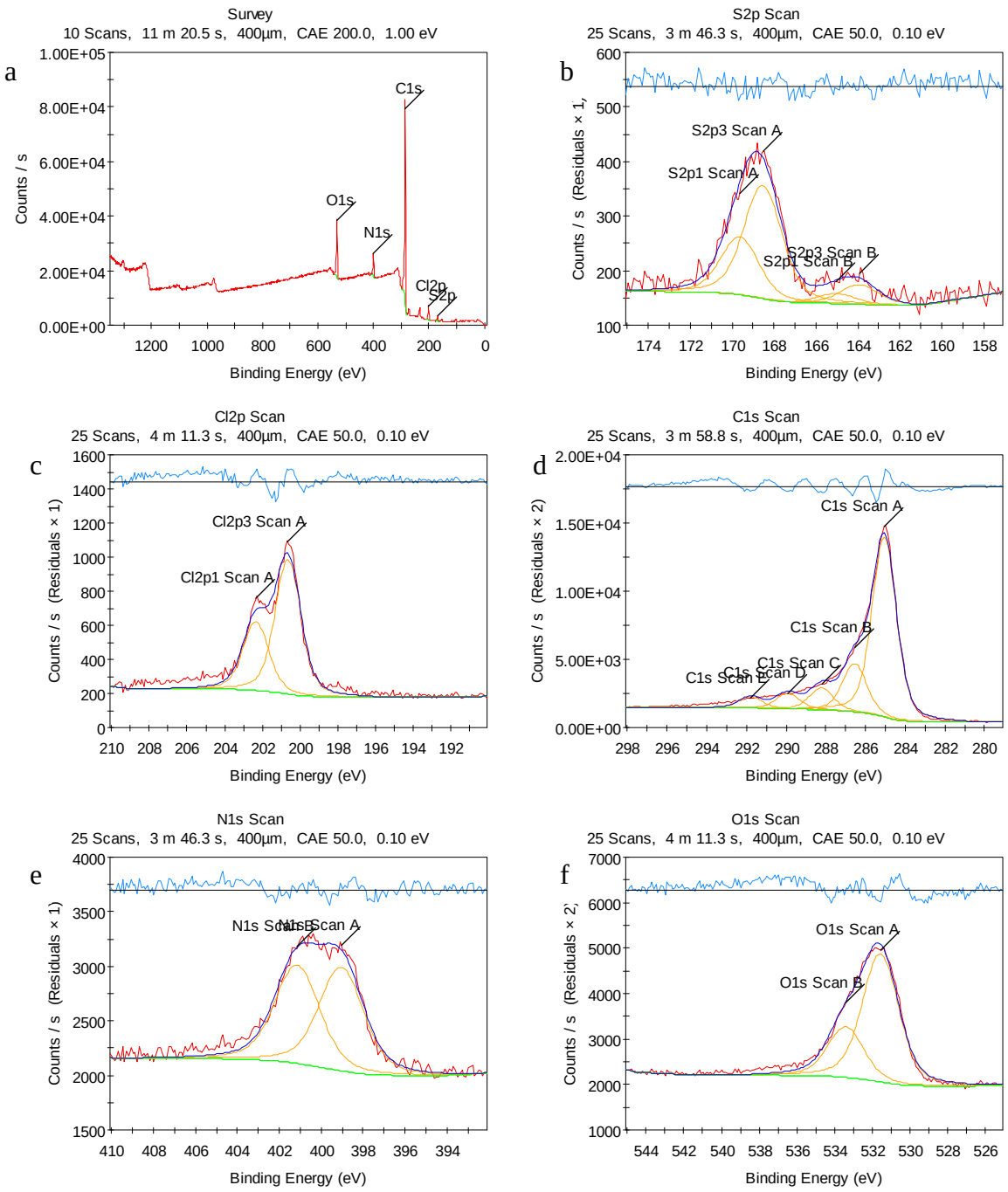

Figure A.45 – X-ray photoelectron spectra for a TiC-CDC sample etched for 0.25 h, held at temperature for an additional 1.25 h, and exposed to aqueous SO2 at 25°C for 6 h. Included spectra are for the a) survey scan, b) S2p scan showing sulfate and a possible sulfonyl groups, c) Cl2p scan showing C-Cl bonds, d) C1s scan showing C-C, C-N/C-O, C=N, C=O, C-Cl/Cl_2 bonds, e) N1s scan showing N-C and N=C bonds, and f) O1s scan showing O-C and O=C bonds.

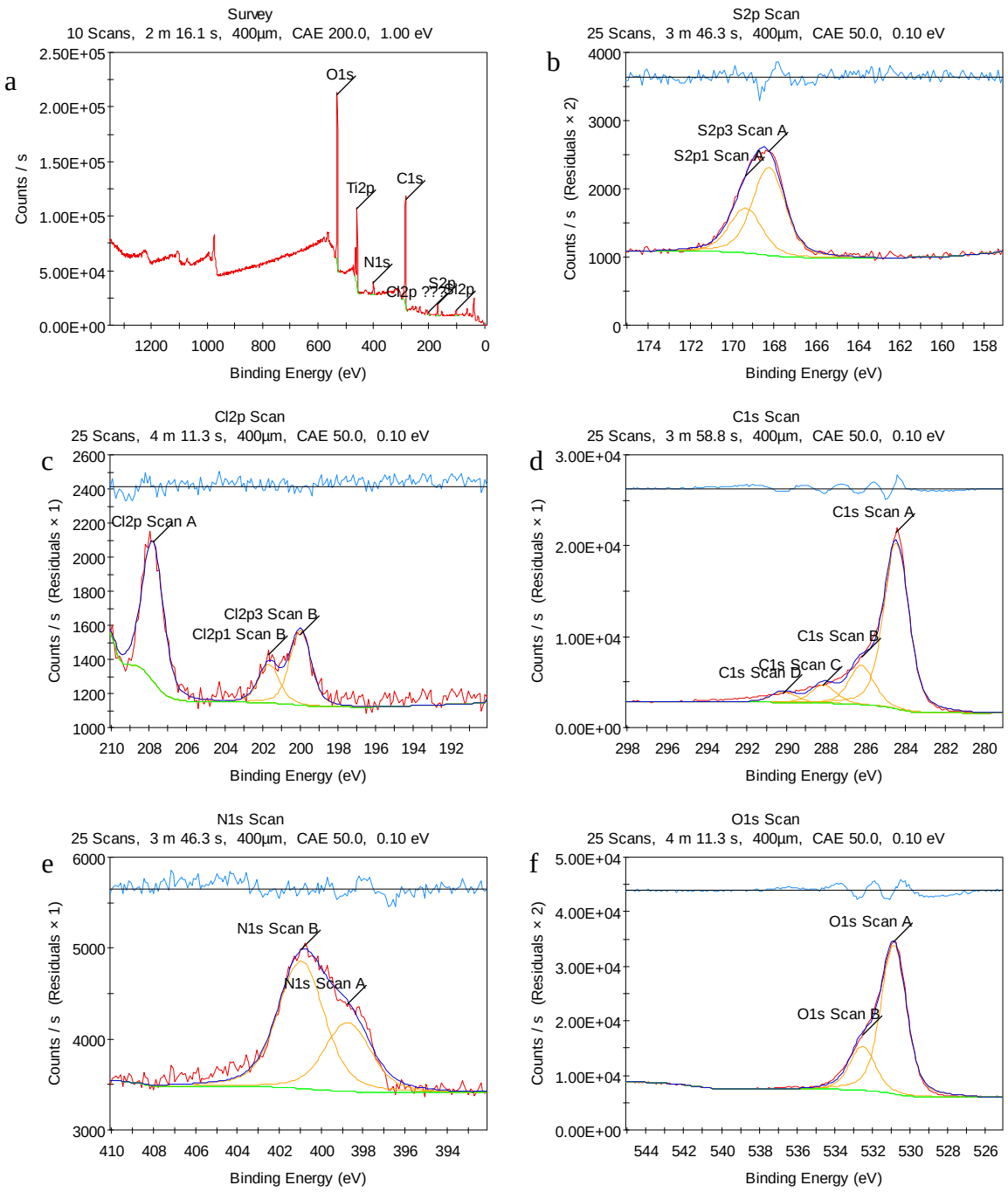

Figure A.46 – X-ray photoelectron spectra for a TiC-CDC sample etched for 0.25 h, held at temperature for an additional 1.25 h, and exposed to humid SO_2 at 25°C for 72 h. Included spectra are for the a) survey scan, b) S2p scan showing sulfate groups, c) Cl2p scan showing C-Cl and C-O bonds, d) C1s scan showing C-C, C-N/C-O, C=N, C=O, C-Cl bonds, e) N1s scan showing N-C and N=C bonds, and f) O1s scan showing O-C and O=C bonds.

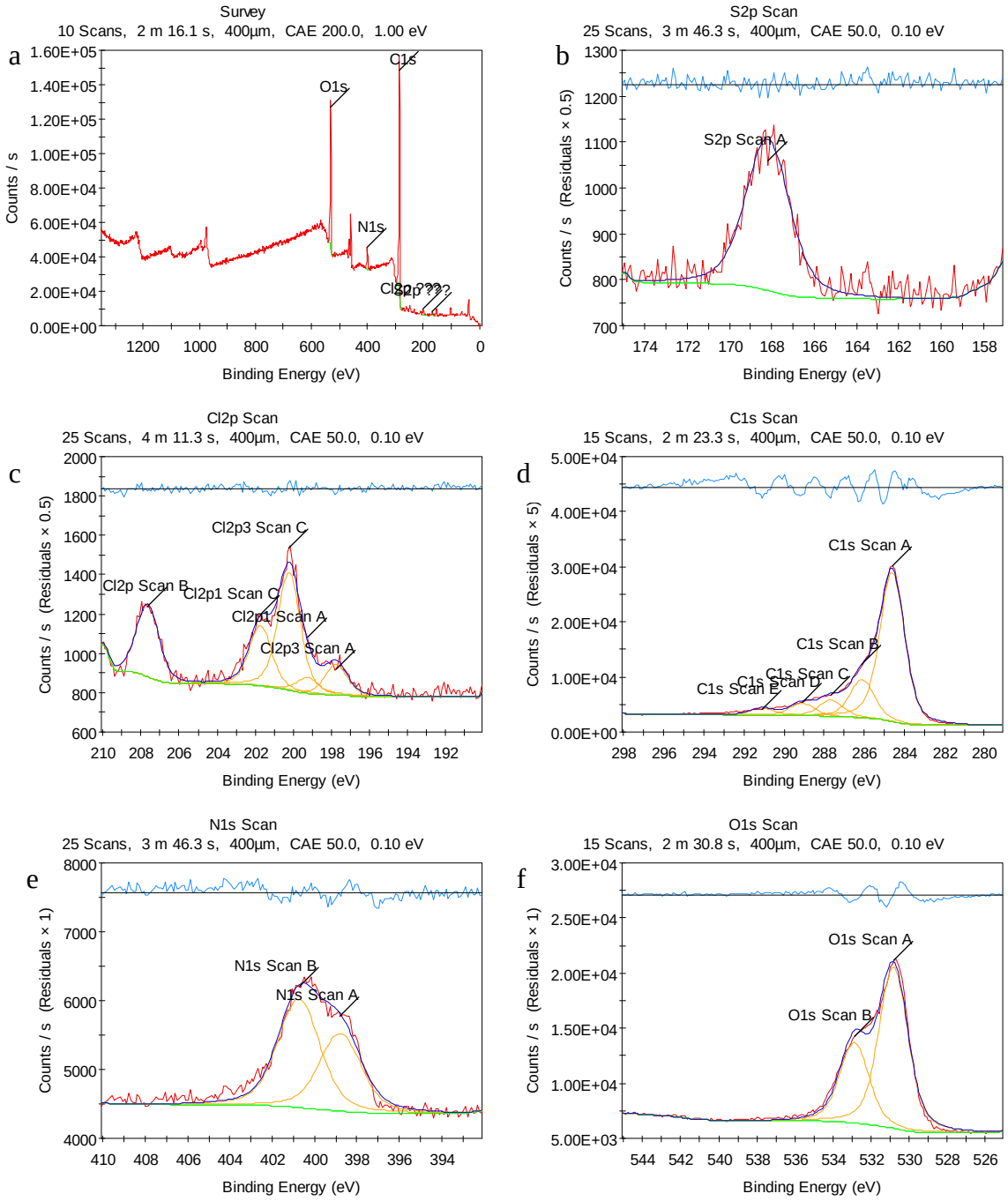

Figure A.47 – X-ray photoelectron spectra for a TiC-CDC sample etched for 0.25 h, held at temperature for an additional 1.25 h, exposed to humid SO_2 at 25°C for 72 h, and decanted with water. Included spectra are for the a) survey scan, b) S2p scan showing sulfate groups, c) Cl2p scan showing elemental Cl_2, C-Cl, and Cl-O bonds, d) C1s scan showing C-C, C-N/C-O, C=N, C=O, C-Cl/Cl_2 bonds, e) N1s scan showing N-C and N=C bonds, and f) O1s scan showing O-C and O=C bonds.

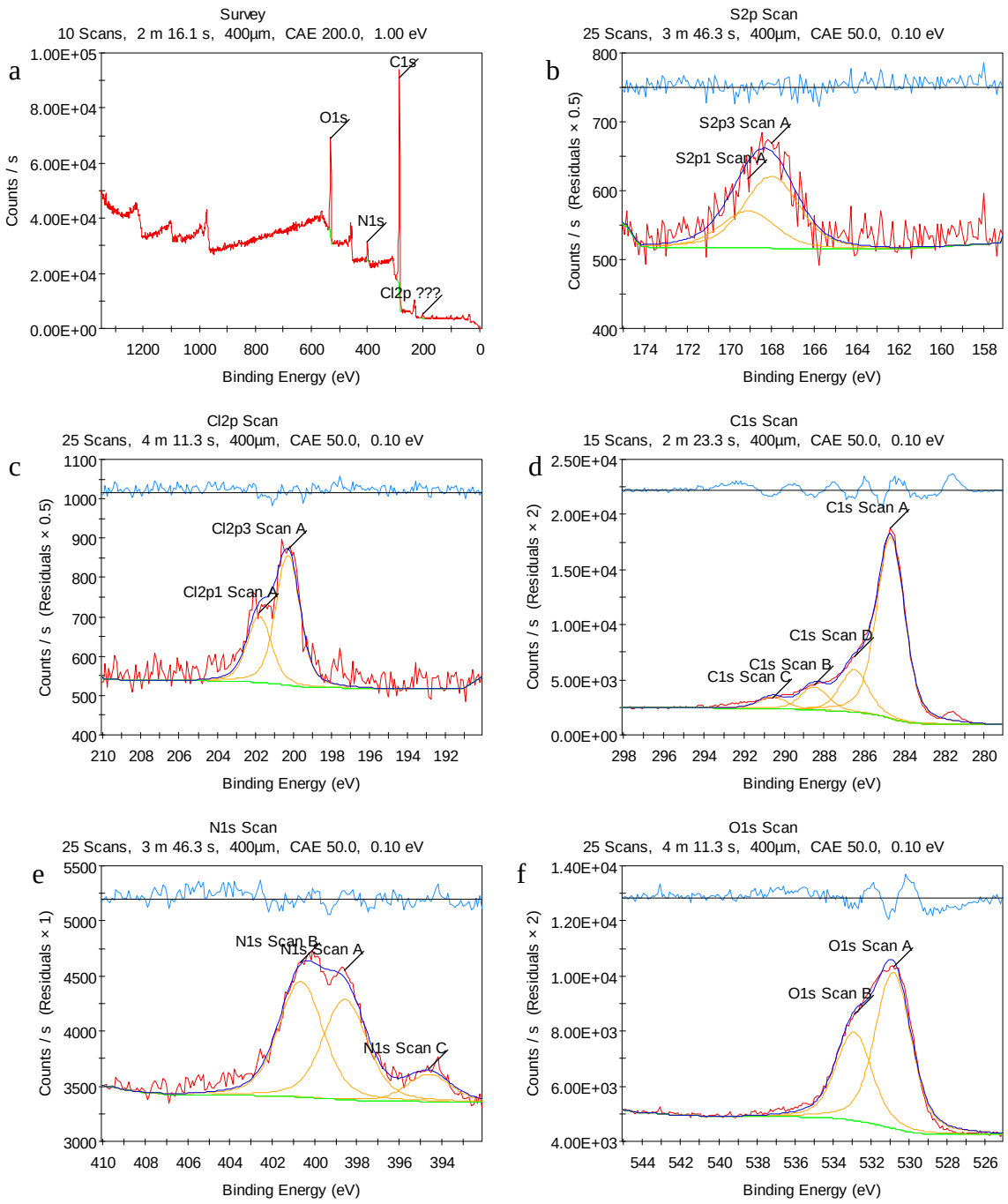

Figure A.48 – X-ray photoelectron spectra for a TiC-CDC sample etched for 0.25 h, held at temperature for an additional 1.25 h, exposed to humid SO_2 at 25°C for 72 h, and sonicated with water. Included spectra are for the a) survey scan, b) S2p scan showing sulfate groups, c) Cl2p scan showing C-Cl bonds, d) C1s scan showing C-C, C-N/C-O, C=N, C=O, C-Cl bonds, e) N1s scan showing N-C and N=C bonds, and f) O1s scan showing O-C and O=C bonds.

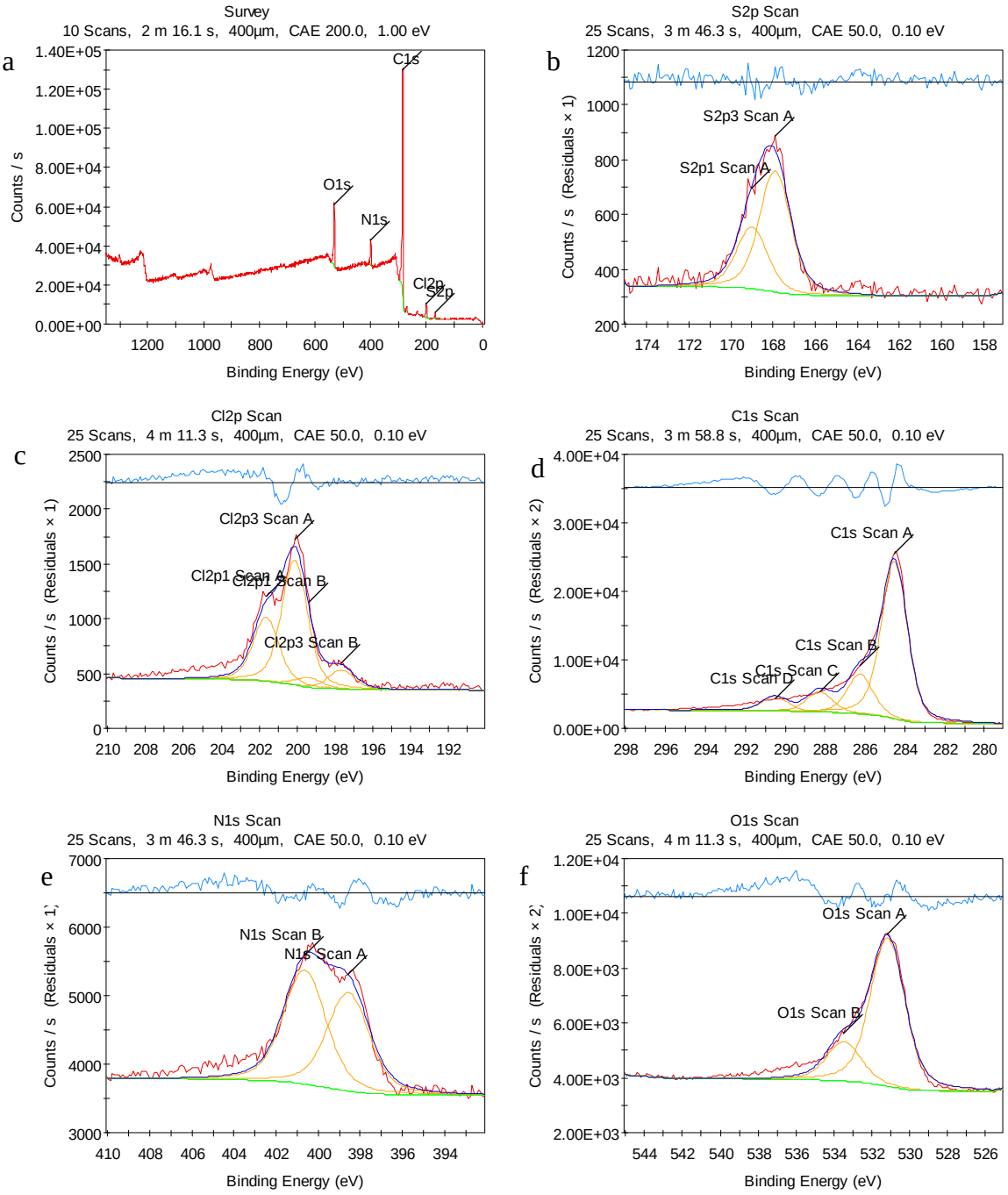

Figure A.49 – X-ray photoelectron spectra for a TiC-CDC sample etched for 0.25 h, held at temperature for an additional 1.25 h, and exposed to dry at 25°C for approximately 3 h. Included spectra are for the a) survey scan, b) S2p scan showing sulfate groups, c) Cl2p scan showing elemental Cl_2 and C-Cl bonds, d) C1s scan showing C-C, C-N/C-O, C=N, C=O, C-Cl bonds, e) N1s scan showing N-C and N=C bonds, and f) O1s scan showing O-C and O=C bonds.

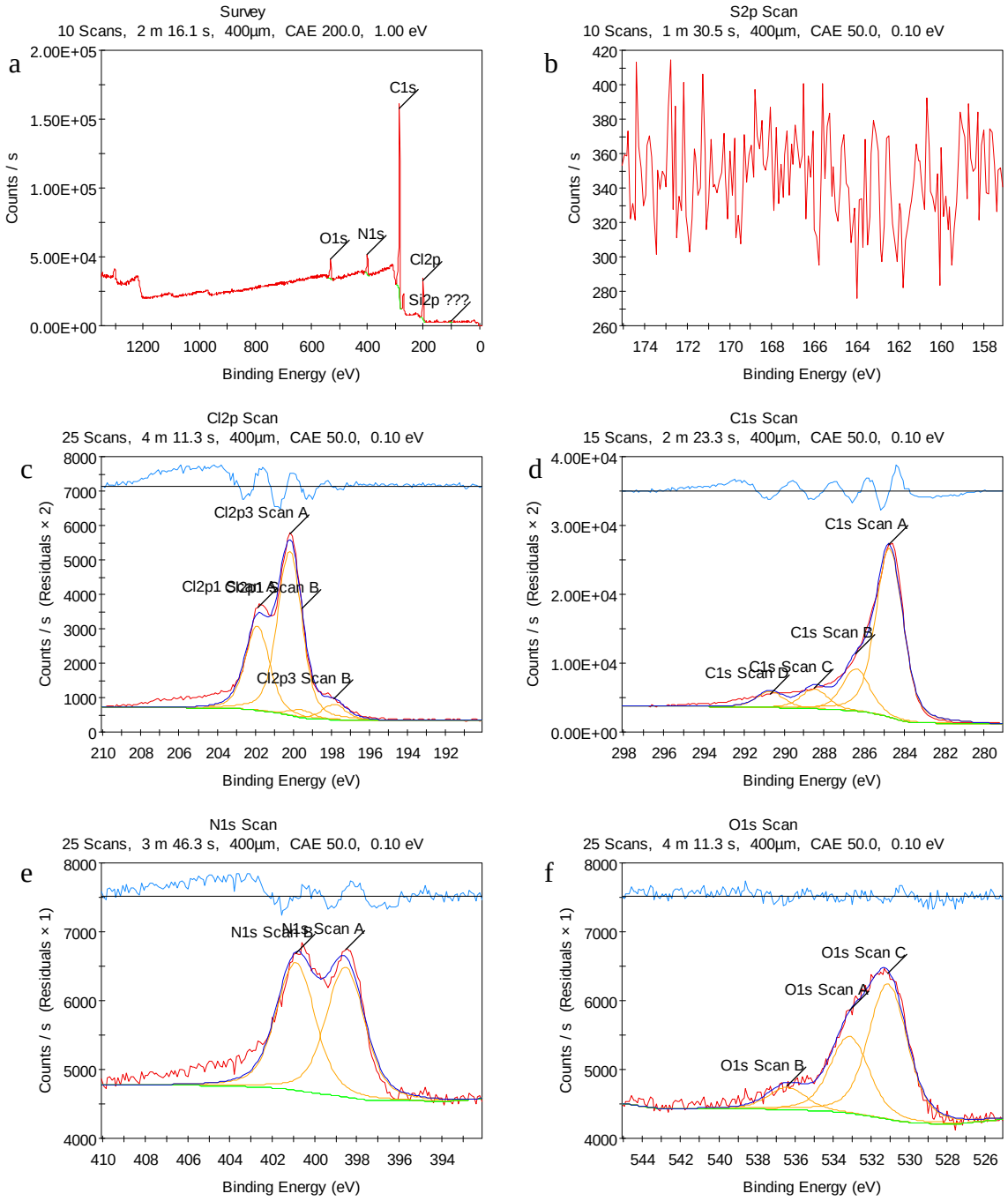

Figure A.50 – X-ray photoelectron spectra for a TiC-CDC sample etched for 1.50 h. Included spectra are for the a) survey scan, b) S2p scan showing no sulfur species, c) Cl2p scan showing elemental Cl_2 and C-Cl bonds, d) C1s scan showing C-C, C-N/C-O, C=N, C=O, C-Cl bonds, e) N1s scan showing N-C and N=C bonds, and f) O1s scan showing O-C and O=C bonds.

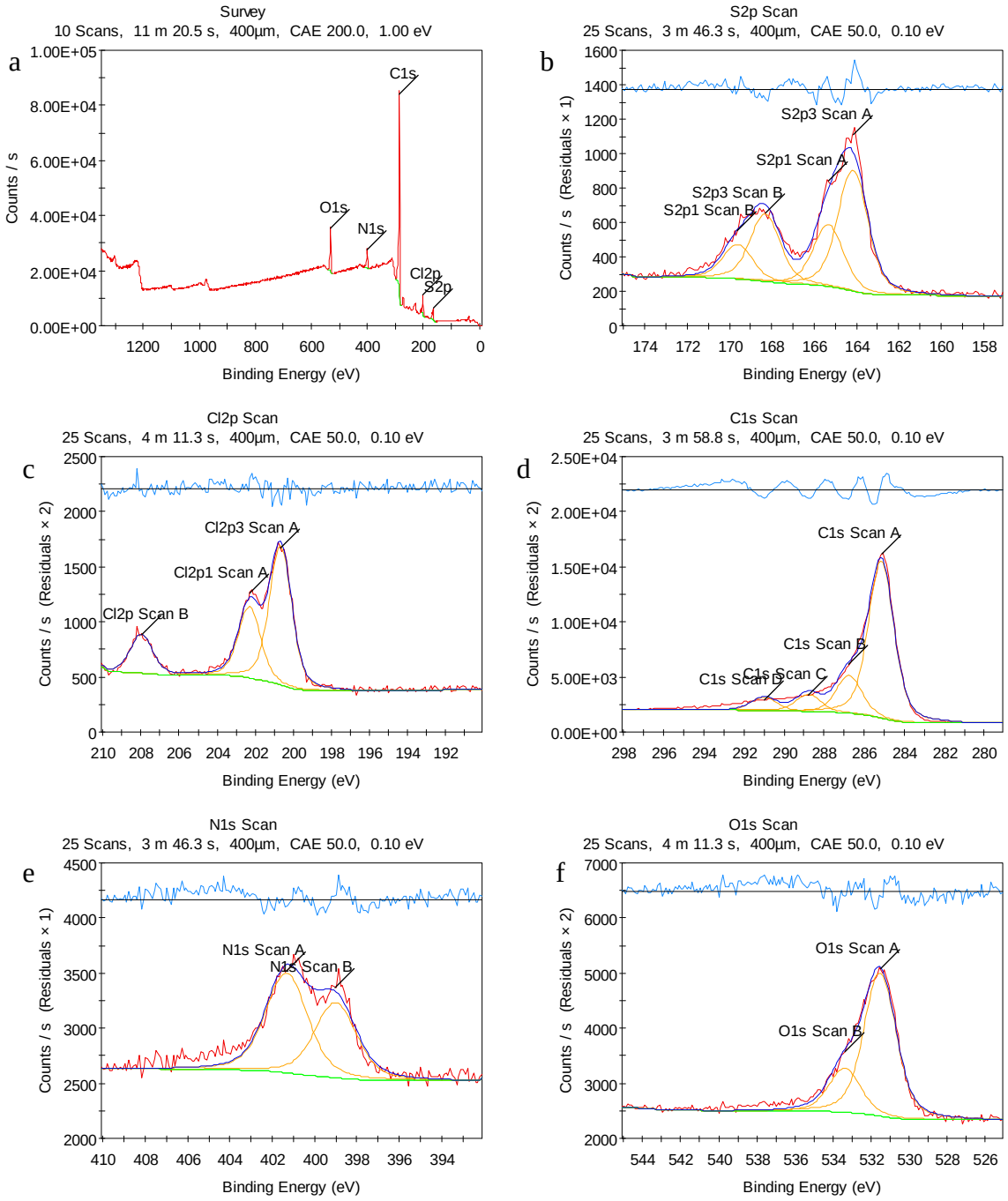

Figure A.51 – X-ray photoelectron spectra for a TiC-CDC sample etched for 1.50 h, and exposed to aqueous SO_2 at 75°C for 72 h. Included spectra are for the a) survey scan, b) S2p scan showing sulfate and a possible sulfonyl groups, c) Cl2p scan showing C-Cl and Cl-O bonds, d) C1s scan showing C-C, C-N/C-O, C=N, C=O, C-Cl bonds, e) N1s scan showing N-C and N=C bonds, and f) O1s scan showing O-C and O=C bonds.

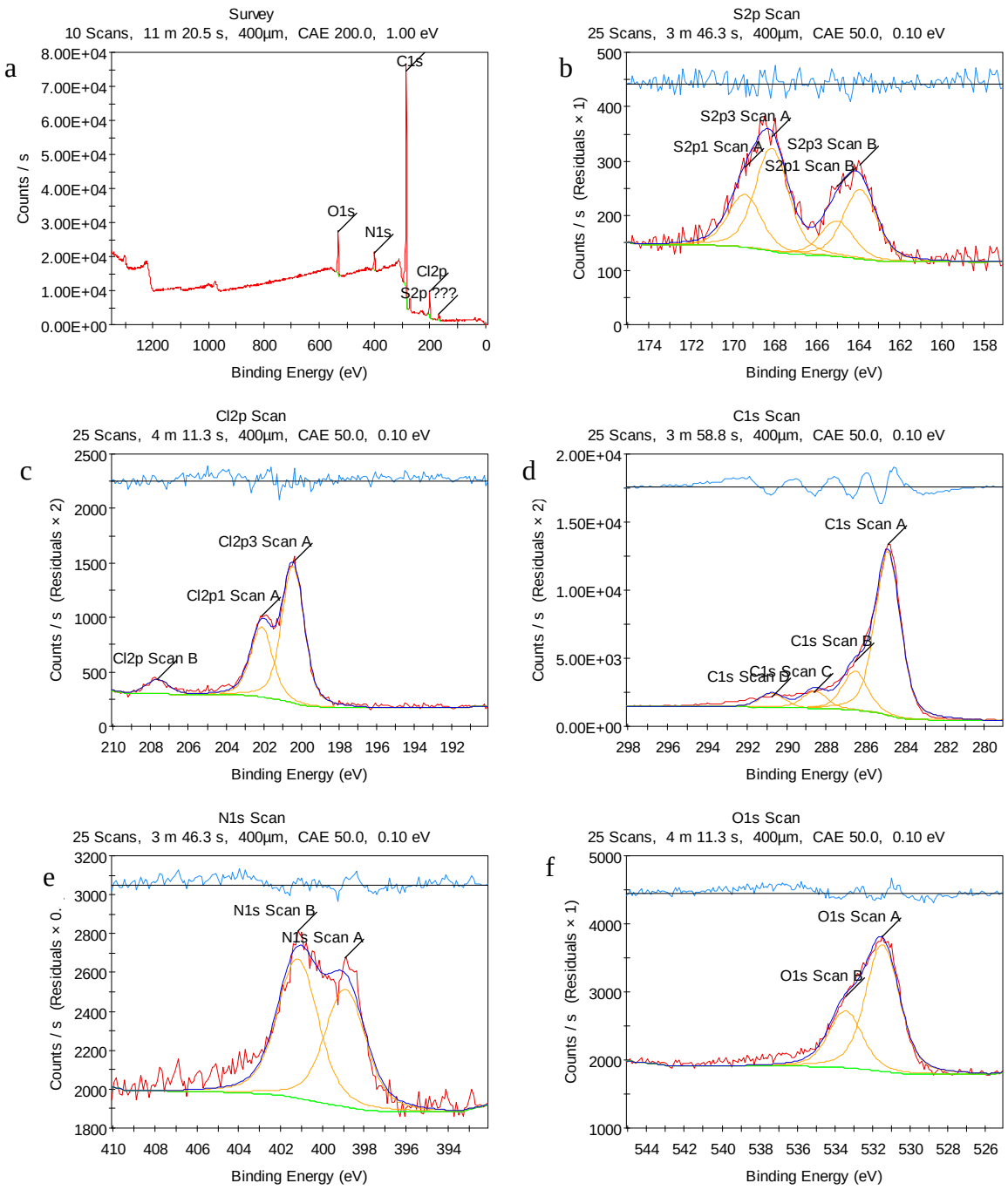

Figure A.52 – X-ray photoelectron spectra for a TiC-CDC sample etched for 1.50 h, and exposed to aqueous SO_2 at 75°C for 24 h. Included spectra are for the a) survey scan, b) S2p scan showing sulfate and a possible sulfonyl groups, c) Cl2p scan showing C-Cl and Cl-O bonds, d) C1s scan showing C-C, C-N/C-O, C=N, C=O, C-Cl bonds, e) N1s scan showing N-C and N=C bonds, and f) O1s scan showing O-C and O=C bonds.

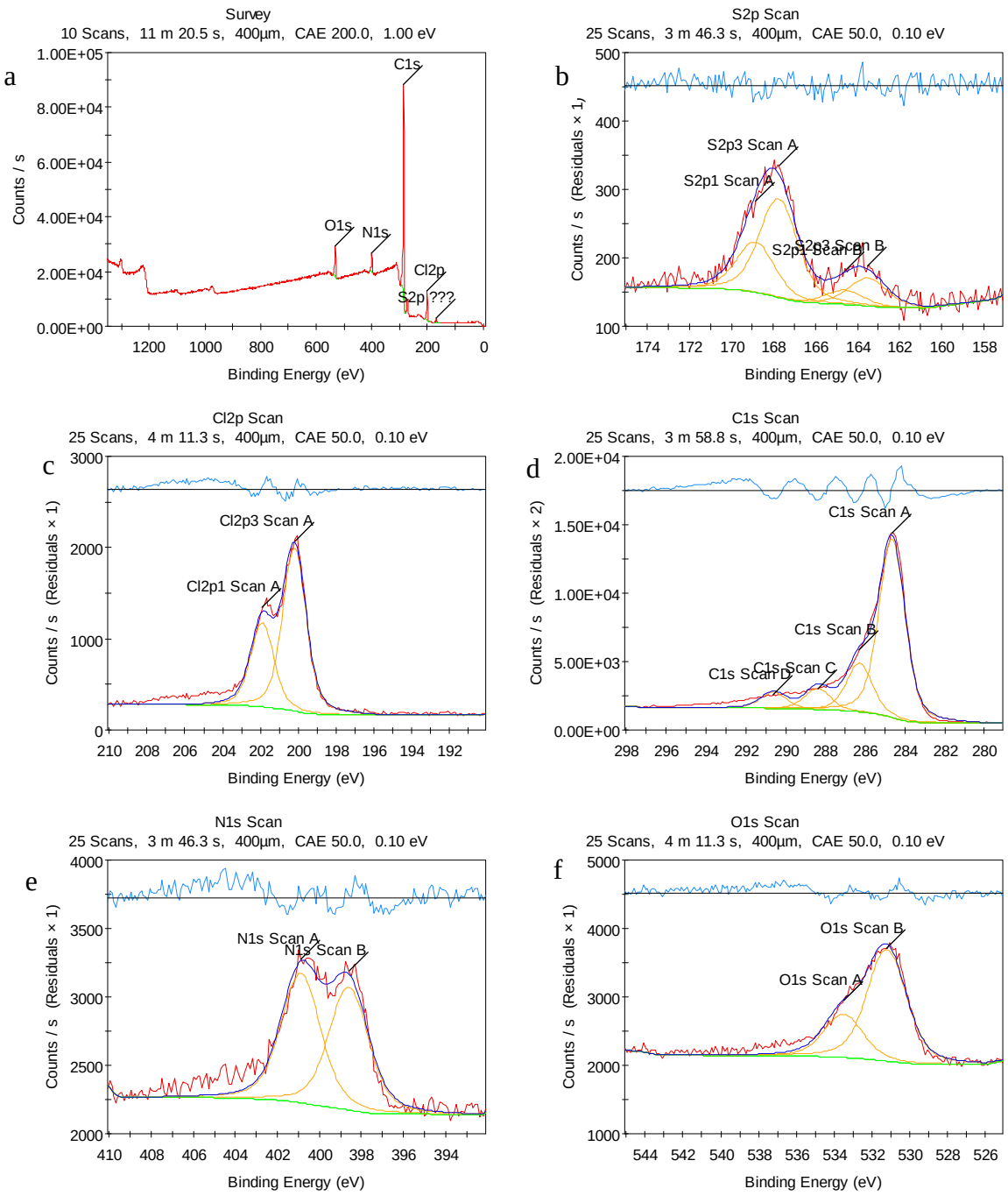

Figure A.53 – X-ray photoelectron spectra for a TiC-CDC sample etched for 1.50 h, and exposed to aqueous SO_2 at 75°C for 6 h. Included spectra are for the a) survey scan, b) S2p scan showing sulfate and a possible sulfonyl groups, c) Cl2p scan showing C-Cl bonds, d) C1s scan showing C-C, C-N/C-O, C=N, C=O, C-Cl bonds, e) N1s scan showing N-C and N=C bonds, and f) O1s scan showing O-C and O=C bonds.

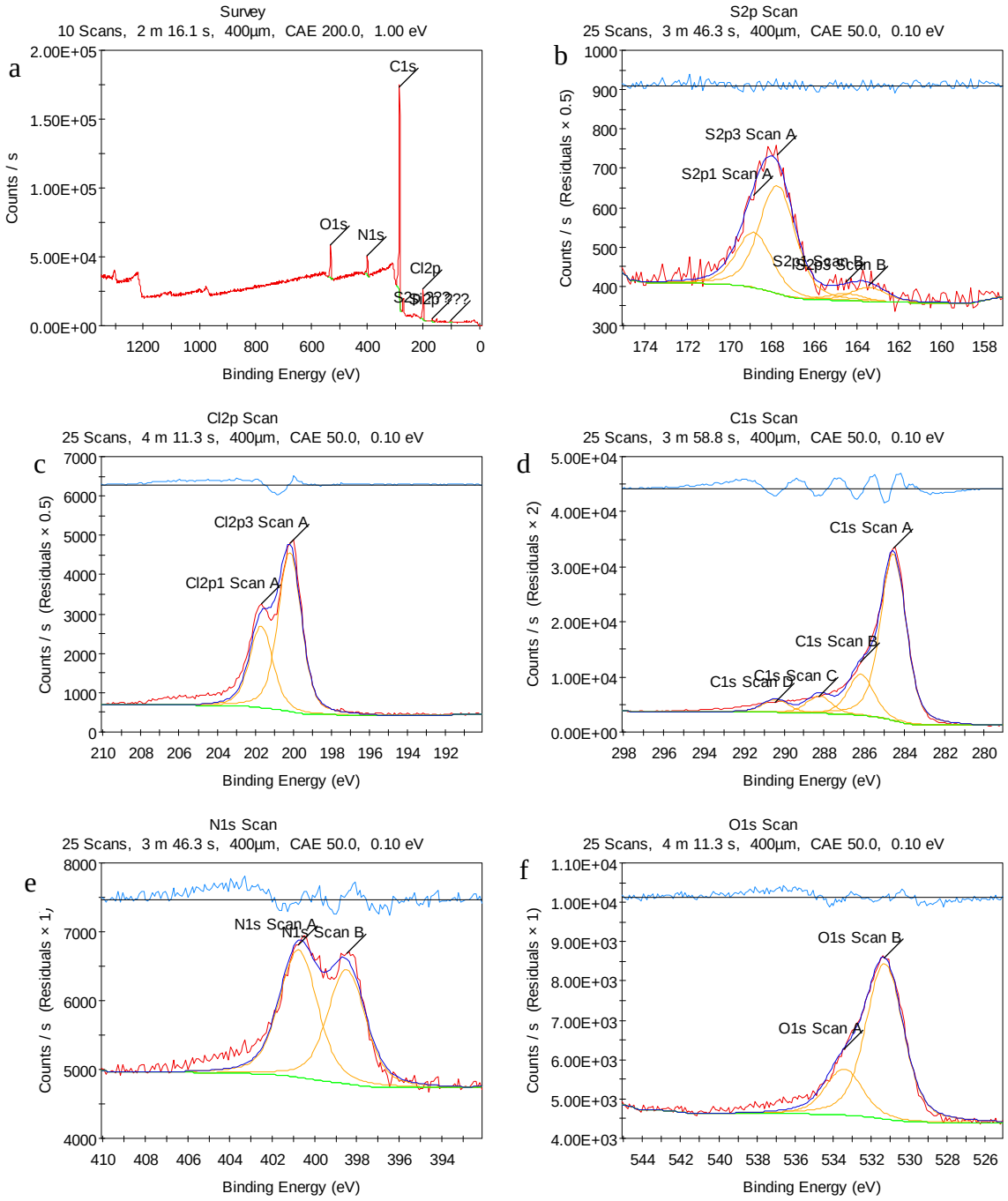

Figure A.54 – X-ray photoelectron spectra for a TiC-CDC sample etched for 1.50 h, and exposed to aqueous SO_2 at 25°C for 72 h. Included spectra are for the a) survey scan, b) S2p scan showing sulfate and a possible sulfonyl groups, c) Cl2p scan showing C-Cl bonds, d) C1s scan showing C-C, C-N/C-O, C=N, C=O, C-Cl bonds, e) N1s scan showing N-C and N=C bonds, and f) O1s scan showing O-C and O=C bonds.

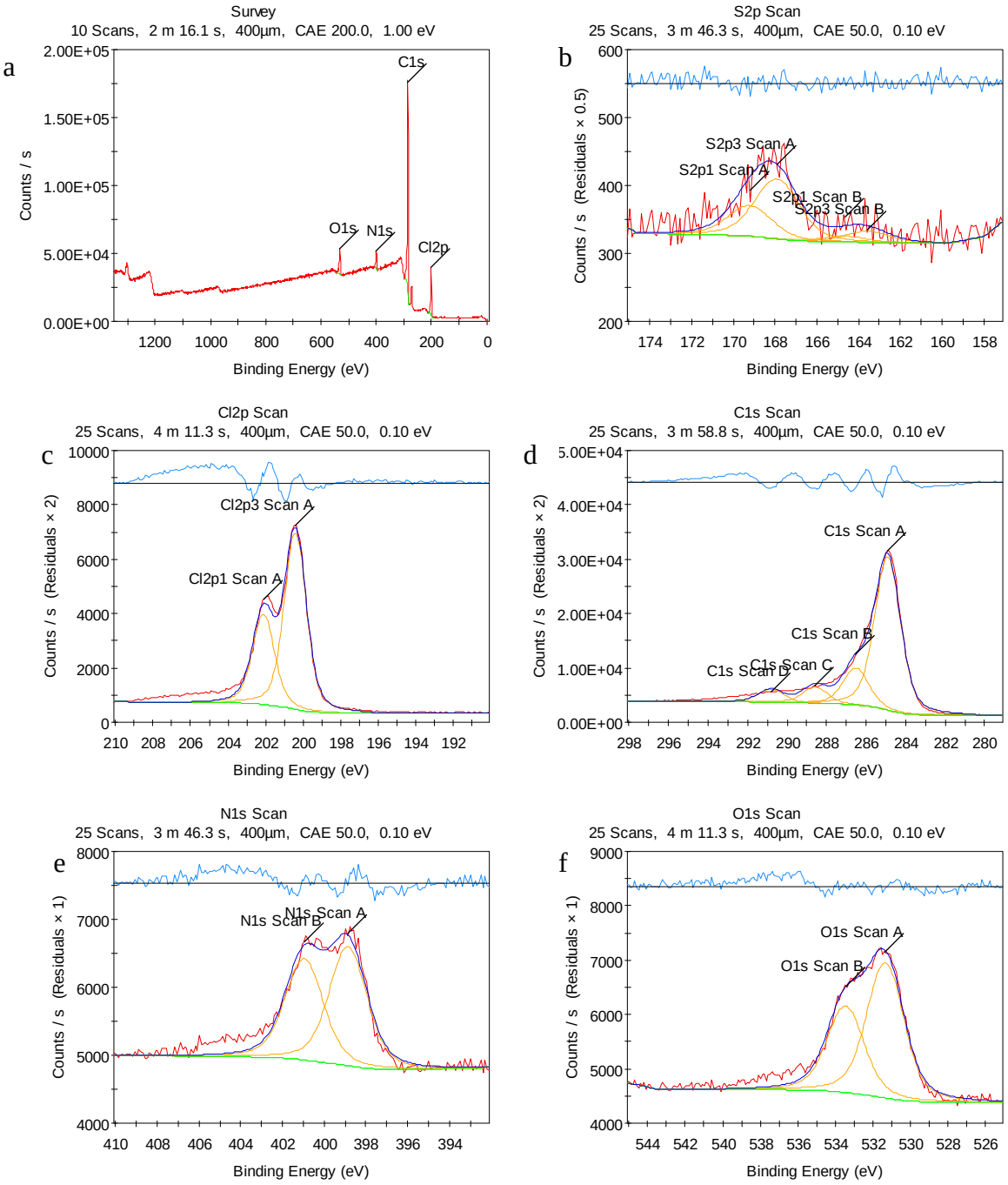

Figure A.55 – X-ray photoelectron spectra for a TiC-CDC sample etched for 1.50 h, and exposed to aqueous SO_2 at 25°C for 24 h. Included spectra are for the a) survey scan, b) S2p scan showing sulfate and a possible sulfonyl groups, c) Cl2p scan showing C-Cl bonds, d) C1s scan showing C-C, C-N/C-O, C=N, C=O, C-Cl bonds, e) N1s scan showing N-C and N=C bonds, and f) O1s scan showing O-C and O=C bonds.

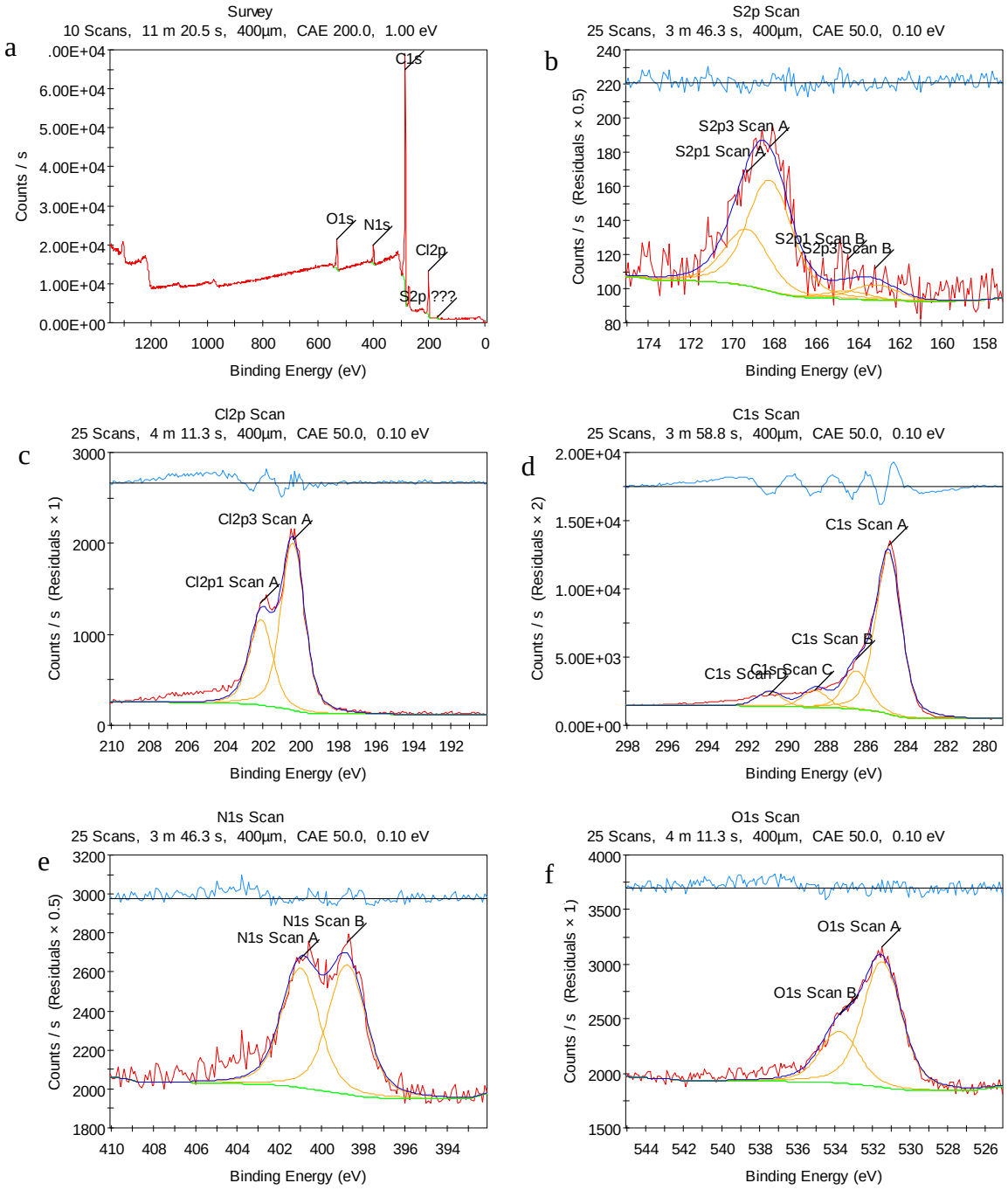

Figure A.56 – X-ray photoelectron spectra for a TiC-CDC sample etched for 1.50 h, and exposed to aqueous SO_2 at 25°C for 6 h. Included spectra are for the a) survey scan, b) S2p scan showing sulfate and a possible sulfonyl groups, c) Cl2p scan showing C-Cl bonds, d) C1s scan showing C-C, C-N/C-O, C=N, C=O, C-Cl bonds, e) N1s scan showing N-C and N=C bonds, and f) O1s scan showing O-C and O=C bonds.

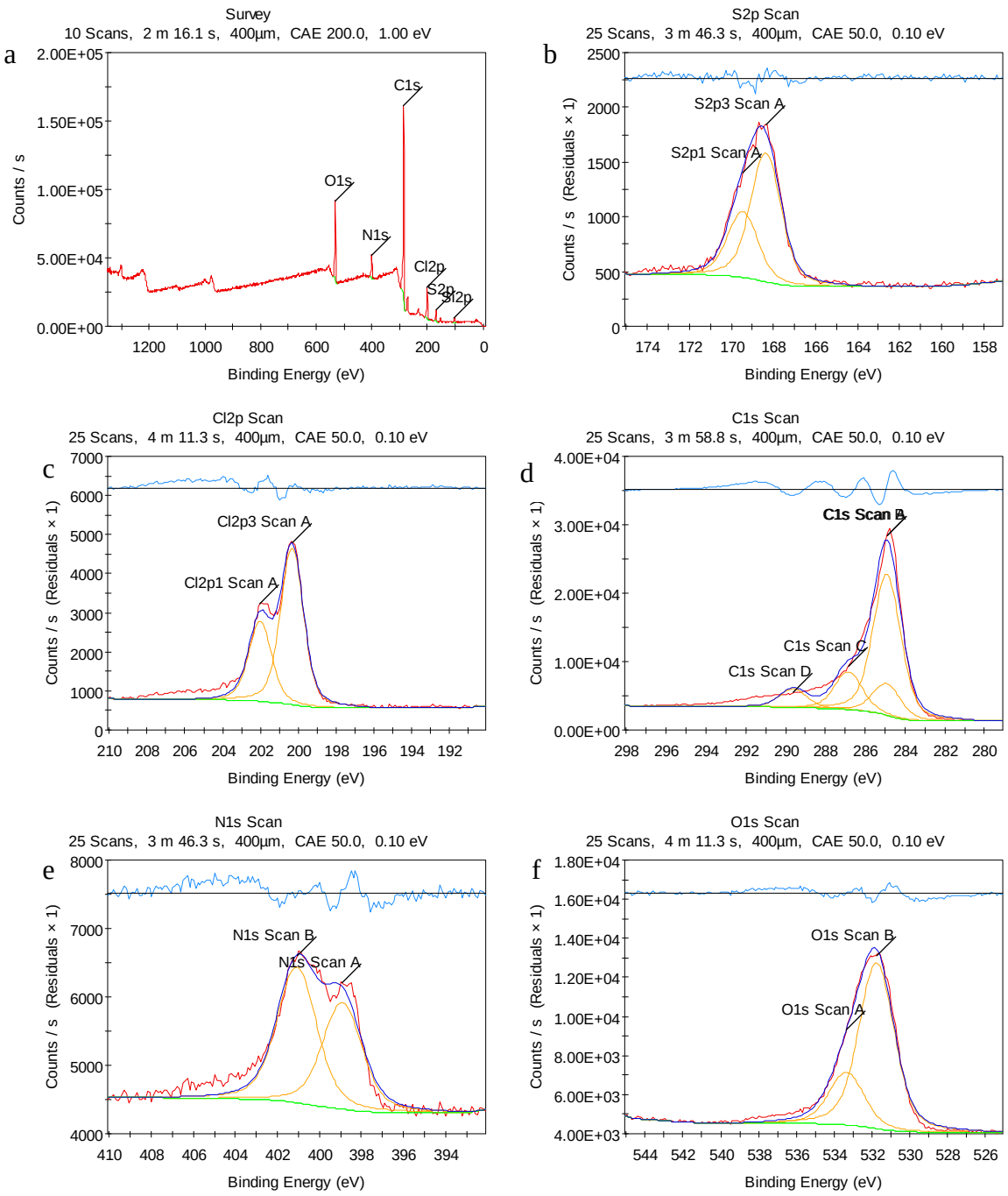

Figure A.57 – X-ray photoelectron spectra for a TiC-CDC sample etched for 1.50 h, and exposed to humid SO_2 at 25°C for 72 h. Included spectra are for the a) survey scan, b) S2p scan showing sulfate groups, c) Cl2p scan showing C-Cl bonds, d) C1s scan showing C-C, C-N/C-O, C=N, C=O, C-Cl bonds, e) N1s scan showing N-C and N=C bonds, and f) O1s scan showing O-C and O=C bonds.

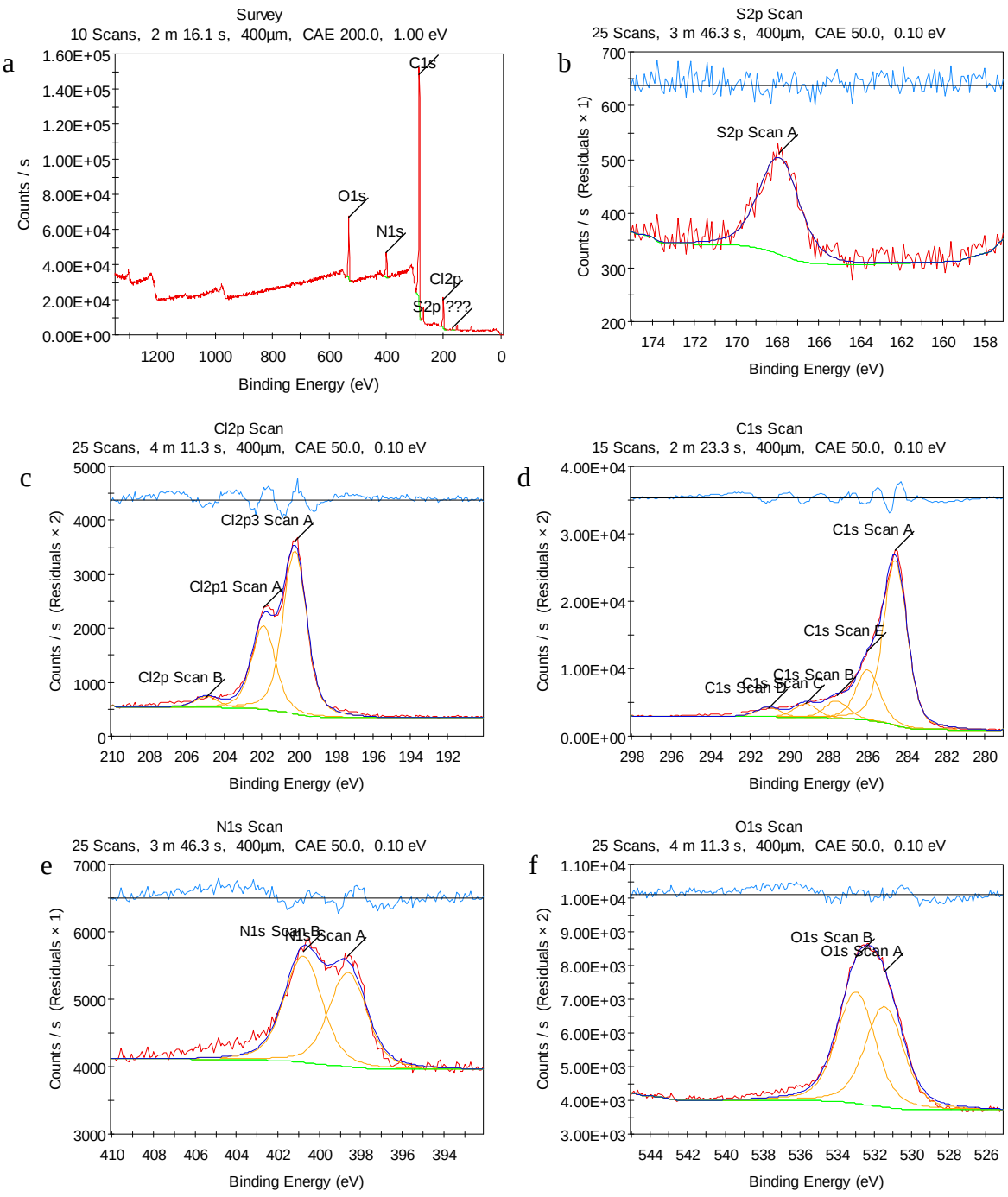

Figure A.58 – X-ray photoelectron spectra for a TiC-CDC sample etched for 1.50 h, exposed to humid SO_2 at 25°C for 72 h, and decanted with water. Included spectra are for the a) survey scan, b) S2p scan showing sulfate groups, c) Cl2p scan showing C-Cl and Cl-O bonds, d) C1s scan showing C-C, C-N/C-O, C=N, C=O, C-Cl bonds, e) N1s scan showing N-C and N=C bonds, and f) O1s scan showing O-C and O=C bonds.

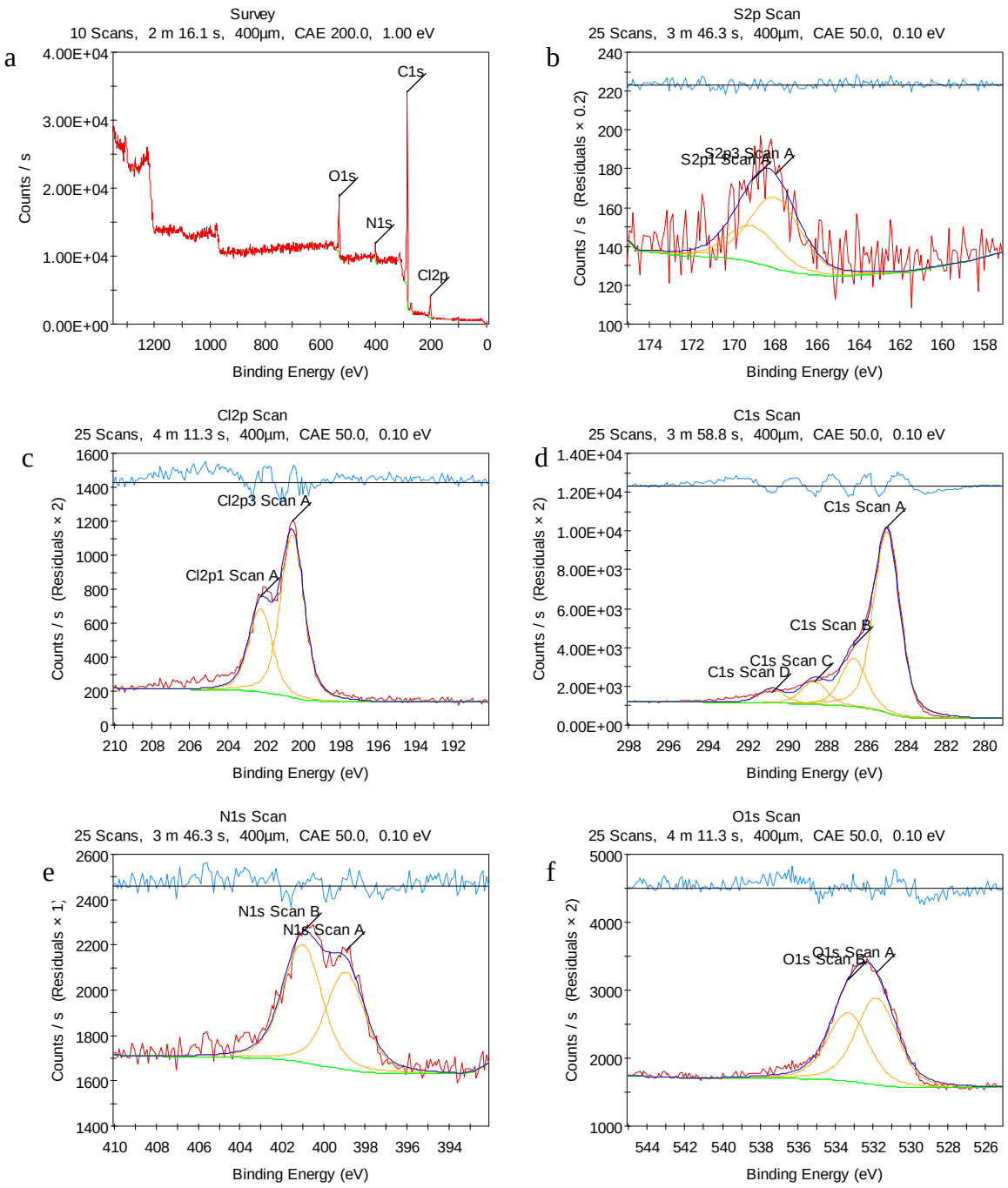

Figure A.59 – X-ray photoelectron spectra for a TiC-CDC sample etched for 1.50 h, exposed to humid SO_2 at 25°C for 72 h, and sonicated with water. Included spectra are for the a) survey scan, b) S2p scan showing sulfate groups, c) Cl2p scan showing C-Cl bonds, d) C1s scan showing C-C, C-N/C-O, C=N, C=O, C-Cl bonds, e) N1s scan showing N-C and N=C bonds, and f) O1s scan showing O-C and O=C bonds.

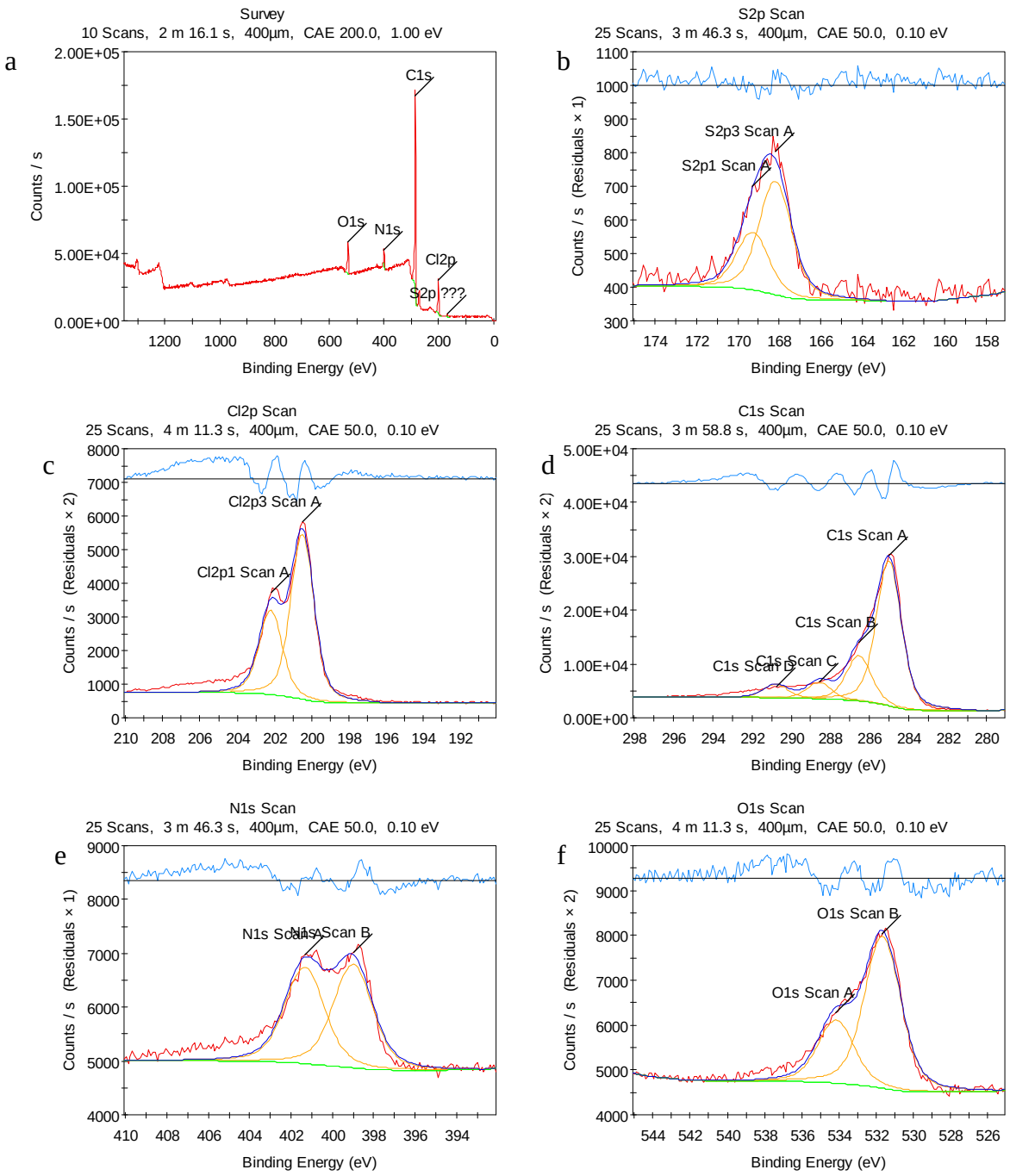

Figure A.60 – X-ray photoelectron spectra for a TiC-CDC sample etched for 1.50 h, and exposed to dry SO_2 at 25°C for approximately 3 h. Included spectra are for the a) survey scan, b) S2p scan showing sulfate groups, c) Cl2p scan showing C-Cl bonds, d) C1s scan showing C-C, C-N/C-O, C=N, C=O, C-Cl bonds, e) N1s scan showing N-C and N=C bonds, and f) O1s scan showing O-C and O=C bonds.

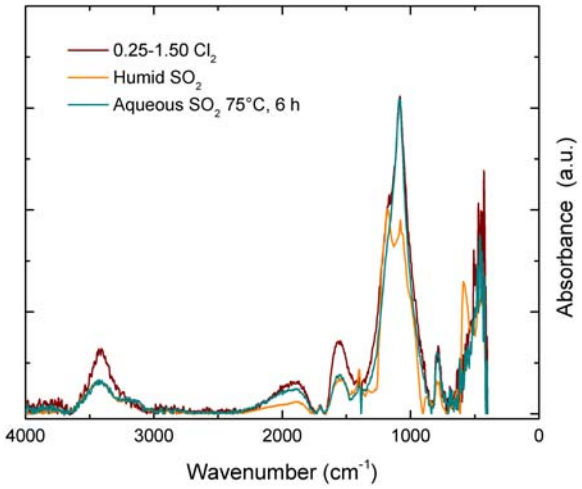

Figure A.61 – IR spectra for select samples to determine if a thiol group was added to the carbon structure. The absence of a peak at 2500 cm^{-1} indicates there is no thiol group.

A.3 Chapter 5: Synthesizing Partially Etched Manganese Carbide-Derived Carbon

A.3.1 Supplemental and Raw Data for Chapter 5

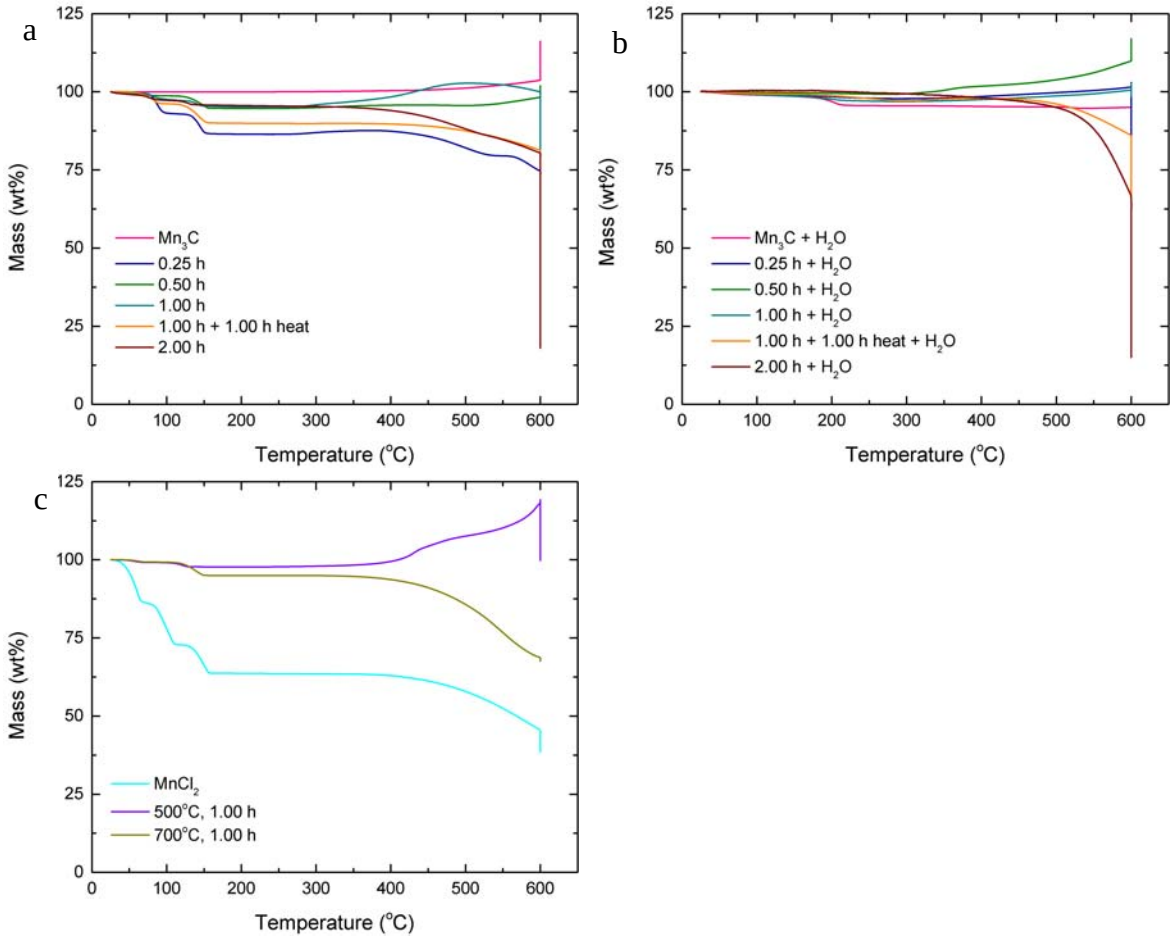

Figure A.62 – TGA curves for (a) samples etched at 900°C without soaking in water, (b) samples etched at 900°C and soaked in water, and (c) samples etched at 500 and 700°C with $MnCl_2$.

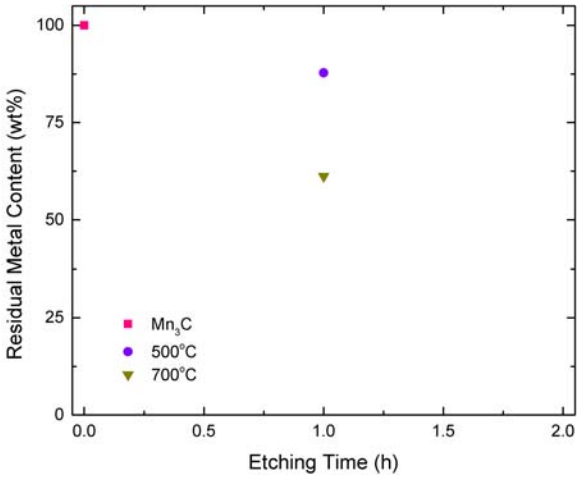

Figure A.63 – Residual metal content for samples etched at 500 and 700°C for 1 h.

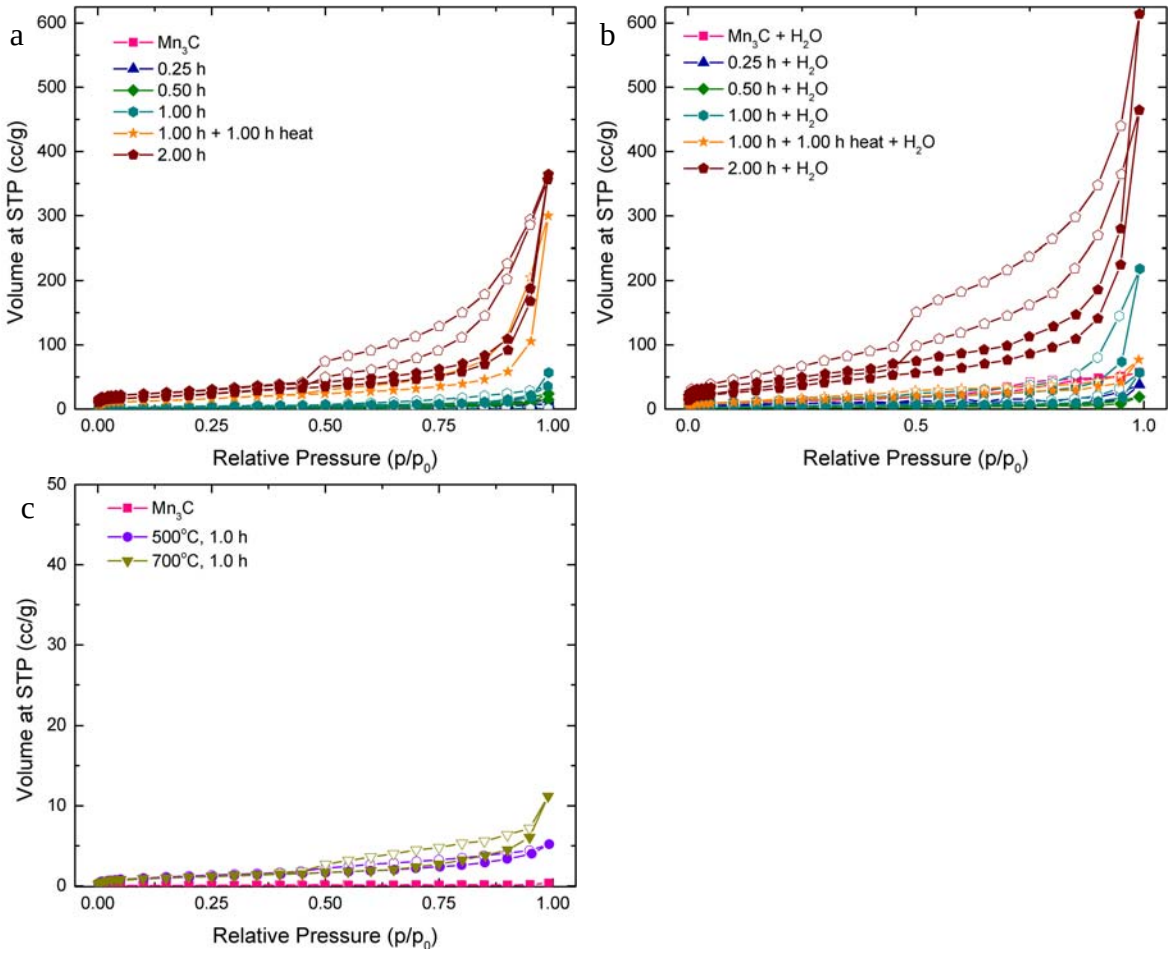

Figure A.64 – N_2 isotherms at 77 K for (a) samples etched at 900°C, (b) samples etched at 900°C and soaked in water, and (c) samples etched at 500 and 700°C for 1 h.

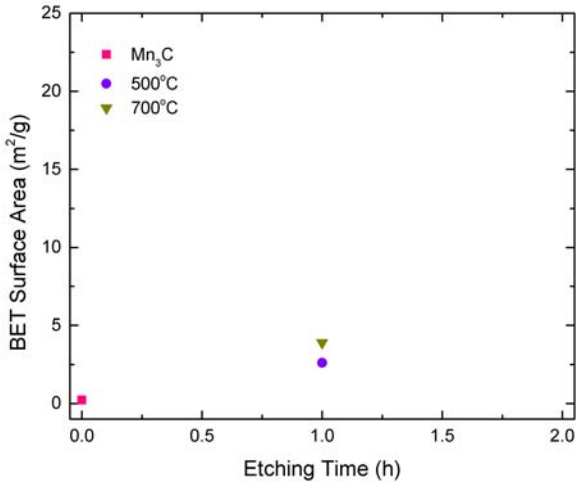

Figure A.65 – BET surface areas for samples etched at 500 and 700°C for 1 h.

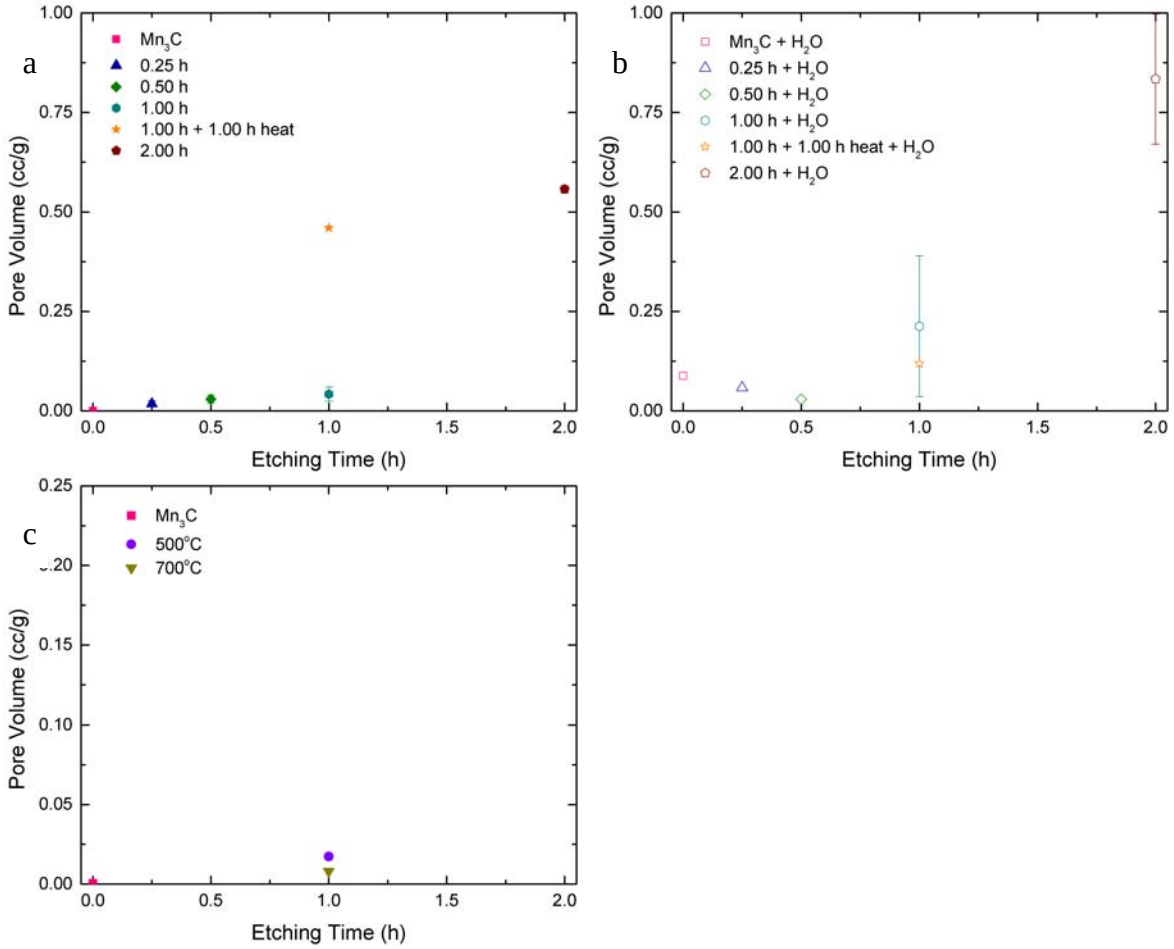

Figure A.66 – Pore volumes for (a) samples etched at 900°C, (b) samples etched at 900°C and soaked in water, and (c) samples etched at 500 and 700°C.

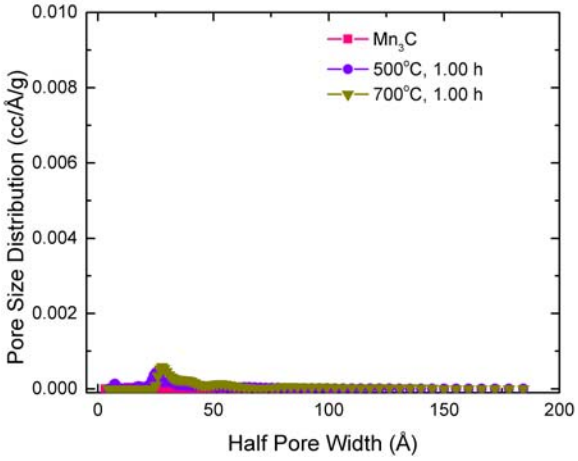

Figure A.6.67 – PSD for samples etched at 500 and 700°C for 1 h.

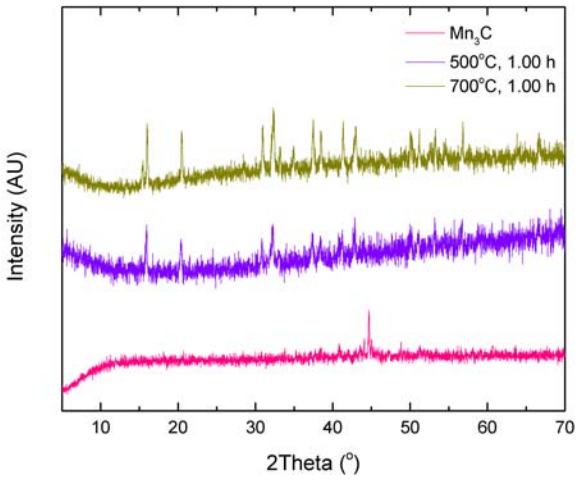

Figure A.68 – PXRD patterns for samples etched at 500 and 700°C for 1 h.

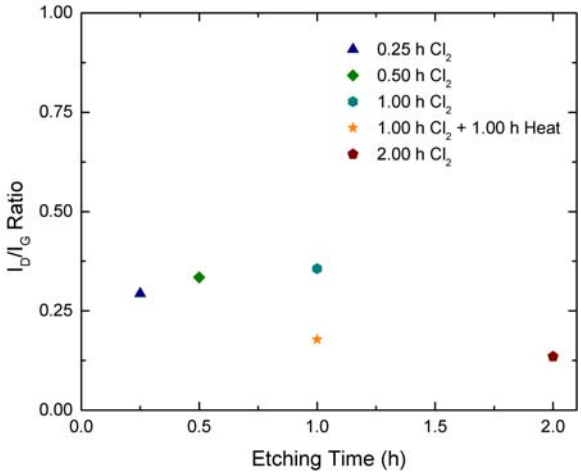

Figure A.69 – I_D/I_G ratios based on Raman spectra for samples etched at 900°C.

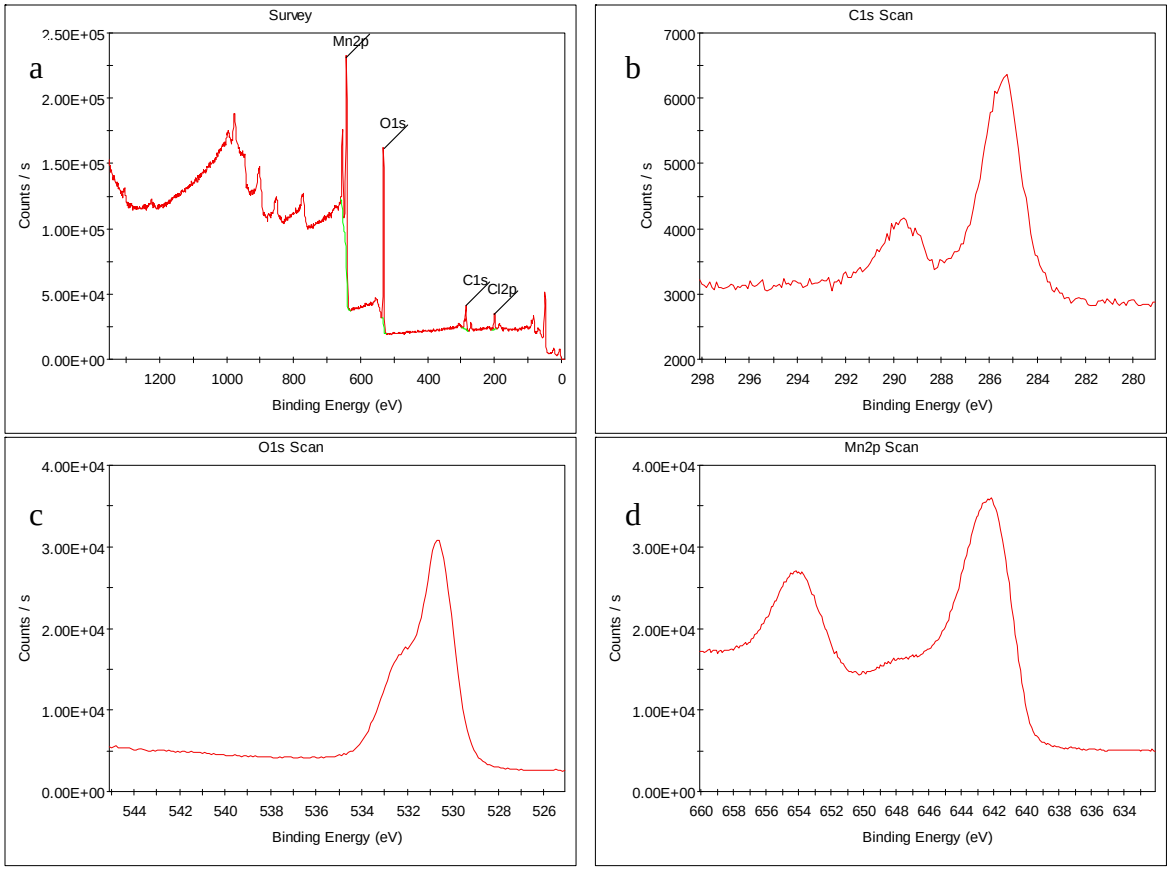

Figure A.70 – XPS spectra for Mn_3C for the (a) overall, (b) carbon, (c) oxygen, and (d) manganese scans.

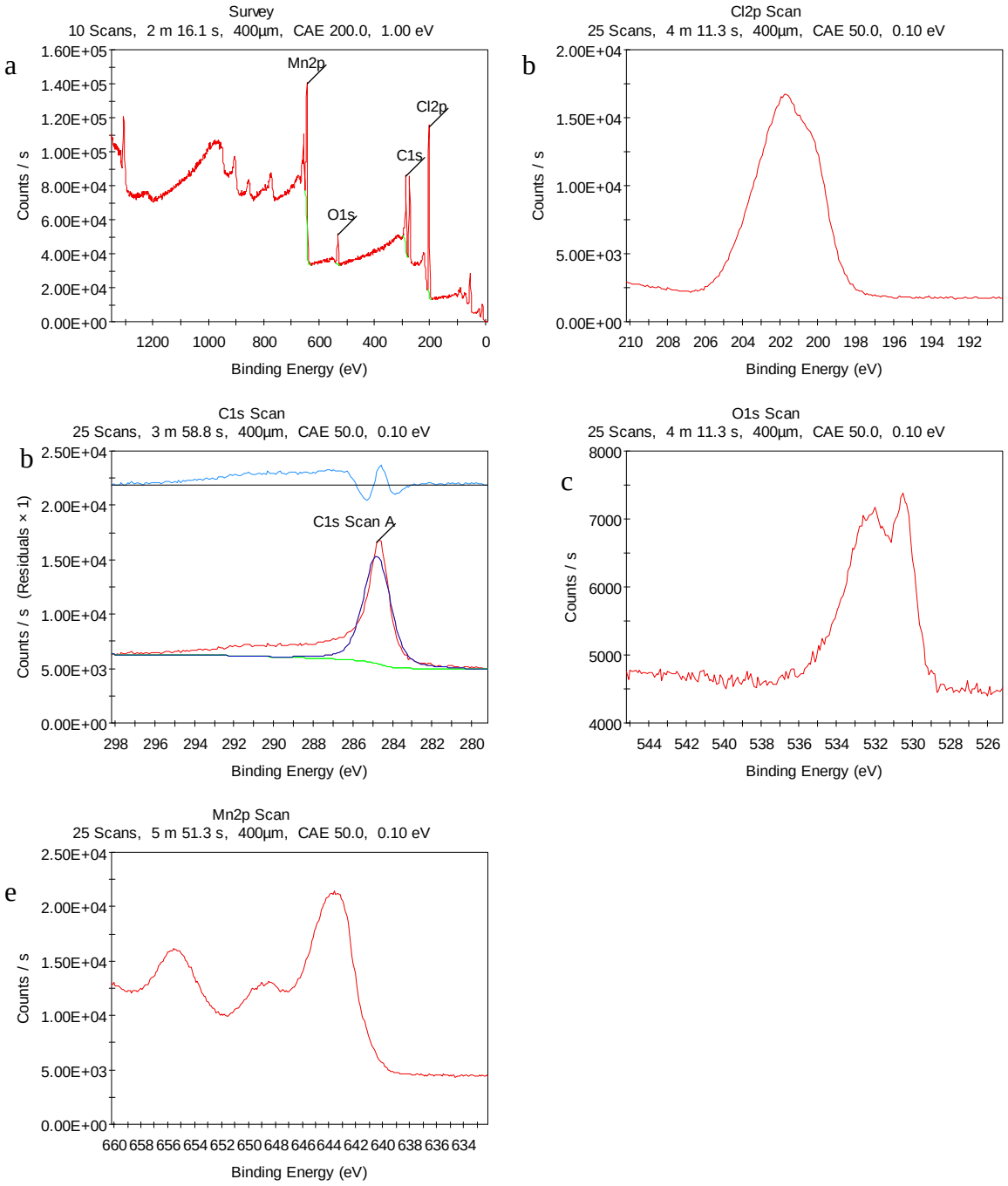

Figure A.71 – XPS spectra for Mn_3C-CDC etched for 0.25 h for the (a) overall, (b) chlorine, (c) carbon, (d) oxygen, and (e) manganese scans.

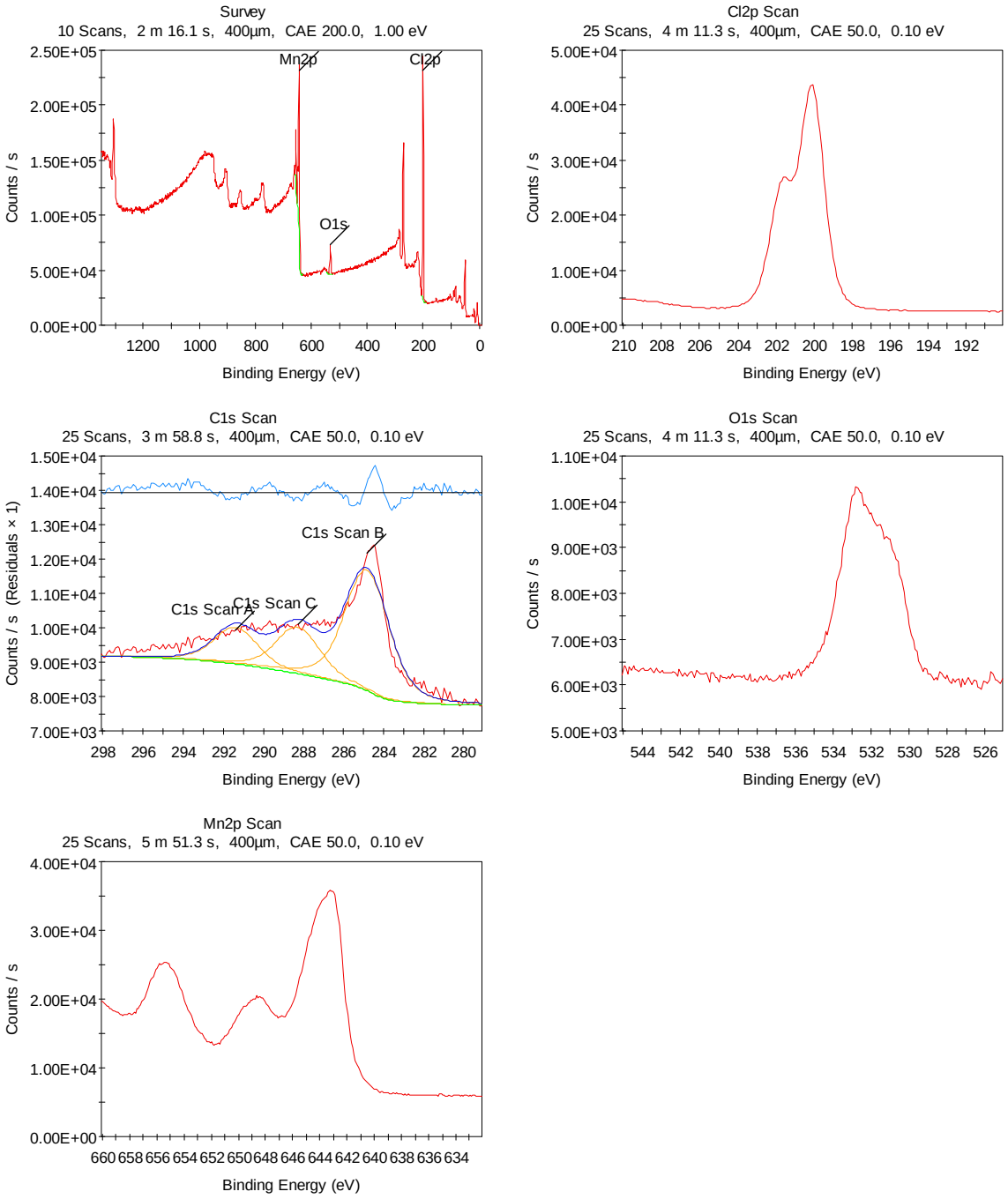

Figure A.72 – XPS spectra for Mn_3C-CDC etched for 0.50 h for the (a) overall, (b) chlorine, (c) carbon, (d) oxygen, and (e) manganese scans.

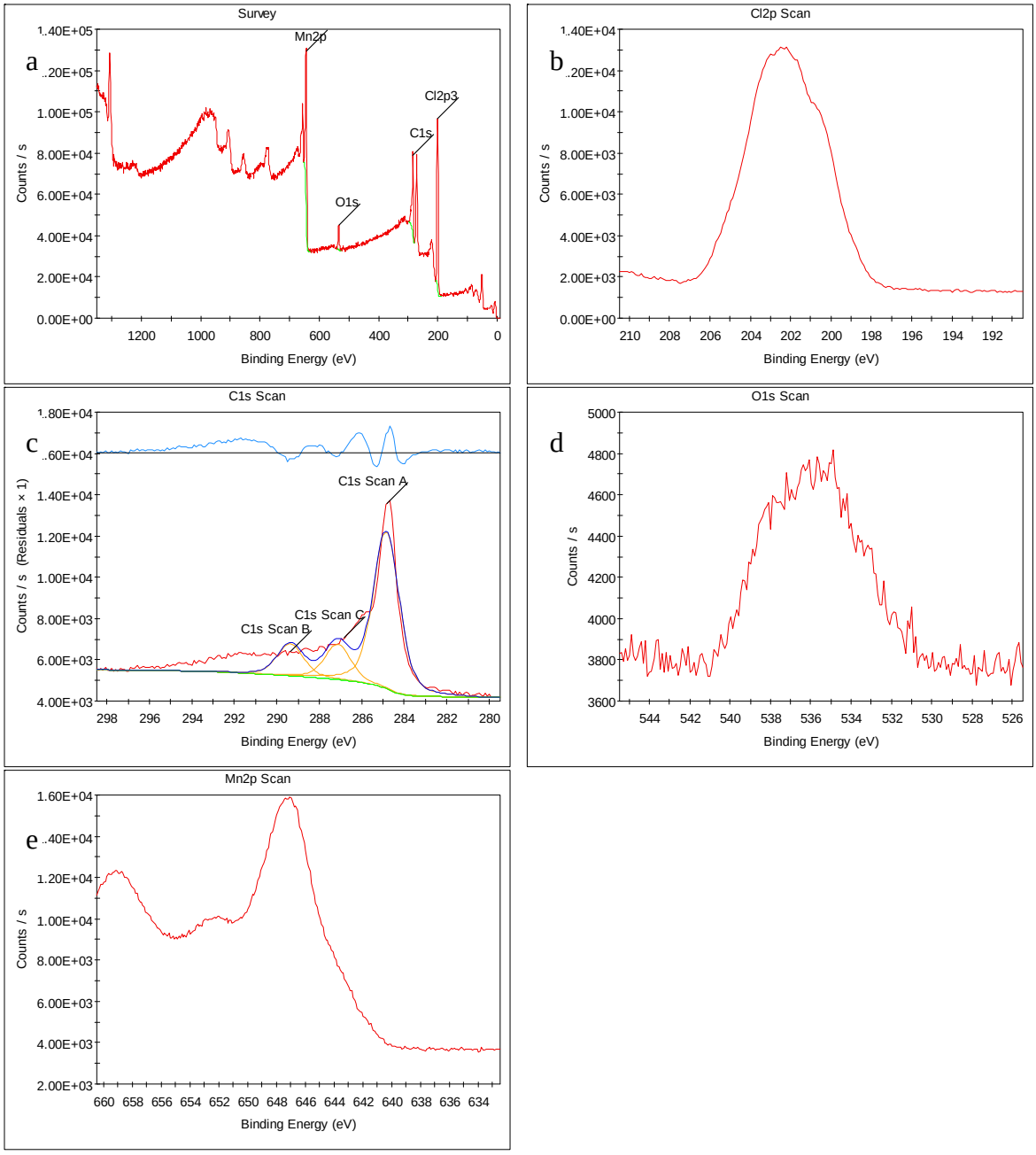

Figure A.73 – XPS spectra for Mn_3C-CDC etched for 1.00 h for the (a) overall, (b) chlorine, (c) carbon, (d) oxygen, and (e) manganese scans.

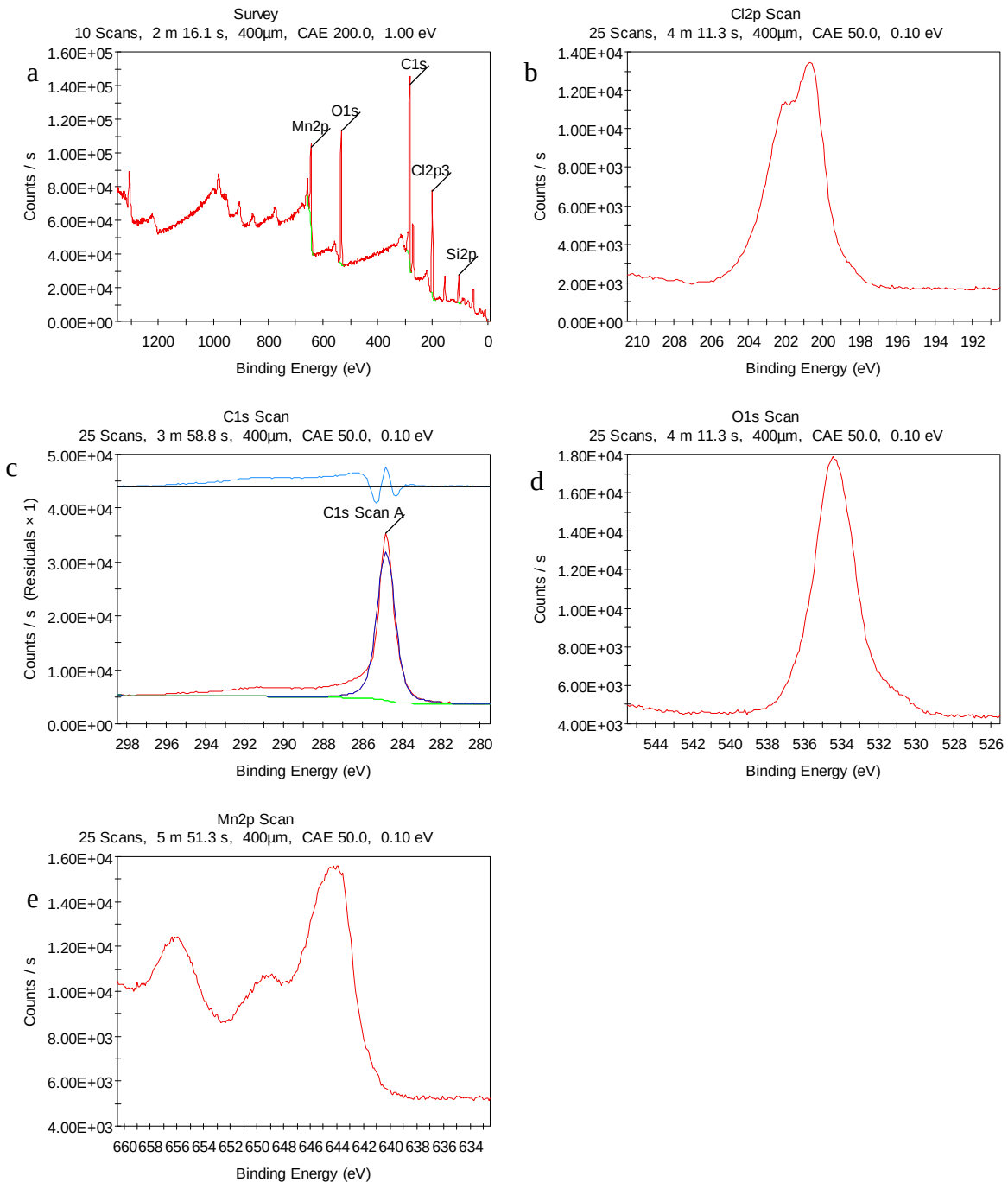

Figure A.74 – XPS spectra for Mn_3C-CDC etched for 1.00 h and held at temperature for an additional 1.00 h for the (a) overall, (b) chlorine, (c) carbon, (d) oxygen, and (e) manganese scans.

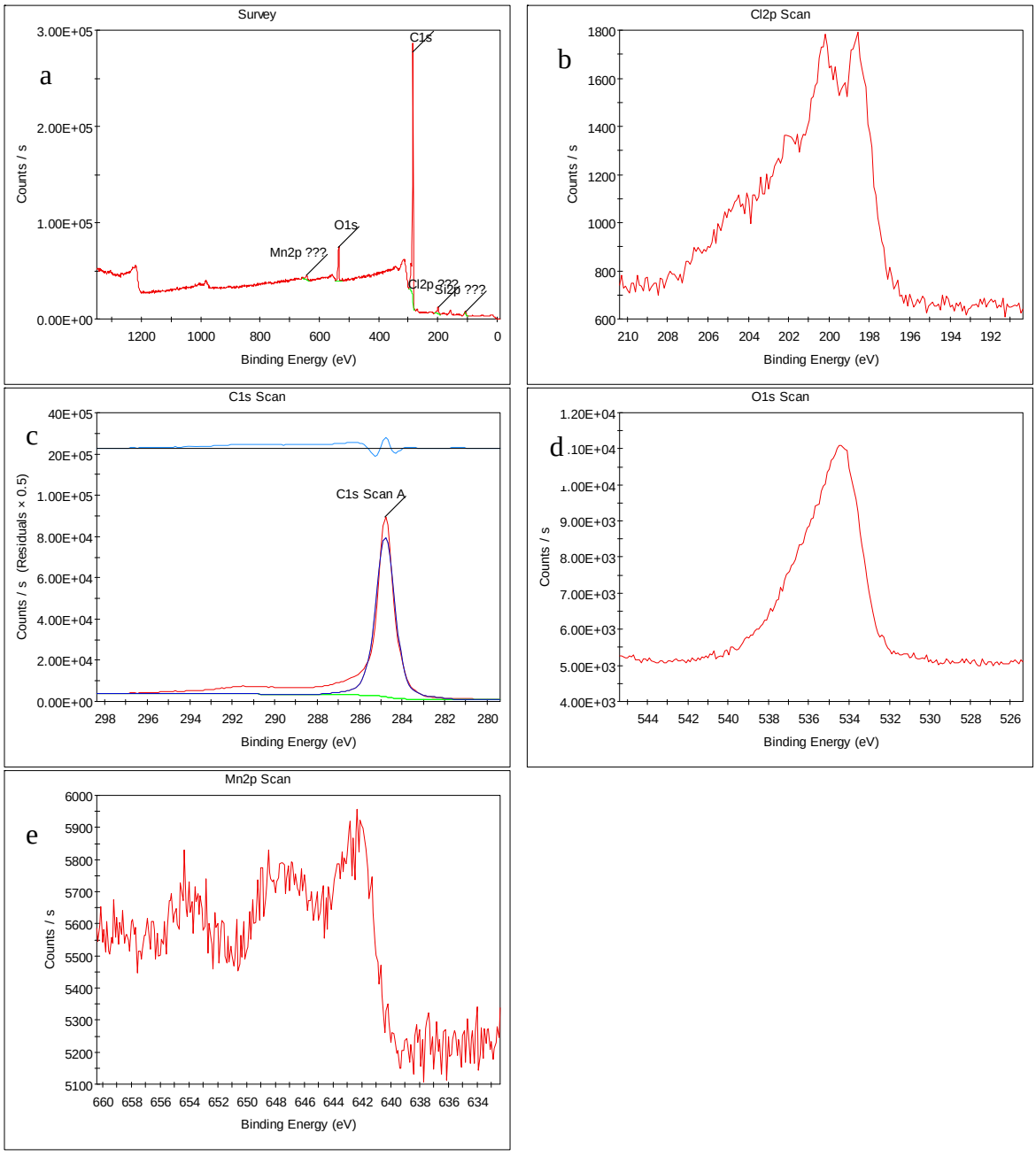

Figure A.75 – XPS spectra for Mn_3C-CDC etched for 2.00 h for the (a) overall, (b) chlorine, (c) carbon, (d) oxygen, and (e) manganese scans.

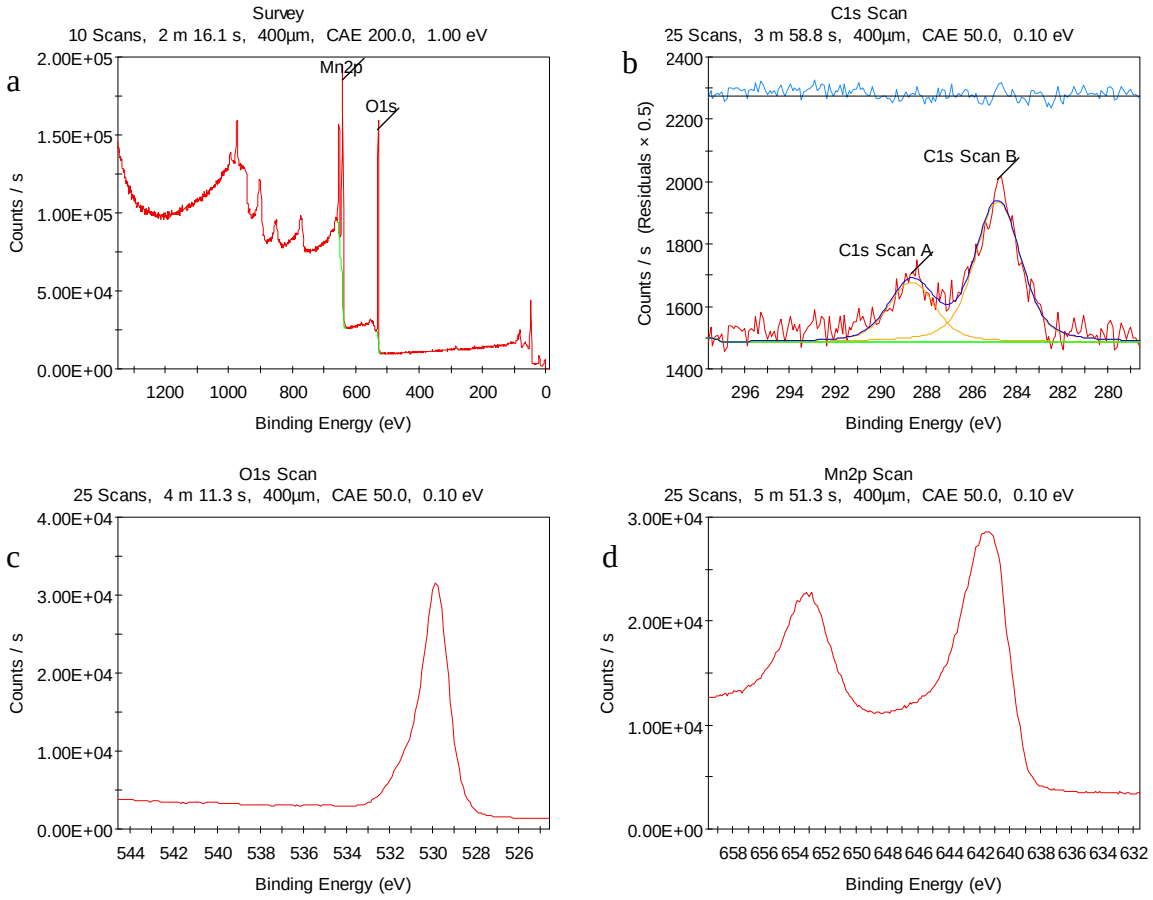

Figure A.76 – XPS spectra for Mn_3C soaked in water for 24 h for the (a) overall, (b) carbon, (c) oxygen, and (d) manganese scans.

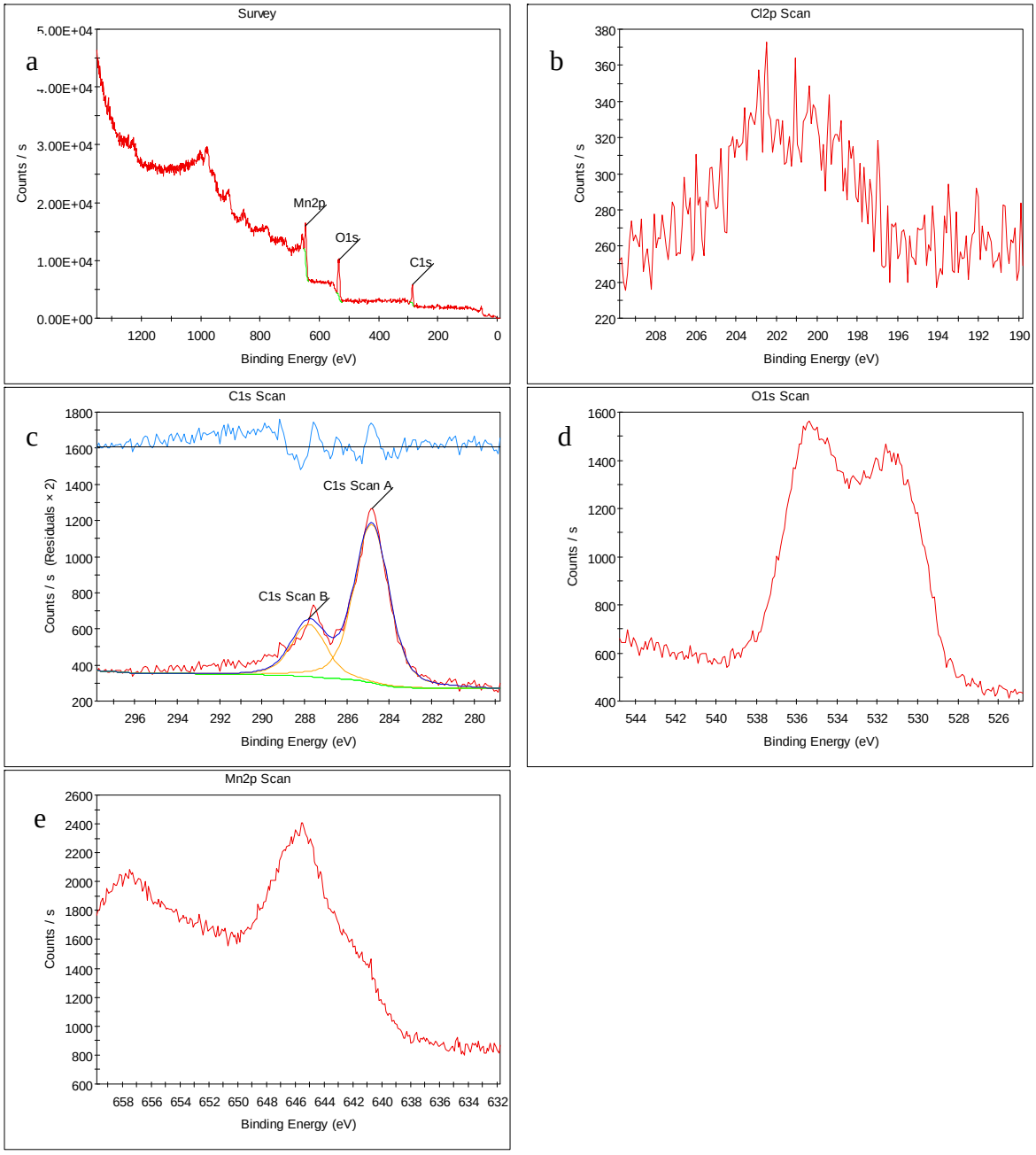

Figure A.77 – XPS spectra for Mn_3C-CDC etched for 0.25 h and soaked in water for 24 h for the (a) overall, (b) chlorine, (c) carbon, (d) oxygen, and (e) manganese scans.

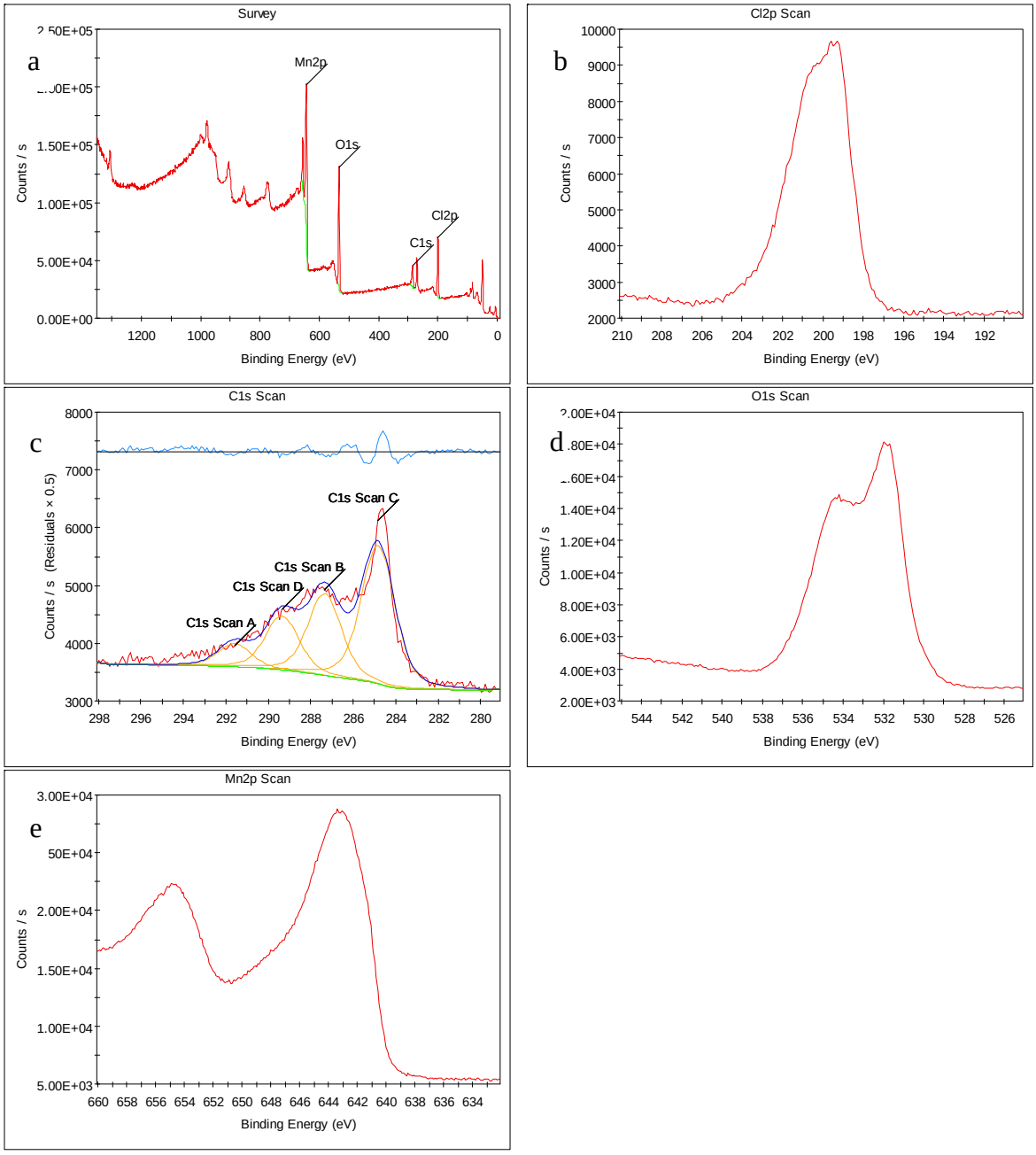

Figure A.78 – XPS spectra for Mn_3C-CDC etched for 0.50 h and soaked in water for 24 h for the (a) overall, (b) chlorine, (c) carbon, (d) oxygen, and (e) manganese scans.

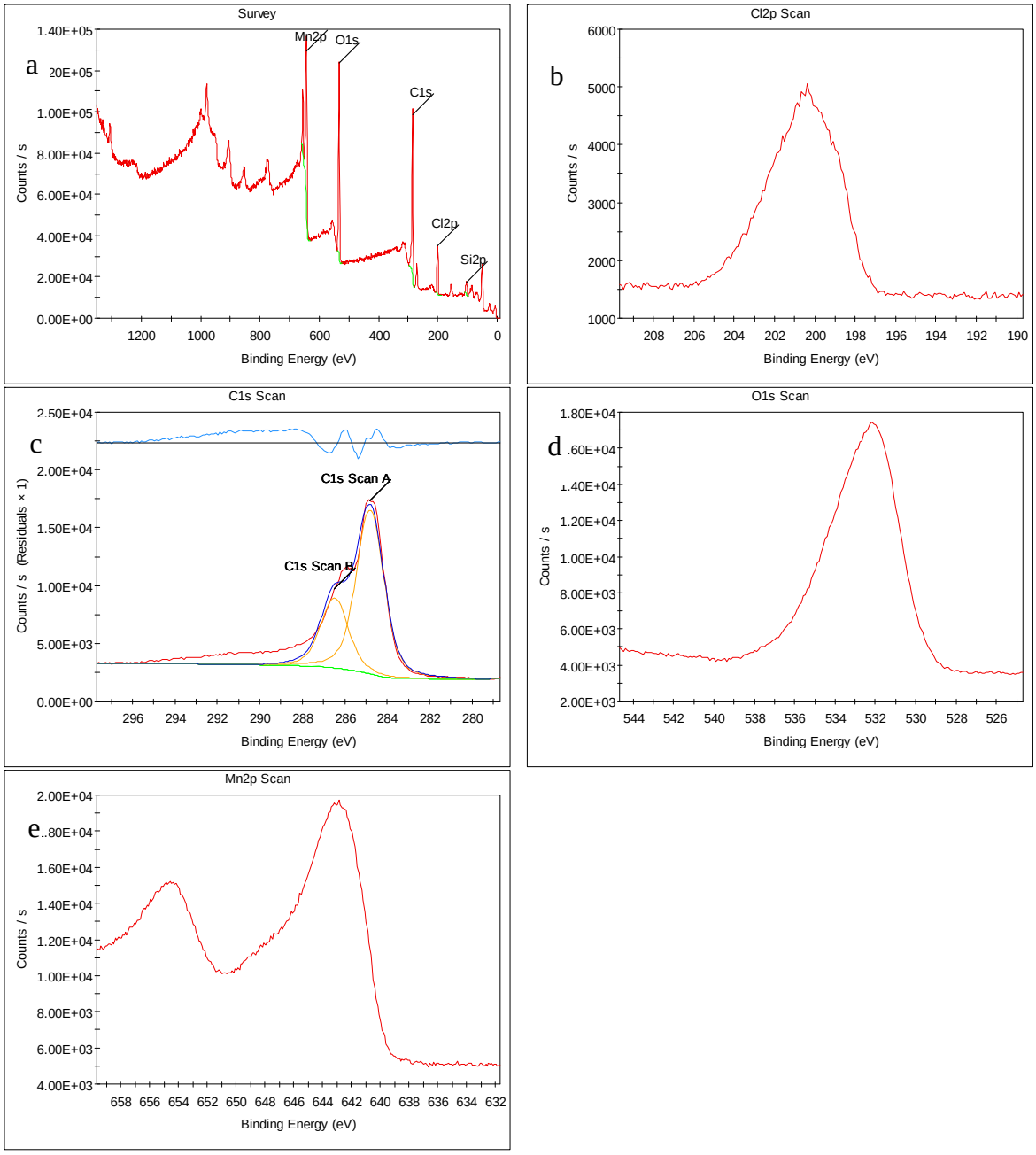

Figure A.79 – XPS spectra for Mn_3C-CDC etched for 1.00 h and soaked in water for 24 h for the (a) overall, (b) chlorine, (c) carbon, (d) oxygen, and (e) manganese scans.

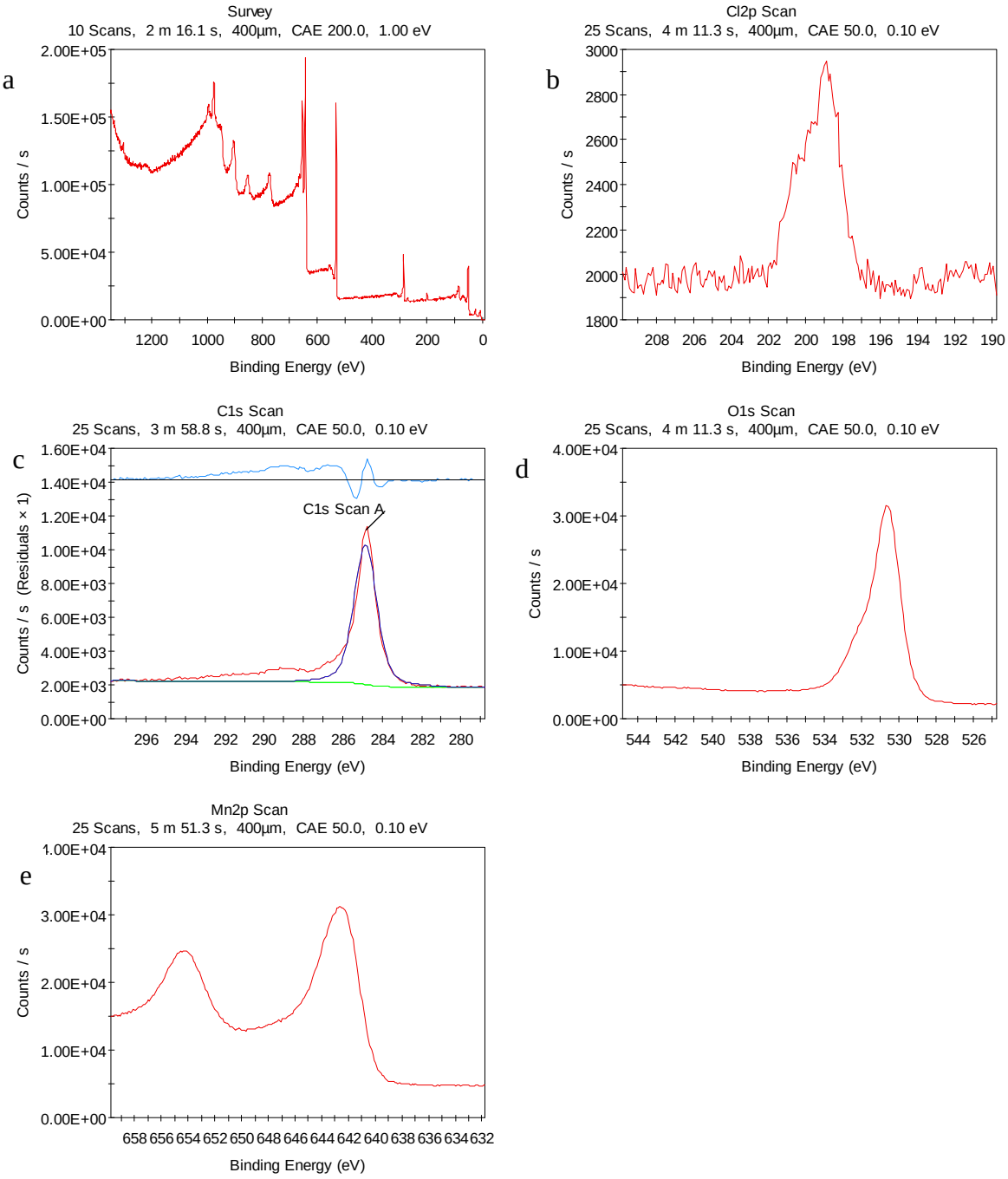

Figure A.80 – XPS spectra for Mn_3C-CDC etched for 1.00 h, held at temperature for an additional 1.00 h, and soaked in water for 24 h for the (a) overall, (b) chlorine, (c) carbon, (d) oxygen, and (e) manganese scans.

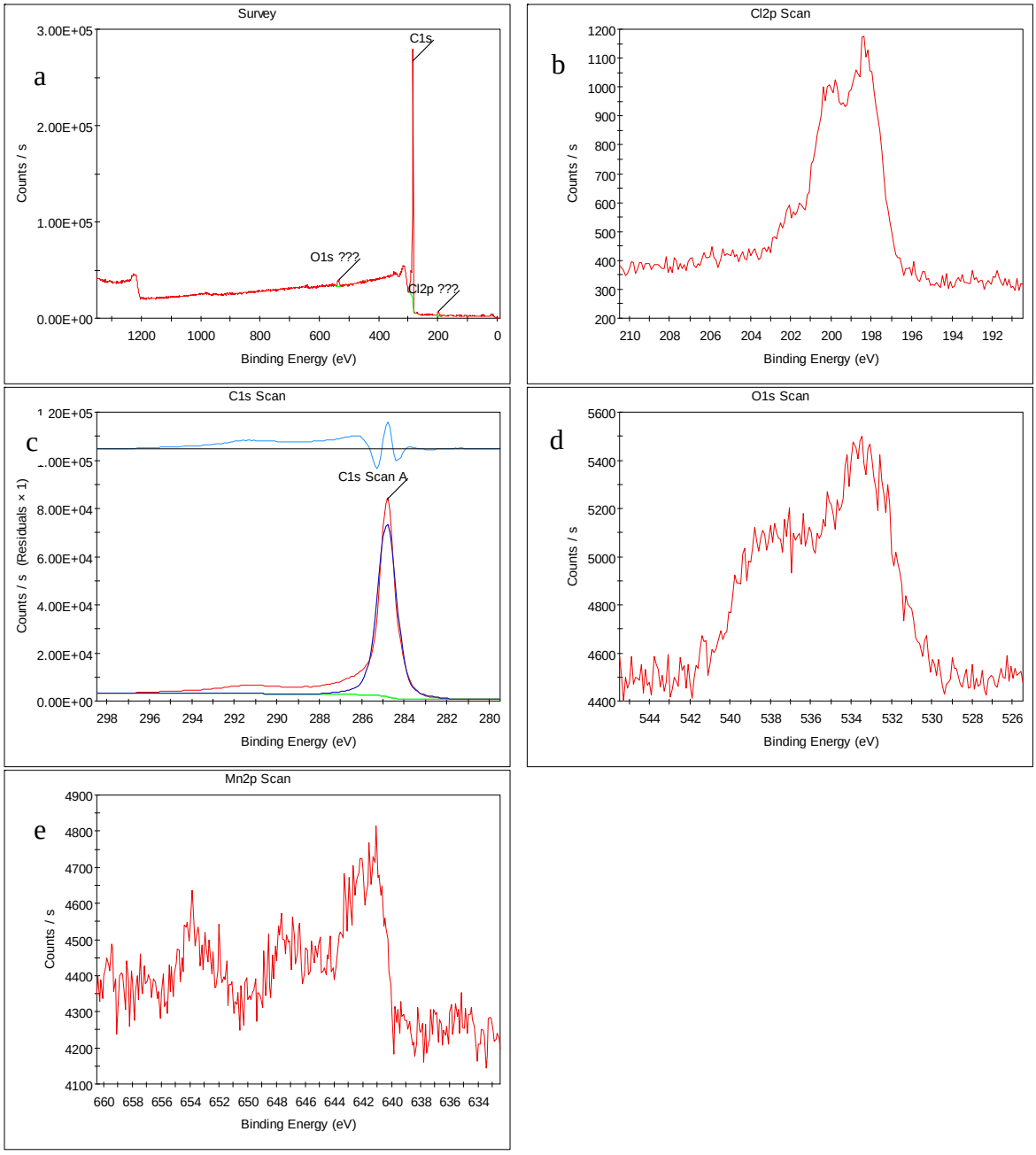

Figure A.81 – XPS spectra for Mn_3C-CDC etched for 2.00 h and soaked in water for 24 h for the (a) overall, (b) chlorine, (c) carbon, (d) oxygen, and (e) manganese scans.